An Investigation of Isodynes in Coarse Grained Ionic Liquid Models

Peter Alexander Knudsen
PhD Thesis in Physics
Roskilde University

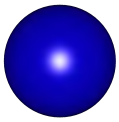

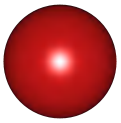

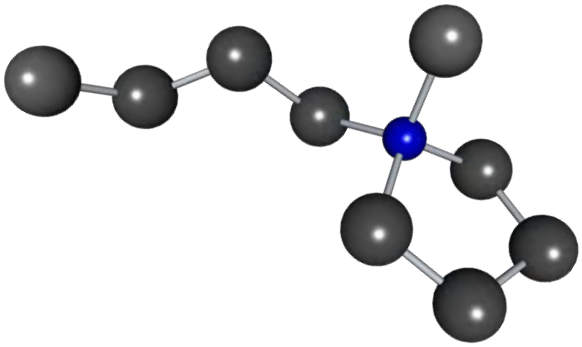

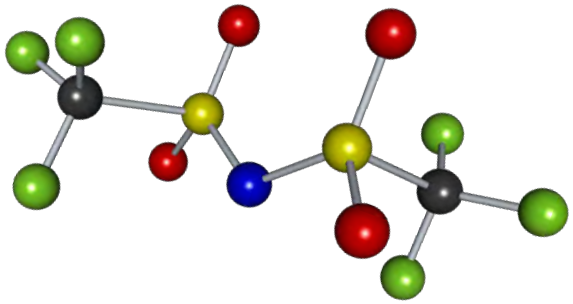

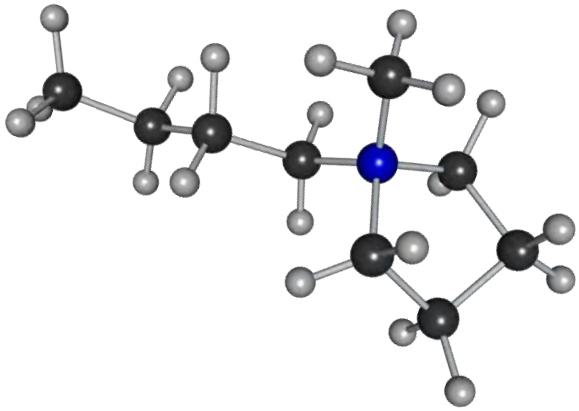

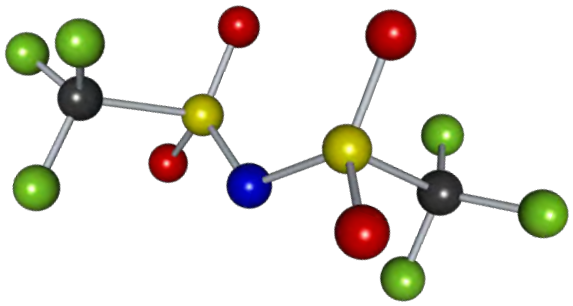

INM - Roskilde University

PhD in Physics

An Investigation of Isodynes in Coarse Grained Ionic Liquid Models

Author:
Peter A. Knudsen

Supervisors:
Nicholas P. Bailey
& Kristine Niss

2019 - 2022

This thesis has been submitted to the PhD School of Science and Environment

Contents

List of Figures

List of Tables

Abstract

Since the end of the 20th century there has been a rapidly increasing interest in ionic liquids because of their potential applications. *Hansen et al., Phys. Chem. Chem. Phys. 22, 14169 (2020)* studied experimentally an ionic liquid and found that many dynamical quantities were invariant along certain lines. Along these lines, they also found the main peak structure factor to be invariant, while the charge peak decreased in intensity and got shifted to lower reduced wavenumbers as temperature increased.

We investigate ionic liquids using the framework of isomorph theory, which predicts that some systems have lines in the phase diagram, where structure and dynamics are invariant. The structure was not invariant in the experimental study, however, we found isomorph theory to be a useful tool for analysing lines of invariant dynamics.

We analyse the structure and dynamics of three ionic liquid models using molecular dynamics computer simulations. The three models have different amounts of detail in order to isolate what features cause different behaviours of the liquid. This includes the simple *atomic* salt model from *Hansen and McDonald, Phys. Rev. A 11, 2111 (1975)*, a *molecular* united atom model of the ionic liquid $Pyr_{14}TFSI$ which was analysed in *Hansen et al.*, and a *molecular* all-atom model of the same ionic liquid.

We find that both the atomic and molecular models have curves in the phase diagram where dynamics are invariant. This includes diffusion coefficient, viscosity and characteristic times from the self-intermediate scattering function. All models also obey the reduced Stokes-Einstein relation. Furthermore, for the molecular models we found that some molecular-rotations showed invariance along these curves. The molecular-rotations, which showed invariance, seemed to be the ones with high moment of inertia. We refer to these curves of invariant dynamics as "*isodynes*". In *Hansen et al.*, isodynes were only analysed in a density range of 2%. However, for the molecular models we analysed different density ranges around 20% and found isodynes in the entire interval. For the atomic model an isodyne was analysed where the density was changed by a factor of 6.6 and showed only small to no changes in dynamics for the entire interval. This tells us that isodynes are a very stable feature of ionic liquids, and cover a much broader part of the phase diagram than what was shown experimentally. This is one of the main results of this work.

Although, the united atom model is between 2-3 times faster than the all-atom model, the shape of isodynes in the united atom model are still very good approximations of the isodynes in the all-atom model. This means that the hydrogen does not change the overall dynamical behaviour significantly, other than slowing down everything.

We also analyse the structure factor peaks along these isodynes. We find that the charge peak show the same changes as in the experiment for all three models. Since this behaviour was also present in the simple atomic model its cause must be found in the charge interaction and not in the molecular structure (which is not present in that model). *Hansen et al.* reported the main structure factor peak to be invariant, however, we find this to be a consequence of the limited density range, which was studied. When limiting the density range to 2% we also see the main peak to be invariant, and thus is in agreement with the experimental study.

For the molecular models, we find a substructure between close ion pairs. This substructure was analysed for the united atom model. We find it is caused by the interactions between the tetrahedral structure in the cation and N^- in the anion. This creates a preferred orientation of the anion relative to the cation, which allows the pair to get close together. This substructure was most prevalent in the high density, low temperature region, and was shown to be varying along isodynes. The significance of this substructure is unknown. However, based on partial redial distribution functions we believe that this substructure is present in the all-atom model and might be even more pronounced than in the united atom model.

Lastly, we perform a study of the preferred orientations of the cation tail for the united atom model. We found that the part of the tail closest to the ring is dominated by intra-molecular interactions. On the other hand, the end of the tail is affected by the surrounding molecules. Here the end of the tail shows some invariance along isodynes.

Resume (in Danish)

Siden slutningen af det 20. århundrede har der været en stadig stigende interesse i ionvæsker grundet deres potentielle applikationer. *Hansen et al., Phys. Chem. Chem. Phys. 22, 14169 (2020)* foretog eksperimentelle studier af ionvæsker og fandt bestemte linjer, hvor flere dynamiske egenskaber er invariante. De fandt, at langs disse linjer er det primære maximum i strukturfaktoren invariant, og ladnings-maximum falder i intensitet og bliver skubbet til lavere reducerede bølgenumre ved stigende temperaturer.

Vi undersøger ionvæsker ved at anvende isomorfteorien, som forudser at visse systemer har linjer i fasediagrammet med invariant struktur og dynamik. Strukturen var ikke invariant i det eksperimentelle studie, men vi finder stadig at isomorfteorien er et brugbart redskab til at analysere linjer med invariant dynamik.

Vi analyserer strukturen og dynamikken i tre ionvæskemodeller via molekylærdynamiske computersimuleringer. De tre modeller har forskellige mængder af detaljer for at isolere hvilke egenskaber, der forårsager hvilken opførsel i væsken. Dette inkluderer den simple *atomare* saltmodel fra *Hansen and McDonald, Phys. Rev. A 11, 2111 (1975)*, en *molekylær* forenet-atom saltmodel af ionvæsken $Pyr_{14}TFSI$, som blev analyseret i *Hansen et al.*, og en *molekylær* al-atom model af den samme ionvæskemodel.

Vi fandt, at både den atomare og de molekylære modeller har kurver i fasediagrammet, hvor dynamikken er invariant. Dette inkluderer diffusionskoefficient, viskositet og karakteristiske tider for den intermediære spredningsfunktion. Alle modellerne overholder også den reducerede Stokes-Einstein relation. Vi fandt endvidere, at nogen molekylære rotationer var invariante langs disse linjer for de molekylære modeller. De molekylære rotationer, som viste invarians, havde højt inertimoment. Vi refererer til disse linjer med invariant dynamik som "*isodyner*". I *Hansen et al.* blev isodyner kun analyseret i et densitetsinterval på 2%. I vores molekylære modeller analyserede vi densitetsintervaller på 20% og fandt isodyner i hele intervallet. For den atomare model analyserede vi en isodyne, hvor densiteten blev ændret med en faktor 6,6 og viste kun små til ingen dynamiske ændringer i hele intervallet. Dette fortæller os at isodyner er en meget stabil egenskab for ionvæsker, og den dækker en meget større del af fasediagrammet end hvad tidligere er blevet vist eksperimentelt. Dette er et af hovedresultaterne fra dette projekt.

Selvom at den forenet-atom model er 2-3 gange hurtigere end al-atom modellen er formen på den forenet-atom models isodyner stadig gode approksimationer af isodynerne for al-atom modellen. Dette betyder, at hydrogen ikke ændrer den overordnede dynamiske opførsel signifikant udover at gøre alt langsomere.

Vi analyserede også struktur faktor maxima langs isodyner. Vi fandt, at i alle tre modeller havde ladnings-maximum samme opførsel som i eksperimentet. Da denne opførsel også er tilstede i den atomare model må den være forårsaget af

ledningerne og ikke den molekylære struktur (som ikke er tilstede i denne model). *Hansen et al.* rapporterede, at det primære maximum i struktur faktoren er invariant, men vi fandt, at dette er en konsekvens af det begrænsede densitetsinterval, som blev analyseret. Når vi begrænser densitetsintervallet til 2% for vores data, ser vi også at det primære maximum er invariant.

For de molekylære modeller fandt vi en substruktur imellem tætte ionpar. Denne substruktur blev analyseret for den forenet-atom model. Vi fandt, at substrukturen kom fra interaktionerne mellem tetrahedral strukturen i kationen og N^- i anionen. Dette skaber en foretrukken orientering for anionen relativt til kationen, hvilket tillader ionerne at komme tættere sammen. Denne substruktur var mest udbredt ved høje densiteter og lave temperaturer, og er ikke invariant langs isodyner. Signifikansen af denne substruktur er ukendt. Baseret på partiel radial distributions funktioner, tror vi at denne substruktur er tilstede i al-atom modellen og kunne endda være mere udtalt end i den forenet-atom model.

Tilsidst studerede vi den foretrukne orientering af kation-halen for den forenet-atom model. Vi fandt, at den del af halen som er nærmest ringen var domineret af intra-molekylære interaktioner. Enden af halen er derimod påvirket af de omkringliggende molekyler. Her viser enden af halen en delvis invarians langs isodyner.

Acknowledgements

First and foremost I would like thank my supervisor Professor *Kristine Niss* for initially approaching me about this PhD position. If not for her I would not have started this journey. Since the main focus of this project is computational Lector *Nicholas P. Bailey* got involved very early in the process and later became my primary supervisor. I would like to thank them both for being there and guiding me on this journey.

As a part of this project I became a member of the *Glass and Time* research group at Roskilde University. I would like to thank the *Glass and Time* group for their input to my work and for the perspective I gained from hearing about and discussing their research.

A PhD is a learning process, and since I did not have much experience in this field beforehand there was a lot to learn. This demanded a lot of reading and studying, ans I would like to thank *Lorenzo Costigliola* for being there afterwards to discuss the different concepts with me. He also help me with programming and simulation problems I encountered along the way, which increased my intuition about the methods. IT problems are bound to occur during a project like this, and I am grateful that *Heine Larsen* was there to help me for which he deserves a great thanks.

Despite the global pandemic I got the opportunity to study in London at Imperial College for a couple of months. Here I became a part of the *Tribology Group* in the Department of Mechanical Engineering under the supervision of Professor *Daniele Dini*. I would like to thank the *Tribology Group* for welcoming me with open arms and helping me with problems both related to my research but also those which can arrive when travelling to a different country. However, a huge thanks goes to my local supervisors during my stay Professor *Daniele Dini* and Professor *David M. Heyes*, for their amazing insight, kindness, and interest in my project. I always found their input helpful and encouraging which was a blessing when things were difficult or did not work.

As a person with a diagnose of mild dyslexia I am very grateful to the people who helped me read through this work. Their input has undoubtedly increased its quality and understandability. For this effort a special thanks goes to *Pia I. Larsen*, *Kira L. Eliasen*, *Lorenzo Costigliola*, *Ian M. Douglass* and of course both of my supervisors *Kristine Niss* and *Nicholas P. Bailey*.

Lastly, but definitely not least, I would like to thank my loving and supporting family and friends. Despite not understanding much of my work they still listened to my excited rambles about new results and frustrated grumble over a new problem. But most importantly they help me with personal struggles and they supported me when things seemed unmanageable. Thank you all!

Chapter 1

Introduction

Molten salts and ionic liquids

We do not often encounter molten salts in our everyday life due to their high melting points. A well known example of this is kitchen salt (NaCl), which has a melting point of 801 °C at ambient pressure. This and many other scientific works are interested in the subgroup of molten salts, that are liquid at room temperature. More specifically, the melting points are less than 100 °C [Walden, 1914]. This subgroup has different names such as *room temperature molten salts* and *room temperature ionic liquids*. However, we will simply refer to it as *ionic liquids* (ILs) which is commonly used in the literature.

The interest in ILs has increased massively since the end of the 20th century. This is because of their potential use in different technologies, e.g. solar cells [Zakeeruddin and Grätzel, 2009], as solvents in batteries [Webber and Blomgren, 2002], and as lubricants [Ye et al., 2001]. ILs are desired in these fields because they can be designed to have different physical properties. Consequently, ILs were famously referred to as "*designer solvents*" in Freemantle [1998] due to their flexibility in combining and designing cations and anions. Some examples of common chemical structures for cations and anions are illustrated in Fig. 1.1.

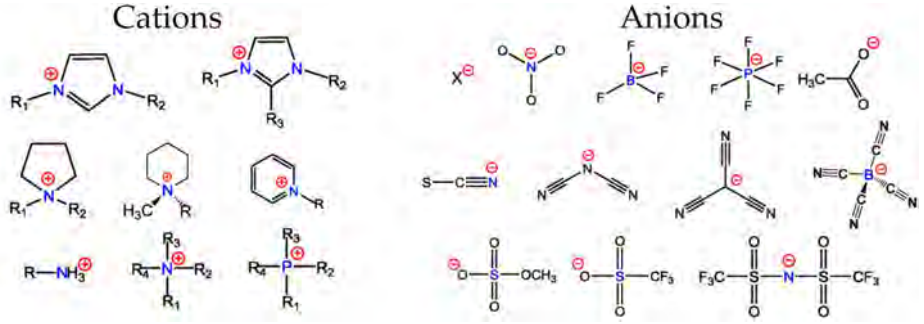

Figure 1.1: Modified version of Fig. 1 from Wang et al. [2020]. Examples of chemical structures of typical cations and anions for ILs.

The low melting points of ILs are believed to be caused by the size and asymmetry of the ions, which affect their packing [Hallett and Welton, 2011]. Additionally, properties inherent for all ILs are a low vapour pressure, and consequently low flammability [Freemantle, 1998]. This is associated with their low melting points and strong Coulomb interactions [Bier and Dietrich, 2010]. These two qualities alone, make ILs safe to use because they ensure the liquid will not vaporise or ignite as easily as other alternatives. An example could be the IL $[C_4mim][PF_6]$, which was found to have a vapour pressure of 100 pPa at 25 °C [Paulechka et al., 2003]. For comparison, the vapour pressure of water at the same temperature is 3.1690 kPa [Lide, 2004], which is a difference of 10^{13}. However, before their potential application can be realized we need a better understanding of the behaviour of ILs. Hence the rapid development of this scientific field.

Inspiration for this work

A historical overview of ILs with a focus on experimental results can be found in Welton [2018]. It covers the earliest works like Walden [1914] to present day. However, in this section we only go through works, that explain key concepts of ILs or that directly inspired the direction and goal of this work.

The structure of different ILs has already been studied using both experiments and simulations. This had led to the understanding of some structural features, which seem to be general for ILs. These are nicely illustrated by Araque et al. [2015], who used small angle X-ray scattering on a series of ILs. These features involve two extra peaks in the structure factor, that appear as a consequence of long range structures in the liquid. The three peaks can be seen for different ILs in Fig. 1.2, which shows Fig. 1a from Araque et al. [2015]. The interpretation of these three structure factor peaks for ILs (in order of decreasing q) is:

1. The *main peak* arises from the periodic distance between neighbouring ions. Consequently, it is also referred to as the *adjacency peak*.

2. The presence of charges creates a preference of neighbouring molecules to be of different types. Consequently, this creates a periodic structure that reaches longer than the molecule neighbour distance. This results in an extra peak in the structure factor which, due to its causation, is called the *charge peak*.

3. Lastly, some ILs have cations with long alkyl chains (sometimes referred to as tails). This has been shown to add polarity to the liquid, which creates a periodic structure that reaches even longer than the charge peak. These long range structures create a peak in the structure factor called the *polarity* or the *pre-peak*.

This correlation between the cation's tail length and the long range structure, that causes the pre-peak, was illustrated in Fig. 1a from Aguilera et al. [2015] (see Fig. 1.2). The aim of this work was to investigate how lithium salt doping effects the structure of two families of ILs with different tail lengths. This was done using small-angle X-ray scattering experiments, with the goal to further increase knowledge, which leads to ILs' application in batteries. They found that lithium salt doping greatly affected the length scale, which gives rise to the charge peak. However, they also analysed the structure of these ILs with no lithium salt, and found a clear connection between the tail length and the structure causing the pre-peak.

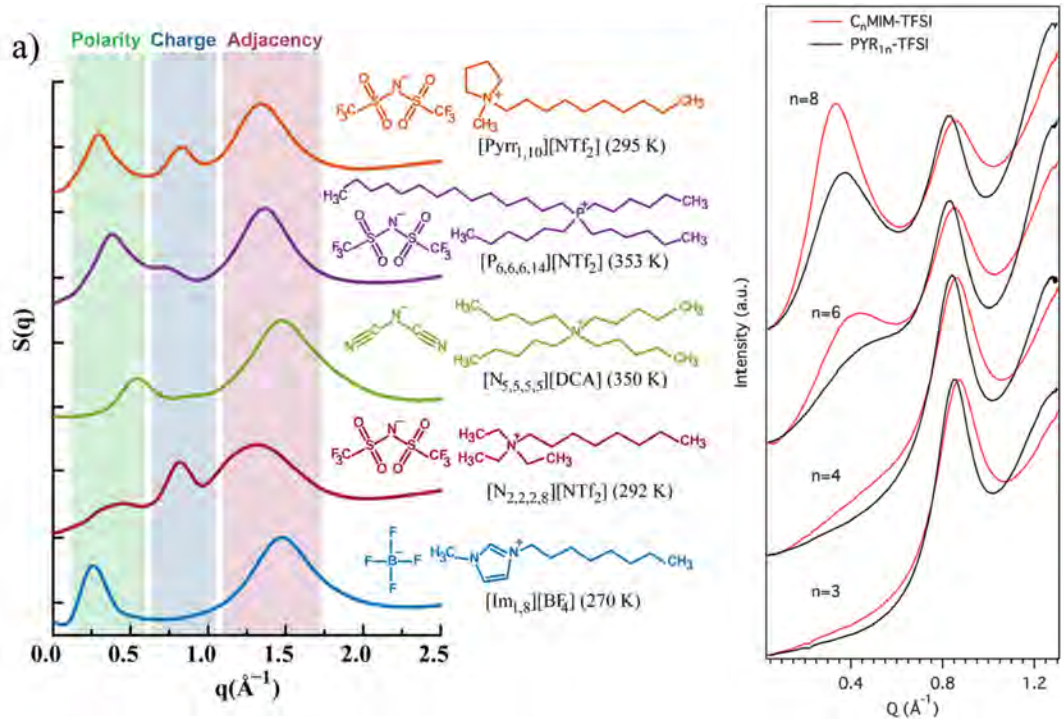

Figure 1.2: Structure factor peaks for ionic liquids obtained with small-angle X-ray scattering.
(Left) Fig. 1a from Araque et al. [2015]. Structure factor peaks for different ILs. There are three types of peaks; pre-peak (polarity), charge peak, and main peak (adjacency).
(Right) Fig. 1a from Aguilera et al. [2015]. Structure factor peaks for two families of ILs with varying tail lengths. Different cation tail lengths are shown here; $n = 3$, $n = 4$, $n = 6$, and $n = 8$. Both the main and charge peaks are present at all tail lengths. However, there is a clear correlation between the tail length and the length scale, which gives rise to the pre-peak.

The dynamics of ILs has also been a subject of great study. A part of this involved testing if density scaling applies to ILs. The idea of density scaling is that the dynamics of a system depends on the specific combination of density and temperature i.e. $\Gamma = \rho^{\gamma}/T$, where ρ is density, T is temperature, and γ is the density scaling exponent. One result from López et al. [2011] showed that for six ILs the viscosity, electrical conductivity and molar conductivities have similar γ.

With this understanding of ILs' structure and dynamics Hansen et al. [2020] asked the question of: "*how these nano-scale structures influence transport properties and dynamics on different timescales* ". To answer this question, Hansen et al. [2020] studied the IL $Pyr_{14}TFSI$ for a wide range of structure, dynamics and transport properties using different methods. This IL is similar to the first IL in Fig. 1.2 but with a shorter tail, which is why $Pyr_{14}TFSI$ does not have a pre-peak. The Hansen et al. [2020] study included; the structure factor with X-ray scattering, conductivity with dielectric spectroscopy, and microscopic dynamics with neutron spectroscopy. They also used viscosity and self-diffusion data from literature. With this data, they tested if density scaling applies for the system. They found that not only does it apply for all the dynamics (charge transport, microscopic α-relaxation, phonon dynamics, viscosity and self-diffusion data), they all have the same density scaling exponent $\gamma = 2.8$. Furthermore, they found that when presenting the structure factor as a function of $\tilde{q} = \rho^{-1/3}q$ the main peak also obeyed density scaling. However, the same was not true for the charge peak. This can be seen in Fig. 1.3, which shows Fig. 5b from Hansen et al. [2020]. The cause of this behaviour is not well understood, which leads to the subject of this work.

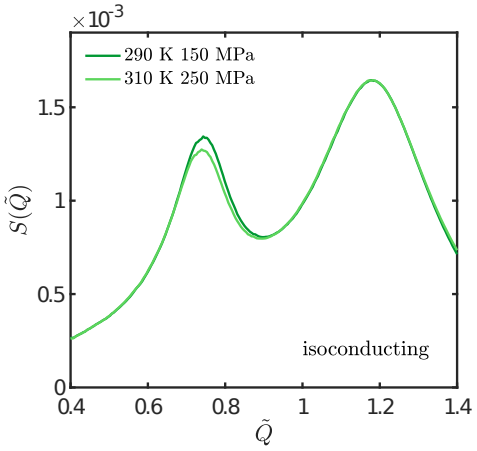

Figure 1.3: This is figure 5b from Hansen et al. [2020] showing X-ray data for the structure factor along lines of equal electrical conductivity. The main peak is invariant, while the charge-peak decreases in amplitude and gets shifted to lower q as the temperature increases.

The aim of this work

In this work, we would like to investigate this phenomenon further and try to explain the connection between structural and dynamical invariance. To do this, we would like to apply "*isomorph theory*" which has been developed at Roskilde University in Denmark since 2008. An in-debt explanation of isomorph theory will be provided in Chap. 4, but for now it is sufficient to know the following; isomorph theory is a theoretical framework, that applies to a special class of systems called "*R-simple*". When applying a specific scaling, the theory predicts structural and dynamical invariance along configurational adiabat, that is curves of constant excess entropy ($\Delta S_{ex} = 0$). If this is true, the curve is considered an isomorph.

The scaling of q used in Hansen et al. [2020] ($\tilde{q} = \rho^{-1/3}q$) is the same as in isomorph theory. However, the curve of constant electrical conductivity from Hansen et al. [2020] is not an isomorph, since the charge peak is not invariant. However, it has been shown that systems with Coulomb interactions generally do not have isomorphs [Dyre, 2014]. Instead we hypothesise that this curve could be an approximate isomorph, or related in some way. This hypothesis is based on the connection between isomorph theory and density scaling.

To test this, it would be interesting to find which dynamical quantities are invariant along the same curves in the phase diagram. Furthermore, it would be relevant to investigate the behaviour of the structure (especially the structure factor) along these lines. This has lead to the following research questions:

1. Do simulated ILs have lines in the phase diagram where multiple dynamical quantities are invariant? If so, how can these lines be found, and what dynamical quantities are invariant along them?

2. Which aspects of structure are invariant, and which ones are not invariant, along these lines of invariant dynamics?

3. What insight in the physics of ILs can be learned from the existence of lines with invariant dynamics, and which microscopic properties are invariant along them?

To our knowledge we are the first to analyse both structure and dynamics of ILs through the lense of isomorph theory.

Method

To answer these questions a computational approach was chosen because of the extra information, that can be obtained, e.g. exact particle positions. Different available methods come with benefits and limitations. *Monte Carlo* methods would only provide structural information, which is not sufficient. Alternatively, *quantum calculations* would provide detailed descriptions, but due to complexity the system size would be massively limited. As a result, we choose to use *molecular dynamics* (MD) computer simulations. MD was chosen because it allows us to analyse both structure and dynamics of "large" systems, which is necessary to answer our questions. It is also commonly used throughout the literature.

Furthermore, we would like to better understand, what IL features give rise to their properties. To do this, we analyse three different models with varying amount of detail, using *coarse-grained modelling*. The essence of coarse-graining is attempting to describe a complex system with a simple model. The argument being that if a simple model can capture the behaviour of a complex system, the details that are absent from the model must not be essential to the behaviour. The three IL models which we analyse are:

1. We analyse how charges affect a simple liquid system. To do this we choose the simple salt model from Hansen and McDonald [1975]. This model contains two types of point particles, which are identical in all respects except they have opposite charge.

2. We analyse how the molecular structure affects the structure and dynamics of ILs. To do this we choose an united atom model of the IL $Pyr_{14}TFSI$ which was used in Hansen et al. [2020]. In united atom modelling all CH-groups are represented by single spheres (in this case it only affects the cation).

3. We want to compare the united atom model with a more detailed all-atom representation of the same IL. In all-atom modelling all C and H atoms are represented by individual spheres. This model will not be studied as thoroughly as the united atom model, since its main purpose is to be used for comparison.

This should allow us to isolate the behaviour, that is caused by the charges, and those that arise as a consequence of the molecular structure. This will provide us with a detailed description of what features are responsible for the behaviour of ILs.

Roskilde University Molecular Dynamics

All simulations in this work are performed using the software Roskilde University Molecular Dynamics also known as *RUMD*. RUMD is a MD simulation package for NVIDIA's GPU. It is optimized for high performance on small to medium sized systems composed of molecules and spherical atoms. RUMD uses a python interface and has a package with post-analysis tools, which we use throughout this work. It is developed by the Glass and Time group, which is funded by the Danish National Research Foundation.

RUMD is freely available at `http://rumd.org/` where more information, including the manual and tutorial, can be found.

Perspective on modelling

This work is computational and consequently only applies directly to simulated ILs. However, this does not mean that we cannot learn from these models. For instance if a model liquid satisfy the assumptions of a theory for real liquids, the theory must also apply for the model liquid. This mentality is nicely summarised by one of my colleagues:

" *Model liquids are liquids too.* "

– Professor Thomas B. Schrøder

Note on figures in this work

All figures in this work have been created for this project, with only four exceptions. These are Fig. 1.1, Fig. 1.2 and Fig. 1.3 and later in Chap. 5 and Chap. 6 where the Hansen et al. [2020] structure factor data (Fig. 1.3) will be shown again. Some illustrations in the theory chapters are inspired by existing figures from other sources in which case the original work is cited.

Reading guide

A quick resume of what the reader can expect to find in the different chapters:

Chap. 2 Molecular Dynamics
Since this work is computational, some time will be spent explaining the general idea and selected tools for molecular dynamics simulations. This includes how to define molecular systems.

Chap. 3 Molecular Scale Structure and Dynamics
We present some general theory of materials, and introduce different structural and dynamical quantities on a molecular scale.

Chap. 4 Isomorph Theory
The concepts from the previous chapter will be used to explain, and be put in the context of isomorph theory.

At this point, the reader should have a basic understanding of the theory and method that will be used. We will therefore proceed to present the three different models that are studied in this work.

Chap. 5 Simple Atomic Ionic Liquid Model
The first model is a simple point particle model, that will be used to find how a simple charged system behaves.

Chap. 6 United Atom Ionic Liquid Model
The second model is a more detailed united atom model, that will help us understand how molecular systems behave.

Chap. 7 All-atom Ionic Liquid Model
The third model is an all-atom version of the second model. This model will not be studied as thoroughly as the second model, and will mainly be used for comparison.

Chap. 8 Summary and Conclusions
A summary of the most important results from the three models. Lastly, suggestions for further work will be provided.

I hope you will enjoy!

Chapter 2

Molecular Dynamics

The goal of this chapter is to introduce the basic principles of molecular dynamics simulations. The focus is on the details for setting-up and running a simulation rather than performance optimisations. This includes; integrators and ensembles, the potential energy function, intra-molecular potentials to simulate molecules, and boundary conditions. In our case the process of creating an initial configuration is not important since we in all cases require equilibration of the system before data is collected. However, a short description of this can be found in Sec. B.1.

2.1 Introduction to Molecular Dynamics

Molecular dynamics (MD) is a classical method to simulate many body systems. In this context classical means that it uses Newton's equations of motion from classical mechanics to determine the dynamics of the system. MD was developed in the early 1950s and has since increased in popularity, with more sophisticated techniques being added while maintaining the main principles.

One of the biggest benefits of MD from a scientific point of view is that we have exact information of positions, velocities, and forces of all particles in the system at different times. Thus we can investigate both the structure and dynamics of the system, which is not possible in most physics experiments.

On the other hand, one of the obvious limitations of MD is that it technically does not tell us anything about reality, it only tells us the behaviour of the simulated model. Another limitation is the available computational resources which puts a practical restriction on the system size and the simulation-time. However, this limit is constantly pushed by the evolution of technology.

2.2 Temperature and pressure

Temperature

We know from classical mechanics that the kinetic energy of an object with mass m and velocity v is

$$E_{kin} = \frac{1}{2}mv^2 \tag{2.1}$$

It turns out that we can define the temperature of the system from it's kinetic energy [Frenkel and Smit, 2002]. The average kinetic energy per degree of freedom is

$$\left\langle \frac{1}{2}mv^2 \right\rangle = \frac{1}{2}k_B T \tag{2.2}$$

The instantaneous temperature is

$$T(t) = \frac{1}{k_B N_f} \sum_{j=1}^{N} m_j v_j^2(t) \tag{2.3}$$

where $N_f = 3N - 3$. This means that if one wishes to scale the temperature with a factor λ they should scale the velocities with $\sqrt{\lambda}$.

Pressure

There are two common ways of calculating the pressure of a molecular system; the atomic pressure (P_a), and the molecular pressure (P_m). We will show how to calculate both. However, it was shown in Akkermans and Ciccotti [2004] that P_a and P_m are equivalent in the thermodynamic limit.

The pressure tensor has 9 components, one for each combination of directions

$$\boldsymbol{P} = \begin{pmatrix} P_{xx} & P_{xy} & P_{xz} \\ P_{yx} & P_{yy} & P_{yz} \\ P_{zx} & P_{zy} & P_{zz} \end{pmatrix}. \tag{2.4}$$

Note that generally $P_{xx} = P_{yy} = P_{zz}$ unless the system is asymmetric and has a preferred direction (or statistics are bad).

Before presenting the two pressure tensors we first establish the notation. We have a system with N molecules and n_j atoms in molecule j. The centre of mass and velocity of molecule j is $\boldsymbol{r_j}$ and $\dot{\boldsymbol{r}}_{\boldsymbol{j}}$ respectively. Likewise, the position of the α'th atom in molecule j is $\boldsymbol{r_{j\alpha}}$. Lastly, the relative position between atom $j\alpha$ and $k\beta$ is $\boldsymbol{r_{j\alpha k\beta}}$, and the force on $j\alpha$ from $k\beta$ is $\boldsymbol{F_{j\alpha k\beta}}$.

In this context when computing the product between two vectors it will be done in such a way that the product is a matrix, e.g.

$$\boldsymbol{rF} = \begin{pmatrix} r_x \\ r_y \\ r_z \end{pmatrix} \begin{pmatrix} F_x & F_y & F_z \end{pmatrix} = \begin{pmatrix} r_x F_x & r_x F_y & r_x F_z \\ r_y F_x & r_y F_y & r_y F_z \\ r_z F_x & r_z F_y & r_z F_z \end{pmatrix} \tag{2.5}$$

With this clarified the atomic pressure tensor is given by [Heyes, 1994]

$$\boldsymbol{P_a} = \frac{1}{V} \left(\sum_{j=1}^{N} m_j \dot{\boldsymbol{r}}_{\boldsymbol{j}}{}^2 + \frac{1}{2} \sum_{j=1}^{N} \sum_{\alpha=1}^{n_j} \sum_{k \neq j}^{N} \sum_{\beta=1}^{n_k} \boldsymbol{r_{j\alpha k\beta}} \boldsymbol{F_{j\alpha k\beta}} + \frac{1}{2} \sum_{j=1}^{N} \sum_{\alpha=1}^{n_j} \sum_{\beta \neq \alpha}^{n_j} \boldsymbol{r_{j\alpha j\beta}} \boldsymbol{F_{j\alpha j\beta}} \right). \tag{2.6}$$

Likewise the molecular pressure tensor is given by

$$\boldsymbol{P_m} = \frac{1}{V} \left(\sum_{j=1}^{N} m_j \dot{\boldsymbol{r}}_{\boldsymbol{j}}{}^2 + \frac{1}{2} \sum_{j=1}^{N} \sum_{k \neq j}^{N} \boldsymbol{r_{jk}} \boldsymbol{F_{jk}} \right), \tag{2.7}$$

where $\boldsymbol{F_{jk}}$ in the total force on molecule j from molecule k. This can also be expressed in terms of the atomic forces

$$\boldsymbol{P_m} = \frac{1}{V} \left(\sum_{j=1}^{N} m_j \dot{\boldsymbol{r}}_{\boldsymbol{j}}{}^2 + \frac{1}{2} \sum_{j=1}^{N} \sum_{\alpha=1}^{n_j} \sum_{k \neq j}^{N} \sum_{\beta=1}^{n_k} \boldsymbol{r_{jk}} \boldsymbol{F_{j\alpha k\beta}} \right). \tag{2.8}$$

Note that the $\boldsymbol{P_a}$ uses the positions of all the atoms, where $\boldsymbol{P_m}$ only uses the centre of mass positions of the molecules. It has been shown that the pressure also depends on the choice of boundary condition for the system [Akkermans and Ciccotti, 2004]. With this the atomic or molecular pressure of the system is

$$P = \frac{P_{xx} + P_{yy} + P_{zz}}{3}. \tag{2.9}$$

2.3 Integrators and ensembles

At the core of MD is the second-order differential known as Newton's second law

$$\boldsymbol{F} = m\ddot{\boldsymbol{r}} \tag{2.10}$$

where $\boldsymbol{F}$ is the force vector, m is the mass, and $\ddot{\boldsymbol{r}}$ is the second order time derivative of the position vector $\boldsymbol{r}$, also known as the acceleration. Our goal is to find $\boldsymbol{r}$ as a function of time. Unfortunately, this is not an equation which we can solve analytically for our complex systems, but we can achieve an approximation by discretize Eq. 2.10.

Since the force-field is conservative this would result in a simulation with constant energy. However, other simulation schemes have been developed to modify the forces so the temperature is constant instead. In this section, we describe two MD-algorithms; one with constant energy (NVE), and one with constant temperature (NVT). Both will be used in this work.

2.3.1 The Verlet algorithm (NVE)

The *Verlet algorithm* is named after the French physicist *Loup Verlet* for his work on MD in 1967 [Verlet, 1967]. For a short derivation of the algorithm, imagine a time step Δt and three functions; position $\boldsymbol{r}(t)$, velocity $\boldsymbol{v}(t)$, and force $\boldsymbol{F}(t)$. First, we use central difference to define $\boldsymbol{v}(t \pm \Delta t/2)$ at a half time step

$$\boldsymbol{v}(t + \Delta t/2) = \frac{\boldsymbol{r}(t + \Delta t) - \boldsymbol{r}(t)}{\Delta t} \tag{2.11}$$

$$\boldsymbol{v}(t - \Delta t/2) = \frac{\boldsymbol{r}(t) - \boldsymbol{r}(t - \Delta t)}{\Delta t} \tag{2.12}$$

With this we can again use central difference to define the force $\boldsymbol{F}(t)$ and write it as a function of $\boldsymbol{r}(t)$

$$\boldsymbol{F}(t) = m\frac{\boldsymbol{v}(t + \Delta t/2) - \boldsymbol{v}(t - \Delta t/2)}{\Delta t} \tag{2.13}$$

$$= m\frac{\boldsymbol{r}(t + \Delta t) - 2\boldsymbol{r}(t) + \boldsymbol{r}(t - \Delta t)}{(\Delta t)^2} \tag{2.14}$$

Now we can isolate $\boldsymbol{r}(t + \Delta t)$ to find the next position in the simulation

$$\boldsymbol{r}(t + \Delta t) = 2\boldsymbol{r}(t) - \boldsymbol{r}(t - \Delta t) + (\Delta t)^2\frac{\boldsymbol{F}(t)}{m} \tag{2.15}$$

This equation is the Verlet algorithm, and it only depends on positions at times t and $t - \Delta t$, and forces at time t (independent of velocities).

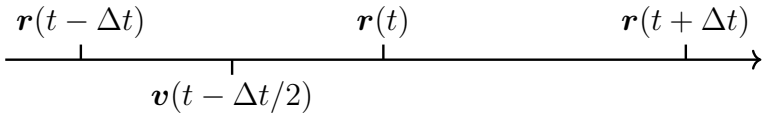

Figure 2.1: Illustration of a timeline for the Verlet algorithm, and the Leap-frog algorithm.

A variation of the Verlet algorithm which is dependent on velocities instead of the previous configuration can be obtained simply by inserting Eq. 2.12 in Eq. 2.15. This is called the *Leap-frog algorithm*, and has the form

$$\boldsymbol{r}(t+\Delta t) = \boldsymbol{r}(t) + \Delta t \boldsymbol{v}(t-\Delta t/2) + (\Delta t)^2 \frac{\boldsymbol{F}(t)}{m} \tag{2.16}$$

An illustration of a timeline can be seen in Fig. 2.1.

2.3.2 The Nosé-Hoover Thermostat (NVT)

The *Nosé-Hoover Thermostat* is named after the Japanese physicist *Shuichi Nosé* and the American physicist *William G. Hoover*. It was first presented in 1986 Posch et al. [1986]. The difference between the Verlet algorithm and the Nosé-Hoover Thermostat is that the forces are shifted with a factor $-\xi \boldsymbol{p_j}(t)$ Frenkel and Smit [2002]. The set of differential equations are

$$\dot{\boldsymbol{r}}_{\boldsymbol{j}}(t) = \frac{\boldsymbol{p_j}(t)}{m_j} \tag{2.17}$$

$$\dot{\boldsymbol{p}}_{\boldsymbol{j}}(t) = \boldsymbol{F_j}(t) - \xi \boldsymbol{p_j}(t) \tag{2.18}$$

$$\dot{\xi}(t) = \left(\sum_j \frac{p_j^2(t)}{m_j} - (3N-\beta)T \right) / \left(2\left(3N-\beta\right) T\tau^2 \right) \tag{2.19}$$

where T is the target temperature, and τ is the relaxation time of the thermostat. If the relaxation time τ is long then the temperature is regulated slowly (if too slow it is effectively NVE), but if τ is too short then ξ dominates the forces and one get unphysical forces. A discretization of Eq. 2.17-2.19 using the Leap-frog scheme gives

$$\boldsymbol{r_j}(t+\Delta t) = \boldsymbol{r_j}(t) + \Delta t \frac{\boldsymbol{p_j}(t+\Delta t/2)}{m} \tag{2.20}$$

$$\boldsymbol{p_j}(t+\Delta t/2) = \frac{\left(1 - \Delta t \frac{\xi(t)}{2}\right) \boldsymbol{p_j}(t-\Delta t/2) + \Delta t \boldsymbol{F}(t)}{1 + \Delta t \frac{\xi(t)}{2}} \tag{2.21}$$

$$\xi(t+\Delta t) = \xi(t) + \Delta t \dot{\xi}(t) \tag{2.22}$$

2.4 The potential energy

When describing the interactions between particles, it is common to define a function $\boldsymbol{V}(\boldsymbol{r})$ for the potential energy between them. From this, one can find the corresponding forces by using

$$\boldsymbol{F}(\boldsymbol{r}) = -\nabla \boldsymbol{V}(\boldsymbol{r}). \tag{2.23}$$

Once the forces are known, one can use Newton's second law of motion to find the new positions of the particles (see Sec. 2.3)

$$\boldsymbol{F} = m\ddot{\boldsymbol{r}}. \tag{2.24}$$

The potential energy function, or simply the potential, only depends on the positions $\boldsymbol{r_j}$ of the N particles in the system. However, it can depend on the positions in a variation of ways, N-ways to be exact. This function can be separated into different parts depending on how many positions it depend on. The total potential can therefore be described as a sum of its individual parts [LeSar, 2013]

$$V_{tot} = V_0 + \sum_{j}^{N} V_1(\boldsymbol{r_j}) + \sum_{j,k}^{N} V_2(\boldsymbol{r_j}, \boldsymbol{r_k}) + \sum_{j,k,l}^{N} V_3(\boldsymbol{r_j}, \boldsymbol{r_k}, \boldsymbol{r_l}) + \ldots, \tag{2.25}$$

where V_0 is a constant, V_1 is the one-body term, V_2 is the two-body term, and so on till V_N, the N-body term. In the following section, we will describe how to use the two-body term for non-bonded interactions, and the two-body, three-body, and four-body terms to describe the bonded interactions in molecules.

2.4.1 Two-body term - Pair potentials

Now we consider the symmetric two-body term, that is $V(\boldsymbol{r_j}, \boldsymbol{r_k}) = V(\boldsymbol{r_k}, \boldsymbol{r_j})$. In this case only the relative positions of the particles matter, meaning that we can change the variable from $(\boldsymbol{r_j}, \boldsymbol{r_k})$ to the distance between the particles $r_{jk} = |\boldsymbol{r_k} - \boldsymbol{r_j}|$, or r for simplicity.

Examples of simple pair potentials

Theoretically one can define the potential in any way imaginable, however, a condition that many potentials follow is that particles can not overlap (at least not without a large energy cost). A simple way of enforcing this is by using an *inverse power law* (IPL) potential

$$V_{IPL}(r) = \epsilon \left(\frac{\sigma}{r}\right)^n, \tag{2.26}$$

where n is a positive real number, and ϵ and σ are characteristic energies and distances, respectively. This is also referred to as a *soft sphere* potential.

One of the most famous pair potentials is the *Lennard-Jones* (LJ) potential which consists of a sum of two IPLs and has the form [Jones and Chapman, 1924a] [Jones and Chapman, 1924b]

$$V_{LJ}(r) = 4\epsilon \left[\left(\frac{\sigma}{r}\right)^{12} - \left(\frac{\sigma}{r}\right)^{6}\right]. \tag{2.27}$$

This potential has a global minima at $r_{min} = 2^{1/6}\sigma \approx 1.12\sigma$ where the potential takes the value $V(r_{min}) = -\epsilon$. The repulsive part of this potential is between $0 < r < r_{min}$ and the attractive part is between $r_{min} < r < \infty$. The first IPL is sometimes referred to as the repulsive term while the second IPL is called the attractive term. The graphs of the LJ and IPL potentials can be seen in Fig. 2.2.

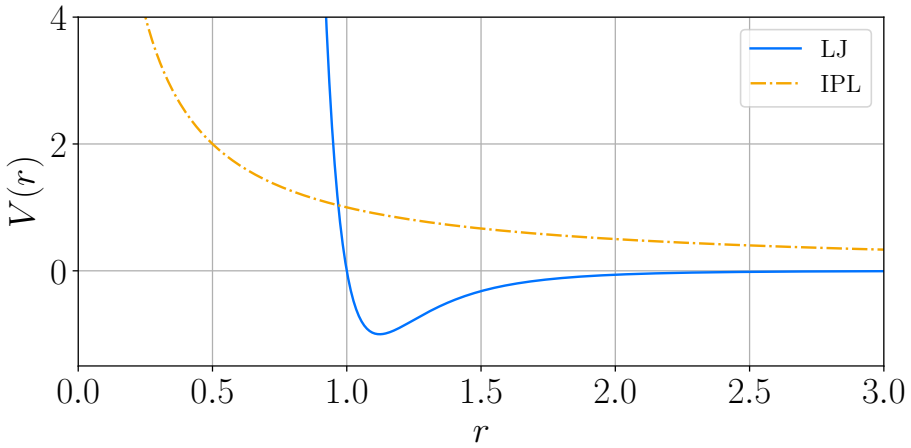

Figure 2.2: The graphs of the LJ, and IPL potentials with $\epsilon = 1$, $\sigma = 1$, and for the IPL $n = 1$ (to represent electrostatic interactions).

Cutoff/Truncation of potentials

The pair potential is defined for every set of particles, which results in many calculations for large systems. However, since the potentials generally are defined to approach 0 as r goes to infinity, many of these interactions' contribution to the potential energy is insignificant. Because of this (and to save computer-power) it is common practice to introduce a truncation of the potential, also known as a cutoff, after which the potential is 0. So a potential $V(r)$ with a truncation at r_{cut} would have the expression

$$V_{cut}(r) = \begin{cases} V(r), & \text{for } r \leq r_{cut} \\ 0, & \text{for } r > r_{cut} \end{cases}. \tag{2.28}$$

However, in most cases this will create a discontinuity in the potential (and forces) which could cause artefacts such as jumps in the potential energy. A common way to fix the energy jumps is by using the *shifted potential* cutoff method instead [Toxvaerd and Dyre, 2011]. This method removes the discontinuity simply be adding a constant. Given a pair potential $V(r)$ with a cutoff at r_{cut} the shifted potential version would be

$$V_{SP}(r) = \begin{cases} V(r) - V(r_{cut}), & \text{for } r \leq r_{cut} \\ 0, & \text{for } r > r_{cut} \end{cases}. \tag{2.29}$$

This does not change the forces between the particles, meaning that they are still discontinues. This corresponds to giving the particles a small 'kick' when they get within the cutoff distance.

A similar method called *shifted force* can be used to make the forces continuous and the potential differentiable. This is done by adding a line to the potential with the slope $-V'(r_{cut})$

$$V_{SF}(r) = \begin{cases} V(r) - V'(r_{cut})r - V(r_{cut}), & \text{for } r \leq r_{cut} \\ 0, & \text{for } r > r_{cut} \end{cases}. \tag{2.30}$$

This changes the forces but it has been shown in earlier studies that the results are still accurate (see Toxvaerd and Dyre [2011] and for Coulomb interactions Hansen et al. [2012]).

Multiple types of particles

Until now, we have only talked about pair-potentials where all particles are of the same type and interact the same way. However, it is possible to define a multicomponent system with different particle interactions. For simplicity, we refer to specific types as A, B etc. and unspecified types as α, β. These particles could interact with different functional form, but assuming they have the same form, such as the LJ-potential, we would need a set of ϵ and σ for each combination of types, $\epsilon_{\alpha\beta}$ and $\sigma_{\alpha\beta}$. This is normally done by finding values for each type ϵ_α and σ_α and defining $\epsilon_{\alpha\beta}$ and $\sigma_{\alpha\beta}$ as a function of these. The standard way to define $\epsilon_{\alpha\beta}$ is by using the Berthelot rule [Berthelot, 1898]

$$\epsilon_{\alpha\beta} = \sqrt{\epsilon_\alpha \epsilon_\beta}, \tag{2.31}$$

however, there are two standard ways to define $\sigma_{\alpha\beta}$

$$\sigma_{\alpha\beta} = \sqrt{\sigma_\alpha \sigma_\beta} \qquad \text{or} \qquad \sigma_{\alpha\beta} = \frac{\sigma_\alpha + \sigma_\beta}{2}. \tag{2.32}$$

The second part of Eq. 2.32 (also known as the Lorentz rule [Lorentz, 1881]) is what we would expect when imagining the particles as hard spheres. This is the version we apply in this work. The multicomponent pair-potential can be written as

$$V_2 = \sum_\alpha \sum_{j<k}^{N_\alpha, N_\alpha} V_{\alpha\alpha}(r_{jk}) + \sum_{\alpha\neq\beta} \sum_{j,k}^{N_\alpha, N_\beta} V_{\alpha\beta}(r_{jk}) \tag{2.33}$$

The potential is separated into a like and unlike part to avoid calculations between a particle with itself.

2.4.2 Intra-molecular potentials - Define a molecule

So far we have only described interactions that are present between pairs of particles. However, to form a molecule some particles have extra interactions that are not present between all particles. We will discuss three common ways particles can be bonded together to form molecules. Firstly, one can fix the distance between two particles, secondly one can fix the angle between three particles, and thirdly one can fix the dihedral angle between four particles. These three constrictions are illustrated in Fig. 2.3.

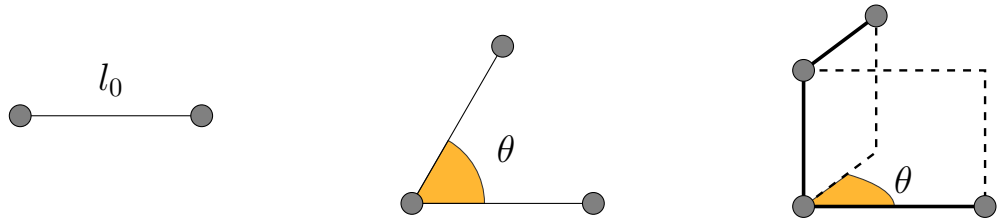

Figure 2.3: Illustrations of particle positions in the case of potential energy from bonds, angles, and dihedrals.

Bond and angle potentials

There are many different versions of bond and angle potentials, but a simple example would be a harmonic oscillator (or a spring) with energy [GRO, 2019]

$$V(x) = \frac{1}{2}k\left(x - x_0\right)^2. \tag{2.34}$$

This is commonly used since it is simply a Taylor approximation around an equilibrium position, x_0. Thus the bond- and angle-potentials can both be described with the functions

$$V_b(r) = \frac{1}{2}\sum k_b\left(r - l_0\right)^2 \qquad \text{and} \qquad V_a(\theta) = \frac{1}{2}\sum k_a\left(\theta - \theta_0\right)^2, \tag{2.35}$$

where k_b and k_a are the spring constants, l_0 is the bond length, and θ_0 is the preferred angle. Some versions of these potentials do not have the factor $1/2$ in which case it is included in the spring constants.

Force calculation - Bonds Two particles at positions $\boldsymbol{r_j}$ and $\boldsymbol{r_k}$ (and relative distance $r_{jk} = r_k - r_j$) with the bond-potential $V_b(r)$ have the forces

$$\boldsymbol{F_j} = \frac{\partial V_b(r)}{\partial r} \cdot \boldsymbol{e_{jk}} \tag{2.36}$$

$$\boldsymbol{F_j} = -\boldsymbol{F_k}, \tag{2.37}$$

where the force acts in the direction $\boldsymbol{e_{jk}} = \boldsymbol{r_{jk}}/r_{jk}$ [Monasse and Boussinot, 2014].

Force calculation - Angles Three particles at positions $\boldsymbol{r_j}$, $\boldsymbol{r_k}$, and $\boldsymbol{r_l}$ with the angle-potential $V_a(\theta)$ form a plane with the normal vector $\boldsymbol{n_{kjl}}$

$$\boldsymbol{r_{kj}} = \boldsymbol{r_j} - \boldsymbol{r_k} \qquad \text{and} \qquad \boldsymbol{r_{kl}} = \boldsymbol{r_l} - \boldsymbol{r_k} \tag{2.38}$$

$$\boldsymbol{n_{kjl}} = \frac{\boldsymbol{r_{kj}} \times \boldsymbol{r_{kl}}}{|\boldsymbol{r_{kj}} \times \boldsymbol{r_{kl}}|} \tag{2.39}$$

and the angle θ between the particles is

$$\cos(\theta) = \frac{\boldsymbol{r_{kj}} \cdot \boldsymbol{r_{kl}}}{|\boldsymbol{r_{kj}}|\ |\boldsymbol{r_{kl}}|} \tag{2.40}$$

The forces on particle j and l act in the directions

$$\boldsymbol{e_j} = -\frac{\boldsymbol{e_{kj}} \times \boldsymbol{n_{kjl}}}{|\boldsymbol{e_{kj}} \times \boldsymbol{n_{kjl}}|} \qquad \text{and} \qquad \boldsymbol{e_l} = \frac{\boldsymbol{e_{kl}} \times \boldsymbol{n_{kjl}}}{|\boldsymbol{e_{kl}} \times \boldsymbol{n_{kjl}}|} \tag{2.41}$$

and the forces on the three particles are

$$\boldsymbol{F_j} = -\frac{\partial V_a(\theta)}{\partial \theta}\frac{1}{r_{kj}}\boldsymbol{e_j} \tag{2.42}$$

$$\boldsymbol{F_l} = -\frac{\partial V_a(\theta)}{\partial \theta}\frac{1}{r_{kl}}\boldsymbol{e_l} \tag{2.43}$$

$$\boldsymbol{F_k} = -\boldsymbol{F_j} - \boldsymbol{F_l} \tag{2.44}$$

An illustration of the forces in an angle-potential can be seen in Fig. 2.4.

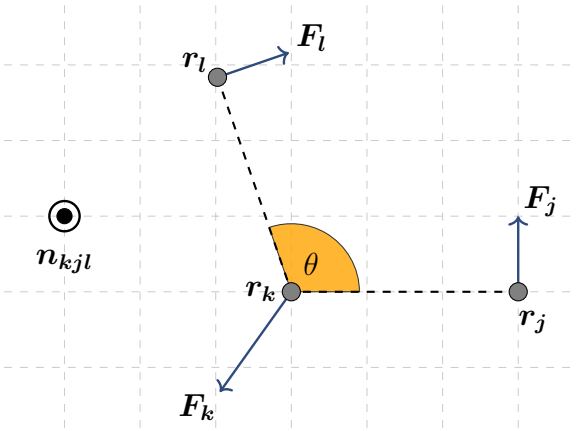

Figure 2.4: Two dimensional illustration of the forces in an angle-potential. The normal vector $\boldsymbol{n_{kjl}}$ is pointing out of the page.

Dihedral potentials

As illustrated in Fig. 2.3, the dihedral potentials describe the angle between two planes determined from four particles. There are two classes of dihedrals; proper- and improper dihedrals. The difference between them is how the zero angle is defined. For proper dihedrals, the cis version corresponds to an angle of zero, where the trans version is zero for improper dihedrals. This has also lead to the convention of using θ for proper dihedrals and $\phi = \theta - 180$ for improper dihedrals. An illustration of the difference between cis and trans configurations can be seen in Fig. 2.5.

Figure 2.5: Illustrations of cis and trans versions of a simple four particle configuration.

In the following section, we will describe three similar types of proper dihedral potentials which will be referenced in this work. The first dihedral potential we present is the *periodic type*, which has the form [GRO, 2019]

$$V(\theta) = K_\theta \left(1 + \cos\left(n\theta - \theta_0\right)\right), \tag{2.45}$$

with energy K_θ, order n, and phase θ_0. The second dihedral potential we present is from the OPLS force field and is called the *Fourier dihedrals* which has the form

$$V(\theta) = \frac{1}{2}\sum_{n=1}^{4} F_n \left[1 + (-1)^{n+1}\cos\left(n\theta\right)\right], \tag{2.46}$$

with four energy parameters F_n. These potentials are similar in the sense that they can describe some of the same functions.

Lastly is the *Ryckaert-Bellemans function* which has the form

$$V(\theta) = \sum_{n=0}^{5} C_n \left(-\cos\left(\theta\right)\right)^n, \tag{2.47}$$

with six energy parameters C_n. There is an exact translation from the Fourier dihedrals to the Ryckaert-Bellemans function. The transformation is

$$\begin{aligned} C_0 &= F_2 + \frac{1}{2}\left(F_1 + F_3\right) & C_1 &= \frac{1}{2}\left(-F_1 + 3F_3\right) & C_2 &= -F_2 + 4F_4 \\ C_3 &= -2F_3 & C_4 &= -4F_4 & C_5 &= 0. \end{aligned} \tag{2.48}$$

Force calculation - Dihedrals

To avoid an overload of symbols we instead use numbers to label the particles in the upcoming example. Imagine four particles at positions $\boldsymbol{r_1}$, $\boldsymbol{r_2}$, $\boldsymbol{r_3}$, and $\boldsymbol{r_4}$ with the dihedral-potential $V_{dihe}(\theta)$ as shown in Fig. 2.6. In this case, the relevant relative position vectors are

$$\boldsymbol{r_{21}} = \boldsymbol{r_1} - \boldsymbol{r_2} \qquad \text{and} \qquad \boldsymbol{r_{23}} = \boldsymbol{r_3} - \boldsymbol{r_2} \qquad \text{and} \qquad \boldsymbol{r_{34}} = \boldsymbol{r_4} - \boldsymbol{r_3}, \tag{2.49}$$

and the normal-vectors to the two planes are

$$\boldsymbol{n_{213}} = \boldsymbol{r_{21}} \times \boldsymbol{r_{23}} \qquad \text{and} \qquad \boldsymbol{n_{324}} = -\boldsymbol{r_{23}} \times \boldsymbol{r_{34}}. \tag{2.50}$$

The angle θ between the planes, which is used to calculate the potential energy is

$$\theta = \arccos\left(\frac{\boldsymbol{n_{213}} \cdot \boldsymbol{n_{324}}}{|\boldsymbol{n_{213}}|\ |\boldsymbol{n_{324}}|}\right). \tag{2.51}$$

However, when calculating the forces on particle 1 and 4, two extra angles are needed

$$\sin(\theta_2) = \frac{\boldsymbol{r_{21}} \times \boldsymbol{r_{23}}}{|\boldsymbol{r_{21}}|\ |\boldsymbol{r_{23}}|} \qquad \text{and} \qquad \sin(\theta_3) = \frac{\boldsymbol{r_{34}} \times \boldsymbol{r_{32}}}{|\boldsymbol{r_{34}}|\ |\boldsymbol{r_{32}}|}. \tag{2.52}$$

The forces on particle 1 and 4 are

$$\boldsymbol{F_1} = -\frac{\partial V_{dihe}(\theta)}{\partial \theta}\frac{1}{r_{21}\sin(\theta_2)}\boldsymbol{n_{213}} \tag{2.53}$$

$$\boldsymbol{F_4} = -\frac{\partial V_{dihe}(\theta)}{\partial \theta}\frac{1}{r_{34}\sin(\theta_3)}(-\boldsymbol{n_{324}}). \tag{2.54}$$

The forces on particle 2 and 3 are

$$\boldsymbol{F_2} = -\left(\boldsymbol{e_{32}} \times \boldsymbol{F_1} + \boldsymbol{r_{34}} \times \boldsymbol{F_4} + \boldsymbol{r_{21}} \times \boldsymbol{F_1}\right) \times \boldsymbol{e_{32}} \tag{2.55}$$

$$\boldsymbol{F_3} = -\left(\boldsymbol{e_{23}} \times \boldsymbol{F_4} + \boldsymbol{r_{34}} \times \boldsymbol{F_4} + \boldsymbol{r_{21}} \times \boldsymbol{F_1}\right) \times \boldsymbol{e_{23}}. \tag{2.56}$$

To confirm the condition $\boldsymbol{F_1} + \boldsymbol{F_2} + \boldsymbol{F_3} + \boldsymbol{F_4} = 0$ we see that the two last terms in Eq. 2.55 and 2.56 are equal in magnitude but with opposite sign

$$\left(\boldsymbol{r_{34}} \times \boldsymbol{F_4} + \boldsymbol{r_{21}} \times \boldsymbol{F_1}\right) \times \boldsymbol{e_{32}} = -\left(\boldsymbol{r_{34}} \times \boldsymbol{F_4} + \boldsymbol{r_{21}} \times \boldsymbol{F_1}\right) \times \boldsymbol{e_{23}} \tag{2.57}$$

and the first term in Eq. 2.55

$$\left(\boldsymbol{e_{32}} \times \boldsymbol{F_1}\right) \times \boldsymbol{e_{32}} = \boldsymbol{F_1} \tag{2.58}$$

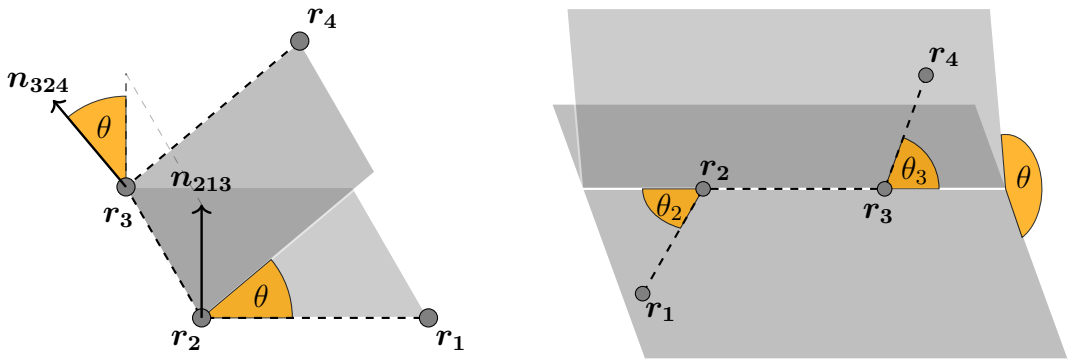

Figure 2.6: Illustration of the dihedral angle between two planes spanned by four particles. The cic version corresponds to an angle of 0. The second part of this illustration is inspired by figure 1.10 in Allen et al. [2017]

Excluded interactions

As mentioned earlier the goal of using bond, angle and dihedral potentials is to restrict a specific distance or angle between a set of atoms. To enforce these conditions it is common to excluding the non-bonded interactions between the first and last particle in the bonded set. So for dihedral 1-2-3-4, angle, 1-2-3, and bond 1-2, one would exclude the non-bonded interactions between particle 1-4, 1-3, and 1-2 respectively, see Fig. 2.7.

In RUMD, the non-bonded interactions in bonds, angles and dihedrals are excluded by default.

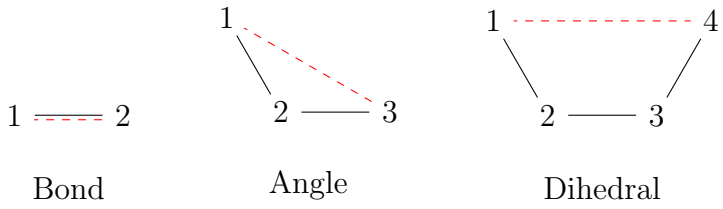

Figure 2.7: Illustrations of bonds, angles, and dihedrals where the red dashed line represents the excluded non-bonded interactions.

2.5 Boundary conditions

Boundary conditions are used to limit the movement of the particles, often by "putting them into a box". This means that if a particle would move out of the box different methods can be used to put it back inside. Some of these methods are described in Allen et al. [2017].

Periodic boundary conditions

A problem with simulations is that we are limited by the available computer processing power. This often leads to a compromise between system size, number of particles, and the computation time. However, there is a way to define the boundary conditions to create the illusion of an infinite system.

If a particle would move out of the box, it will instead be moved to the opposite side. In a box with side length L_x the particle positions would be redefined after each time step to $x_{new} = x_{old} \mod (L_x)$. This also means that we should calculate the interactions with particles on the other side of the box if they are "sufficiently close". A simple way to implement this for particles j and k is with the distance function

$$dx_{jk} = x_{jk} - L_x \text{int}\left(2x_{jk}/L_x\right) \tag{2.59}$$

$$dr_{jk} = \sqrt{dx_{jk}^2 + dy_{jk}^2 + dz_{jk}^2}. \tag{2.60}$$

This is called *periodic boundary conditions*, and Fig. 2.8 illustrates the movement of the particles, and the area of particle interaction when they are applied.

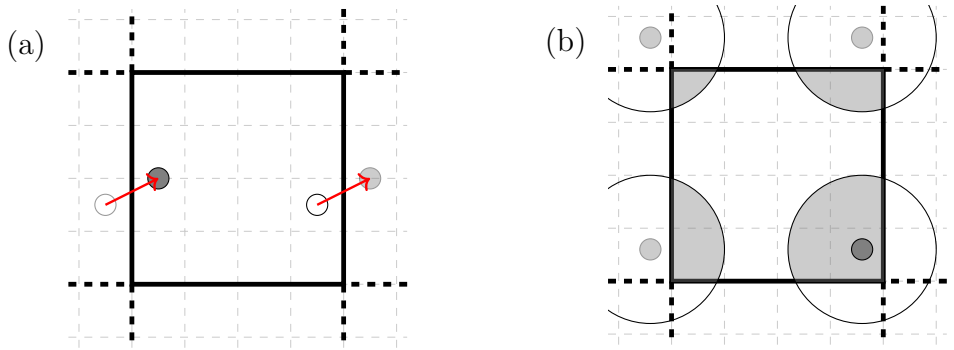

Figure 2.8: (a) An illustration of particle movement in a 2D box with periodic boundary conditions. Note that the movement is exaggerated. (b) An illustration of the area in which particles can interact.

Particle images and dynamics

When calculating dynamical properties such as the mean square displacement (see Sec. 3.4) the distance travelled by the particles is important. Because of this, we should save the number of times a particle has been moved from one side of the box to the other (in three dimensions this would be the integers Im_x, Im_y, and Im_z). Thus the *image* of the particle is

$$\boldsymbol{r_{im}} = \boldsymbol{r} + \begin{pmatrix} Im_x L_x \\ Im_y L_y \\ Im_z L_z \end{pmatrix} \tag{2.61}$$

where L_x, L_y, and L_z are the side lengths of the simulation box.

Box size and cutoff

Due to the periodic boundary conditions, it is possible that a particle j can interact with the same particle k twice, or even itself, if the box becomes too small, this is illustrated in Fig. 2.9. To avoid this, the shortest side-length of the box should be greater than or equal to twice the largest cutoff,

$$L_{min} \geq 2r_{cut} \tag{2.62}$$

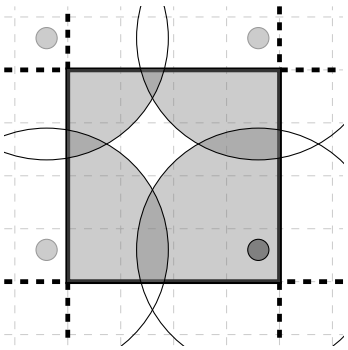

Figure 2.9: Illustration of particle interactions in a box with implemented periodic boundary conditions, where Eq. 2.62 is not satisfied. This is seen by the overlapping areas, meaning that it is possible to interact with the same particle twice.

Chapter 3

Molecular Scale Structure and Dynamics

The goal of this chapter is to explain different ways of describing the *structure*, and *dynamics* of matter on a molecular scale. When it comes to calculating these quantities we will take the perspective of an computational physicist. This means we will assume the position, velocity and forces on the particles are known at different times, as this is the case in simulations.

3.1 Phases of matter

The most common phases of matter that we know from our daily lives are solid, liquid, and gas. The phase of a material depends on its physical quantities such as temperature (T), pressure (P) and density (ρ), a combination of these is called a state point. However, different types of matter do not necessarily partake the same phase at the same state point. Think of water and air; at room temperature and atmospheric pressure they are liquid and gas respectively, but they are both gas at temperatures greater than 100 $°C$. Because of this, it is practical to make diagrams of these different phases for a given material, a *phase diagrams*. It is of course possible to make different kinds of phase diagrams depending on which physical quantities are used to describe the material. This can become a question of what is easier to control. Consequently some experimentalists tend to prefer temperature and pressure, while people doing computer simulations often prefer density and temperature.

Sketches of a $T - P$ and a $\rho - T$ phase diagram can be seen in Fig. 3.1. The three main lines are; the solid-gas line (red), the solid-liquid line (green), and the liquid-gas line (blue). Crossing any of these lines would require the system to absorb or release energy, resulting in a first-order phase transition. The $\rho - T$ phase diagram also has regions where phases can coexist.

Structure and dynamics generally change significantly between phases, but they also change less dramatically within the same phase. Examples could be how viscous liquids (like honey) generally flow more easily at high temperatures than low temperatures. This behaviour within the phases, and the location of the different phases in the phase diagram, is controlled by the interactions between the atoms or molecules in the material. These interactions are dependent on the fundamental forces between the atoms in the material. One of these interactions is the electrostatic force or Coulomb force, named after the French physicist Charles-Augustin de Coulomb. These forces can be attractive or repulsive, and affect matter with charges, such as ions. Consequently ionic materials behave different than materials that are neutrally charged.

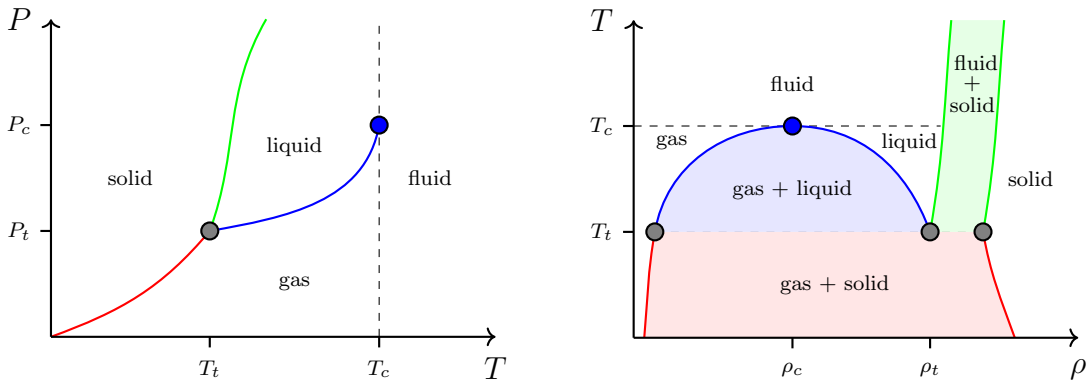

Figure 3.1: Illustration of a $T - P$ and a $\rho - T$ phase diagram. In both diagrams the triple point is marked with a grey circle, and the critical point is marked with a blue circle. The line between solid and gas (red), the solid-liquid line (green), and the liquid-gas line (blue). The red, green, and blue regions of the $\rho - T$ diagram indicate coexistence between the phases. This illustration is inspired by wik [a] and wik [b].

3.2 The van Hove function

Systems which are *amorphous (without shape/form)*, like liquids and gasses do not have a strict pattern to pack space. Consequently their structure cannot be described with a lattice as is the case for solids. However, this does not mean that we cannot describe their structure or dynamics. Instead we can define a counting function, which can give insight into different distributions.

There is one function which is the very important for this analysis of the structure and dynamics since it gives access to many analysis tools. This is the van Hove function $G(\boldsymbol{r}, t)$, Eq. 3.1, which we separate into two parts; a self part $G_s(\boldsymbol{r}, t)$, and a distinct part $G_d(\boldsymbol{r}, t)$. Here the vector $\boldsymbol{r}$ describes the direction and distance that are analysed, and t indicates the difference in time between the particles. Thus the the van Hove function is defined as [Van Hove, 1954]

$$G(\boldsymbol{r}, t) = G_s(\boldsymbol{r}, t) + G_d(\boldsymbol{r}, t) \tag{3.1}$$

$$G_s(\boldsymbol{r}, t) = \frac{1}{N} \left\langle \sum_j \delta(\boldsymbol{r} - \boldsymbol{r_j}(0) + \boldsymbol{r_j}(t)) \right\rangle \tag{3.2}$$

$$G_d(\boldsymbol{r}, t) = \frac{1}{N} \left\langle \sum_{j \neq k} \delta(\boldsymbol{r} - \boldsymbol{r_j}(0) + \boldsymbol{r_k}(t)) \right\rangle, \tag{3.3}$$

where N is the number of particles, $\boldsymbol{r_j}(t)$ and $\boldsymbol{r_k}(t)$ are the positions of particle j and k at time t respectively, $\langle \cdots \rangle$ represents the ensemble average, and the δ-function is defined by

$$\delta(x) = \begin{cases} \infty & , \text{ for } x = 0 \\ 0 & , \text{ for } x \neq 0 \end{cases} \qquad \text{and} \qquad \int_{-\infty}^{\infty} \delta(x) = 1. \tag{3.4}$$

3.3 Molecular scale structure

When analysing structure we generally look at distances between particles at the same time, and compute the average for different configurations at different times. Consequently when using the van Hove function to analyse structure we use the less general static version, that is $G(\boldsymbol{r}) = G(\boldsymbol{r}, 0)$. One can think of this function as the relative particle position distribution in the direction of $\boldsymbol{r}$.

3.3.1 The radial distribution function

Using the static van Hove function, we can define a useful tool for analysing structure, *the radial distribution function* (RDF) $g(\boldsymbol{r})$. It is a scaled version of $G_d(\boldsymbol{r})$. The radial distribution function is defined as [Allen et al., 2017] [Egelstaff, 1994]

$$g(\boldsymbol{r}) = \frac{1}{4\pi|\boldsymbol{r}|^2}\frac{1}{\rho}G_d(\boldsymbol{r}) \tag{3.5}$$

$$= \frac{1}{4\pi|\boldsymbol{r}|^2}\frac{1}{\rho N}\left\langle \sum_{j\neq k}\delta(\boldsymbol{r} - \boldsymbol{r_j} + \boldsymbol{r_k})\right\rangle. \tag{3.6}$$

However, the systems that we will be analysing in this work, are assumed to be *isotropic (equal-way)*, that is they look the same in all directions. This means that we only need to consider the norm of $\boldsymbol{r}$, $r = |\boldsymbol{r}|$. Thus Eq. 3.6 becomes

$$g(r) = \frac{1}{4\pi r^2}\frac{1}{\rho N}\left\langle \sum_{j\neq k}\delta(r - |\boldsymbol{r_j} - \boldsymbol{r_k}|)\right\rangle. \tag{3.7}$$

This makes it possible to show the RDF in a 2 dimensional plot. A schematic drawing of particle positions, and a sketch of a typical RDF for a liquid are shown in Fig. 3.2. The periodicity of the peaks is related to the size of the atoms/molecules in the system. If it was a gas, the RDF would have fewer peaks because the long range structure is even less present in this case. For a solid with a lattice structure, we would see δ-peaks at the corresponding neighbour distances, however, note that a lattice is not isotropic.

Partial radial distribution functions

If the system consists of multiple components we can consider the partial radial distribution functions. Like the standard RDF this function describes the density-fluctuations, but only between particles of type α and β. This can be done by simply changing the sum and the normalisation

$$g_{\alpha\beta}(r) = \frac{1}{4\pi r^2}\frac{1}{c_\alpha c_\beta \rho N}\left\langle \sum_{j,k}^{N_\alpha, N_\beta}\delta(r - |\boldsymbol{r_k^\beta} - \boldsymbol{r_j^\alpha}|)\right\rangle, \tag{3.8}$$

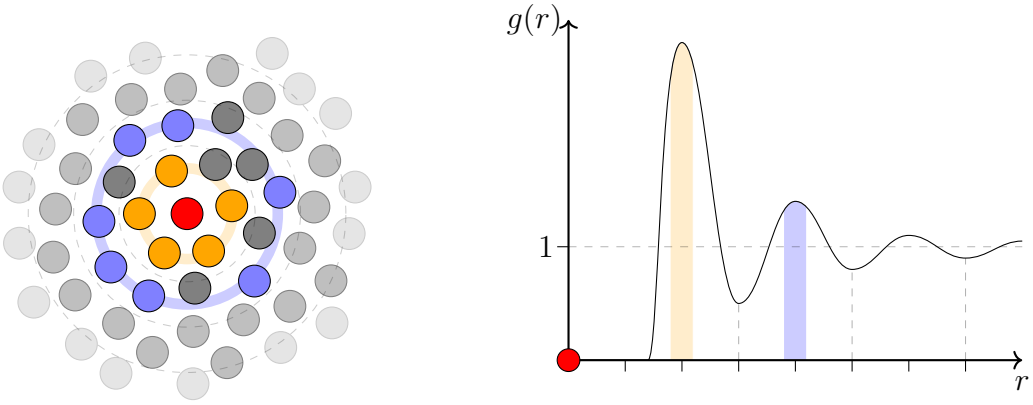

Figure 3.2: On the left is a schematic drawing of particle positions in a liquid. The dashed circles represent the distances at which the probability of finding particles are the lowest. On the right is a sketch of a typical radial distribution function. The probability is 0 for small r-values since particles cannot overlap.

where c_α is the concentration of type α, and $\boldsymbol{r}_j^\alpha$ is the position of the jth α-particle. Note that if the types are equal, e.g. $\alpha = \beta$, then $j \neq k$ in the sum. The construction of Eq. 3.8 ensures that the weighted sum of partial RDFs is equal to the total, that is

$$g(\boldsymbol{r}) = \sum_{\alpha,\beta} c_\alpha c_\beta \; g_{\alpha\beta}(\boldsymbol{r}). \tag{3.9}$$

3.3.2 The static structure factor

From the analysis of the RDF in Sec. 3.3.1, we saw that there are certain length scales which are more common than others (the distance between peaks). A function that can describe these length scales, is *the static structure factor*, $S(\boldsymbol{q})$ where the wave-vector $\boldsymbol{q}$ has dimension of inverse distance. The $S(\boldsymbol{q})$ can be calculated as the Fourier transformation of the RDF, but it can also be calculated directly as [Fischer et al., 2005]

$$\begin{aligned} S(\boldsymbol{q}) &= \int_0^\infty g(\boldsymbol{r}) \exp\left(-i\boldsymbol{q}\cdot\boldsymbol{r}\right) d\boldsymbol{r} \\ &= \frac{1}{N} \left\langle \sum_{j,k} \exp\left(-i\boldsymbol{q}\cdot\boldsymbol{r}_{\boldsymbol{jk}}\right) \right\rangle, \end{aligned} \tag{3.10}$$

where $\boldsymbol{r_{jk}} = \boldsymbol{r_k} - \boldsymbol{r_j}$ and i is the imaginary unit. This equation can be simplified if the system in question is isotropic, and then $S(\boldsymbol{q})$ becomes

$$S(q) = 1 + \frac{1}{N} \left\langle \sum_{j,k \neq j}^{N} \frac{\sin(qr_{jk})}{qr_{jk}} \right\rangle, \tag{3.11}$$

where $q = |\boldsymbol{q}|$ and $r_{jk} = |\boldsymbol{r_{jk}}|$. The distance represented by a given q-value is given by $r = 2\pi/q$.

Partial structure factors

For systems with more than one type of particle, it is possible to calculate the structure factor between particles of type α and β, also known as the *partial structure factors*. This can be done in several different ways, but we focus on the *Faber-Ziman* and the *Bhatia-Thornton* partial structure factors.

Faber-Ziman The Faber-Ziman (FZ) partial structure factors are what we would obtain by calculating the Fourier transformation of the partial RDFs. For an isotropic system it can be written as

$$S_{\alpha\beta}(q) = S_{\beta\alpha}(q) = 1 + \frac{1}{c_\alpha c_\beta N} \left\langle \sum_{j,k \neq j}^{N_\alpha, N_\beta} \frac{\sin(qr_{jk})}{qr_{jk}} \right\rangle, \tag{3.12}$$

where c_α and c_β are the concentrations of particle types α and β, respectively.

Bhatia-Thornton If the system only contains two different types of particles, we can calculate the Bhatia-Thornton (BT) structure factor from Bhatia and Thornton [1970]. This structure factor consists of three parts referred to as number-number (NN), concentration-concentration (CC), and number-concentration (NC). These are defined from the FZ partial structure factors, which therefore must be obtained first.

The NN partial structure factor describes the distribution of atomic number density. It is simply a weighted sum of the FZ structure factors and can be thought of as the total signal. As a consequence of this, $S_{NN}(q)$ is "colour-blind" meaning that it cannot distinguish between the two particle types. It is defined by

$$S_{NN}(q) = c_1^2 S_{11}(q) + c_2^2 S_{22}(q) + 2c_1 c_2 S_{12}(q). \tag{3.13}$$

In contrast to NN which can be thought of as the "colour-blind" total signal, the CC partial structure factor is instead the coloured difference between like and unlike types. It is defined by

$$S_{CC}(q) = c_1 c_2 \left[1 + c_1 c_2 \left(S_{11}(q) + S_{22}(q) - 2S_{12}(q)\right)\right]. \tag{3.14}$$

Information on the ordering of the different atom types can be obtained by calculating the Fourier transform of $S_{CC}(q)$. If the particles are indistinguishable, then $S_{CC} = c_1 c_2$.

The NC partial structure factor describes the correlation between NN and CC and is defined by

$$S_{NC}(q) = c_1 c_2 \left[c_1 \left(S_{11}(q) - S_{12}(q) \right) - c_2 \left(S_{22}(q) - S_{12}(q) \right) \right]. \tag{3.15}$$

If $S_{11}(q) = S_{22}(q)$ and has equal concentrations then $S_{NC} = 0$. From these definitions, it can be shown that

$$S_{NN}(q) > 0, \qquad S_{CC}(q) > 0, \qquad S_{NN}(q) S_{CC}(q) > S_{NC}(q). \tag{3.16}$$

Example of $S(q)$ in a simple ionic liquid

An example of the FZ and BT partial structure factors for a simple ionic liquid model can be seen in Fig. 3.3. An in-debt analysis of the model used in this example (the Hansen and McDonald simple salt model) can be found in Chap. 5. Here we see that $S_{NN}(q)$ (dashed blue) has a peak around 7, and $S_{CC}(q)$ (dashed red) has a peak around 4. The fact that the system has a CC peak tells us that there is type-ordering, and the peaks position relative to the NN peak tells us that it is long range. The FZ partial structure factors in combination with Eq. 3.13 and 3.14 provides a conformation of the BT partial structure factors.

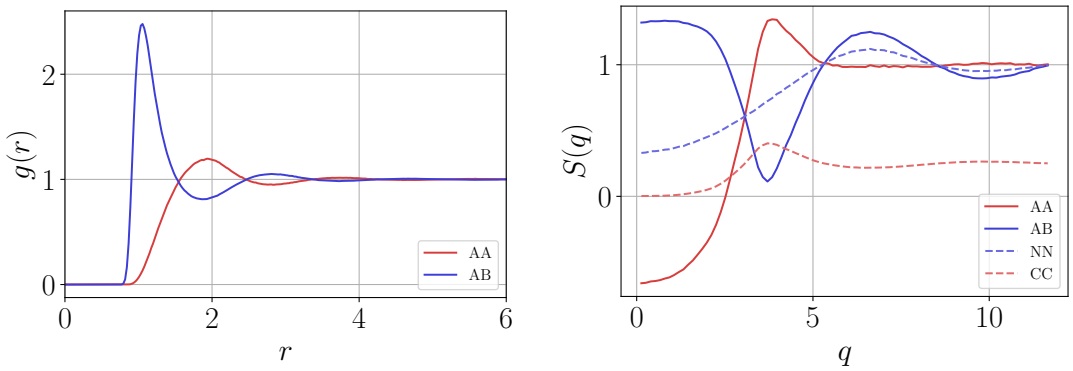

Figure 3.3: Example of simulation data for the Hansen and McDonald simple salt model at $\rho = 0.3$ and $T = 0.1$. (Left) The partial $g(r)$. (Right) Both the Faber-Ziman and Bhatia-Thornton structure factors.

3.4 Molecular scale dynamics

3.4.1 Self-intermediate scattering function

It turns out that the static structure factor $S(\boldsymbol{q})$ from Eq. 3.10 is a special version of a more general function, the dynamic structure factor $S(\boldsymbol{q}, \omega)$, where ω is the frequency. However, we will be using the real time version called the *intermediate scattering function* $F(\boldsymbol{q}, t)$. It can also be thought of as the special Fourier transform of the van Hove function $G(\boldsymbol{r}, t)$, Eq. 3.1, and is defined as

$$F(\boldsymbol{q}, t) = \frac{1}{N} \left\langle \sum_{j,k} \exp\left[i\boldsymbol{q} \cdot (\boldsymbol{r_j}(t) - \boldsymbol{r_k}(0))\right] \right\rangle, \tag{3.17}$$

where N is the number of particles, $\boldsymbol{r_j}(t)$ is the position of particle j at time t, and $\langle \dots \rangle$ denotes the ensemble average [Frenkel and Smit, 2002]. However, using the self part of the Hove function $G_s(\boldsymbol{r}, t)$ instead means that only one particle is considered at different times. This is called the *self-intermediate scattering function* $F_s(\boldsymbol{q}, t)$ and can be calculated as

$$F_s(\boldsymbol{q}, t) = \frac{1}{N} \left\langle \sum_{j}^{N} \exp\left[i\boldsymbol{q} \cdot (\boldsymbol{r_j}(t) - \boldsymbol{r_j}(0))\right] \right\rangle. \tag{3.18}$$

This function describes the correlation of the particles' positions with themselves in time. Here q is a measure of the length-scale in the correlation function. Large wave-vector q represents small distances which would result in faster decorrelation. A schematic drawing of a $F_s(t)$ curve can be seen in Fig. 3.4.

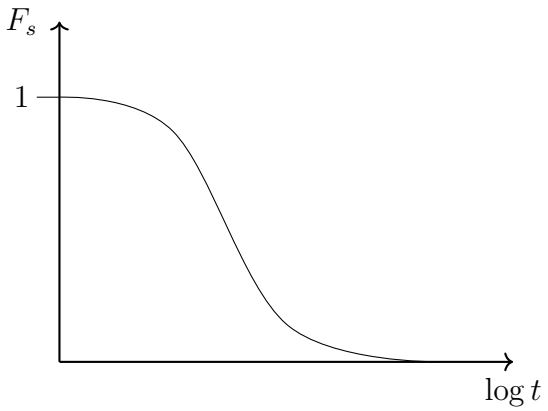

Figure 3.4: Schematic drawing of a $F_s(t)$ curve.

3.4.2 Mean square displacement

When previously describing the structure of liquids, we analysed the distance between pairs of particles at fixed times, that is $|\boldsymbol{r_j}(t_0)-\boldsymbol{r_k}(t_0)|$. Now when describing the dynamics we instead analyse the distance between individual particles at different times, that is $|\boldsymbol{r_j}(t_0+t)-\boldsymbol{r_j}(t_0)|$. It should be noted that this is not the total distance travelled in this time-interval, but rather the distance between the initial and final position (see Fig. 3.5). This is called the *mean square displacement* (MSD), and it is calculated by

$$\mathrm{MSD}(t) = \left\langle |\boldsymbol{r}(t)-\boldsymbol{r}(0)|^2 \right\rangle = \frac{1}{N}\sum_{j=1}^{N} |\boldsymbol{r_j}(t_0+t)-\boldsymbol{r_j}(t_0)|^2, \tag{3.19}$$

where N is the number of particles, $\boldsymbol{r}(t)$ is the position of a particle at time t, $|\ldots|$ is the vector norm, and $\langle\ldots\rangle$ denotes the ensemble average [Frenkel and Smit, 2002].

A common way to represent MSD-data is in a log-log plot. This can show the dynamics on both short and long timescales. On very short timescales the particles move with constant velocity because they have not had time to accelerate. This means that for very short timescales the MSD is

$$\mathrm{MSD}(t) = \left\langle |\boldsymbol{r}(t)-\boldsymbol{r}(0)|^2 \right\rangle \approx \left\langle |\boldsymbol{v}t|^2 \right\rangle = v^2t^2, \tag{3.20}$$

where v is a characteristic velocity that depends on the given state point. From this we see that the MSD is proportional to t^2, and thus has a slope of 2 in a log-log plot. This is referred to as the *ballistic phase*.

Similarly for long timescales the particles generally lose their "memory" of their initial position. This means that the dynamics of the system is analogous to a random walk and becomes diffusive, wherefore it is named the *diffusive phase*.

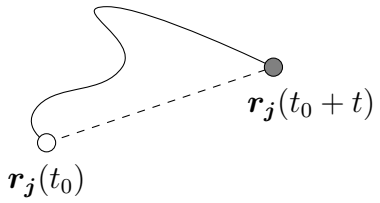

Figure 3.5: Schematic drawing of a particle's movement as a function of time. The full line represents the path travelled by the particle, while the dashed line represents the relative distance between the particle at time t_0 and t_0+t. The mean square displacement calculates the latter.

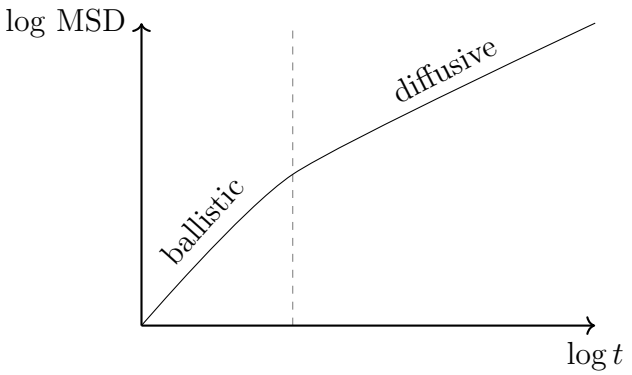

Figure 3.6: Schematic drawing of the ballistic and diffusive phases in the mean square displacement.

Consequently it is common to describe this phase by the *diffusion coefficient* (D), which can be calculated as

$$D = \frac{1}{2d} \lim_{t\to\infty} \left(\frac{d}{dt} \mathrm{MSD}(t) \right), \tag{3.21}$$

where d is the number of spatial dimensions. Some systems have a plateau or other features between the two phases. The different phases are illustrated in Fig. 3.6

3.4.3 Viscosity

The viscosity (η) is a measure of a liquid's resistance to flow. In this section we introduce this concept in two ways;

- First, a classical explanation to build intuition of viscosity.
- Second, a more abstract approach which will be used to calculate the viscosity in this work.

A classical way to think about this is to imagine two parallel plates with area A a distance Δy apart with the liquid in between. One wall is stationary while the other moves parallel with the velocity Δv_x. If the liquid is assumed to be viscous, the movement of the upper plate will drag the closest particles with it which in turn will drag its neighbours with it and so on. This will create a velocity gradient in the liquid, however, we assume that Δy is so small that it is linear. An illustration of this can be seen in Fig. 3.7. In this case, the viscosity is the proportionality constant

$$\frac{F}{A} = \eta \frac{\Delta v_x}{\Delta y}, \tag{3.22}$$

where F/A is the shear stress. We can also think of this example as a small slice of a bigger system, see Fig. 3.8. In this case Eq. 3.22 can be generalized for flows in any direction in the xy-plane

$$\sigma_{xy} = \eta \left(\frac{\partial v_y}{\partial x} + \frac{\partial v_x}{\partial y} \right). \tag{3.23}$$

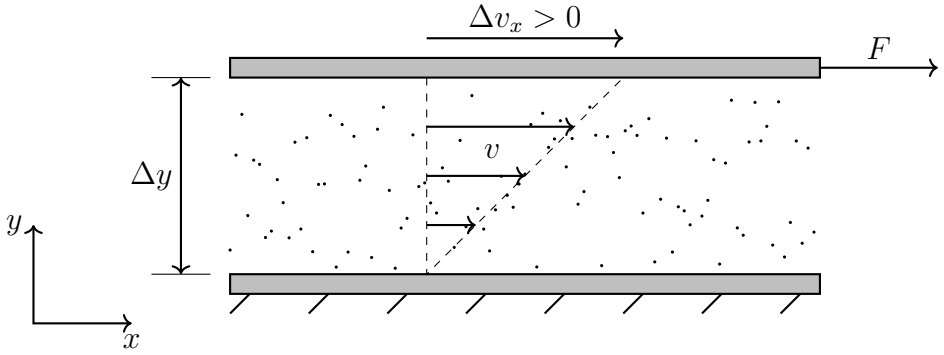

Figure 3.7: Schematic drawing of two parallel plates with a liquid between them. The lower plate is stationary while the upper plate is moving with the velocity Δv_x. This figure is inspired by Fig. 41.1 from Feynman [1964].

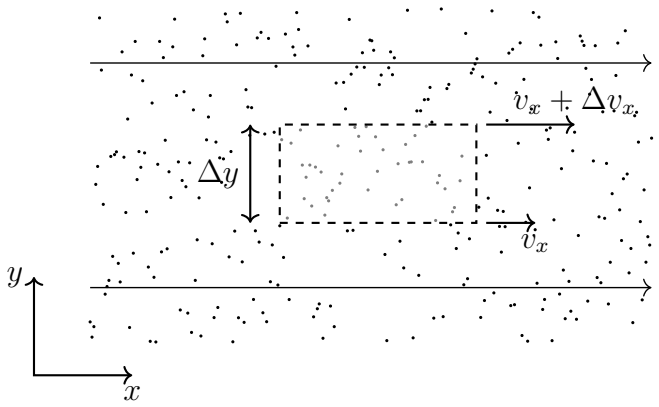

Figure 3.8: Schematic drawing of a liquid motion in the x-direction. The dashes box indicates a slice where the velocity gradient is linear. This figure is inspired by Fig. 41.2 from Feynman [1964].

Setups, which follow this idea, are used to determine the viscosity in both experiments and simulations. However, this approach does not work for systems in equilibrium which we will be working with. Instead we will use the Green-Kubo formula [Allen et al., 2017]

$$\eta = \frac{V}{k_B T} \int_0^\infty \langle \sigma_{xy}(0)\sigma_{xy}(t)\rangle \, dt, \tag{3.24}$$

where V is the volume of the simulation box, k_B is the Boltzmann constant, T is the temperature, and $\sigma_{xy}(t)$ is the xy component of the stress tensor as a function of time t [Heyes et al., 2019]. The xy component of the shear stress is defined from the pressure tensor, Eq. 2.4, by $\sigma_{xy} = -P_{xy}$.

3.4.4 The Stokes-Einstein relation

In computer simulations it is often easier to determine the diffusion coefficient, D, than the viscosity, η. Because of this a relation between the two would be a very important and practical result.

An alternative way to define D (other than Eq. 3.21) is with the *Einstein-Smoluchowski-Sutherland relation* which states that [March and Tosi, 2002]

$$D = \mu k_B T, \tag{3.25}$$

where μ is the "mobility" which describes the drift velocity over the applied force. For non-turbulent flow in a viscous liquid the mobility of a particle can be described by *Stokes' law*

$$\mu = \frac{1}{c\pi\eta\sigma_H}, \tag{3.26}$$

where c is a constant, η is the viscosity and σ_H is the hydrodynamic diameter and is related to the size of the particle. Connecting Eq. 3.25 and 3.26 gives rice to the *Stokes-Einstein relation* which states the following for D and η

$$D\eta = \frac{k_B T}{c\pi\sigma_H}. \tag{3.27}$$

However, by the use of reduced units described in the *isomorph theory* this can be simplified further such that the product reduces to a dimensionless constant α [Costigliola et al., 2019]

$$\tilde{D}\tilde{\eta} = \alpha. \tag{3.28}$$

Here ˜ (tilde) indicated that the parameters has been scaled. The next chapter is dedicated to explain isomorph theory and this scaling.

Chapter 4

Isomorph Theory

The goal of this chapter is to provide an explain of the basics of isomorph theory for the uninitiated. To do this we will first introduce historical background, followed by the definition of the theory and its predictions. Lastly we will show a way of tracing isomorphs in the phase diagram.

4.1 Introduction to isomorph theory

When describing the behaviour of a system it is helpful to analyse different properties along specific curves in the phase diagram. This could be curves of constant temperature T (isotherm), volume V (isochore), pressure P (isobar) etc. However, it turns out that for some systems many structural and dynamical properties are invariant when scaled appropriately along some curves called *isomorphs*.

The isomorph theory is a way to describe the phase diagram of materials with a single parameter, and it has been developed at Roskilde University in Denmark since 2009. The theory was first described in the fourth paper in the series "*Pressure-energy correlations in liquids*" [Gnan et al., 2009] but has since been reworked and clarified in Schrøder and Dyre [2014]. The name isomorph is Greek and means equal shape/form which could be confusing since not only structural properties are expected to be invariant. However, the inspiration for the name came from the mathematical term "isomorphism" which refers to a mapping of specific properties between two sets.

In this chapter we aim to give an overview of isomorph theory including; some background, the definition of isomorphs, the scaling of units, and how to trace isomorphs.

4.2 Invariance and scaling

4.2.1 Excess entropy scaling

Excess entropy (S_{ex}) is defined as the difference in entropy when compared with an ideal gas at the same density and temperature , i.e.

$$S_{ex}(\rho, T) = S(\rho, T) - S_{id}(\rho, T). \tag{4.1}$$

Curves in the phase diagram with constant excess entropy ($\Delta S_{ex} = 0$) are called *configurational adiabats*.

Based on simulations Yaakov Rosenfeld proposed that excess entropy is the controlling parameter for transport coefficients in simple models like hard-spheres, soft-spheres, and Lennard-Jones [Rosenfeld, 1977]. Rosenfeld also introduced the concept of "reduced" transport coefficients which are dimensionless versions obtained by scaling with the state point parameters ρ and T. This work was later continued, where the scaling was shown to be more universal and also hold for dilute gases [Rosenfeld, 1999]. These two cases would later be connected in Bell et al. [2019].

Thus, it was established that there is a scaling which for simple systems result in invariant transport coefficients along configurational adiabats. The reason for this invariance was still not understood. An explanation of this was provided with the introduction of isomorph theory.

4.2.2 Density scaling

Density scaling mainly has its basis in experiments. The main idea of density scaling is that the dynamics of a system is not depending on ρ and T independently, but rather the specific combination [Roland et al., 2005]

$$\Gamma = \frac{\rho^\gamma}{T}, \tag{4.2}$$

where γ is a system specific coefficient. For systems with density scaling the phase diagram can effectively be reduced to 1 dimension with parameter Γ.

There has been some debate weather γ is a constant. However, experimental data from Ransom et al. [2019] showed that it does change at high pressure, but can approximately be considered a constant for smaller changes. Density scaling and Eq. 4.2 is exact for systems where the potential energy can be described by an inverse power law with exponent n (Eq. 2.26). In these simple cases γ is in fact a constant and is equal to $n/3$.

4.3 Definition of isomorphs

As mentioned earlier the isomorph theory was first introduced in Gnan et al. [2009], however, we will be focusing on the more recent version from Schrøder and Dyre [2014].The two versions are of course consistent and it is shown in Schrøder and Dyre [2014] that the old version is the first-order approximation of the new version.

The isomorph theory is true for a class of systems called Roskilde-simple or R-simple for short. A R-simple system has the property that for two configurations $\boldsymbol{R_a}$ and $\boldsymbol{R_b}$ at equal density ρ and potential energy $U(\boldsymbol{R})$ then if

$$U(\boldsymbol{R_a}) < U(\boldsymbol{R_b}) \quad \Leftrightarrow \quad U(\lambda \boldsymbol{R_a}) < U(\lambda \boldsymbol{R_b}) \tag{4.3}$$

$$U(\boldsymbol{R_a}) = U(\boldsymbol{R_b}) \quad \Rightarrow \quad U(\lambda \boldsymbol{R_a}) = U(\lambda \boldsymbol{R_b}), \tag{4.4}$$

for any positive real number λ. From this we see that the isomorph theory is exact if the potential energy $U(\boldsymbol{R})$ is a homogeneous function i.e.

$$f(\lambda \boldsymbol{X}) = \lambda^k f(\boldsymbol{X}), \tag{4.5}$$

where $\boldsymbol{X}$ is a multidimensional variable, and λ and k are positive real numbers. An example of this could be a pair potential consisting of an inverse power law. This idea of scaling the configurations are essential for the theory, specifically scaling with the density such that $\tilde{\boldsymbol{R}} = \rho^{1/3}\boldsymbol{R}$. An illustration of this can be seen in Fig. 4.1. From this it became sufficient to define isomorphs as configurational adiabats and thus the excess entropy is invariant.

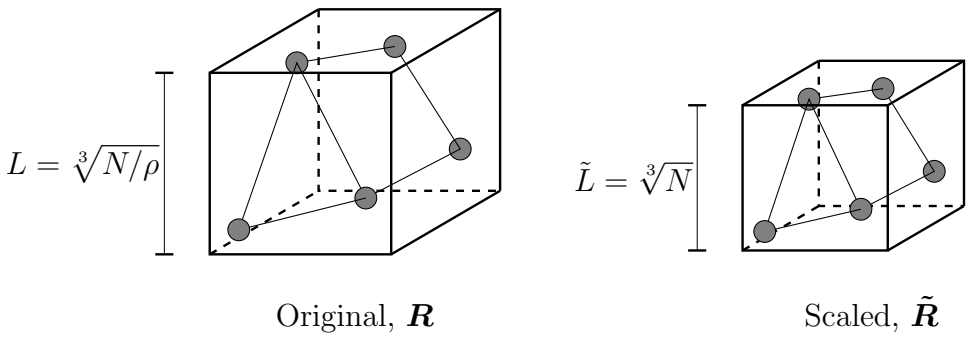

Figure 4.1: Illustration of isomorph scaling of a cubic box. The left box has side-lengths $L = \sqrt[3]{V} = \sqrt[3]{N/\rho}$. Here the average distance between particles is $\rho^{-1/3}$. The right box is scaled with the density such that $\tilde{L} = \sqrt[3]{N}$.

4.3.1 Isomorph scaled units

A list of the characteristic quantities used for the isomorph scaled units can be found in Tab. 4.1. Furthermore a list of some of the reduced units and the necessary scaling factors can be seen in Tab. 4.2. It is common to use ˜ (tilde) to indicate that a quantity has been scaled.

Name	Symbol	SI unit
Number density	ρ	m^{-3}
Temperature	T	K
Characteristic mass	m	kg
Boltzmann constant	k_B	$\mathrm{J\ K}^{-1}$

Table 4.1: List of characteristic quantities for Newtonian dynamics [Gnan et al., 2009].

Quantity		Definition	
Length		l_0	$= \rho^{-1/3}$
Energy		E_0	$= k_B T$
Time		t_0	$= \rho^{-1/3}\sqrt{\frac{m}{k_B T}}$
Velocity	$\tilde{v} =$	$\frac{v}{l_0/t_0}$	$= \sqrt{\frac{m}{k_B T}} v$
Force	$\tilde{F} =$	$\frac{F}{E_0/l_0}$	$= \frac{1}{\rho^{1/3} k_B T} F$
Pressure	$\tilde{P} =$	$\frac{P}{E/l_0^3}$	$= \frac{1}{\rho k_B T} P$
Diffusion coefficient	$\tilde{D} =$	$\frac{D}{l_0^2/t_0}$	$= \rho^{1/3}\sqrt{\frac{m}{k_B T}} D$
Viscosity	$\tilde{\eta} =$	$\frac{\eta}{E_0 t_0/l_0^3}$	$= \frac{1}{\rho^{2/3}\sqrt{m k_B T}} \eta$
Heat conductivity	$\tilde{\kappa} =$	$\frac{\kappa}{k_B/(l_0 t_0)}$	$= \frac{\sqrt{m/(k_B T)}}{\rho^{2/3} k_B} \kappa$

Table 4.2: List of scaling factors for conversion to isomorph reduced units [Gnan et al., 2009].

4.3.2 Predictions of isomorph theory

In this section we quickly go through the derivation of the most important predictions of isomorph theory. However, for a more detailed description we refer to the original paper Schrøder and Dyre [2014].

Equal excess entropy

First we define the *microscopic excess entropy function* as the thermodynamic excess entropy of a system

$$S_{ex}(\boldsymbol{R}) \equiv S_{ex}(\rho, U(\boldsymbol{R})), \tag{4.6}$$

where $U(\boldsymbol{R})$ is the average potential energy for the density ρ with configuration $\boldsymbol{R}$.

Assume we have two configurations $\boldsymbol{R_1}$ and $\boldsymbol{R_2}$ at densities ρ_1 and ρ_2 respectively, with equivalent reduced representation, i.e. $\tilde{\boldsymbol{R}}_\mathbf{1} = \rho_1^{1/3}\boldsymbol{R_1} = \rho_2^{1/3}\boldsymbol{R_2} = \tilde{\boldsymbol{R}}_\mathbf{2}$. The microcanonical expression for the excess entropy for the two configurations is given by

$$\frac{S_{ex}(\boldsymbol{R_1})}{k_B} = -N\ln(N) + \ln\left(\mathrm{Vol}\left\{\tilde{\boldsymbol{R}}' | U(\rho_1^{-1/3}\tilde{\boldsymbol{R}}') < U(\boldsymbol{R_1})\right\}\right) \tag{4.7}$$

$$\frac{S_{ex}(\boldsymbol{R_2})}{k_B} = -N\ln(N) + \ln\left(\mathrm{Vol}\left\{\tilde{\boldsymbol{R}}' | U(\rho_2^{-1/3}\tilde{\boldsymbol{R}}') < U(\boldsymbol{R_2})\right\}\right), \tag{4.8}$$

where "Vol" is the reduced-coordinate configuration volume. If these configurations are from a R-simple system they will per definition obey Eq. 4.3. By using Eq. 4.3 on the second term of Eq. 4.7 and choosing $\lambda = \rho_1^{1/3}\rho_2^{-1/3}$ we get

$$U(\rho_1^{-1/3}\tilde{\boldsymbol{R}}') < U(\boldsymbol{R_1}) \Leftrightarrow U(\rho_2^{-1/3}\tilde{\boldsymbol{R}}') < U(\rho_1^{1/3}\rho_2^{-1/3}\boldsymbol{R_1}) = U(\boldsymbol{R_2}) \tag{4.9}$$

which is the second term in Eq. 4.8. From this it follows that $S_{ex}(\boldsymbol{R_1}) = S_{ex}(\boldsymbol{R_2})$. This means that for R-simple systems $S_{ex}(\boldsymbol{R})$ only depends on the reduced configuration, i.e.

$$S_{ex}(\boldsymbol{R}) = S_{ex}(\tilde{\boldsymbol{R}}). \tag{4.10}$$

Thus the potential energy can be written as

$$U(\boldsymbol{R}) = U(\rho, S_{ex}(\boldsymbol{R})) = U(\rho, S_{ex}(\tilde{\boldsymbol{R}})). \tag{4.11}$$

This description of potential energy from Eq. 4.11 is an important result which will be used in the following derivations.

Invariance of structure and dynamics

The reduced forces are defined as

$$\tilde{\boldsymbol{F}} \equiv \boldsymbol{F}\frac{\rho^{-1/3}}{k_B T}. \tag{4.12}$$

Eq. 4.11 implies that the force is

$$\boldsymbol{F} = -\nabla U = -\left(\frac{\partial U}{\partial S_{ex}}\right)_{\rho} \nabla S_{ex}(\tilde{\boldsymbol{R}}) = -T\nabla S_{ex}(\tilde{\boldsymbol{R}}), \tag{4.13}$$

which when combined with Eq. 4.12 shows that the reduced force is

$$\tilde{\boldsymbol{F}} = -\nabla S_{ex}(\tilde{\boldsymbol{R}})\frac{\rho^{-1/3}}{k_B}. \tag{4.14}$$

This means that the reduced force is a function of the reduced configuration $\tilde{\boldsymbol{R}}$ and not just $\boldsymbol{R}$. It then follows from Eq. 4.6 that two points along a configurational adiabat must have equal reduced forces and consequently identical reduced dynamics. Likewise the use of the same reduced configurations also implies invariance of the reduced structure. This feature of invariant structure and dynamics is the main prediction of isomorph theory.

Potential energy and virial correlation

The virial of a configuration $\boldsymbol{R}$ with potential energy $U(\boldsymbol{R})$ is defined as

$$W(\boldsymbol{R}) \equiv -\frac{1}{3}\boldsymbol{R}\cdot\nabla U(\boldsymbol{R}). \tag{4.15}$$

We would like to show a connection between potential energy U and virial W. To do this we use two configurations $\boldsymbol{R_a}$ and $\boldsymbol{R_b}$ at the same density with equal potential energy. Assuming the system is R-simple Eq. 4.4 then gives $U(\lambda\boldsymbol{R_a}) = U(\lambda\boldsymbol{R_b})$. Differentiating this with respect to λ gives

$$\boldsymbol{R_a}\cdot\nabla U(\lambda\boldsymbol{R_a}) = \boldsymbol{R_b}\cdot\nabla U(\lambda\boldsymbol{R_b}). \tag{4.16}$$

Setting $\lambda = 1$ and using Eq. 4.15 yields

$$W(\boldsymbol{R_a}) = W(\boldsymbol{R_b}). \tag{4.17}$$

This means that W is a function of U and ρ, which implies that W and U theoretically should be perfectly correlated. However, no real system has perfect correlations, but this result can still be used to predict the "quality"of an isomorph. We refer to this correlation as R

$$R\,(\rho,T) = \frac{\langle \Delta W \Delta U\rangle}{\sqrt{\langle(\Delta W)^2\rangle\,\langle(\Delta U)^2\rangle}}. \tag{4.18}$$

In the first version of the theory a configurational adiabat was only considered an isomorph when it had strong correlations, i.e. $R > 0.9$. However, for some systems invariance has also been observed at lower R [Veldhorst et al., 2014]

Another relevant quantity for the WU correlation is the coefficient of proportionality between the two, also referred to as density scaling exponent γ. For this the definition of γ from the first version of the theory is reused [Gnan et al., 2009]

$$\gamma\left(\rho, S_{ex}\right) \equiv \left(\frac{d\ln T}{d\ln \rho}\right)_{S_{ex}} = \frac{\langle \Delta W \Delta U\rangle}{\langle (\Delta U)^2\rangle}. \tag{4.19}$$

This quantity can be used to trace the isomorphs in the phase diagram.

4.3.3 Tracing isomorphs

Different methods have been developed for tracing isomorphs in the phase diagram. However, in this section we will only go through one of the simpler methods. For this we will be using the Euler iteration method which calculates the next step y_{n+1} as

$$y_{n+1} = y_n + hf(x_n, y_n) \tag{4.20}$$

This method combined with Eq. 4.19 can be used to trace a configurational adiabat in the $\rho - T$ phase diagram.

$$d\ln T = \gamma_n \left(d\ln \rho\right) \tag{4.21}$$

$$\ln T_{n+1} - \ln T_n = \gamma_n \left(\ln \rho_{n+1} - \ln \rho_n\right) \tag{4.22}$$

$$T_{n+1} = T_n \left(\frac{\rho_{n+1}}{\rho_n}\right)^{\gamma_n}, \tag{4.23}$$

where γ_n is a function of ρ_n and T_n.

Other methods for tracing isomorphs (e.g. *direct isomorph check*) has been developed, but they will not be utilised in this work. However, a description is provided in Gnan et al. [2009].

Tracing isomorphs in molecular systems

These methods for tracing isomorphs are generally known to not work for molecular systems, at least systems with flexible bonds. This is because the bonded potentials generally decorrelates U and W [Olsen et al., 2016]. In these cases other methods are needed.

The approach we will be using for our molecular system is to analyse isochores and describe their dynamical properties as a function of T. From this we can extrapolate and find a temperature for each density where the dynamics are invariant.

Chapter 5

Simple Atomic Ionic Liquid Model

In this chapter we analyse the *simple salt model* from Hansen and McDonald [1975]. The main focus is on the potential existence of isomorphs. This is despite knowing from previous studies that systems with strong Coulomb interactions generally do not have isomorphs [Dyre, 2014]. However, experimental studies such as Hansen et al. [2020] show density scaling applying for ILs. This makes us believe that ILs could have an isomorphs-like behaviour in the weak Coulomb regime.

The results from this study have been published in the *Journal of Chemical Physics* with the title *Quantifying dynamical and structural invariance in a simple molten salt model* [Knudsen et al., 2021]. It should be noted that this publication was written before this chapter, and hence will undoubtedly be many similarities between the two since they report the same findings. Since this publication, more simulations have been performed to investigate even lower densities, however, this does not change the conclusions from the paper. The paper is provided in Chap. D.

5.1 Model details and analysis

One of the most distinctive properties of ionic liquids when compared with other liquids are there charges, wherefore their name. To better understand this characteristic we start by investigating a very simple model which has this as its primary feature. For this we choose the *simple salt model* from Hansen and McDonald [1975]. Contrary to Hansen and McDonald we generally study higher densities to gain insight in both the Coulomb dominated region and the weak Coulomb region.

5.1.1 The potential energy

The Hansen and McDonald simple salt model contains two types of particles, which we refer to as A and B. These are point particles, identical in every way except for their opposite charge. Because of this symmetry, we will only show results for types A, AA, and AB since they are identical to B, BB, and BA, respectively.

The potential energy between the particles is defined as a sum of two inverse power laws (IPLs). The first is always repulsive, insuring that the particles do not overlap; the second represents the Coulomb interactions, and its sign is therefore dependent on the particle types. Say that any particle type can be represented by either α or β then the potential energy is described by

$$V_{\alpha\beta}(r) = \frac{1}{9}\left(\frac{\sigma}{r}\right)^9 + \epsilon_{\alpha\beta}\left(\frac{\sigma}{r}\right), \tag{5.1}$$

where $\epsilon_{AA} = 1$, $\epsilon_{AB} = -1$, and the characteristic distance parameter σ (the location of the minimum in V_{AB}) is absorbed in r or simply set equal to 1. We choose a cutoff at $r_{cut} = 6$ and applied the shifted force method described in Sec. 2.4.1. The graph of the cut and uncut potential can be seen in Fig. 5.1, and a test of the chosen cutoff value is provided in Sec. 5.2.1.

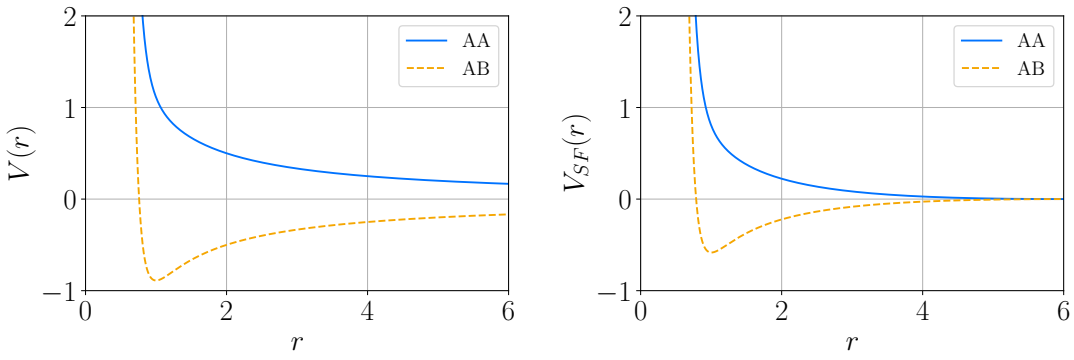

Figure 5.1: The graphs of the potential for the simple salt model, Eq. 5.1. On the left is a graphs of the potential with no truncation. On the right is a graphs of the potential with the shifted force method and a cutoff at 6.

5.1.2 Scaling the electrostatic interactions

As will be described in Sec. 5.3, we analysed this model in a large density and temperature interval. One of the reasons for this is that we can artificially change the strength of the electrostatic interactions by moving around in the phase diagram. To better understand this, we study a more general version of Eq. 5.1 where the Coulomb term (the second IPL) is scaled by a positive dimensionless scalar λ, and the exponent in the first IPL is $n > 1$

$$V_{\alpha\beta}(r) = \epsilon \left(\frac{1}{n} \left(\frac{\sigma}{r} \right)^n + \epsilon_{\alpha\beta} \lambda \frac{\sigma}{r} \right). \tag{5.2}$$

It turns out that we can remove the λ by scaling the total potential and r, such that the potential becomes

$$V_{\alpha\beta}(r) = \epsilon' \left(\frac{1}{n} \left(\frac{\sigma'}{r} \right)^n + \epsilon_{\alpha\beta} \frac{\sigma'}{r} \right), \tag{5.3}$$

where $\epsilon' = \epsilon \lambda^{n/(n-1)}$ scales the overall energy, and $\sigma' = \sigma \lambda^{-1/(n-1)}$ is the rescaled distance. The minimum for the rescaled $V_{AB}(r)$ is located at $\left(\sigma'; \frac{1-n}{n}\epsilon'\right)$.

This rescaling implies that each state point $(\rho_0; T_0)$ simulated with Eq. 5.1 is equivalent to a different state point $(\rho; T)$, where the Coulomb term has been scaled by λ. This new state point would be

$$\begin{pmatrix} \rho \\ T \end{pmatrix} = \begin{pmatrix} \lambda^{3/(1-n)} \rho_0 \\ \lambda^{n/(1-n)} T_0 \end{pmatrix}. \tag{5.4}$$

This traces out a curve, which turns out to be a simple power law with the form

$$T = (\rho/\rho_0)^{n/3} T_0 \qquad \text{along which} \qquad \lambda = (\rho/\rho_0)^{\frac{1-n}{3}}. \tag{5.5}$$

Since $n > 1$, increasing the electrostatic interactions would correspond to decreasing the density. This makes sense since we expect the Coulomb term to dominate at long distances.

This means that the results of our analysis will also be valid for other values of λ. It should be noted that properties will change when presented in isomorph scaled units, since they are dependent on the state point. However, if a property is invariant along a line in the phase diagram, this will still be the case after the λ-scaling, but the line and value of the property will be different in the new phase diagram.

5.1.3 Density dependence of the density scaling exponent

It would be interesting to get an idea of the density scaling exponent γ dependence on density. Both because it controls the shape of the configurational adiabats but also because it can be compared with experiments. To do this, we start by analysing the fluctuation of the potential energy, which can be separated into two terms representing the repulsive IPL and the Coulomb interactions

$$\Delta U = \Delta U_{IPL} + \Delta U_C. \tag{5.6}$$

The same can be done for the fluctuation of the virial using Eq. 4.15

$$\begin{aligned} \Delta W &= \Delta W_{IPL} + \Delta W_C \\ &= 3\Delta U_{IPL} + \frac{1}{3}\Delta U_C. \end{aligned} \tag{5.7}$$

By using the definition of γ from Eq. 4.19, and the two expressions for ΔU and ΔW above we get

$$\begin{aligned} \gamma &= \frac{\langle \Delta W \Delta U \rangle}{\langle (\Delta U)^2 \rangle} \\ &= \frac{3\left\langle (\Delta U_{IPL})^2 \right\rangle + \frac{10}{3}\left\langle (\Delta U_{IPL}\Delta U_C) \right\rangle + \frac{1}{3}\left\langle (\Delta U_C)^2 \right\rangle}{\left\langle (\Delta U_{IPL})^2 \right\rangle + 2\left\langle (\Delta U_{IPL}\Delta U_C) \right\rangle + \left\langle (\Delta U_C)^2 \right\rangle}. \end{aligned} \tag{5.8}$$

The value of $\langle (\Delta U_{IPL}\Delta U_C) \rangle$ was calculated for a couple of state points along a configurational adiabat (A1), see Fig. 5.2. Here we see that at high densities the correlation is close to zero.

Based on this, we presume that $\langle \Delta U_{IPL}\Delta U_C \rangle = 0$ which allows us to simplify the expression to

$$\gamma = \frac{3 + X/3}{1 + X} \qquad \text{where} \qquad X \equiv \frac{\left\langle (\Delta U_C)^2 \right\rangle}{\left\langle (\Delta U_{IPL})^2 \right\rangle}. \tag{5.9}$$

We would expect X to approach 0 at high densities, meaning that $\gamma = 3$ in this limit. Likewise at low densities γ would theoretically have at limit at 1/3.

As will be shown later in Fig. 5.6, we see that γ becomes less than 1/3 at the lowest densities along the isotherms. However, this is not surprising since we saw in Fig. 5.2 that ΔU_{IPL} and ΔU_C are not uncorrelated at low densities.

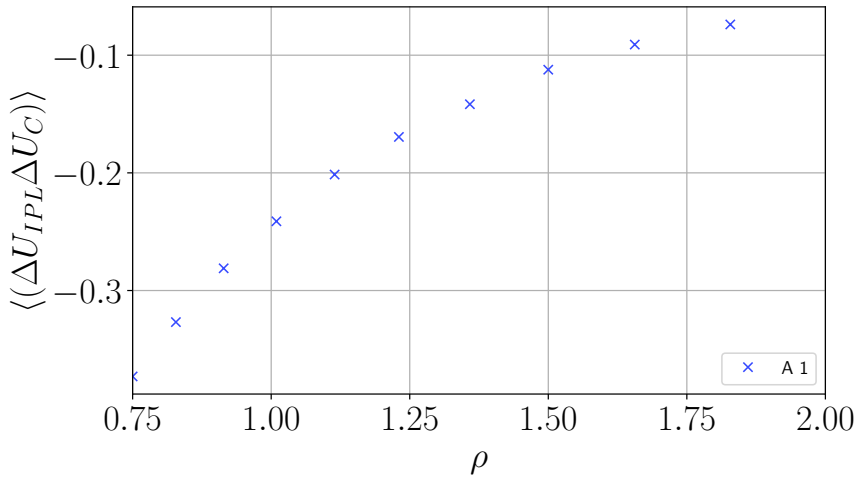

Figure 5.2: Correlation between U_{IPL} and U_C for selected points along a configurational adiabat (A1).

5.2 Test of model implementation

5.2.1 Test cutoff

In our studies of this model we used the shifted force cutoff method and a cutoff value of 6σ. We would like to test if this cutoff value was sufficiently large or if this choice affected the results significantly. To do this we performed a set of simulations at three different state points $\rho = 0.75$ and $T = 0.1; 0.5; 1.0$ and with three different cutoff values $r_{cut} = 3; 4; 5$.

Then we analysed the Bhatia-Thornton partial structure factor with a focus on the small q. The Bhatia-Thornton structure factor was calculated from density fluctuations to avoid artefacts from Fourier transforming the radial distribution function. The biggest changes in this region was observed at the high temperature so that will be shown in Fig. 5.3 at the three tested cutoff values and the value 6 from our simulations.

Here we find that the NN curves does not change much when varying the cutoff value. On the other hand, the CC curves does change, but only significantly at small q. There are visible changes between 3, 4, and 5 at small q. However, the difference between 5 and 6 are very small suggesting that a cutoff value of 5 is sufficient and 6 (which we used) is safe.

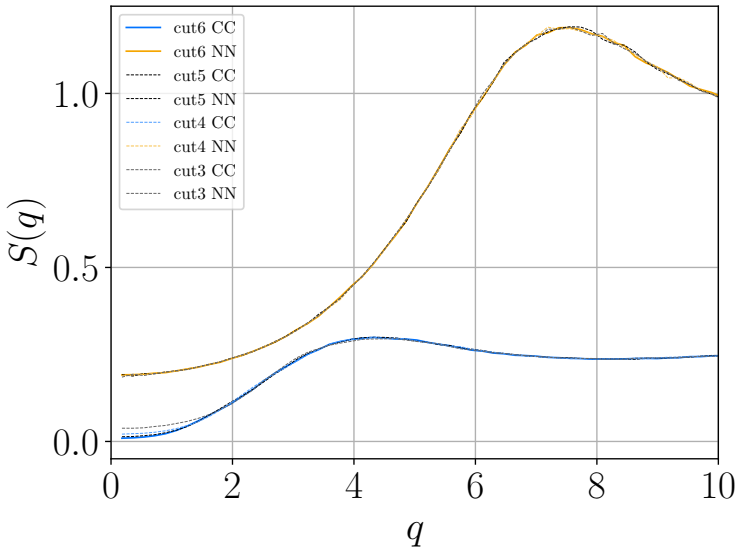

Figure 5.3: Bhatia-Thornton partial structure factors at $\rho = 0.75$ and $T = 1.0$ with four different cutoff values; 3, 4, 5 and 6σ. This structure factor is calculated from density fluctuations to avoid artefacts from Fourier transforming the radial distribution function.

5.3 Simulation details

We have simulated three configurational adiabats which will be referred to as A1, A2, and A3. They were all simulated to a max density around 2. A2 and A3 start at state points $(1.0; 0.1)$, and $(1.2; 0.1)$, respectively, while A1 passes through $(0.75; 0.1)$ but got extended to low densities, 0.3, to check the behaviour in this region. For comparison, we also simulated six isotherms at $T = 0.1; 0.15; 0.2; 0.3; 0.5; 1.0$ in a density interval from 0.1 to 2.0. These will be referred to as T0.1, T0.15, T0.2, T0.3, T0.5, and T1.0, respectively. We performed more simulations between densities 0.7 and 2.0 to get a better insight into the models behaviour in this region. Fig. 5.4 shows all the simulated state points in a $\rho - T$ phase diagram. Some simulations along isotherms crystallized in the high density low temperature region. The structure observed here was similar to that of an CsCl crystal, see Fig. 5.5. These simulations will not be analysed further.

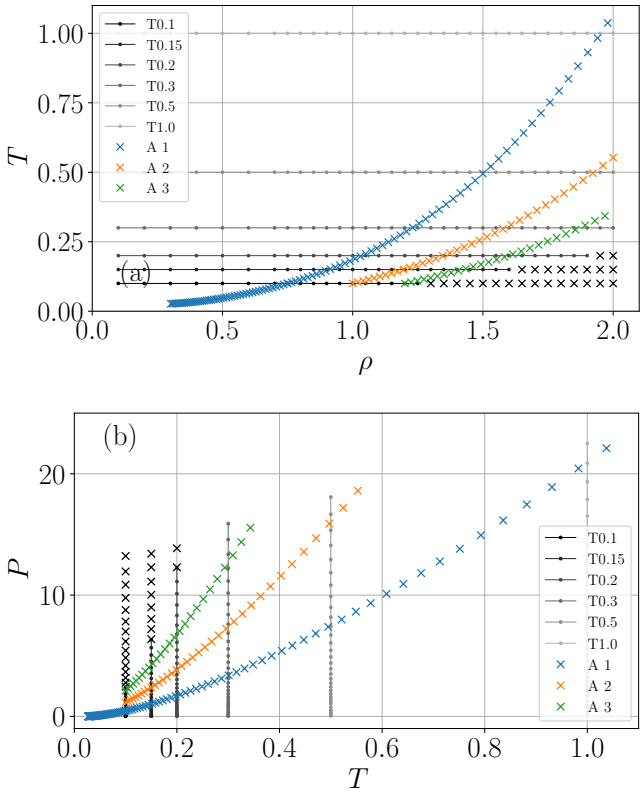

Figure 5.4: Simulated configurational adiabats and isotherms in (a) a $\rho - T$ phase diagram and (b) with P as a function of T. The state points, where crystallization was observed are marked with a black X.

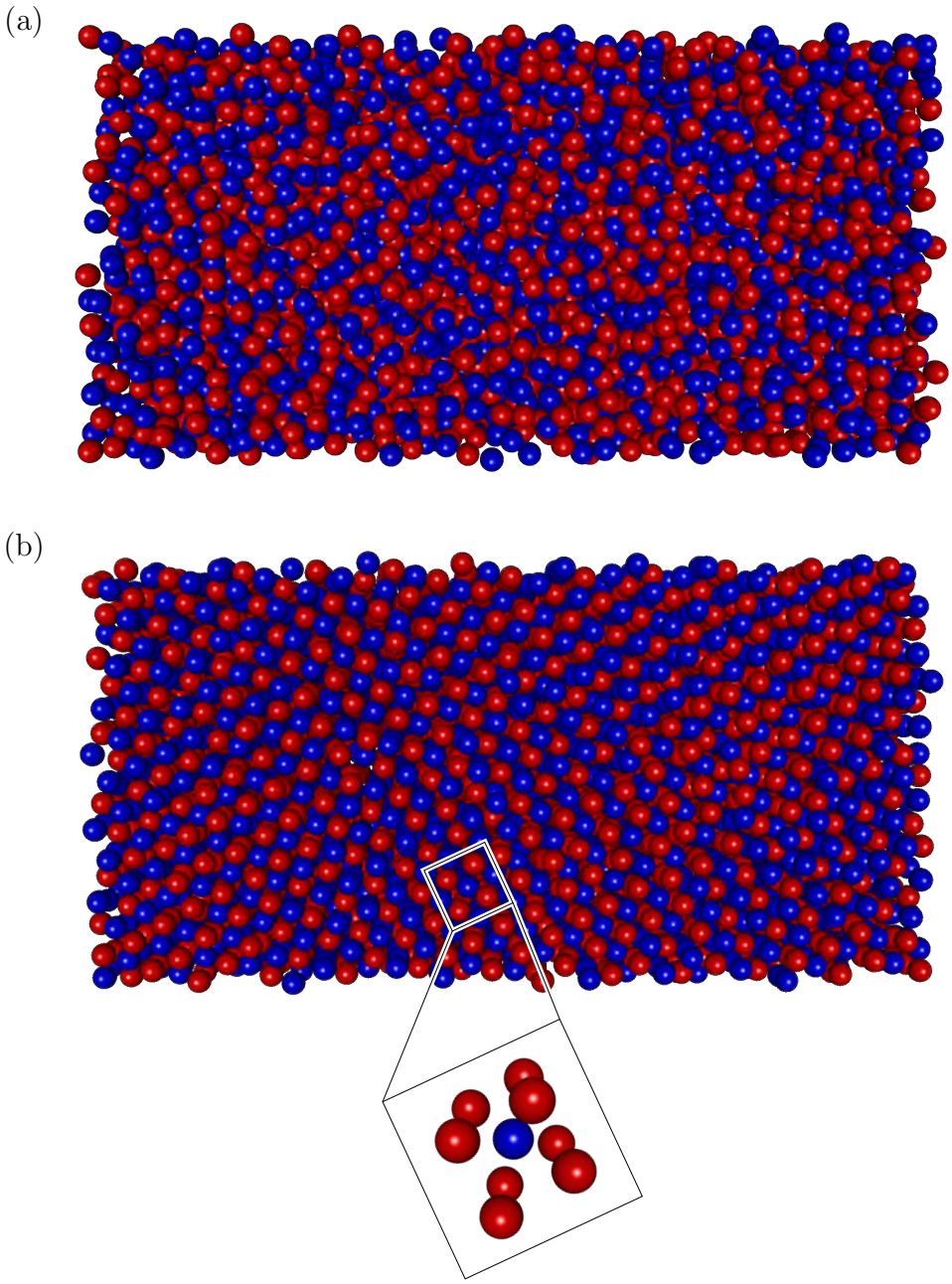

Figure 5.5: (a) An example of a liquid configuration at $\rho = 1.35$ and $T = 1.0$. Note that there is no long range structure. (b) An example of a crystalized configuration at $\rho = 1.35$ and $T = 0.1$. The crystal structure observed during the these simulations was similar to that of an CsCl crystal.

To check if the three configurational adiabats A1, A2, and A3 are isomorphs, we calculated the correlation coefficient between the potential energy and virial (Eq. 4.18), and checked if it was greater than 0.9. This criteria turns out only to be satisfied at high densities, meaning that these curves are not isomorphs in the entire simulated range, and will therefore not be referred to as such. We traced the configurational adiabats with the density scaling exponent γ (Eq. 4.19) as described in Sec. 4.3.3. The density was scaled with 2% between each simulation

$$T_{n+1} = T_n \left(\frac{\rho_{n+1}}{\rho_n} \right)^{\gamma_n} . \tag{5.10}$$

Fig. 5.6 show R and γ as a function of density for all configurational adiabats and isotherms. We see that γ is monotonically increasing as a function of density, and it seems to slowly approach 3.

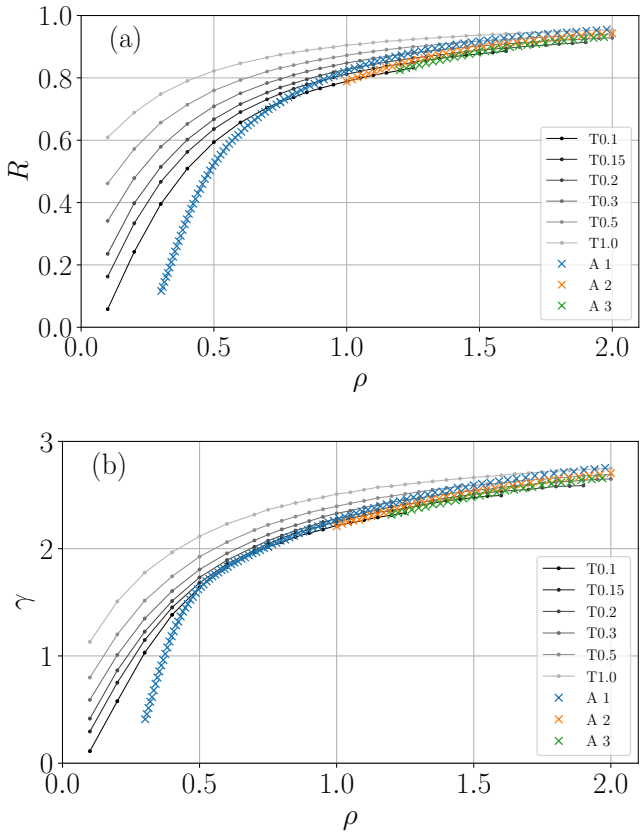

Figure 5.6: (a) Correlation coefficient R along configurational adiabats and isotherms as a function of density. (b) Density scaling exponent γ along configurational adiabats and isotherms as a function of density.

All simulations contained 8000 particles, and had a data collection run of $100 \cdot 2^{17}$ timesteps with an isomorph scaled timestep of $\tilde{t}_{step} = 0.004$. Since state points along an isotherm in the NVT ensemble are independent of each other, they could run in parallel. All particles started in a face centred cubic lattice (randomized by type) and were equilibrated for $2 \cdot 10^6$ time steps. We checked that this initial lattice had melted by analysing the radial distribution function and the particle configurations. On the other hand, the points along the configurational adiabats are dependent on each other, and therefore had to be run in series. However, since we do not expect big changes, only the first point equilibrated for $2 \cdot 10^6$ time-steps, the next point started at the previous end-configuration and was equilibrated for 10^6 time-steps.

The Nosé-Hoover Thermostat (see Sec. 2.3) was used to preform these NVT simulations. The thermostat relaxation time was set to 0.2 for all simulations.

All simulations were performed in an elongated box with size $2L \times L \times L$ and periodic boundary conditions. For this model the structure factor is calculated from density fluctuations which means that the smallest q is limited by the size of the simulation box. This was done to avoid artefacts from Fourier transforming the radial distribution function. Thus an elongated box was chosen to get a better resolution in the structure factor without increasing the number of particles.

5.4 Results: Dynamics

In this and the next section, we present and discuss various structural and dynamics properties of the model along the simulated configurational adiabats and isotherms. Since we compare simulations at many different state points, we will focus on quantities with a scalar representation to make the results more clear. However, we will still provide examples of the raw data from which these quantities are calculated.

We will first go through dynamical properties followed by structural properties. All results in this section will be presented in the isomorph scaled units described in Tab. 4.2.

5.4.1 The self-intermediate scattering function

Firstly, we analyse the self-intermediate scattering function, F_s (see Sec. 3.4.1). When calculating F_s we used $\tilde{q} = 7.1$, because it roughly corresponds to the position of the peak in S_{NN} at high densities.

We have found and compared the time when $F_s = e^{-1}$. We tried different methods to determine this time but got the best result when fitting the data to a stretch exponential

$$f(t) = A \exp\Big(-(t/\tau)^{\beta}\Big), \tag{5.11}$$

where A, τ, and β are coefficients. The correlation between the data and the fit was greater than 0.998 in all cases. We also tried with a more restrictive fit where $A = 1$, but this yielded worse results in the relevant time interval. However, A was close to 1 for all fits. Consequently, we refer to the time at which $F_s = e^{-1}$ as $t_{1/e}$ and not the coefficient τ from the fit.

Fig. 5.7 show all F_s curves along A1 and T1.0. Here we should notice that we have no plateaus, rather F_s goes directly from 1 to 0, meaning that there is no two-step relaxation. The second thing is that all the curves along A1 collapse which is not the case for T1.0. This trend is also true for the other isotherms and configurational adiabats.

The second part of Fig. 5.7 shows the isomorph scaled time $\tilde{t}_{1/e}$ as a function of density for all isotherms and configurational adiabats. Here we should notice that along the configurational adiabats $\tilde{t}_{1/e}$ increases slightly at high densities, where as the isotherms changes significantly in the same density interval. It is also worth noting that A1 seems to have a minima around $\rho = 0.7$. We do not know why this is the case, however, this could imply that the invariance vanishes at densities lower than 0.3.

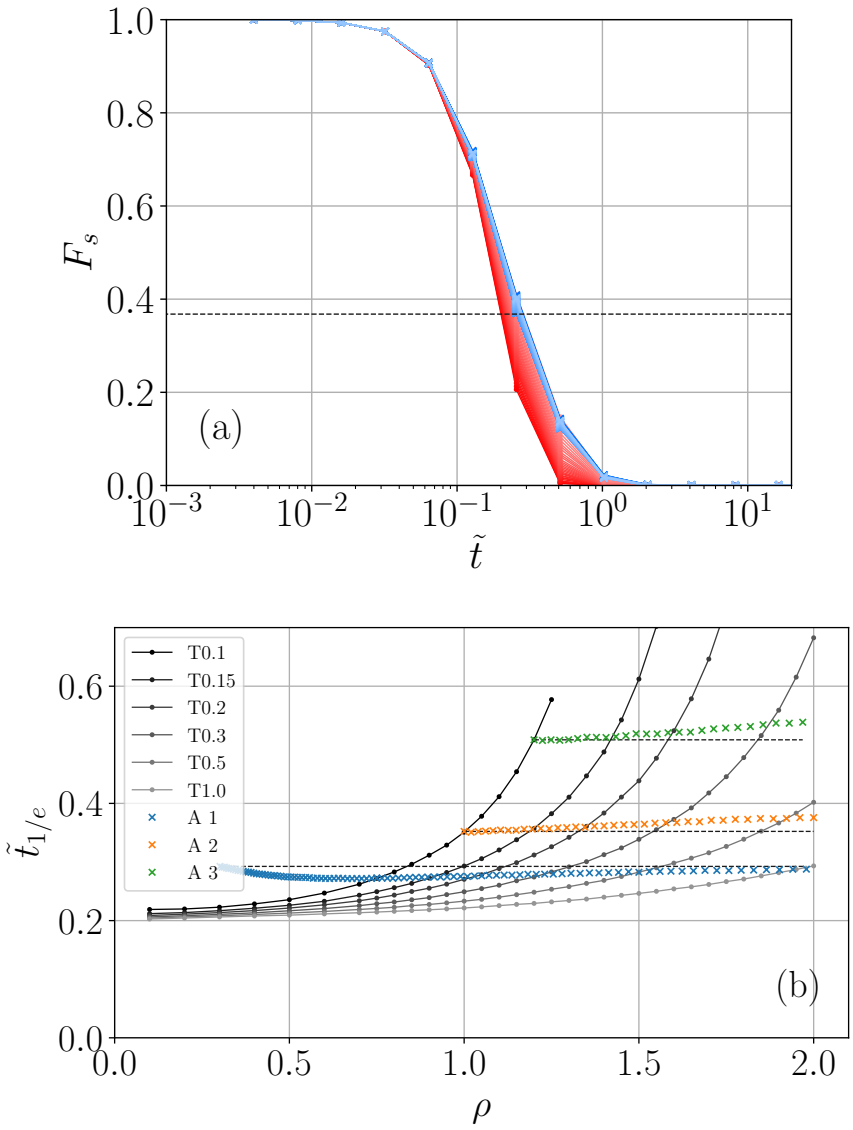

Figure 5.7: (a) All 96 F_s curves along A1 (blue), and all 33 F_s curves along T1.0 (red). The horizontal dashed line indicates the value $e^{-1} \approx 0.37$. (b) The time $\tilde{t}_{1/e}$ as a function of density for all isotherms and configurational adiabats. The horizontal dashed lines going through the first point of A1, A2, and A3 are guides for the eye.

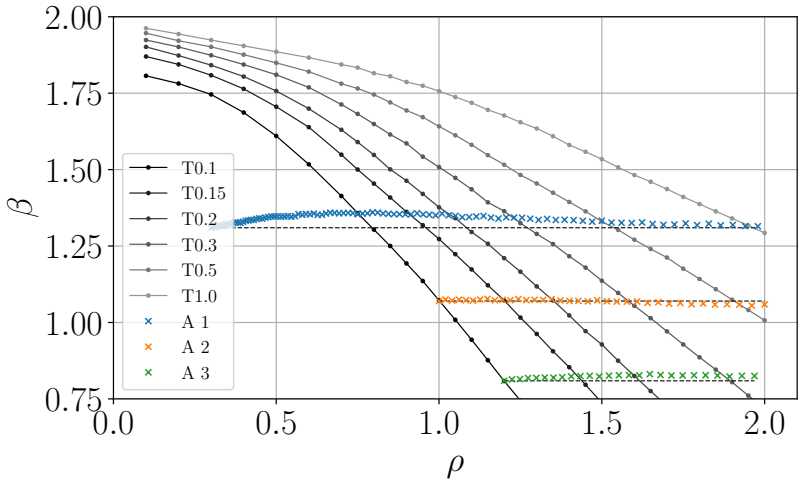

Figure 5.8: Plot of the fitting parameter β from the stretched exponential fit of the F_s data, Eq. 5.11. The horizontal dashed lines going through the first point of A1, A2, and A3 are guides for the eye.

As previously mentioned, we found that a stretched exponential was a better fit then a regular exponential. As a result of this we checked how stretched or compressed the exponential was, so we plotted β from the fit as a function of density in Fig. 5.8. Here we see that the fit switches between being stretched and compressed, and for the isotherms β approaches 2 at low densities corresponding to a Gaussian function. We also see that the data for A1 show a maximum around $\rho = 0.7$, which coincides with the minimum we saw in $t_{1/e}$ at the same density.

5.4.2 The viscosity

We used the Green-Kubo formula described in Sec. 3.4.3 to calculate the viscosity. Computing the integration turned out to be challenging due to the different features and noise in the data. We found that the best results were obtained when fitting the data and performing an analytical integration of the fit. We used to following fitting function

$$f(\tilde{t}) = \begin{cases} a_0 + a_2\tilde{t}^2 + a_3\tilde{t}^3 & \text{for } \tilde{t} \leq 0.06 \\ b_1 \exp\left(-\tilde{t}/\tau_1\right) + b_2 \exp\left(-\tilde{t}/\tau_2\right) & \text{for } 0.06 < \tilde{t} \end{cases}, \tag{5.12}$$

where $\tilde{t}$ is the isomorph scaled time. The first order term in the 3rd order polynomial is set to zero because the slope is zero at $\tilde{t} = 0$. This is because the autocorrelation function is smooth and time-reversible and therefore an even function of time [Hansen and McDonald, 2013].

The first part of Fig. 5.9 shows examples of the stress-autocorrelation. There are two curves along A1 (light and dark blue), and two curves at the density 1.5 (red and orange). Here it should be noted that the two curves along A1 are much more similar then the ones at $\rho = 1.5$.

The second part of Fig. 5.9 shows the reduced viscosity $\tilde{\eta}$ as a function of density for all configurational adiabats and isotherms. Again we see invariance along all configurational adiabats but not the isotherms.

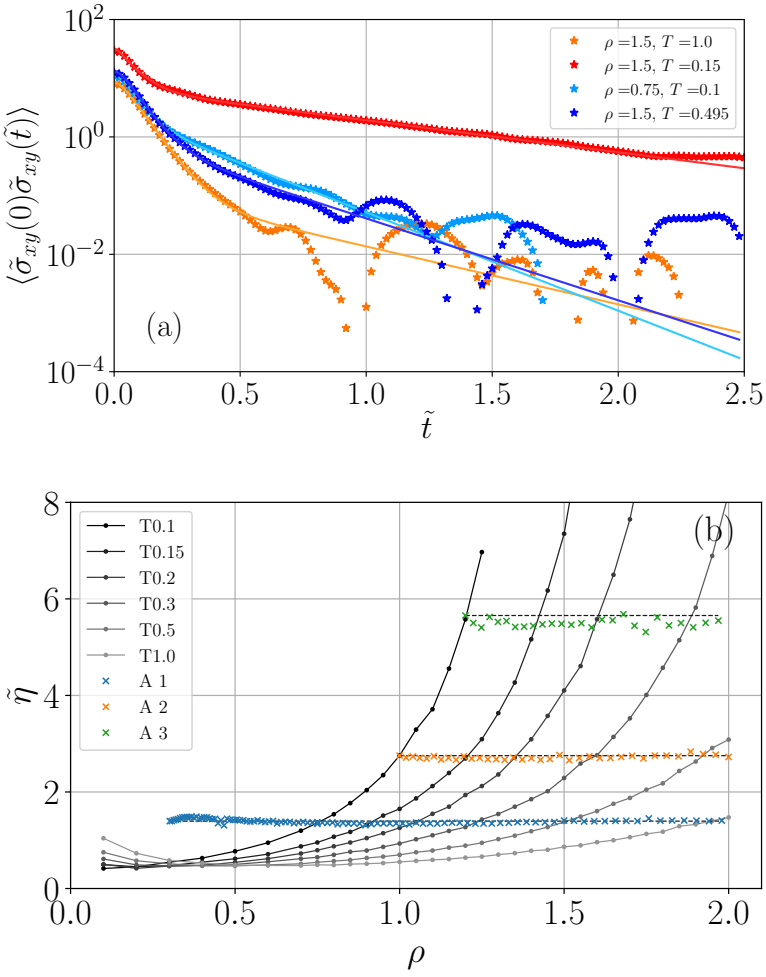

Figure 5.9: (a) Selected stress-autocorrelation curves. The two blue curves are both from A1 and are visibly similar. This is in contrast to the red and orange curves which are on the same isochore with $\rho = 1.5$. (b) The isomorph scaled viscosity as a function of density along all configurational adiabats and isotherms. The horizontal dashed lines going through the first point of A1, A2, and A3 are guides for the eye.

5.4.3 The mean square displacement

Here we present the mean square displacement (MSD) and the diffusion coefficient (D), which are explained in Sec. 3.4.2. The first part of Fig. 5.10 shows all MSD curves along A1 and T1.0. As was the case for F_s, we see that curves along A1 collapse, which is not the case for T1.0 (the same is true for the other configurational adiabats and isotherms).

The second part of Fig. 5.10 show the isomorph scaled diffusion coefficient as a function of density for all configurational adiabats and isotherms. It turns out that $\tilde{D}$ is invariant along the configurational adiabats but not along the isotherms.

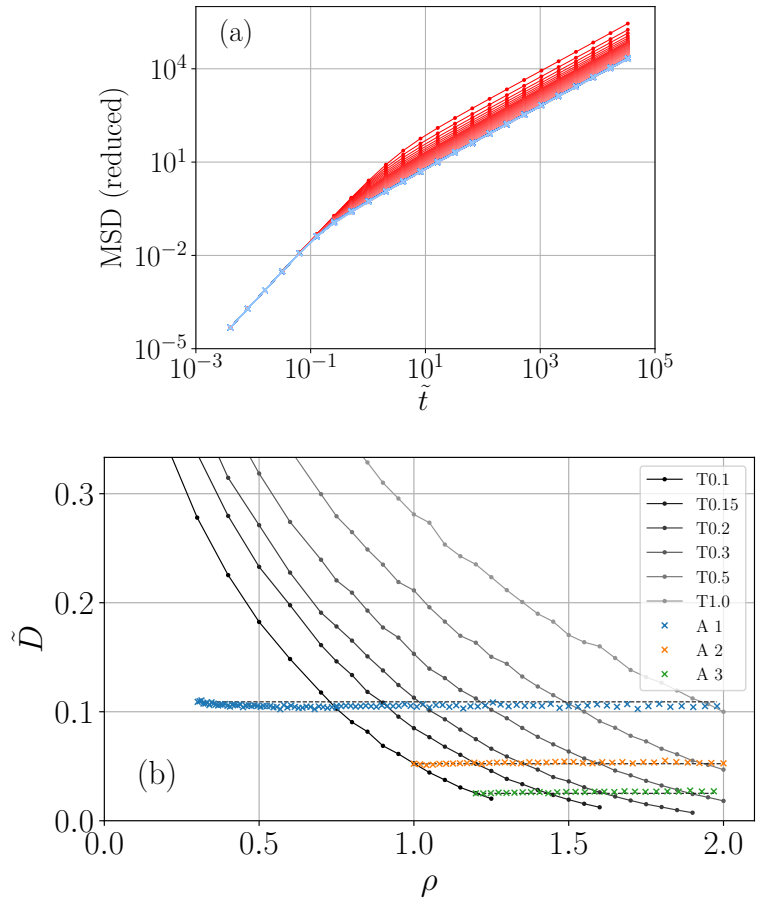

Figure 5.10: (a) All 96 MSD curves along A1 (blue) and all 33 MSD curves along T1.0 (red). (b) The isomorph scaled diffusion coefficient as a function of density along all configurational adiabats and isotherms. The horizontal dashed lines going through the first point of A1, A2, and A3 are guides for the eye.

5.4.4 The Stokes-Einstein relation

The Stokes-Einstein relation (see Sec. 3.4.4) can be used to relate the diffusion coefficient (D) and viscosity (η). However, from the perspective of isomorph theory we use the scaled quantities $\tilde{D}$ and $\tilde{\eta}$ [Costigliola et al., 2019]. Thus, the reduced Stokes-Einstein relation can be seen in Fig. 5.11 for all simulations. Here we see that the relation holds except for the low density high temperature region. The rest of the range has a plateau around 0.15.

Based on the previously observed invariance of $\tilde{D}$ and $\tilde{\eta}$ along configurational adiabats it is not surprising that their product is invariant. However, it is significant that they have the same product since this is a higher level of invariance.

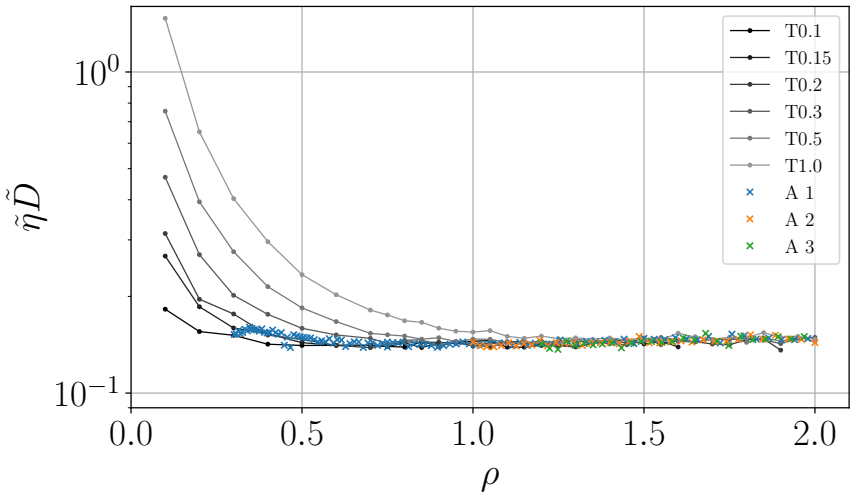

Figure 5.11: The reduced Stokes-Einstein relation along all configurational adiabats and isotherms as a function of density.

5.5 Results: Structure

5.5.1 The partial radial distribution function

Now that we have shown that the system has invariant dynamics along configurational adiabats we turn our attention to the structure, starting with the radial distribution function (RDF) (see Sec. 3.3.1). An example of RDF curves along A1 and T1.0 can be seen in Fig. 5.12. The first striking thing is that there are big changes along A1 when compared to the invariances observed of the dynamics. The second thing is that $g_{AA}(r)$ and $g_{AB}(r)$ are approximately in phase at high densities, and out of phase at low densities. This makes sense since the particles primarily feel repulsive forces from their nearest neighbours at high densities, but both attractive and repulsive forces at low densities. The third thing is that the first peak in $g_{AA}(r)$ along T1.0 disappears around densities lower than 0.7. This is also true for the other isotherms. Because of this the AA data in this region will not be shown.

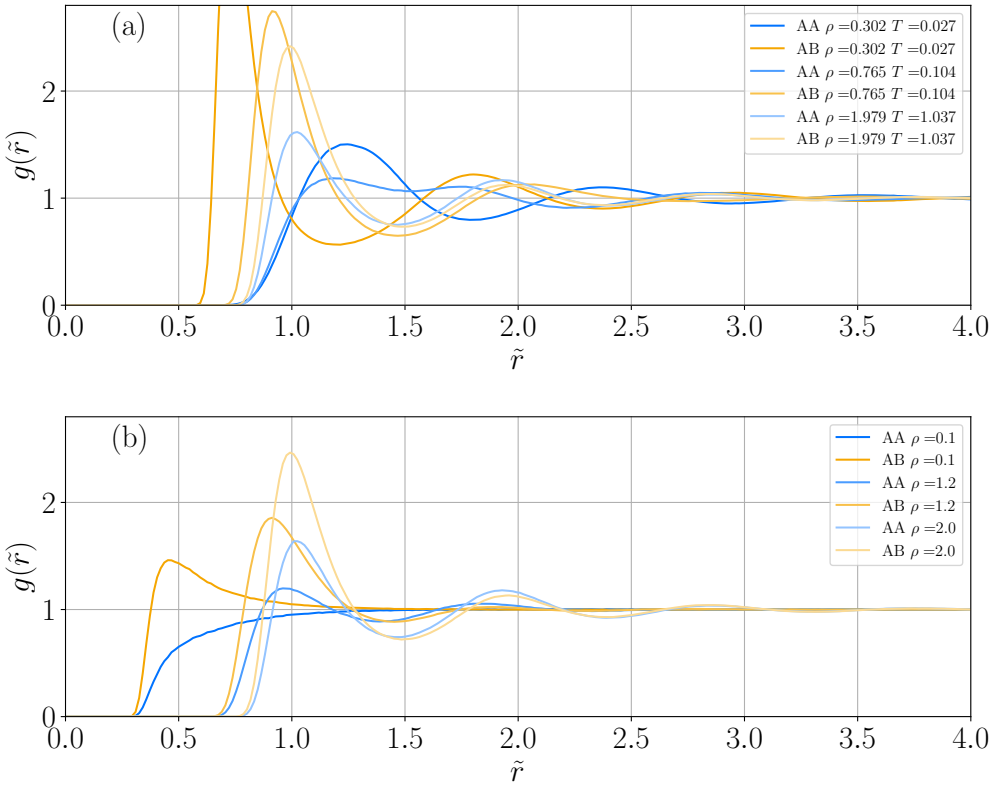

Figure 5.12: Example of $g(\tilde{r})$ data from (a) A1 and (b) T1.0. Notice that the peak in $g_{AA}(\tilde{r})$ disappears at low densities along T1.0.

To quantify the overall changes in the RDF we start by analysing the position of the critical points (i.e. maxima and minima). This was done along A1 for both $g_{AA}(\tilde{r})$ and $g_{AB}(\tilde{r})$ as a function of density, see Fig. 5.13. Note that at long distances the RDF becomes more flat (see Fig. 5.12) which makes it more difficult to locate the critical points in this region, resulting in noisy data.

From this it is more clear that $g_{AA}(\tilde{r})$ and $g_{AB}(\tilde{r})$ are out of phase at low densities, and in phase at high densities. At high densities the positions of the critical points are: $\tilde{r} \approx 1.0$ (maximum), $\tilde{r} \approx 1.5$ (minimum), $\tilde{r} \approx 1.9$ (maximum), $\tilde{r} \approx 2.4$ (minimum), $\tilde{r} \approx 2.8$ (maximum), and $\tilde{r} \approx 3.3$ (minimum).

In $g_{AA}(\tilde{r})$ we observe that an extra minimum and maximum gets created at $\rho \approx 0.7$ and $\tilde{r} \approx 1.7$ which remains at higher densities. Likewise in $g_{AB}(\tilde{r})$ we observe that a minimum becomes two minima and a maximum at $\rho \approx 0.8$ and $\tilde{r} \approx 2.8$.

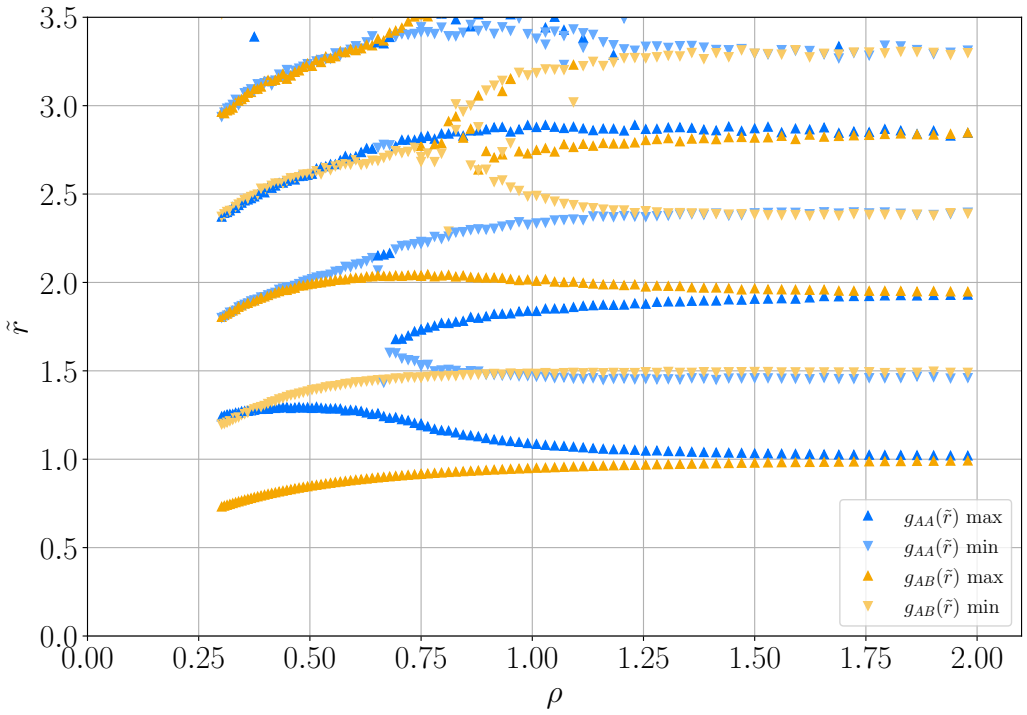

Figure 5.13: The position of critical points in $g_{AA}(\tilde{r})$ (blue) and $g_{AB}(\tilde{r})$ (orange) as a function of density along A1. Here maxima are marked with "$\triangle$", and minima are marked with "$\triangledown$".

To quantify the changes in the RDF further we analyse the position and height of the first peak in both AA and AB. These were found by fitting a 4th order polynomial to the points around the peak. The result of this analysis can be seen in Fig. 5.14. The first thing we notice when looking at the position and height of the first peak in $g(\tilde{r})$ is that they generally vary a lot. However, the data seem to become more invariant at higher densities.

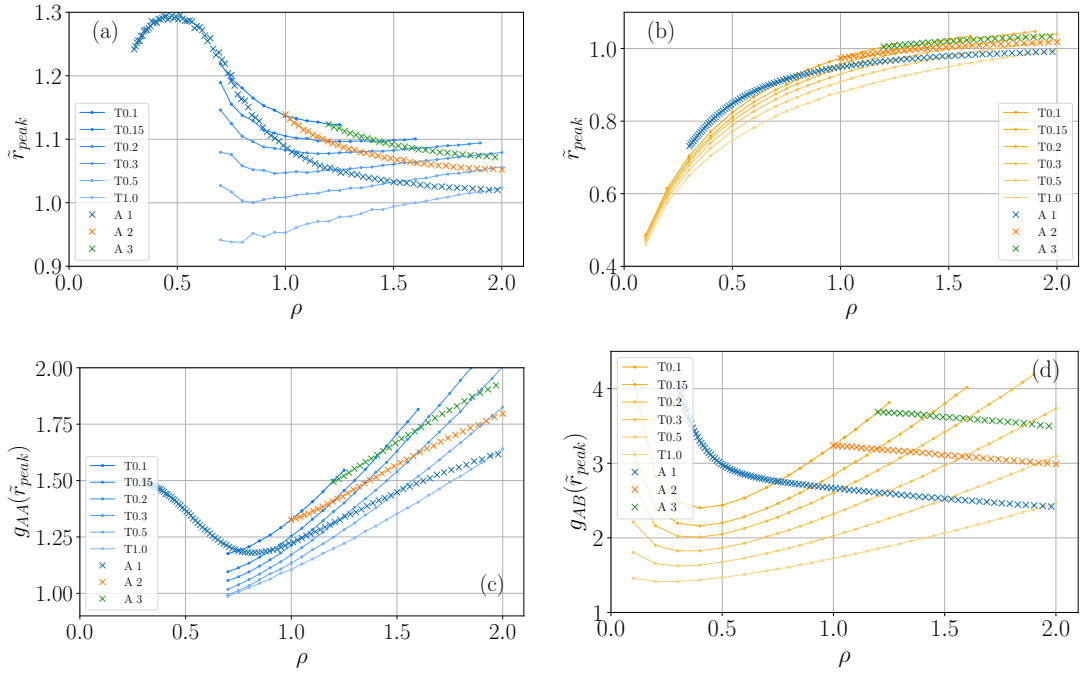

Figure 5.14: The position and height of the first peak in $g_{AA}(\tilde{r})$ and $g_{AB}(\tilde{r})$ as a function of density for all configurational adiabats and isotherms. (a) position of peak in $g_{AA}(\tilde{r})$, (b) position of peak in $g_{AB}(\tilde{r})$, (c) height of peak in $g_{AA}(\tilde{r})$, and (d) height of peak in $g_{AB}(\tilde{r})$.

In a similar way we analyse the position and height of first minimum for both $g_{AA}(r)$ and $g_{AB}(r)$, see Fig. 5.15. It is difficult to determine the exact position of the minimum at low densities. This is especially true for $g_{AA}(r)$ which does not even have a peak at $\rho < 0.7$.

From this we see that the position of the first minimum for both $g_{AA}(r)$ and $g_{AB}(r)$ is $\tilde{r} \approx 1.5$ and changes very little at high densities. At low densities the position varies more significantly. We also find that the height of the minimum in $g_{AA}(r)$ decreases as a function of density. Lastly, the height of the minima in $g_{AB}(r)$ does not change much along configurational adiabats in the high density region.

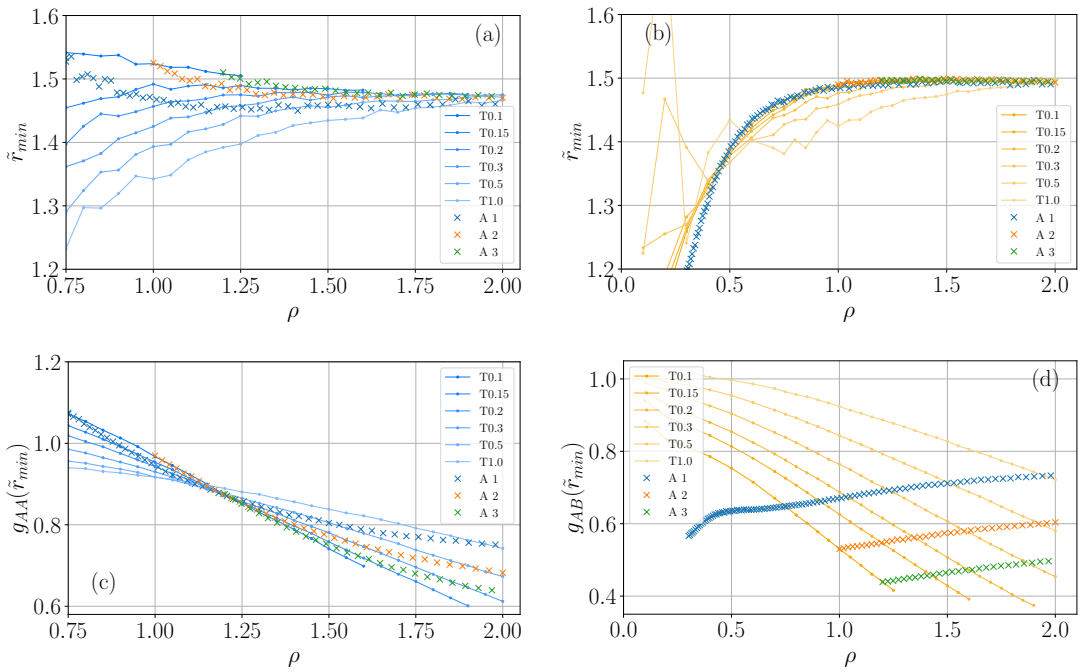

Figure 5.15: The position and height of the first minima in $g_{AA}(\tilde{r})$ and $g_{AB}(\tilde{r})$ as a function of density for all configurational adiabats and isotherms. (a) position of minimum in $g_{AA}(\tilde{r})$, (b) position of minimum in $g_{AB}(\tilde{r})$, (c) height of minimum in $g_{AA}(\tilde{r})$, and (d) height of minimum in $g_{AB}(\tilde{r})$.

5.5.2 The partial structure factor

We also analysed the Bhatia-Thornton partial structure factor (see Sec. 3.3.2). Due to its relation with $g(r)$ we do not expect $S(q)$ to be invariant, however, it will still give an insight into the behaviour of the model. We only show $S_{NN}(q)$ and $S_{CC}(q)$ since $S_{NC}(q) = 0$ due to the symmetries in the model and the chosen concentrations.

Selected curves along A1 and T1.0 can be seen in Fig. 5.16. At low densities the position of the first peak in $S_{NN}(\tilde{q})$ rapidly goes to large q. Likewise, the peak in $S_{CC}(\tilde{q})$ becomes so flat that the exact position is difficult to determine. The peak even seems to disappear along T1.0 at $\rho = 0.1$. This is not surprising since we also saw the vanishing of the first peak in $g_{AA}(r)$.

As for the RDF, we analyse the position and height of the first peak in $S_{NN}(\tilde{q})$ and $S_{CC}(\tilde{q})$, which can be seen in Fig. 5.17. As expected, the data change a lot but generally become more invariant at high densities. This is especially true for $S_{NN}(\tilde{q})$. Based on this we can imagine that at even higher densities $S_{NN}(\tilde{q})$ would be invariant, and $S_{CC}(\tilde{q})$ would also be invariant, or continue to move to lower q and decrease in height as the density increases. In the later case, the model would behave the same as the experimental data presented in Hansen et al. [2020].

To further emphasise this point $S_{CC}(\tilde{q})$ curves from the high density region of A1 can be seen in Fig. 5.18 (similar figures can be made for A2 and A3). Here a density interval of 12.6% are shown, and the behaviour is similar to the experimental data from Hansen et al. [2020] (which had a density interval of 2%).

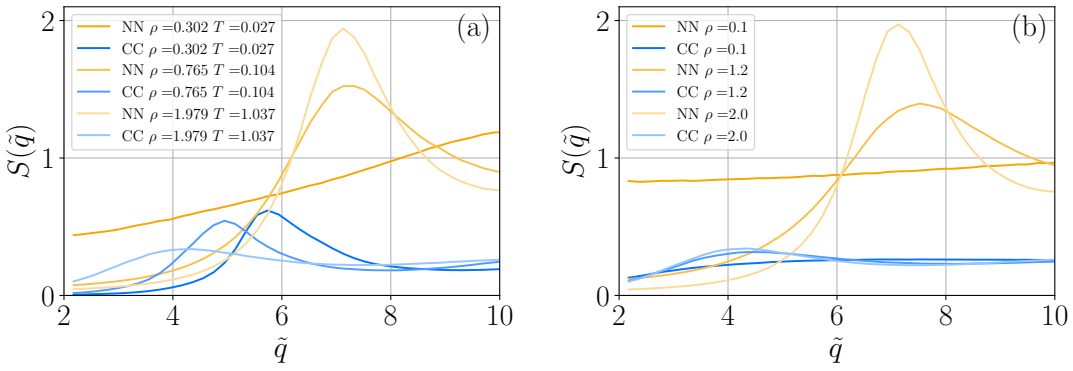

Figure 5.16: Selected $S(\tilde{q})$ data from (a) A1 and (b) T1.0. At low densities we generally see that the peak in $S_{NN}(\tilde{q})$ goes to high $\tilde{q}$-values which makes it difficult to define.

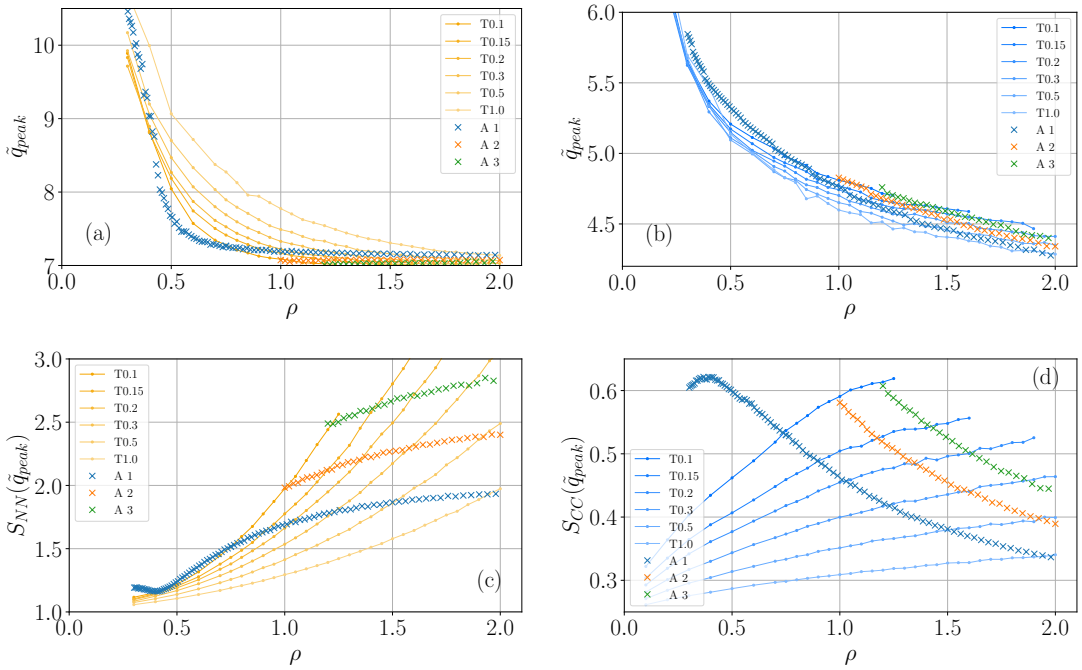

Figure 5.17: The position and height of the first peak in $S_{NN}(\tilde{q})$ and $S_{CC}(\tilde{q})$ as a function of density for all configurational adiabats and isotherms. (a) position of peak in $S_{NN}(\tilde{q})$, (b) position of peak in $S_{CC}(\tilde{q})$, (c) height of peak in $S_{NN}(\tilde{q})$, and (d) height of peak in $S_{CC}(\tilde{q})$.

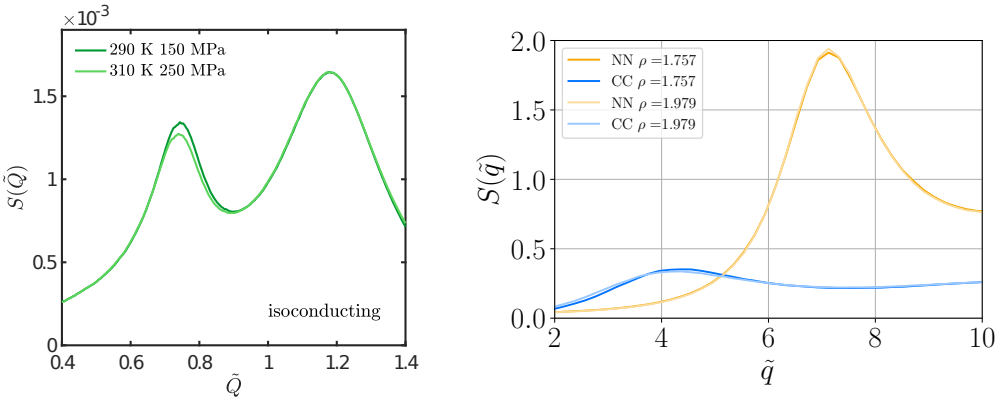

Figure 5.18: Compare $S(\tilde{q})$ with experimental data. (Left) Figure 5b from Hansen et al. [2020] showing X-ray data in a density interval of 2%. (Right) $S(\tilde{q})$ curves along A1 in the high density region ($1.757 - 1.979$ corresponding to a change of 12.6%).

5.5.3 The number of nearest neighbours

The number of nearest neighbours of type α around a type β is

$$N_{\alpha\beta} = 4\pi c_\alpha \rho \int_0^R g_{\alpha\beta}(r) r^2 dr, \tag{5.13}$$

where c_α is the concentration of α, $g_{\alpha\beta}(r)$ is the partial RDF for α and β, and R is the limit for the integral, which is often chosen to be the first minimum.

When choosing the integration limit R we initially defined it as the minimum for each curve, which resulted in very noisy data. To avoid this we decided to choose a fixed R around the minimum. Based on Fig. 5.13 we choose the integration limit $R = 1.5\rho^{-1/3}$. However, it should be noted that this choice is based on the high density region, since a fixed limit will not work at low density due to the big changes in $g(r)$.

The number of nearest neighbours for like (N_{AA}) and unlike (N_{AB}) particles along all configurational adiabats and isotherms can be seen in Fig. 5.19. The first thing we should note is that the y-axis shows a small interval of 0.8, meaning that these numbers generally do not change much. N_{AA} is approximately 6 while N_{AB} is approximately 7.5. This makes sense when comparing with the crystal structure, which is shown in Fig. 5.5. Here we saw that the system prefers a crystal structure similar to that of CsCl, which has first nearest neighbours 8 and second nearest neighbours 6.

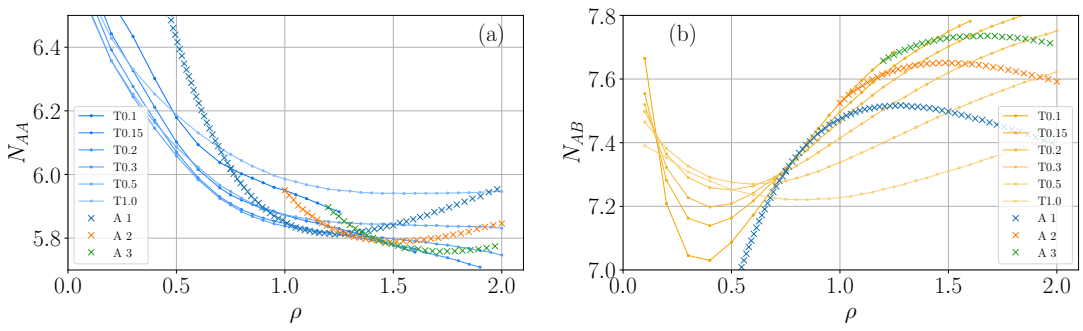

Figure 5.19: The number nearest neighbours (a) like (N_{AA}) and (b) unlike (N_{AB}).

When studying N_{AA} and N_{AB} for the configurational adiabats we notice that they behave opposite to each other. This let us to analyse the total number of nearest neighbours $Z = N_{AA} + N_{AB}$ and the concentration $f_{AA} = N_{AA}/Z$, see Fig. 5.20. Here we see that the differences in N_{AA} and N_{AB} along the configurational adiabats almost cancel out resulting in a Z which does not change much.

The concentrations f_{AA} change very little and are in the interval $0.42 - 0.48$. Along isotherms f_{AA} are decreasing and crystallises before 0.42. This makes sense since f_{AA} for the crystal structure observed in Fig. 5.5 is $6/14 \approx 0.43$. For configurational adiabats f_{AA} is increasing at high densities. At sufficiently high densities we would expect f_{AA} to approach 50% as the charges become less dominant.

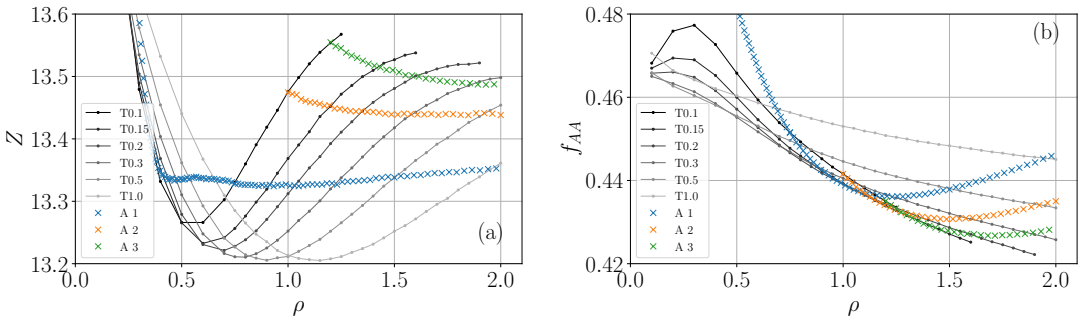

Figure 5.20: (a) The total number of nearest neighbours Z, and (b) the concentration of like particles f_{AA}. At the lowest simulated density along A1 (which can not be seen here) the concentration is 0.520.

5.6 Conclusion

In this chapter we analysed the simple salt model from Hansen and McDonald [1975] in a broad density range. This included simulating various isotherms and configurational adiabats.

Density scaling exponent

In Sec. 5.1.3 we analysed the density scaling exponent γ analytically for this model. We obtained Eq. 5.9 for the high density region where $\langle \Delta U_{IPL} \Delta U_C \rangle \approx 0$ (see Fig. 5.9). This explains qualitatively that γ increases as a function on increasing density as the electrostatic interactions become less dominant. This was also shown to be the case in our simulations (see Fig. 5.6).

As mentioned in the beginning of this chapter, these results were published in Knudsen et al. [2021]. Since then K. R. Harris found experimental verification of this density scaling behaviour for high-temperature molten salts [Harris, 2022].

Curves of invariant dynamics: Isodynes

This model show a high level of dynamical invariance along configurational adiabats when isomorph scaling is applied. This included; viscosity, the diffusion coefficient, and the time it takes the self-intermediate scattering function to reach $e^{-1} \approx 0.37$. Furthermore, even the MSD and F_s shows invariance along the configurational adiabats. This is remarkable since the configurational adiabat A1 covers a density range of 660%. With the exception of the lowest densities and highest temperatures the model also satisfies the reduced Stokes-Einstein relation. Going forward we refer to these curves of invariant dynamics as *isodynes*. The existence of isodynes was also shown in the experimental data from Hansen et al. [2020], however, there they were only analysed a density range of 2%. An important result from the analysis of this model is how stable the existence of isodynes are in the phase diagram.

Structure along isodynes

The structure along both isodynes and isotherms were studied. We do not see structural invariance on the same scale as the dynamical invariance. Along isodynes the structure is generally more invariant in the high density region. This turned out to be true for the position of multiple critical points in the radial distribution function (even at longer distances), see Fig. 5.13.

To compare with the experimental results from Hansen et al. [2020] we computed the Bhatia-Thornton partial structure factor. Along isodynes the charge peak decreased in intensity and shifted to smaller q with increasing temperature.

This is the same behaviour as in Hansen et al. [2020]. However, the main peak increased in intensity and slightly shifted to smaller q as temperature increased. Hansen et al. [2020] found the main peak to be invariant, however, this experimental study only covered a density interval of 2%. Our main peak also looks invariant when presented in a smaller density interval.

Due to the simplicity of this model the charges must be a fundamental part of this structural behaviour. Additionally, if the charges were removed from the model (the second IPL in Eq. 5.1) we can tell from the definition of the Bhatia-Thornton partial structure factor (Eq. 3.14) that there would be no charge peak.

The behaviour of the charge peak seen in Hansen et al. [2020] is also present in this model, and thus can not be related to molecular structures (which are not present in this model). Consequently, this behaviour most be caused by the charges themselves.

Number of nearest neighbours

The number of like and unlike neighbours (N_{AA} and N_{AB}) was similar to that of the crystal structure which we observed for the system (6 and 8 respectively), see Fig. 5.5. We found this the number of nearest neighbours generally did not change much in the simulated range, i.e. less than 0.8 for both AA (like) and BB (unlike) neighbours, see Fig. 5.19. Bigger changes were observed in the low density region, however, this is because the chosen integration limit does not correspond to the first minimum in the radial distribution function. We also found that the total number of neighbours, while generally not changing much, showed more invariance along the isodynes than the isotherms, see Fig. 5.20. Lastly, we analysed at the concentration of like and unlike neighbours. We found that between $42\% - 48\%$ of the neighbours are of the same type (like). Due to the charges it makes sense that there would be a preference towards unlike types. We also see that along the isodynes this preference becomes smaller as density increases in the high density region. However, the opposite is true for the isotherms.

Chapter 6

United Atom Ionic Liquid Model

In this chapter we analyse a united atom model of the ionic liquid from Hansen et al. [2020]. The model is simulated in two regions; a narrow density region at room temperature for comparison with experimental data, and a larger density region at higher temperatures to find if the model has isodynes. To test the latter, we analyse different dynamical properties and find which of these (if any) have the same contours in the phase diagram. Then we analyse the structure along these curves and compare them with isotherms, isochores and the experimental structure data from Hansen et al. [2020].

6.1 Model details

The model which we study in this chapter is based on the ionic liquid which was studied in Hansen et al. [2020]. That is, it consists of the cation 1-Butyl-1-methylpyrrolidinium (Pyr_{14}) and the anion bis(trifluoromethylsulfonyl)imide (TFSI). An illustration of the molecules can be seen in Fig. 6.1.

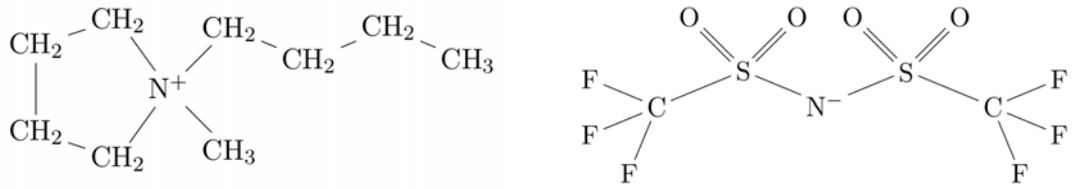

Figure 6.1: An illustration of the molecules in this salt model. (Left) The cation Pyr_{14} and (Right) the anion TFSI.

This is a *united atom model* which means that each CH group will be considered as one sphere, while all other atoms will be represented as individual spheres. Note that the anion has an all-atom representation since it has no CH_2 or CH_3 groups.

On the basis of our previous versions of this model, we choose to apply partial charges in this final version. This means that each atom/sphere have some charge such that their sum is equal to the net-charge of the molecule.

6.1.1 Simulation parameters

All-atom parameters

When simulating detailed models we have to carefully consider the different parameters to insure that the model can represent reality. This has lead to the development of different force fields such as the *Assisted Model Building with Energy Refinement* (AMBER) force field, which was developed by Peter Kollman's group at the University of California, San Francisco. Another similar force field is the *Optimized Potentials for Liquid Simulations* (OPLS) force field, which was first developed in the 1980s in Jorgensen et al. [1983] and Jorgensen and Tirado-Rives [1988] and has since been developed further in other works such as Jorgensen et al. [1996]. Both of these force fields are commonly used, and we will therefore be using parameters from both but transform them to OPLS.

The increased interest in ionic liquids has also lead to the development of simulation parameters for this class of liquids. This is evident from papers such as Sambasivarao and Acevedo [2009] where the all-atom OPLS parameters for various ionic liquids have been developed and verified. This was later built upon in Doherty et al. [2017].

The earliest set of OPLS parameters we found for the anion (TFSI) is in Canongia Lopes and Pádua [2004]. This paper seems to be the primary reference for simulating TFSI, and provides all non-bonded interactions (including partial charges) and all bonded interactions; bonds, angles, and dihedrals.

For our cation (Pyr_{14}) we used the parameters from the paper Xing et al. [2013]. They used standard bonded and non-bond parameters from Cornell et al. [1996] and Liu et al. [2004]. Furthermore, Xing et al. [2013] obtained the partial charges from the optimized geometry using the RESP method with the R.E.D.-III.4 package.

Now we have obtained a full set of all-atom simulation parameters. However, we wanted this to be a simpler united atom model of the molecule.

The united atom

We only use united atoms for the CH_2 and CH_3 groups in Pyr_{14}. In this work, we used the non-bonded parameters from Jorgensen et al. [1984] which are identical to those in Smondyrev and Berkowitz [1999]. To get the partial charges of the united atoms we simply computed the total charge of the C and H.

The size of a single C from Xing et al. [2013] is $\sigma = 3.400$ Å, while a CH_2 or CH_3 group from Jorgensen et al. [1984] is $\sigma = 3.905$ Å.

6.1.2 Simulation units

When it comes to the development of simulation-parameters there are different standards in the choice of units. The most common units for distances are Angstrom (Å) and nanometre (nm) which are easily converted. There are also two standards for energy; kcal/mol and kJ/mol, with the conversion rate of 1 calorie = 4.184 joules. In the end, we choose the unit system where distances will be in Angstrom (Å), energies are in kilo calories pr. mole (kcal/mol), masses are in dalton (u), and charges in elementary charge (e). The molecular number density (ρ) will be presented it in nm^{-3} for convenience. A list of all the simulation units and the corresponding SI units can be seen in Tab. 6.1.

Name	Symbol	Sim. unit	SI unit
Length	L	Å	10^{-10} m
Energy	E	$\frac{\text{kcal}}{\text{mol}}$	$6.948 \cdot 10^{-21}$ J
Mass	m	u (g/mol)	$1.661 \cdot 10^{-27}$ kg
Charge	q	e	$1.602 \cdot 10^{-19}$ C
Boltzmann const.	k_B	$1.987 \cdot 10^{-3}$ $\frac{\text{kcal}}{\text{mol}}$ K^{-1}	$1.381 \cdot 10^{-23}$ J K^{-1}
Coulomb const.	k_e	$3.321 \cdot 10^{2}$ $\frac{\text{kcal}}{\text{mol}}$ Å e^{-2}	$8.988 \cdot 10^{9}$ J m C^{-2}
Time	$L\sqrt{m/E}$		$4.889 \cdot 10^{-14}$ s
Velocity	$\sqrt{E/m}$		$2.045 \cdot 10^{3}$ m s^{-1}
Diffusion	$L\sqrt{E/m}$		$2.045 \cdot 10^{-7}$ m^2 s^{-1}
Force	$L^{-1}E$		$6.948 \cdot 10^{-11}$ N
Pressure	$L^{-3}E$		$6.948 \cdot 10^{9}$ Pa
Viscosity	$L^{-2}\sqrt{mE}$		$3.397 \cdot 10^{-4}$ Pa s
Mass density	mL^{-3}		$1.661 \cdot 10^{3}$ kg m^{-3}

Table 6.1: List of the simulation units and the corresponding SI units used in the simulations of the molecular salt model.

6.1.3 Non-bonded interactions

Potential energy and cutoff

All the non-bonded interactions are modelled as LJ potentials (Eq. 2.27) together with a first order inverse power law which represents the Coulomb interactions

$$V_{\alpha\beta}(r_{jk}) = 4\epsilon_{\alpha\beta}\left[\left(\frac{\sigma_{\alpha\beta}}{r_{jk}}\right)^{12} - \left(\frac{\sigma_{\alpha\beta}}{r_{jk}}\right)^{6}\right] + k_e\frac{q_\alpha q_\beta}{r_{jk}}, \tag{6.1}$$

where r_{jk} is the distance between particle j and k, with type α and β respectively. We use the Lorentz-Berthelot combination rules when defining the energy $\epsilon_{\alpha\beta}$ (Eq. 2.31), and distance $\sigma_{\alpha\beta}$ (Eq. 2.32)

$$\epsilon_{\alpha\beta} = \sqrt{\epsilon_\alpha\epsilon_\beta} \qquad \text{and} \qquad \sigma_{\alpha\beta} = \frac{\sigma_\alpha + \sigma_\beta}{2}. \tag{6.2}$$

The shifted force method was used for all non-bonded interactions (see Sec. 2.4.1). The cutoff of these LJ potentials are given by $r_{cut,\alpha\beta} = 2.5\sigma_{\alpha\beta}$ Å and the cutoff for the Coulomb interactions was set to 18 Å. The choice 18 Å was based on the simple atomic salt model (from Chap. 5) in which the cutoff was 6 and the particle size (σ) was 1. However, in this model σ is between 2.9 and 4 Å, so we simply scaled the cutoff of 6 with the particle size 3 to reach 18 Å.

United atoms in the cation

The cation contains both united atom representations of CH_2- and CH_3-groups. However, we need to describe these with more than two types since they have different partial charges. Instead of defining nine different CH-groups we added some symmetry to the ring. The two CH_2-groups in the ring closest to N^+ will be referred to as R_1, the other two CH_2-groups in the ring will be referred to as R_2. The four CH-groups in tail are represented by three types; the group closest to the ring is T_1, the two middle groups are T_m, and the fourth and last group is T_4. Lastly, the single CH_3-group attached to N^+ will be referred to as C_e.

When finding the partial charges, we simply added the charges of C and H. In the cases where there are more than one of each type (e.g. R_1, R_2 and T_m) the given partial charges were slightly different. Here the average partial charge was used in keeping with the symmetry we have chosen to enforce. The partial charges for Pyr_{14} from Xing et al. [2013] were given with 3-4 decimals. However, to maintain charge neutrality of the system we did not round off the result when calculating the united atom partial charges.

Charge scaling

Previous studies have shown the importance of electronic polarization effects when considering interactions between charges. A computationally costly method for capturing this is using polarizable force fields. Because of this it is still common to use nonpolarizable force fields which can lead to artifacts. However, there is a simpler method to account for polarization effects, and it only involves scaling the charges with some factor α. This method has been described in studies such as Leontyev and Stuchebrukhov [2011] and Kirby and Jungwirth [2019]. It is common to choose $\alpha = 0.8$ but new studies have shown that it can be even lower depending on the system [Doherty et al., 2017] [Barbosa et al., 2022]. We also made tests to find the best choose of α for this model (see Sec. 6.2.3), but we ended up using the standard 0.8 for the final version, which is presented in this work.

The full list of the non-bonded parameters used in this model and a particle-type reference can be found in Tab. 6.2. The masses of Pyr_{14} and TFSI are 142.257 u and 280.143 u, respectively. We exclude the non-bonded interactions between particles with bond, angle and dihedral potentials, see Sec. 2.4.2.

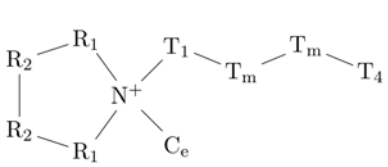

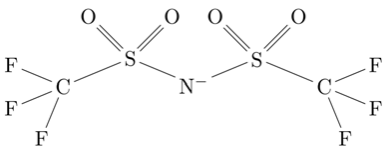

Non-bonded					
Name	σ [Å]	ϵ [kcal/mol]	m [u]	q [e]	$q_{0.8}$ [e]
N^+	3.250	0.170	14.007	0.1040	0.0832
CH_2 (R_1)	3.905	0.118	14.026	0.1518	0.12144
CH_2 (R_2)	3.905	0.118	14.026	0.08365	0.06692
CH_2 (T_1)	3.905	0.118	14.026	0.1011	0.08088
CH_2 (T_m)	3.905	0.118	14.026	0.05095	0.04076
CH_3 (T_4)	3.905	0.175	15.034	0.0279	0.02232
CH_3 (C_e)	3.905	0.175	15.034	0.1942	0.15536
N^-	3.25	0.170	14.007	-0.66	-0.528
S	3.55	0.250	32.065	1.02	0.816
O	2.96	0.210	15.999	-0.53	-0.424
C	3.50	0.066	12.011	0.35	0.280
F	2.95	0.053	18.998	-0.16	-0.128

Table 6.2: United atom OPLS parameters for non-bonded interactions. The Pyr_{14} united atom ϵ and σ parameters for CH_2 and CH_3 are from Jorgensen et al. [1984]. All Pyr_{14} charges are from Xing et al. [2013].All TFSI parameters are from Canongia Lopes and Pádua [2004].

6.1.4 Intra-molecular interactions

The potential for bonds and angles is simply the harmonic potential from Eq. 2.35. The Pyr_{14} dihedral parameters from Xing et al. [2013] were written for the periodic dihedral potential, Eq. 2.45 which is not implemented in RUMD. However, because the angle $\theta_0 = 0$ and $n = 3$ in all cases they can be translated to Fourier dihedrals, Eq. 2.46, and then Ryckaert-Bellemans function, Eq. 2.47, which is implemented in RUMD.

A full list of all parameters for bonded interactions are shown in Tab. 6.3. The dihedral parameters are shown in the Ryckaert-Bellemans Dihedral form because this potential is implemented in RUMD and hence this was the version which was used. However, in appendix B.3 the dihedral parameters can be found in the Fourier Dihedral form where the parameters are simpler. When using the Fourier Dihedral form it is clear that all dihedrals in the model except S-N-S-C can be described by the function

$$V_3 \left(1 + \cos\left(3\theta\right)\right)/2, \tag{6.3}$$

where the S-N-S-C dihedral is more complex. To illustrate this the graphs of the dihedral potential for C-C-C-C and S-N-S-C can be seen in Fig. 6.2. Here we also see that the S-N-S-C potential is stronger than the others. From this C-C-C-C dihedral we can also see that the ring in Pyr_{14} does not prefer to be flat, but rather slightly twisted.

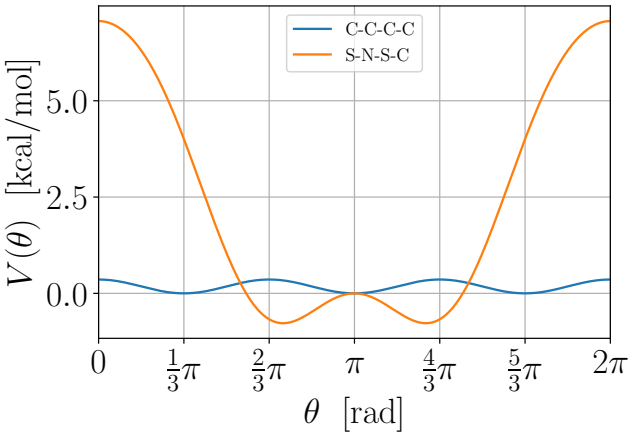

Figure 6.2: Dihedral potentials for C-C-C-C and S-N-S-C.

$\frac{1}{2}k_b\left(r_{jk}-l_0\right)^2$

Bonds

Name	l_0 [Å]	k_b [kcal/(mol Å^2)]
C-C	1.526	620.0
N-C	1.471	734.0
S-O	1.442	1274
S-N	1.570	744.0
S-C	1.818	470.8
C-F	1.323	883.6

$\frac{1}{2}k_a\left(\theta_{jkl}-\theta_0\right)^2$

Angles

Name	θ_0 [°]	k_a [kcal/mol]
C-C-C	109.5	80.0
N-C-C	111.2	160
C-N-C	109.5	100
S-N-S	125.6	160
O-S-O	118.5	232
N-S-O	113.6	189
O-S-C	102.6	208
N-S-C	100.2	195
S-C-F	111.8	166
F-C-F	107.1	187

$\sum_{n=0}^{5}C_n\left(-\cos\left(\theta\right)\right)^n$

Ryckaert-Bellemans Dihedrals

Name	C_0	C_1	C_2	C_3	C_4	C_5 [kcal/mol]
C-C-C-C	0.180	0.540	0.0	-0.720	0.0	0.0
C-C-C-N	0.156	0.467	0.0	-0.622	0.0	0.0
C-C-N-C	0.156	0.467	0.0	-0.622	0.0	0.0
N-S-C-F	0.1580	0.4739	0.0	-0.6319	0.0	0.0
S-N-S-O	-0.0018	-0.0054	0.0	0.0072	0.0	0.0
S-N-S-C	1.044	-5.062	2.490	1.527	0.0	0.0
O-S-C-F	0.1734	0.5202	0.0	-0.6936	0.0	0.0

Table 6.3: United atom OPLS parameters for bonded interactions. All Pyr_{14} parameters are from Xing et al. [2013]. All TFSI parameters are from Canongia Lopes and Pádua [2004].

6.2 Test of model implementation

6.2.1 Test time step

To test the size of the time step (Δt) we ran a series of NVE-simulations at $\rho = 4.0$ nm^{-3} and $T \approx 500$ K for 13107200 steps where energies were saved every 50th step. All simulations started at the same configuration, and time steps between 0.25 fs and 6.0 fs were tested with an interval of 0.25 fs. However, data from time steps greater than 5.25 fs will not be shown as these simulations crashed.

The first part of Fig. 6.3 shows the variance of the total energy as a function of time step. The black line is a 4th order power law, which is meant to guide the eye. We start seeing bigger deviations from the power law for time steps smaller than 0.75 fs and larger than 4 fs. The second part of Fig. 6.3 shows the total energy as a function of time for $\Delta t = 1$ fs, 2 fs, 3 fs, 4 fs, and 5 fs. There is a clear drift in energy for 5 fs, which confirms that this time step is too large. However, this is not the case for smaller time steps.

From this analysis, we find that it would be possible to use a Δt up to approximately 4 fs at this state point. However, if we use this Δt in the high density, high temperature region ($\rho = 4.8$ nm^{-3} and $T \approx 998.15$ K) the simulations might crash due to fast vibrations. Consequently, we will use the same reduced (or isomorph scaled) time step $\tilde{\Delta t}$ for all simulations. We choose $\Delta t = 2$ fs at this state point ($\rho = 4.0$ nm^{-3} and $T \approx 500$ K) which corresponds to a $\tilde{\Delta t} \approx 0.0150$. This reduced time step will be used for all the simulations going forward.

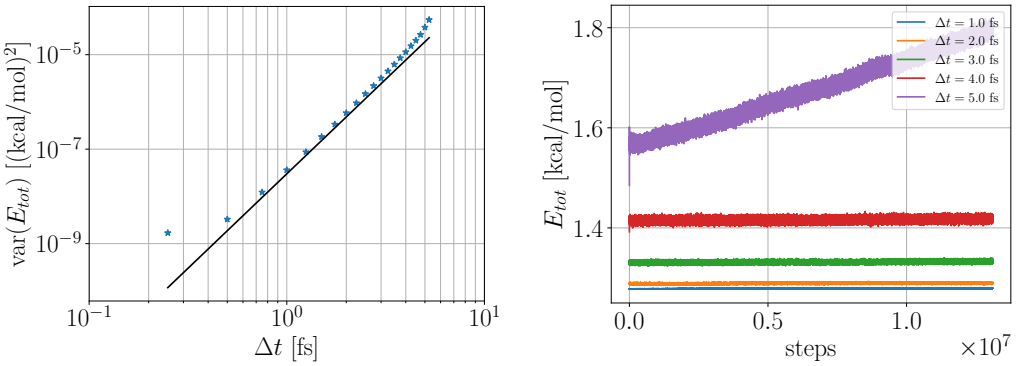

Figure 6.3: NVE simulation at $\rho = 4.0$ nm^{-3} and $T \approx 500$ K to test time step. (Left) Variance of the total energy as a function of time step. The black line is a power law with exponent 4, which is meant to guide the eye. (Right) The total energy at selected Δt.

6.2.2 Test the cutoffs influence on pressure

Since this model will be compared with experimental data, it will be useful to analyse the pressure of the model. Using a cutoff for the potential changes the pressure due to the missing interactions. To get an idea of the change in pressure, we performed some tests with different cutoff values. This was done separately for the Lennard-Jones and electrostatic interactions. We analyse configurations from simulations with the previously chosen cutoffs of $r_{cut,LJ} = 2.5\sigma_{LJ}$ and $r_{cut,C} = 18$ Å and computed what the pressure would have been at different cutoffs. This was done for 4 state points in the region, where we have experimental data;

- At $\rho = 3.84$ nm^{-3} with $T = 10$ °C and $T = 75$ °C.
- At $\rho = 4.16$ nm^{-3} with $T = 10$ °C and $T = 75$ °C.

Note the size of the simulation box gives an upper limit of approximately 24 Å for the cutoff.

Lennard-Jones cutoff

The Lennard-Jones cutoff contribution to the pressure for different state points can be seen in Fig. 6.4. Here we see that as the cutoff increases, the pressure decreases and stabilises as the Lennard-Jones interactions become weaker at longer distances. By analysing these (and other state points which have not been shown) we find that the pressure decreases with approximately $100 - 200$ MPa depending on the state point. This is more than we expected and will in some cases result in negative pressure. Due to this big cutoff dependence we will not present data as a function of pressure. This is also true when comparing dynamical quantities between experiments and our models.

Electrostatic cutoff

We also test the pressure contribution from the electrostatic interactions, since we used the shifted force cutoff method and not an *Ewald summation*. The pressures dependents on the electrostatic cutoff can be seen in Fig. 6.5 for different state points. The first thing we notice is that the pressure has not stabilised at the largest cutoff that we can compute with our simulated configuration. However, the changes in pressure is only a couple of MPa in the range we have access to. That is a percent of the contribution from the Lennard-Jones interactions, and comparable to the size of the error bars.

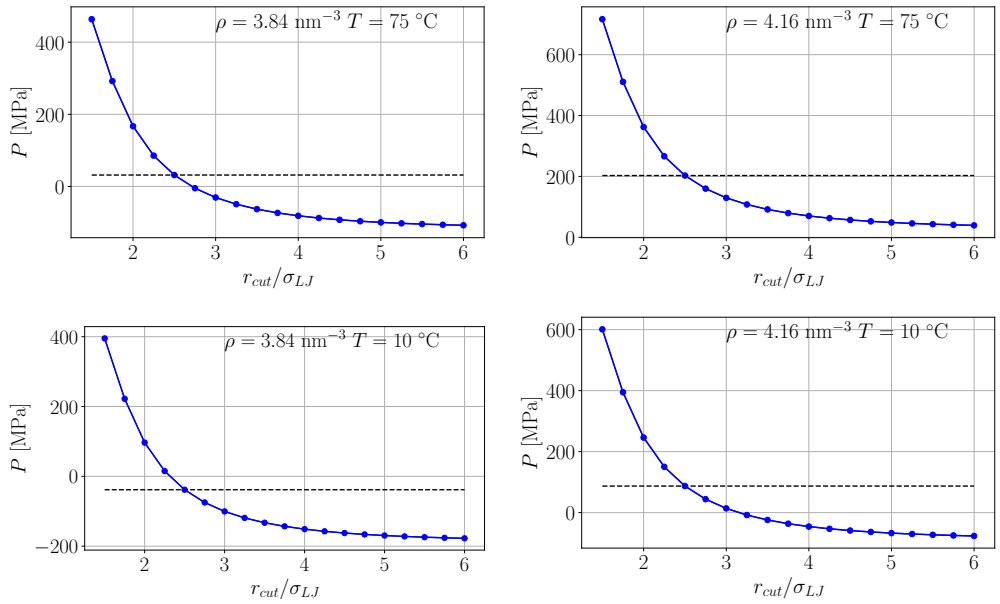

Figure 6.4: Test of how the Lennard-Jones cutoff effects the pressure. The error bars are smaller that the symbol size. The horizontal dashed line indicates the pressure, that was obtained in the simulations.

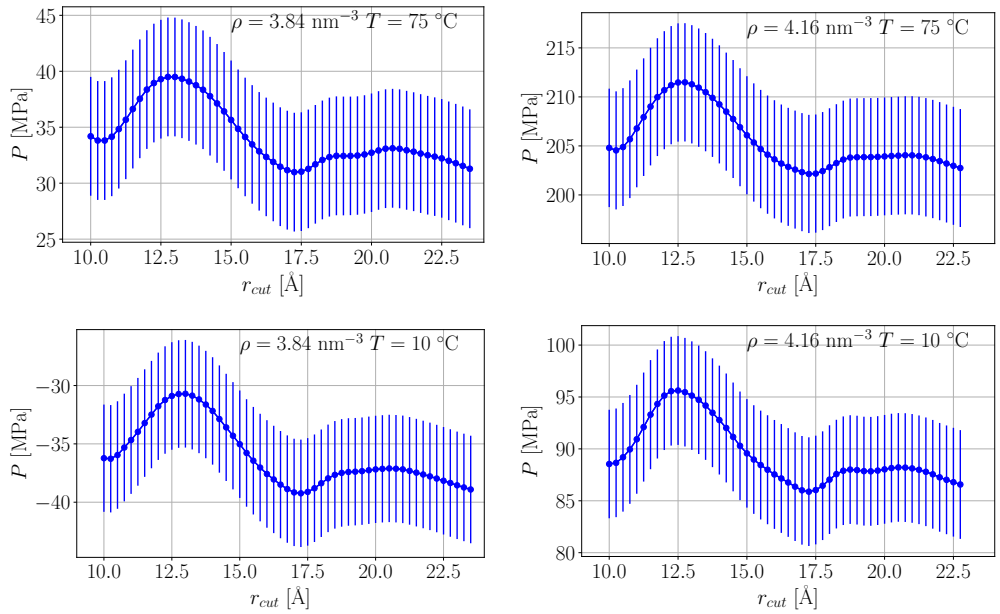

Figure 6.5: Test of how the electrostatic cutoff effects the pressure.

6.2.3 Test Coulomb strength

It is common to scale the charges by a factor of 0.8 to account for electronic polarization effects when simulating systems with electrostatic interactions. However, since we have access to experimental data for our models real life counterpart we decided to test if other scaling factors would bring the model closer to the real system. To do this we simulate at the same density and temperature as the experimental data. This experimental data comes from Harris et al. [2011].

We chose the following three $\rho - T$ state points where experimental data was available

- Point 1: $\rho = 3.977$ nm^{-3} and $T = 75$ °C
- Point 2: $\rho = 3.978$ nm^{-3} and $T = 25$ °C
- Point 3: $\rho = 4.146$ nm^{-3} and $T = 25$ °C

These points were chosen to represent different parts of the region with experimental data. The state points with experimental data and our three chosen state points can be seen in Fig. 6.6. We performed a set of simulations where we scaled the charges of the atoms for each of the chosen state points. We refer to this scaling factor as C-scale. This was done in an range from 0 to 1 with an interval of 0.1. We do not expect the optimal C-scale to be close to zero, however, it is still interesting to see how the system behaves at low to zero charge.

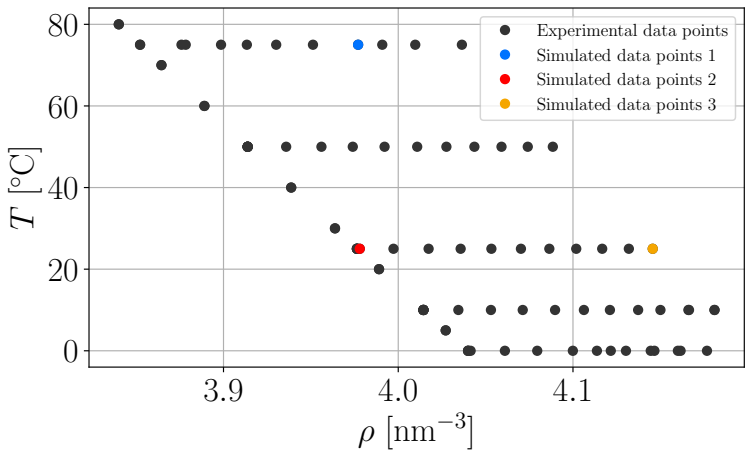

Figure 6.6: Plot of the experimental state points and the three points we simulated for this analysis.

Pressure and viscosity

The pressure as a function of C-scale is shown in Fig. 6.7 for the three chosen state points. Here only the atomic pressure is shown, but it is very similar to the molecular pressure. Furthermore, the experimental pressure is shown as a horizontal, dashed line. The intersection between the experimental and simulated curves will ideally represent the optimal C-scaling. We see that this intersection is between 0.8 and 0.9, but differs between the three state points. This means that we can not choose a single C-scale that will match the experimental data at all points, however, this was not expected. Based on this pressure analysis, we would argue that the optimal C-scale is between 0.8 and 0.9.

We will now do a similar analysis for the viscosity to find how it compares with the experimental data. The viscosity as a function of C-scale is shown in Fig. 6.8 for the three chosen state points. Since the viscosity at the three points are quite different in magnitude so the results are shown on a logarithmic y-axis. Note that error bars are included for our data, but in some cases they are smaller than the symbol size.

From this we conclude again that the optimal C-scale is between 0.8 and 0.9, however, no specific choice within this range seems to be preferred. Based on this analysis of the pressure and viscosity, we do not find a reason to choose a specific C-scale for this system. We will therefore be using the standard scaling of 0.8, since this is within the range of our results.

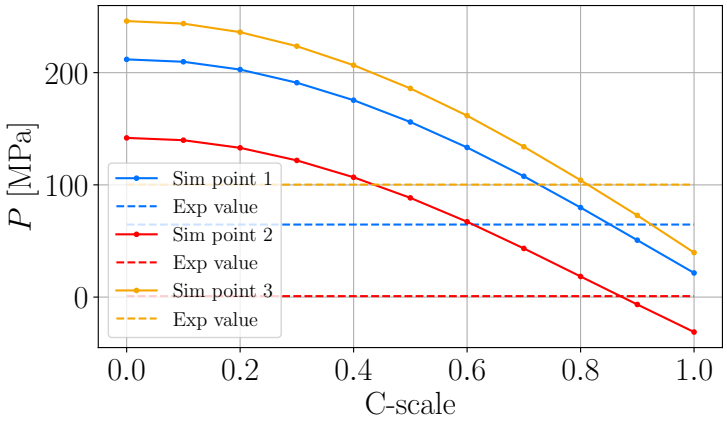

Figure 6.7: The pressure as a function of C-scale at three state points. The horizontal, dashed lines represent the experimental pressure.

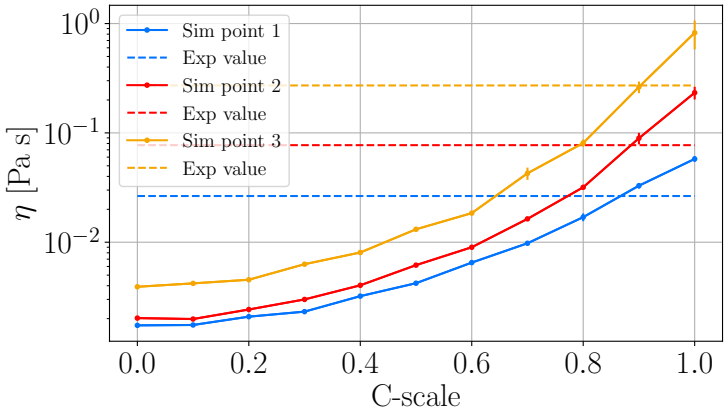

Figure 6.8: The viscosity as a function of C-scale at three state points. The horizontal, dashed lines represent the experimental viscosity.

Isomorph R and γ

It is interesting to see how the charges influence the correlation between U and W (R from Eq. 4.18) and the density scaling exponent for configurational adiabats (γ from Eq. 4.19). In Fig. 6.9, we see R as a function of C-scale. First, we notice that R is very small which makes sense because on the bonded interactions [Olsen et al., 2016]. Second, we see that R is largest at low C-scale. This means that electrostatic interactions further decorrelate the potential energy and virial. Furthermore, R is largest at point 3 which has a higher density than the other two points. It is also noticeable that the curves for point 1 and 2 are close. This means that R is more dependent on density than temperature.

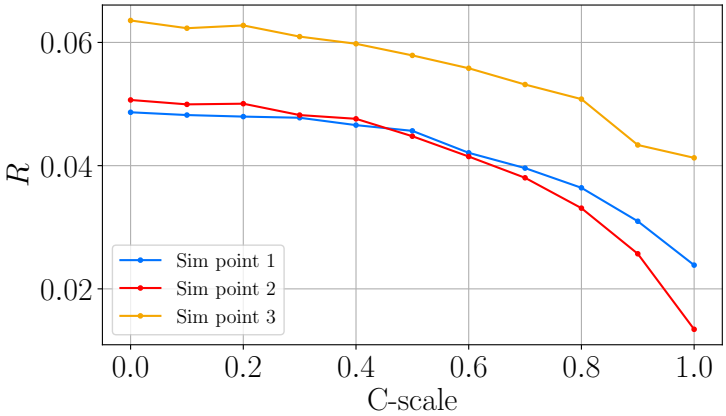

Figure 6.9: The correlation between U and W as a function of C-scale.

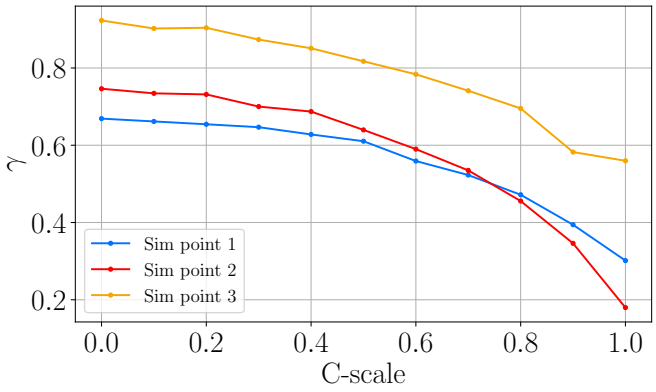

Figure 6.10: The density scaling exponent for configurational adiabats (γ) as a function of C-scale.

The density scaling exponent for configurational adiabats (γ) as a function of C-scale can be seen in Fig. 6.10. Here we see a behaviour similar to that of R. The values are largest at low C-scale, and γ is more dependent on density than temperature.

The static structure factor

We also want to check how the static structure factor depends on the C-scale. The total $S(q)$ at point 2 with different C-scales can be seen in Fig. 6.11. Here we see two peaks; the charge peak, and the main peak. It is clear that the charge peak is strongly associated with the charges, since it disappears as C-scales approaches 0.

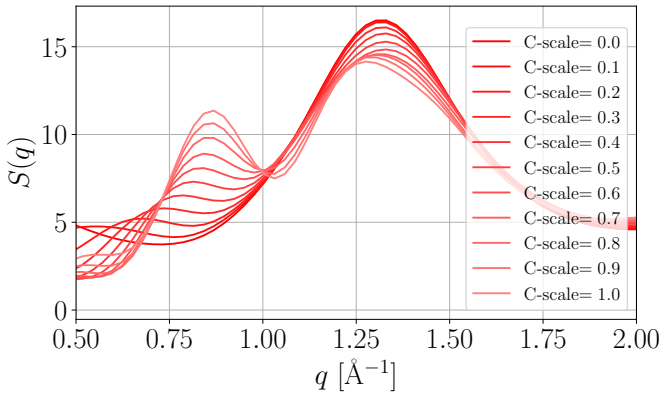

Figure 6.11: The total structure factor at simulation point 2 ($\rho = 3.978$ nm^{-3} and $T = 25$ °C.) with varying C-scale.

6.3 Simulation details

6.3.1 Simulation protocol

For the main analysis of this united atom IL model we simulate two regions, that are shown in Fig. 6.12;

- A limited density range at temperatures lower than 400 K. This region is for comparison with experiments.
- A larger density region with temperatures up to 1000 K. This is to test the model more broadly. We know from Xu and Cheng [2021] that the real molecule breaks down around 720 K. However, we still find it interesting to simulate at higher temperatures to get a better understanding of the model.

Fig. 6.12 has two coloured regions; a grey region that indicates negative pressure, and a red region where the dynamics become slow. The line with $P \approx 0$ was found by fitting surrounding data to a simple polynomial. This was done for both isotherms and isochores, that yielded the same results, which tells us that this is not a plot-sensitive process. The red region was defined in a similar way, however, it indicates where simulations takes more than 1 ns for the self-intermediate scattering function of N^+ to reach a value of $e^{-1} \approx 0.368$. In these cases, the corresponding q was chosen to be the position of the main structure factor peak. This is state point dependent, but it is between 0.7 and 0.9 $Å^{-1}$.

All simulations contained 200 ion-pairs corresponding to 5000 spheres/atoms and had periodic boundary conditions. They also used start configurations in the liquid state. First, they equilibrated for $2 \cdot 10^7$ timesteps followed by a data collecting run for $100 \cdot 2^{20} = 104\ 857\ 600$ timesteps. All simulations used the same isomorph-scaled timestep $\tilde{dt} \approx 0.015$ which corresponds to a real timestep of 2 fs at $\rho = 4.0$ nm^{-3} and $T = 500$ K (as was shown in Sec. 6.2.1).

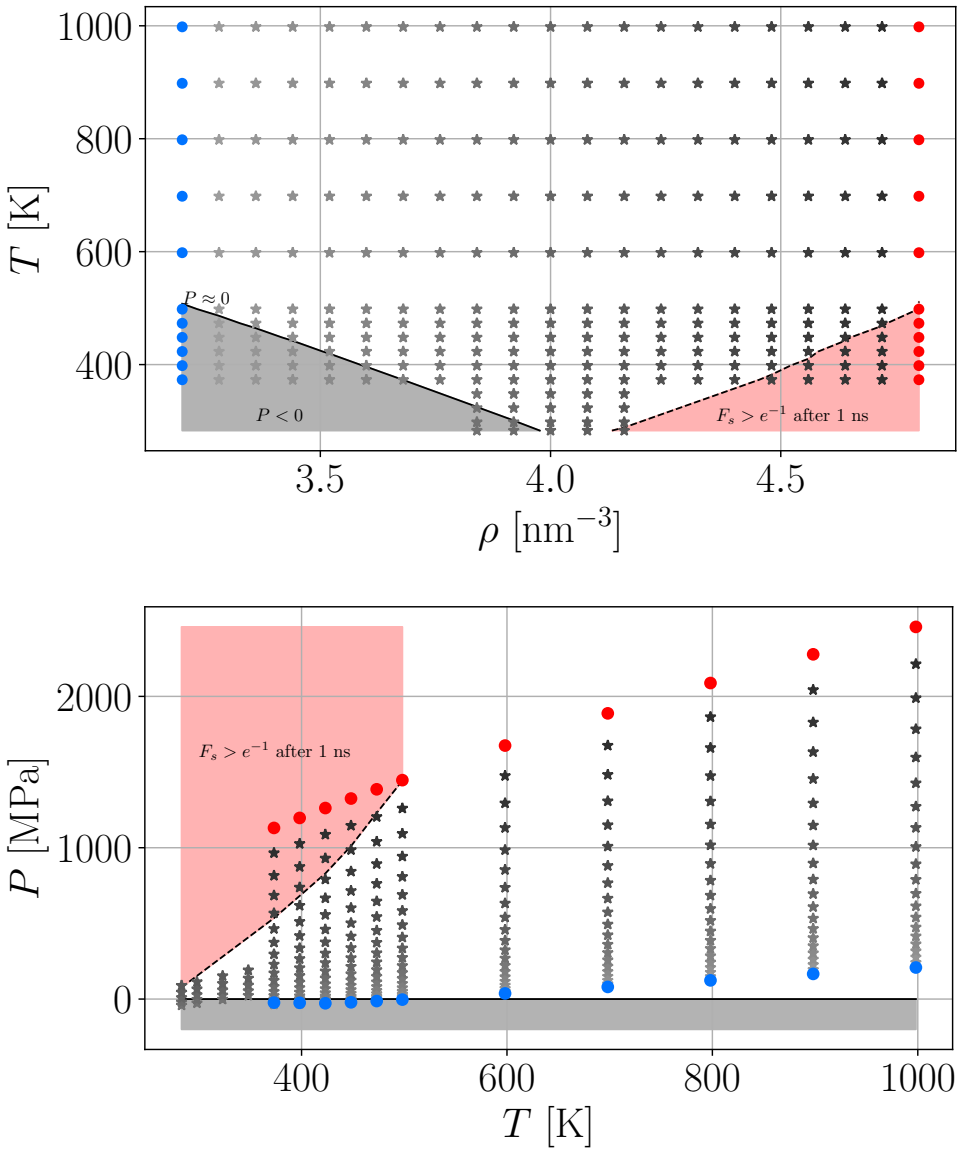

Figure 6.12: (Top) Plot of simulated state points in a $\rho - T$ diagram and (Bottom) the pressure at the simulated points as a function of T. Simulation points in the grey region have negative pressure, and points in the red region took more than 1 ns for F_s of N^+ to reach a value of e^{-1}. The two isochores at $\rho = 3.2$ nm^{-3} and 4.8 nm^{-3} have been highlighted with different colours because they will be used for an example in the upcoming section.

6.3.2 Calculating diffusion coefficient and viscosity

Calculating diffusion coefficient

We use Eq. 3.21 when calculating the diffusion coefficient. However, to do this we first need to find the region of the mean square displacement, where the system has become diffusive. We know this is the case when the MSD has the shape of a power law with power 1. We did not fix the number of points used for the fit, in an effort to get a better approximation of the diffusive region and thereby D. Instead we made fits to different number of end points and chose the one where the power of the fit was closest to 1. However, we set the restrictions that the fit will always use the last 4 points, and never the first 2/3 of data (saved in log time).

When calculating the standard deviation of the diffusion coefficient the simulation was separated into 10 parts from which D was calculated for each. These calculations follow the same procedure as before.

Calculating viscosity

We used the Green-Kubo formula (Eq. 3.24) when calculating the viscosity. When computing the integral we used on a combination of fitting and numerical integration. For each simulation we found the times $t_{0.10}$ and $t_{0.05}$ which represent the first time at which the stress autocorrelation was equal to 10% and 5% of its initial value at time zero, respectively. We then performed a numerical integration from $t = 0$ to $t_{0.05}$. For the long time region we fit the data for $t > t_{0.10}$ to a stretched-exponential

$$f(t) = A \exp\left(-\left(\frac{t}{\tau}\right)^{\beta}\right). \tag{6.4}$$

Then a numerical integration of the fit is performed from $t_{0.05}$ to a millionth of the initial value. The fit also used data in the region between times $t_{0.10}$ and $t_{0.05}$ to get a better estimate of β.

When calculating the standard deviation of the viscosity the simulation was separated into 10 parts from which η was calculated for each. These calculations follow the same procedure as before with the only difference, that the β used for the fit is the one from the full simulation.

6.4 Results: Dynamics

6.4.1 Comparing dynamics with experiments

In this section, we compare our simulation data with experimental data from Harris et al. [2011]. We use two data sets from this paper:

- data for ρ, P, and η from Tab. 3.
  The temperature range for this data is; 0°C, 10°C, 25°C, 50°C, and 75°C.
- data for P, D_+, and D_- from Tab. 6.
  The temperature range for this data is; 30°C, 50°C, 65°C, and 75°C.

When we tested the pressure in Sec. 6.2.2, we found that it depends greatly on the cutoff of the potential interactions. Consequently, we find it more meaningful to compare results as a function of density. To find the densities for the diffusion data we used the equation of state from Hansen et al. [2020]

$$\rho(T,P) = \left(V_0 \exp(\alpha_0 T)\left\{1 - C\ln\left[1 + \frac{P}{b_0 \exp(-b_1 T)}\right]\right\}\right)^{-1}, \tag{6.5}$$

where ρ is in g/cm^3, P is in MPa and T is in °C. The fitting parameters are $V_0 = 0.706 \pm 0.01$, $\alpha_0 = 6.36 \pm 0.04 \cdot 10^{-4}$, $C = 8.6 \pm 0.3 \cdot 10^{-2}$, $b_0 = 188 \pm 5$ and $b_1 = 4.4 \pm 0.2 \cdot 10^{-3}$. As a consistency check, we used Eq. 6.5 on the data from Harris et al. [2011] where density was already given. The given and calculated densities can be seen in Fig. 6.13. Here we find a good correspondence between the data with the biggest difference being less than 0.3%. Based on this analysis we use Eq. 6.5 to find ρ for the diffusion data from Harris et al. [2011].

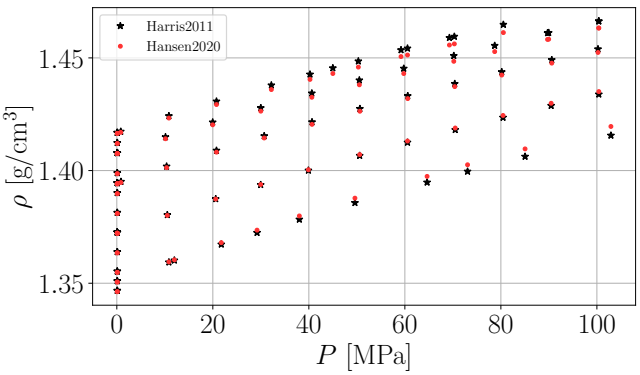

Figure 6.13: Comparison of ρ from Harris et al. [2011] and the corresponding ρ calculated via Eq. 6.5 from Hansen et al. [2020].

For this comparison we have simulated temperatures 10°C, 25°C, 50°C, and 75°C. These temperatures were chosen to have enough data to compare both η and D directly. The simulated and experimental state points can be seen in Fig. 6.14. Furthermore, Fig. 6.15 also shows the relation between ρ and P. The simulations generally have higher pressure than the experiments in this region . However, the experimental data generally look to be more density dependent than the simulated data. This means that at higher densities the experimental pressure would exceed the simulated pressure.

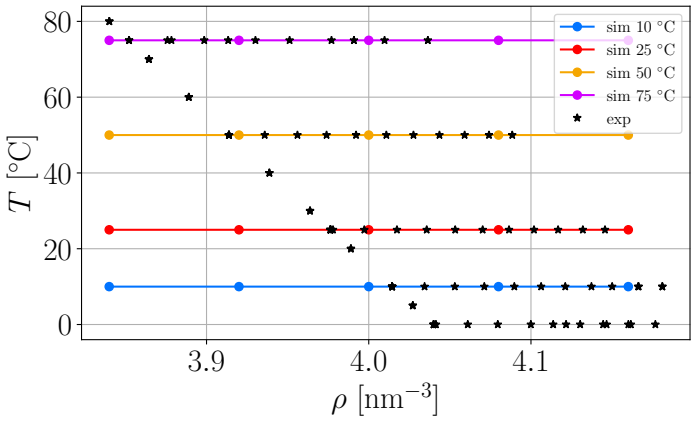

Figure 6.14: Simulated and experimental temperature as a function of density.

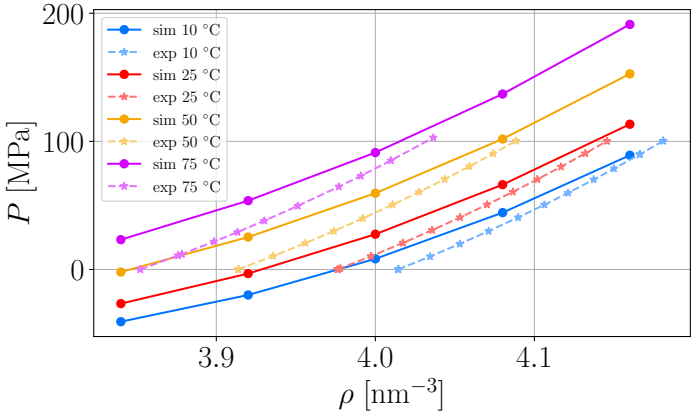

Figure 6.15: Simulated and experimental pressure as a function of density.

A comparison between our simulated data and the experimental diffusion coefficient data from Harris et al. [2011] can be seen in Fig. 6.16. The data are shown as a function of ρ which was calculated using Eq. 6.5. We show the data on a logarithmic y-axis to emphasize the data' approximate exponential behaviour. To avoid confusion from an overload of data, we only show isotherms 50 °C and 75 °C since they are available in both simulations and experiment. The simulations are more diffusive than the experiments (approximately a factor of 2). However, the shape of the curves (their slopes) matches very well.

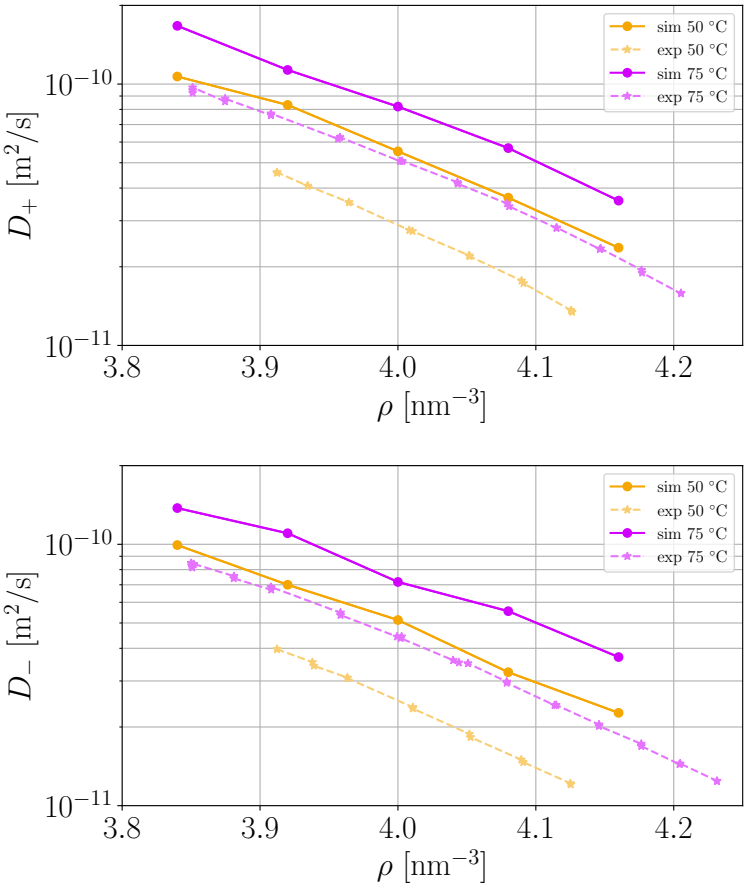

Figure 6.16: Simulated and experimental D as a function of density for both the cation and anion. Error bars are included for the simulated data, however, in many cases they is smaller that the symbol size.

A comparison of our simulated viscosity with the experimental viscosity data from Harris et al. [2011] Tab. 3 can be seen in Fig. 6.17 as a function of ρ. The four temperatures have their own colours where experimental data are shown as dashed lines, and simulation data as full lines. A logarithmic y-axis was again used to emphasize the data' approximate exponential behaviour. The exponential behaviour is striking for the experimental data and the simulated isotherms 50°C and 75°C. The first point on the simulated isotherms 10°C and 25°C does not follow this behaviour. However, this could be related to the large negative pressure at those points. The simulations are generally less viscous than the experiments (approximately a factor of 2). Again, the shape of the curves (their slopes) matches very well.

From this analysis we find that the model is a good qualitative representation of the dynamics in the experiments.

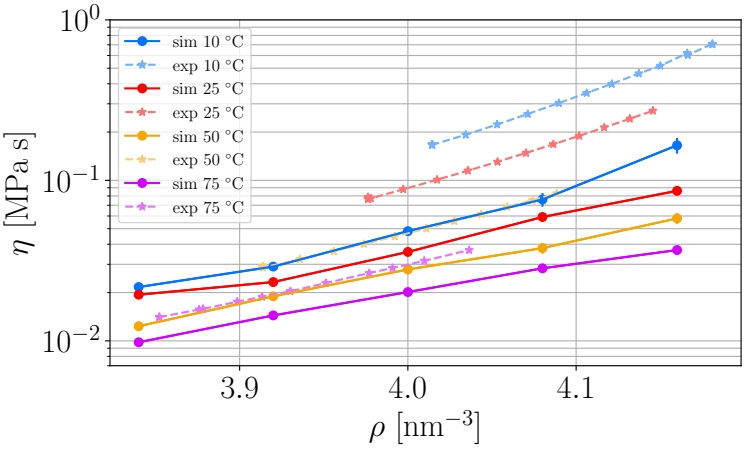

Figure 6.17: Simulated and experimental η as a function of ρ. Error bars are included for the simulated data, however, in many cases it is smaller that the symbol size.

6.4.2 Dynamics along isochores

To get an idea of the dynamics and relaxation of the system, we analyse the self-intermediate scattering function and the mean square displacement along the two isochore at the boundary, i.e. $\rho = 3.2$ nm^{-3} and 4.8 nm^{-3}, see red and blue points in Fig. 6.12. Since the system contains 12 different particle types, we will only be showing data from N^+ here, see Fig. 6.18.

The wave-vector in F_s was automatically chosen as the position of the main peak in $S(q)$. For $\rho = 3.2$ nm^{-3} this was between 0.79 Å^{-1} and 0.82 Å^{-1}, while for 4.8 nm^{-3} it was between 0.84 Å^{-1} and 0.87 Å^{-1}. The dashed lines indicate points with $T < 580$ K, i.e. points with negative pressure or slow dynamics, respectively.

The first thing, that should be noted is that the data in the slow-dynamics-region (high density and low temperature) have not run long enough to relax. This means that quantities like the diffusion coefficient can not be obtained without running longer. The second thing to notice is the beginning of a two-step relaxation as the system gets slower. This is mostly visible on the high density curves (red).

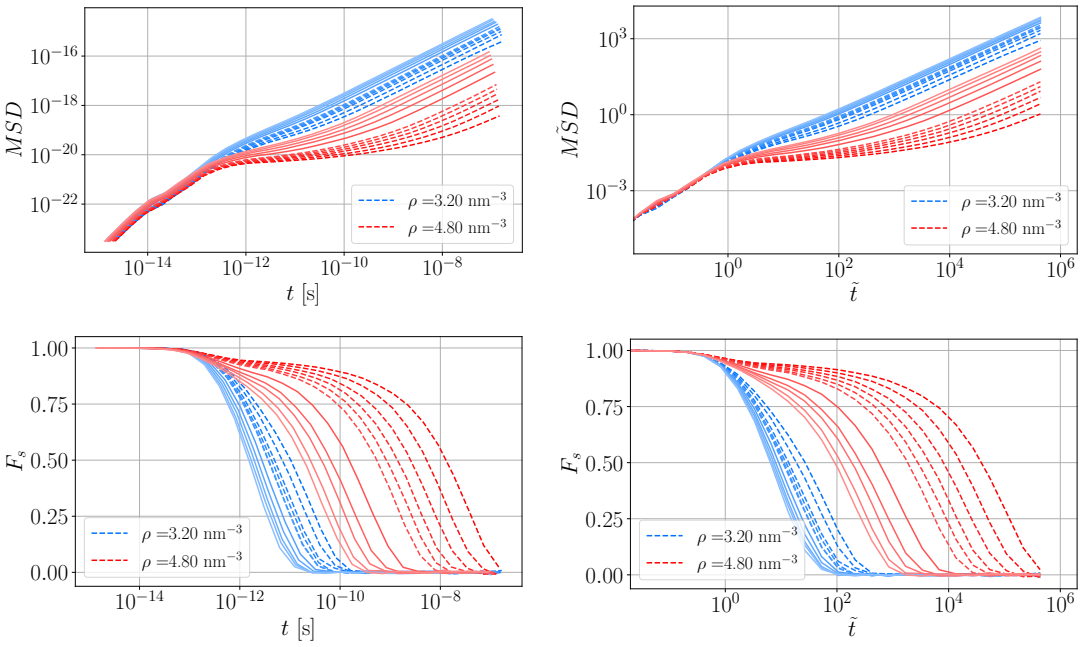

Figure 6.18: Mean square displacement and self-intermediate scattering function along isochore $\rho = 3.2$ nm^{-3} and 4.8 nm^{-3} in both SI and isomorph scaled units. Dashed lines indicate negative pressure or slow dynamics, see Fig. 6.12.

The stress autocorrelation along the two isochore at the boundary $\rho = 3.2$ nm^{-3} and 4.8 nm^{-3} can be seen in Fig. 6.19. We notice that in SI units, the stress-autocorrelation function has features in the range $10^{-13} < t < 10^{-11}$ s which occur at the same real time for all the curves. These could be related to intra-molecular vibrations.

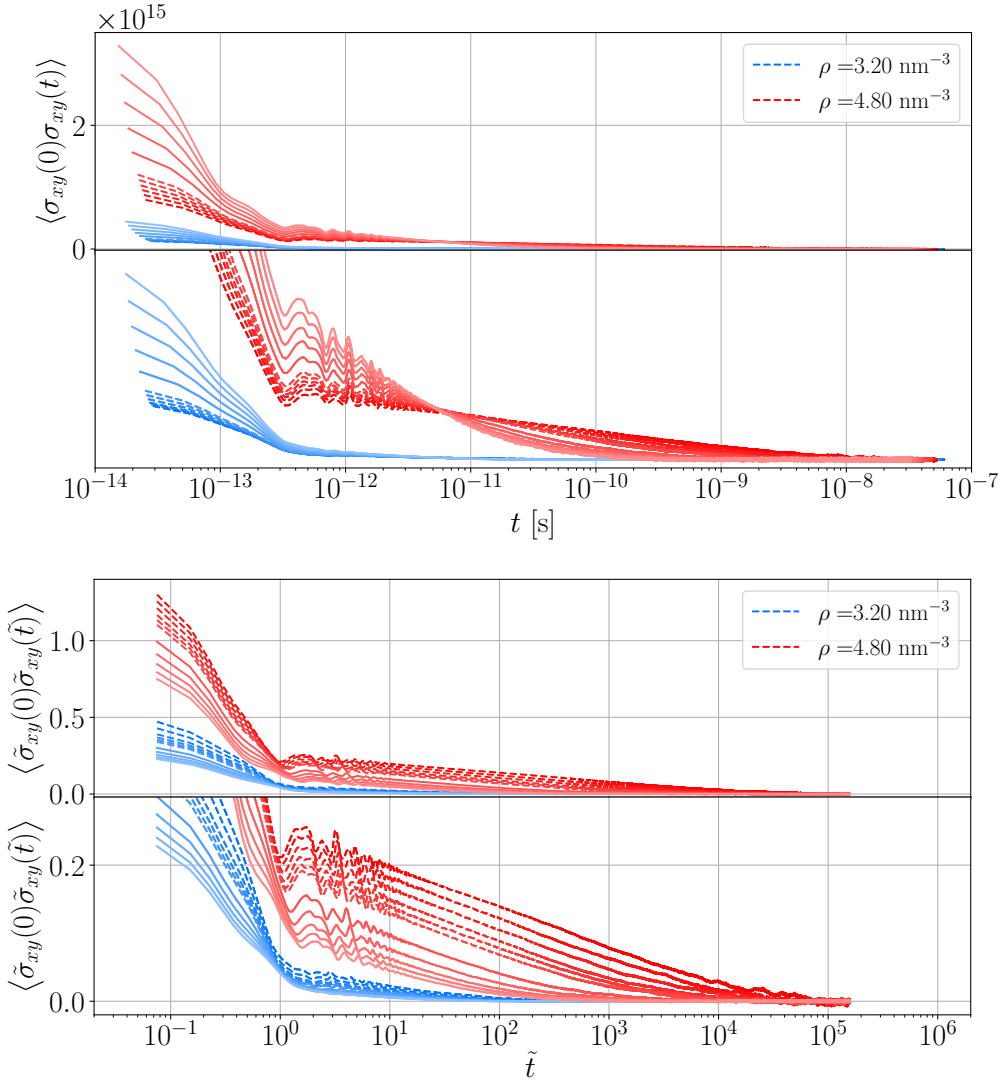

Figure 6.19: Graphs of the stress autocorrelation function along isochore $\rho = 3.2$ nm^{-3} (blue) and 4.8 nm^{-3} (red). A zoom-in on the long-time region is provided to better see this behaviour. (Top) Data in IS units and (Bottom) data in isomorph scaled units. Dashed lines indicate negative pressure or slow dynamics, see Fig. 6.12.

6.4.3 Does the model have isomorphs?

The isomorph R and γ for the simulated state points can be seen in Fig. 6.20. Since R is close to zero, we should not expect this system to have isomorphs in the region of the phase diagram, that we have simulated. This is not surprising due to the bonded interactions in the model, as was discussed in Sec. 4.3.3. Additionally, not even the simpler atomic model from Chap. 5 had isomorphs. We also see that R is more dependent on density than temperature and looks approximately linear.

The γ is also mainly dependent on density, however, it becomes more temperature dependent at higher densities. It should also be noted that γ is approximately linear as a function of density.

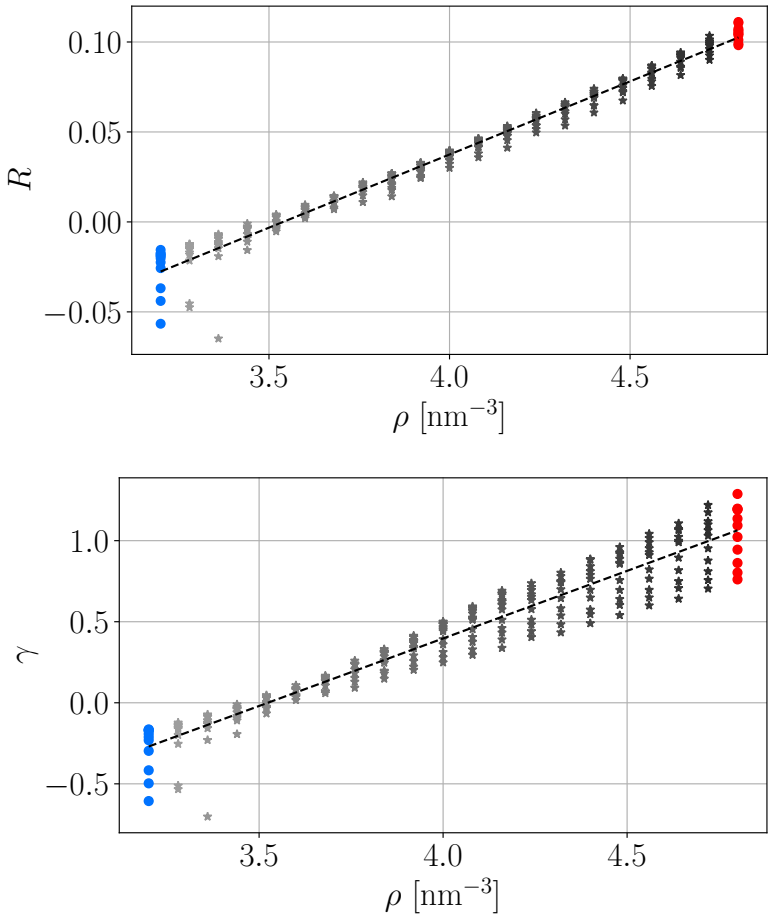

Figure 6.20: The R and γ for all simulated state points. The dashed lines are linear fits to the data meant to guide the eye. Isochore $\rho = 3.2$ nm^{-3} and 4.8 nm^{-3} are highlighted with blue and red, respectively.

6.4.4 Does the model have isodynes?

To determine if this model could have lines of invariant dynamics we plot some contours for the diffusion coefficient of N^+ and the viscosity, see Fig. 6.21. We choose contours which go through the points $\rho = 3.2;\ 3.6;\ 4.0;\ 4.4;\ 4.8\ \mathrm{nm}^{-3}$ and $T = 598.15$ K. From this we find that the contours cross each other in SI units, but they have the same shape in isomorph scaled units. This means that the system at least has curves along which both diffusion and viscosity are invariant.

Another way of showing this with a single parameter is with the Stokes-Einstein relation (see Sec. 3.4.4). Thus Fig. 6.22 shows the effective hydrodynamic radius and the product of $\tilde{\eta}$ and $\tilde{D}$. The effective hydrodynamic radius is approximately 6 Å, which is around the size of the molecules. The product $\tilde{\eta}\tilde{D}$, while not perfect, is still remarkably independent of both ρ and T. This tells us that approximately

$$\tilde{D}(\rho, T) \propto \frac{1}{\tilde{\eta}(\rho, T)} \qquad \text{(approximately)} \tag{6.6}$$

This confirms the existence of curves along which both quantities are invariant. However, this result is actually stronger than the previous one from Fig. 6.21. This is because Fig. 6.21 only confirms that the shape of the contours are the same (nothing about their value), while Eq. 6.6 also confirms that the product of the two is (approximately) invariant. Additionally, invariance is true for the entire simulated region and not only for each contour.

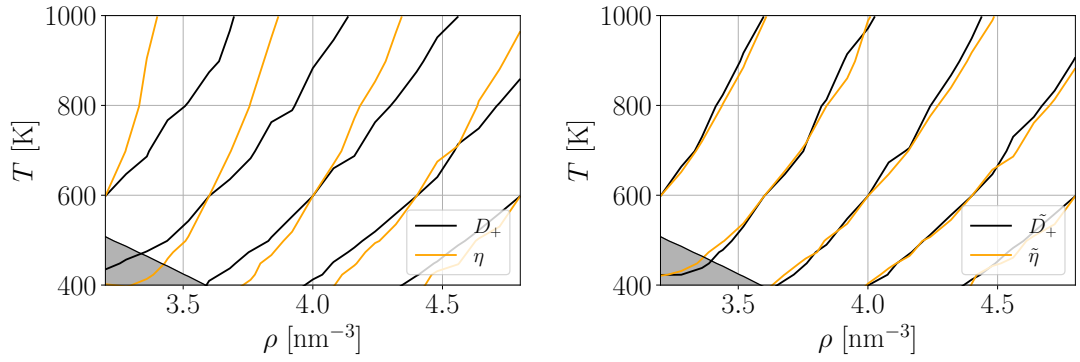

Figure 6.21: Contours for D_+ (orange), and $1/\eta$ (black). These contours were found using the *contour* function from the *matplotlib* python package. (Left) Data in SI units and (Right) data in isomorph scaled units.

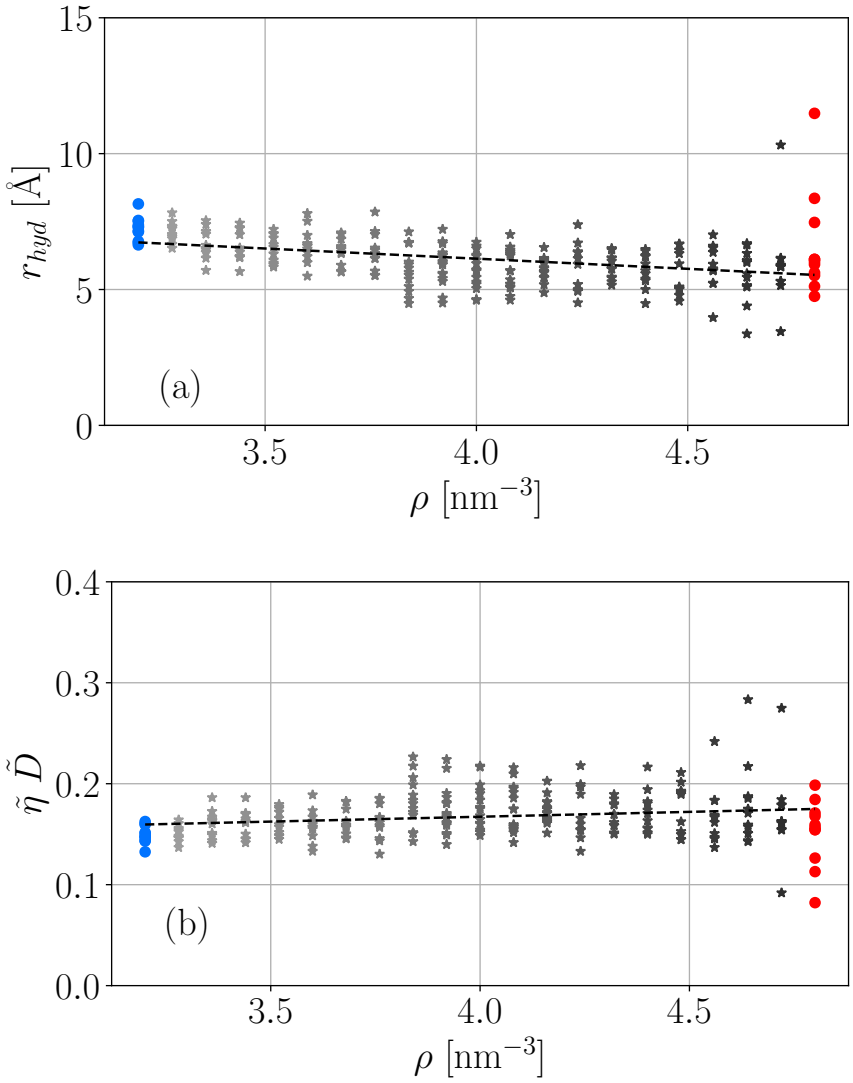

Figure 6.22: Test of the Stokes-Einstein relation. (a) A plot of the effective hydrodynamic radius as a function of ρ. (b) A plot of $\tilde{\eta}\tilde{D}$ as a function of ρ. The dashed lines are linear fits to the data meant to show the ρ dependence.

Now that we know the system has curves where both $\tilde{\eta}$ and $\tilde{D}$ are invariant, the question is how to trace these curves more precisely. To answer this question we analyse the diffusion coefficient and the inverse viscosity i.e. the fluidity. We choose fluidity instead of viscosity due to its relation with the diffusion coefficient from Eq. 6.6. This leads us use a similar procedure when analysing both types of data.

We decided to fit the data as a function of T for each density. Initially a linear fit was used, which was sufficient for the narrow density range from 3.84 to 4.16 nm^{-3}. However, when a broader density range was analysed, it became clear that a linear fit was not sufficient, especially at low densities. Consequently, we a 3rd order polynomial was used to fit the $1/\tilde{\eta}$ data instead. However, the $\tilde{D}$ data has more noise so to avoid overfitting 2nd order polynomial was used. These can be seen seen in Fig. 6.23.

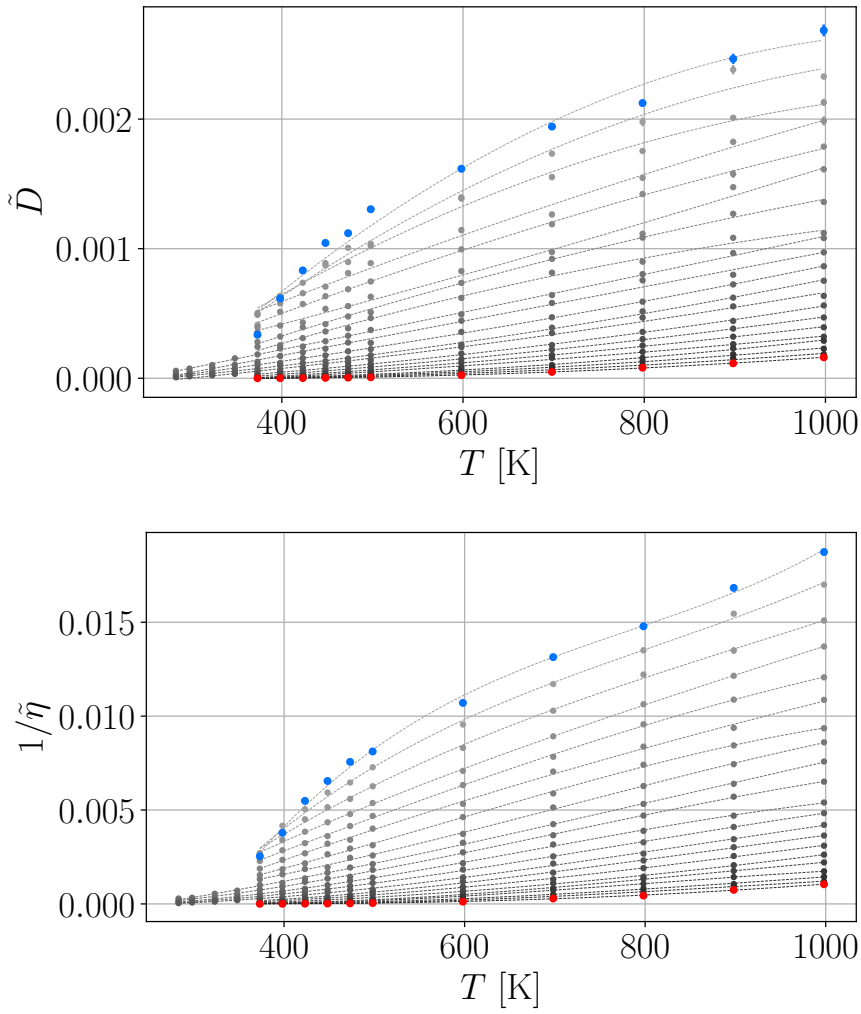

Figure 6.23: Plot of $\tilde{D}$ and $1/\tilde{\eta}$ as a function of temperature for each density. $\tilde{D}$ is fitted to a 2nd order polynomial, and $\tilde{\eta}$ is fitted to a 3rd order polynomial. Error bars are included but are in most cases smaller than the symbol size.

All these fits (and the data) are monotonically increasing as a function of temperature. Consequently, the fits have a unique inverse in the simulated region. This means that for each of our simulated densities we can find the temperature which gives a specific $\tilde{D}$ or $1/\tilde{\eta}$ (assuming the value exists for that density in the simulated temperature range). This allows us to choose a $\tilde{D}$ or $1/\tilde{\eta}$ and get the corresponding densities and temperatures where the chosen value is constant.

We find that $\tilde{D}$ and $1/\tilde{\eta}$ result in very similar contours when using this method. However, the polynomial fits seem slightly better for $1/\tilde{\eta}$ and we therefore decide to use these when choosing the curves.

This method was used to trace isodynes from which a total of 7 were simulated; 4 with the linear fit (isodyne 1-4), and 3 with the 3rd order polynomial fit (isodyne 5-7). Isodyne 5, 6 and 7 were chosen to cover the entire simulated range with isodyne 5 being the slowest and isodyne 7 being the fastest. Furthermore, all points along them have positive pressure which is not the case for the other isodynes. All 7 isodnes are shown in a $\rho - T$ phase diagram in Fig. 6.24.

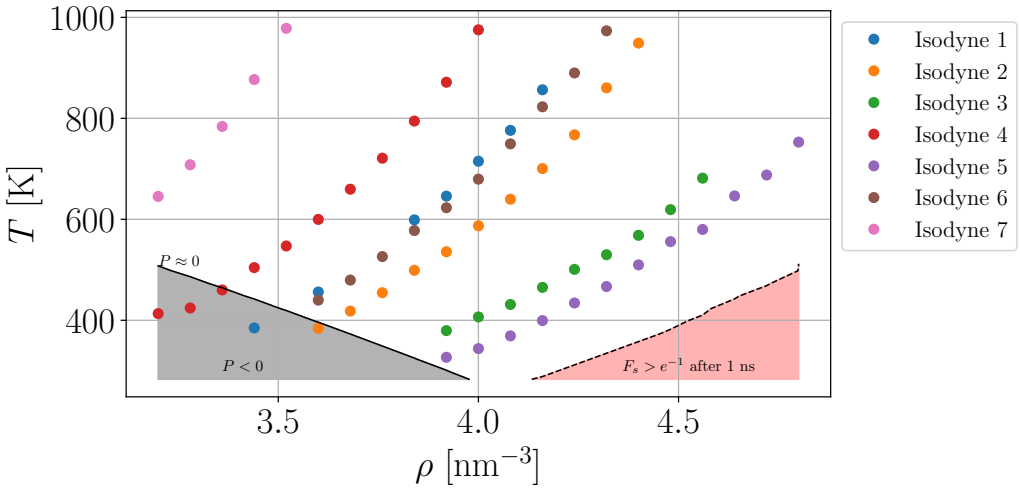

Figure 6.24: All the simulated isodynes in a $\rho - T$ phase diagram. As in Fig. 6.12 there are two coloured regions; a grey region that indicates negative pressure, and a red region where the dynamics become slow.

A list of all $\rho - T$ state points along the simulated isodynes can be found in Tab. 6.4. All points along each isodyne have been given a unique ID which will be used when referencing them in the upcoming analysis. This was done to lighten the notation, and remove the need to specify ρ and T for every point.

Isodyne 1		
ID	ρ [nm^{-3}]	T [K]
d1:1	3.44	384.83
d1:2	3.60	456.05
d1:3	3.84	598.92
d1:4	3.92	645.92
d1:5	4.00	715.07
d1:6	4.08	776.18
d1:7	4.16	856.57

Isodyne 2		
ID	ρ [nm^{-3}]	T [K]
d2:01	3.60	383.94
d2:02	3.68	418.25
d2:03	3.76	454.64
d2:04	3.84	499.00
d2:05	3.92	535.75
d2:06	4.00	587.18
d2:07	4.08	639.75
d2:08	4.16	700.49
d2:09	4.24	767.31
d2:10	4.32	860.40
d2:11	4.40	948.98

Isodyne 3		
ID	ρ [nm^{-3}]	T [K]
d3:1	3.92	379.56
d3:2	4.00	406.65
d3:3	4.08	431.36
d3:4	4.16	465.18
d3:5	4.24	500.86
d3:6	4.32	529.89
d3:7	4.40	568.30
d3:8	4.48	619.21
d3:9	4.56	681.55

Isodyne 4		
ID	ρ [nm^{-3}]	T [K]
d4:01	3.20	413.26
d4:02	3.28	424.31
d4:03	3.36	460.14
d4:04	3.44	504.33
d4:05	3.52	547.21
d4:06	3.60	599.82
d4:07	3.68	659.61
d4:08	3.76	721.13
d4:09	3.84	794.59
d4:10	3.92	871.54
d4:11	4.00	975.28

Isodyne 5		
ID	ρ [nm^{-3}]	T [K]
d5:01	3.92	326.72
d5:02	4.00	343.93
d5:03	4.08	369.09
d5:04	4.16	399.41
d5:05	4.24	434.30
d5:06	4.32	466.85
d5:07	4.40	509.75
d5:08	4.48	555.83
d5:09	4.56	579.84
d5:10	4.64	646.32
d5:11	4.72	687.79
d5:12	4.80	752.92

Isodyne 6		
ID	ρ [nm^{-3}]	T [K]
d6:01	3.60	439.98
d6:02	3.68	479.65
d6:03	3.76	526.19
d6:04	3.84	577.76
d6:05	3.92	622.94
d6:06	4.00	679.57
d6:07	4.08	749.41
d6:08	4.16	822.87
d6:09	4.24	889.89
d6:10	4.32	973.35

Isodyne 7		
ID	ρ [nm^{-3}]	T [K]
d7:1	3.20	645.32
d7:2	3.28	708.10
d7:3	3.36	783.98
d7:4	3.44	876.86
d7:5	3.52	978.33

Table 6.4: List of $\rho - T$ state points for all our simulated isodynes.

6.4.5 Shape of isodynes and density scaling γ

We analyse the shape of the isodynes in the $\rho - T$ diagram. Furthermore, we also compute the density scaling exponent γ by using the first part of Eq. 4.19. Note that this is not the same γ from Fig. 6.20 which applies for configurational adiabats. Instead we analyse the shape of the curves. This analysis will be performed for isodyne 5, 6, and 7, since they cover the simulated region.

First, we see if the shape of the curve can be described by a power law. To visualise this the data can be seen in a linear and a log-log plot in Fig. 6.25. The correlation between the data and the fits are greater than 0.998 in all three cases. The γ is between 4.27 and 4.44 with the lowest value at isodyne 5 (the high viscosity of the simulated isodynes). This is greater than the experimental value from Hansen et al. [2020] which was 2.8.

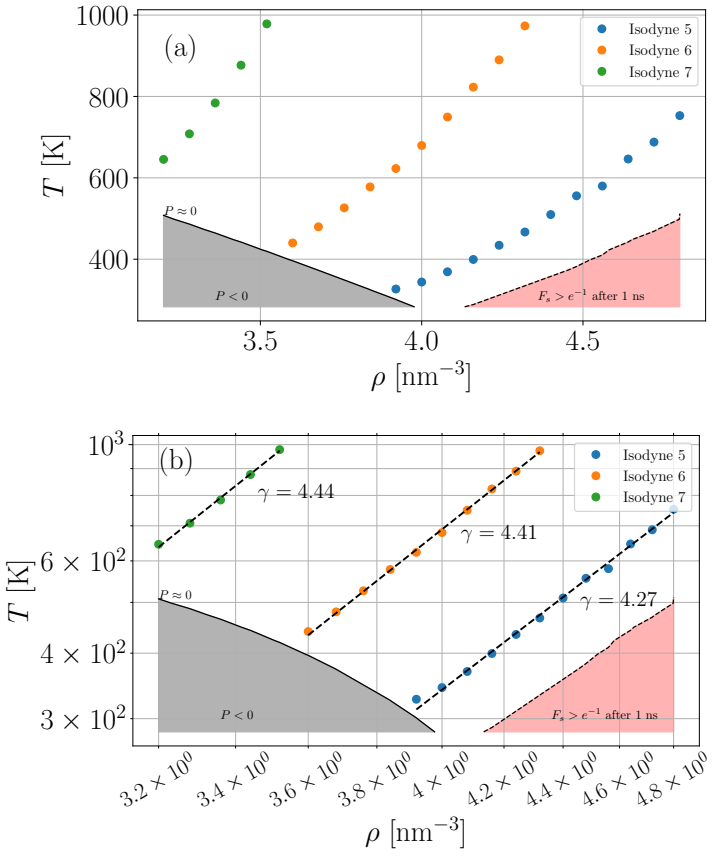

Figure 6.25: Plot of isodyne 5, 6, and 7 in a $\rho - T$ diagram, in (a) a linear plot, and (b) a log-log plot. The numbers next to the data are the density scaling exponents γ.

We also tested if the data could have the shape of an exponential function. In this case γ is not constant along the curve. A plot of the isodyne curves and the corresponding γ can be seen in Fig. 6.26. The correlation between the data and the fits are greater than 0.999 in all cases. Again, we see that γ is bigger than the experimental data from Hansen et al. [2020]. Here the changes in γ are the same as for the density interval of the isodyne, i.e. 22%, 20% and 10%.

We can conclude that the data have a shape similar to both a power law and an exponential function. However, with the data we have available we cannot argue if one is better than the other. In either case, the density scaling γ is bigger than in the experimental observations where $\gamma = 2.8$ [Hansen et al., 2020].

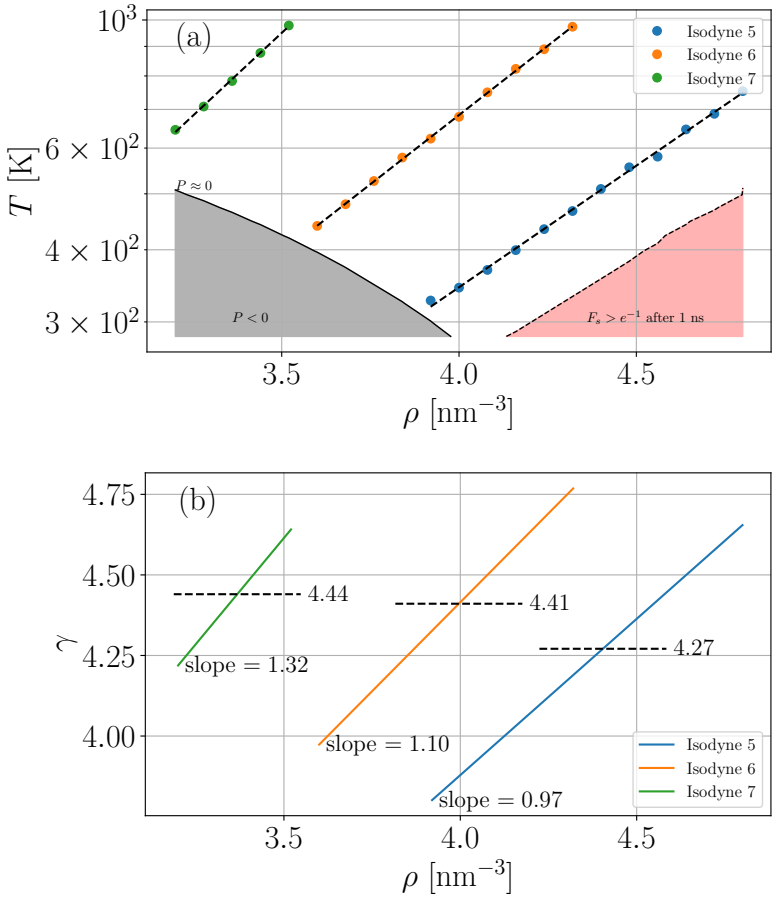

Figure 6.26: (a) Plot of isodyne 5, 6, and 7 and their exponential fits in a lin-log $\rho - T$ diagram. (b) The density scaling exponent γ from the exponential fits. For comparison the γ from the power law fit (see Fig. 6.25) are included as dashed black lines.

6.4.6 Dynamics along isodynes (check)

Our isodynes were chosen to have invariant viscosity, and consequently invariant diffusion coefficient. To test how well our tracing method worked we show $\tilde{D}$ for N^+ and $\tilde{\eta}$ along the simulated isodynes in Fig. 6.27. As expected the data is not perfectly invariant, however, it will still prove useful for the purpose of this work.

We also analyse the shape on the data used to calculate these quantities to find if this dynamical invariance is more general. Thus, examples of the mean square displacement and the self-intermediate scattering functions for N^+ along isodyne 2 in scaled units can be seen in Fig. 6.28. Here we see that the curves collapses, which is even striking when comparing the similar curves along isochores, see Fig. 6.18.

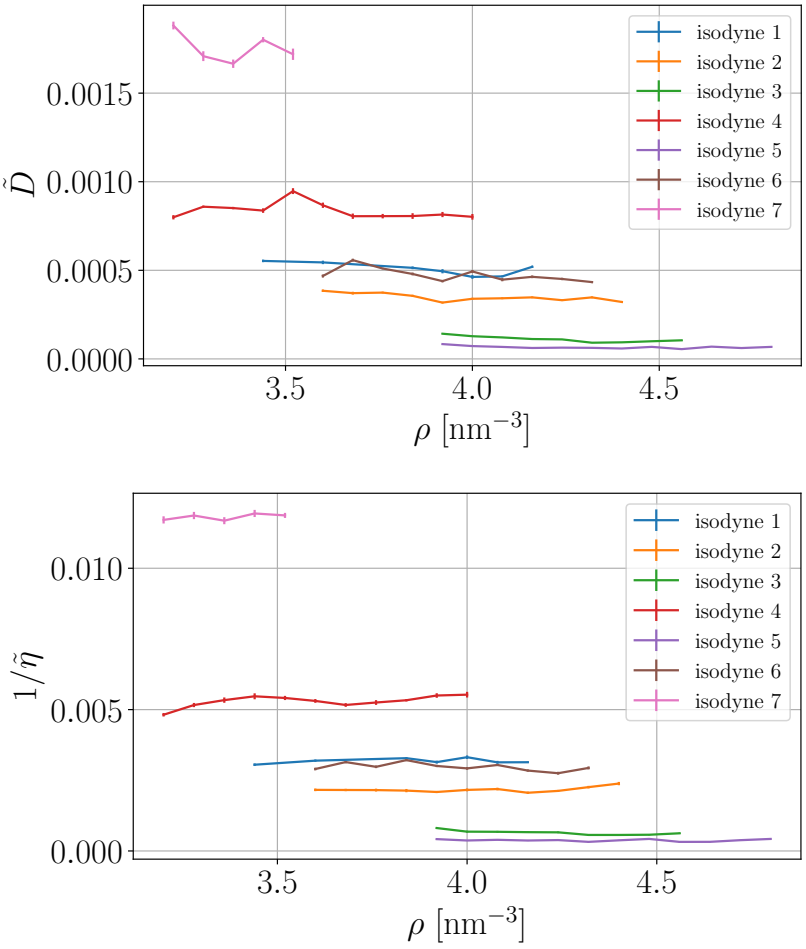

Figure 6.27: Dynamics data in isomorph scaled units along the simulated isodynes. (Top) $\tilde{D}$ for N^+ and (Bottom) $1/\tilde{\eta}$.

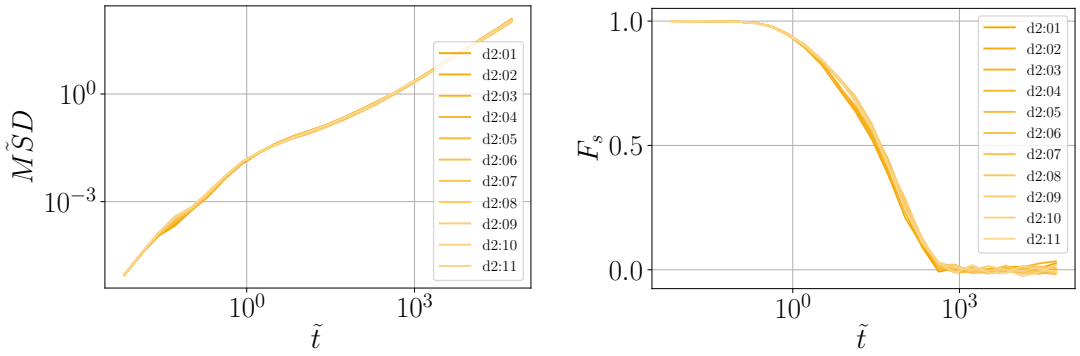

Figure 6.28: Dynamics for N^+ along isodyne 2 in isomorph scaled units. (Left) Mean square displacement, and (Right) self-intermediate scattering function. A list of isodyne labels can be found in Tab. 6.4.

We also analysed the stress-autocorrelation function used for calculating the viscosity, see Fig. 6.29. A zoom-in of the long-time behaviour is also shown. The curves do not collapse as well at time $t = 0$ as in the long-time domain. This means that either this is not really invariant or it is a sign that this is only an approximate isodyne. On the other hand, the long-time domain collapses well in scaled units, which means that it is important for the viscosity. The general collapse of these curves is in contrast to the stress-autocorrelation function curves along isochores from Fig. 6.19.

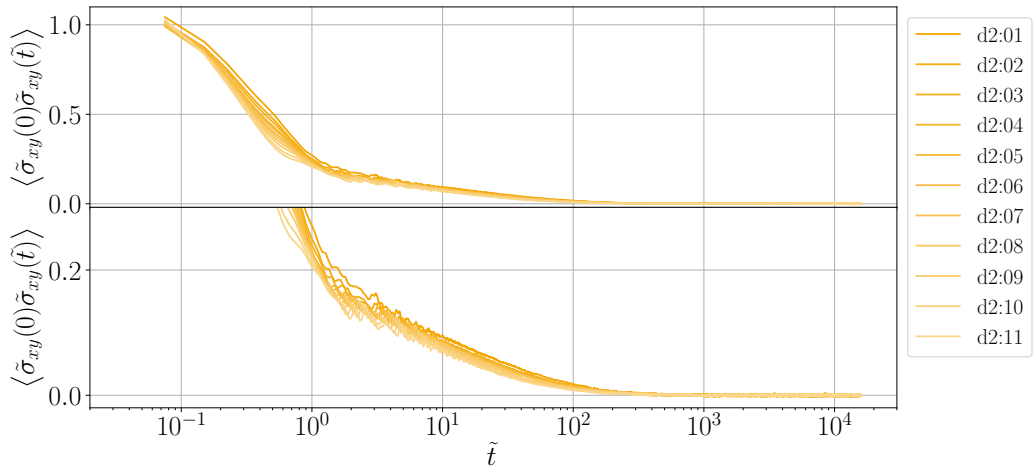

Figure 6.29: Stress-autocorrelation function along isodyne 2 in scaled units. A zoom-in on the long-time region is provided to better see this behaviour. A list of isodyne labels can be found in Tab. 6.4.

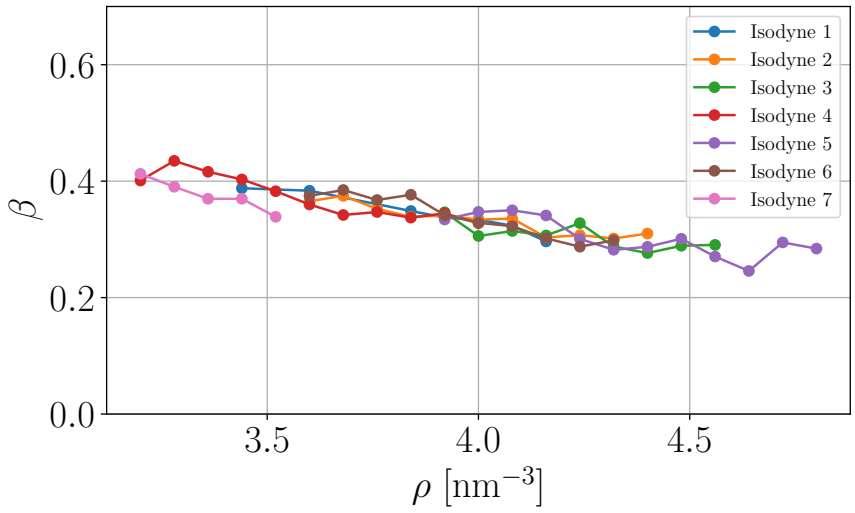

Figure 6.30: The stretching exponent β from the viscosity calculation as a function of density.

To quantify the collapse of the data in the long-time domain we plotted the stretching exponent β from the stretched exponential fit that was used to calculate η, see Fig. 6.30. We see that β changes, but it seems to only depend on density and not temperature. Thus the long time domain becomes more stretched as the density increases. This also means that the collapse is not perfect.

6.4.7 Rotation of molecules

In addition to the measures of dynamics that we have shown so far, we would like to analyse the rotations of the molecules. This is possible since molecular dynamics simulations give us access to atomic configurations at different times. Thus, we can define different normalised vectors ($\boldsymbol{n}$) between atoms within a molecule and compute the autocorrelation function in time to gain rotational information

$$R\left(\tilde{t}\right) \equiv \left\langle \boldsymbol{n}(0) \cdot \boldsymbol{n}(\tilde{t}) \right\rangle . \tag{6.7}$$

This will be done for isodyne 2, isodyne 5, and isodyne 6. Furthermore, for comparison purposes we also analyse isotherm 325 °C, but only within the same density range as isodyne 5 to make the comparison more useful.

Molecular rotation of the cation

We would like to analyse the rotation of the ring. This will be done in two ways. First, we define the normal-vector to the plane spanned by N^+, and the two R_1 groups. The autocorrelation function for this vector can be seen in Fig. 6.31. Here there is a clear change along the isotherm, while all the isodynes show invariance.

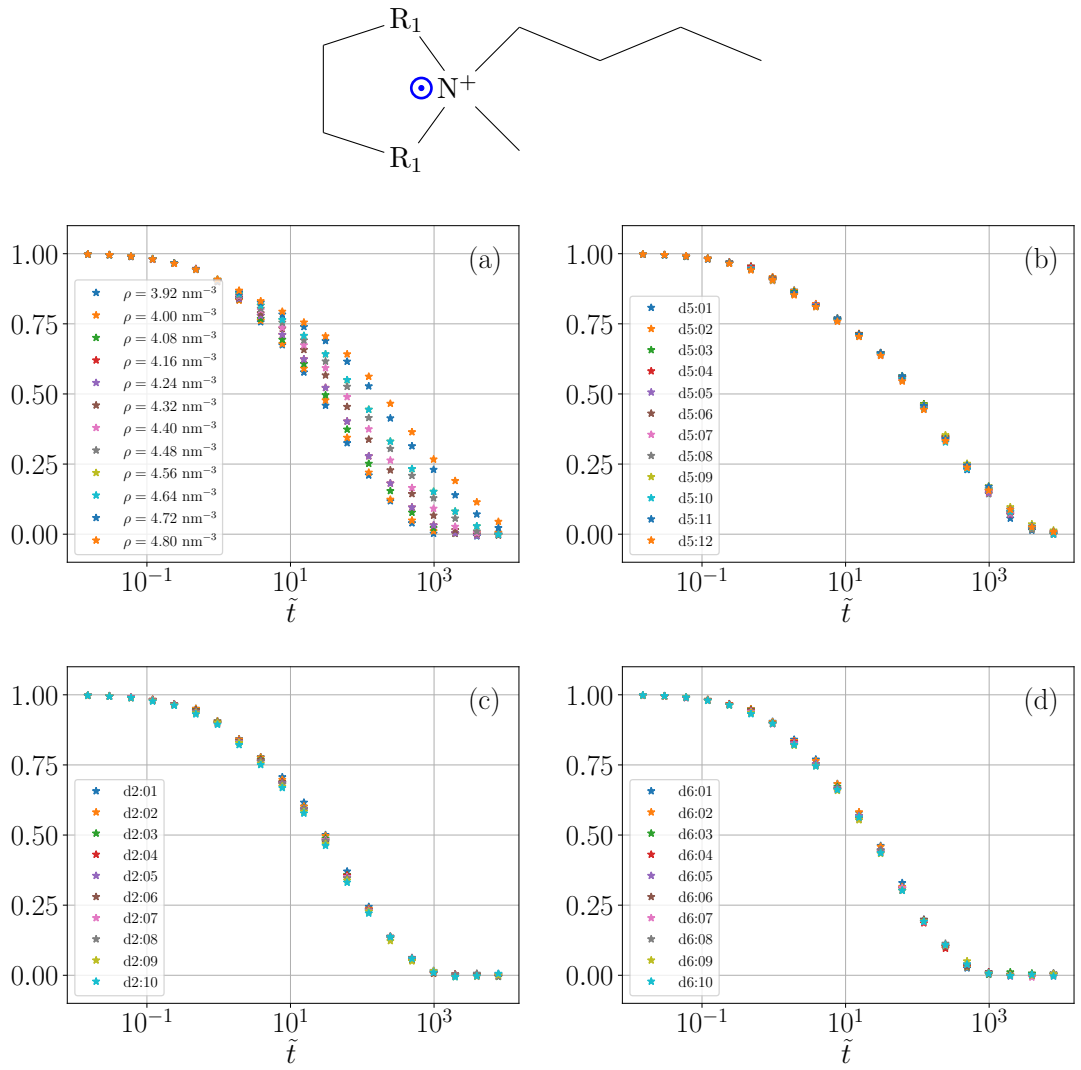

Figure 6.31: Autocorrelation function of the normal-vector to the plane spanned by N^+, and the two R_1 groups. (a) Isotherm 325 °C, (b) isodyne 5, (c) isodyne 2 and (d) isodyne 6. A list of isodyne labels can be found in Tab. 6.4.

The second way we analyse the rotation of the ring is by defining the vector from N^+ to the point between the two R_2 groups.The autocorrelation function for this vector can be seen in Fig. 6.32. Here we see the same behaviour as for the other ring rotation.

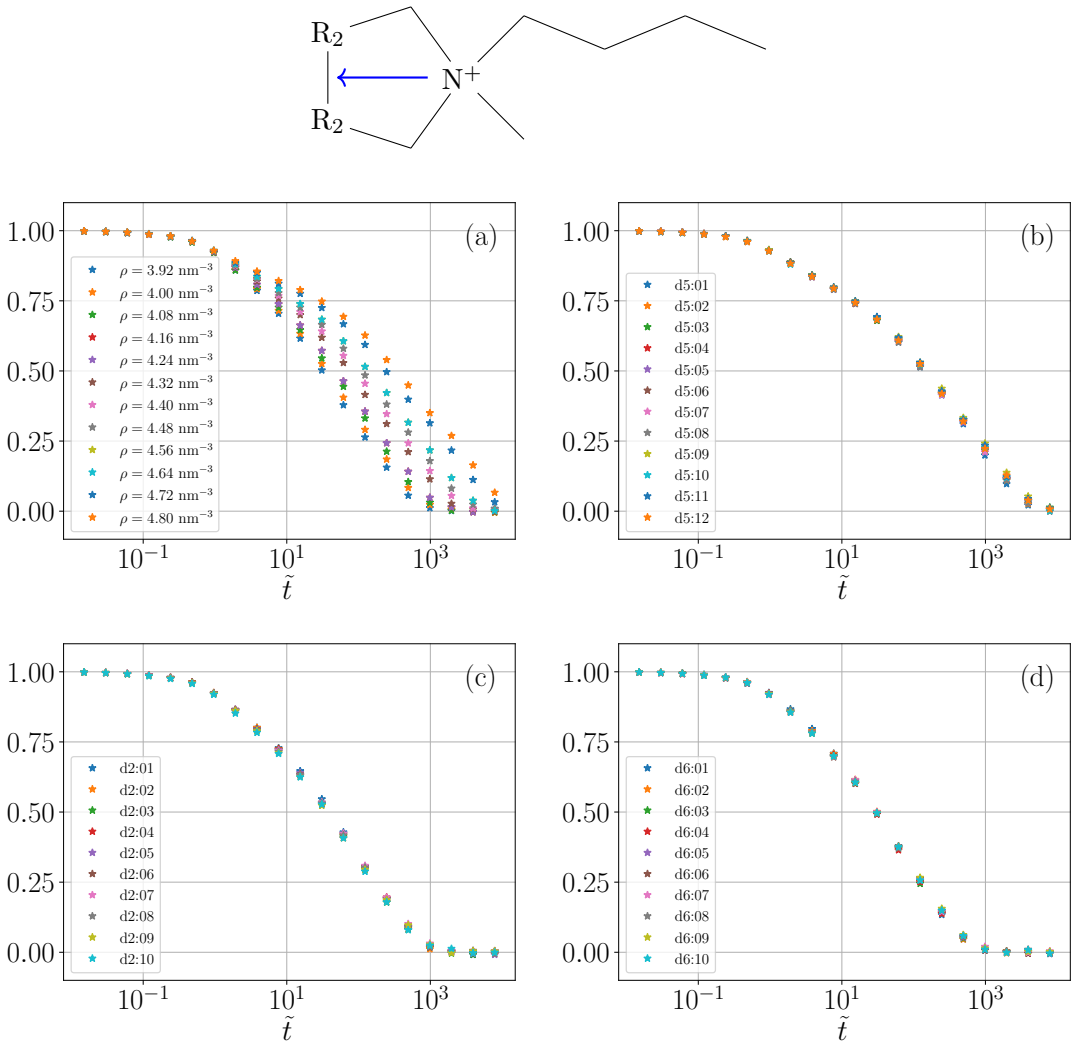

Figure 6.32: Autocorrelation function of the vector from N^+ to the point between the two R_2 groups. (a) Isotherm 325 °C, (b) isodyne 5, (c) isodyne 2 and (d) isodyne 6. A list of isodyne labels can be found in Tab. 6.4.

We also study the rotation of the tail in the cation. This was defined as the normalised vector between N^+ and the end of the tail (T_4).The autocorrelation functions are shown in Fig. 6.33. Again, we see a clear change along the isotherm and invariance along the isodynes. However, there is greater variation along isodyne 5 than the other isodynes at long times. We do not believe this is related to the quality of the isodyne since this would also have affected the rotation of the ring which did not show this variance. Isodyne 5 does have the highest viscosity of all the simulated isodynes, however, we do not know if this is related.

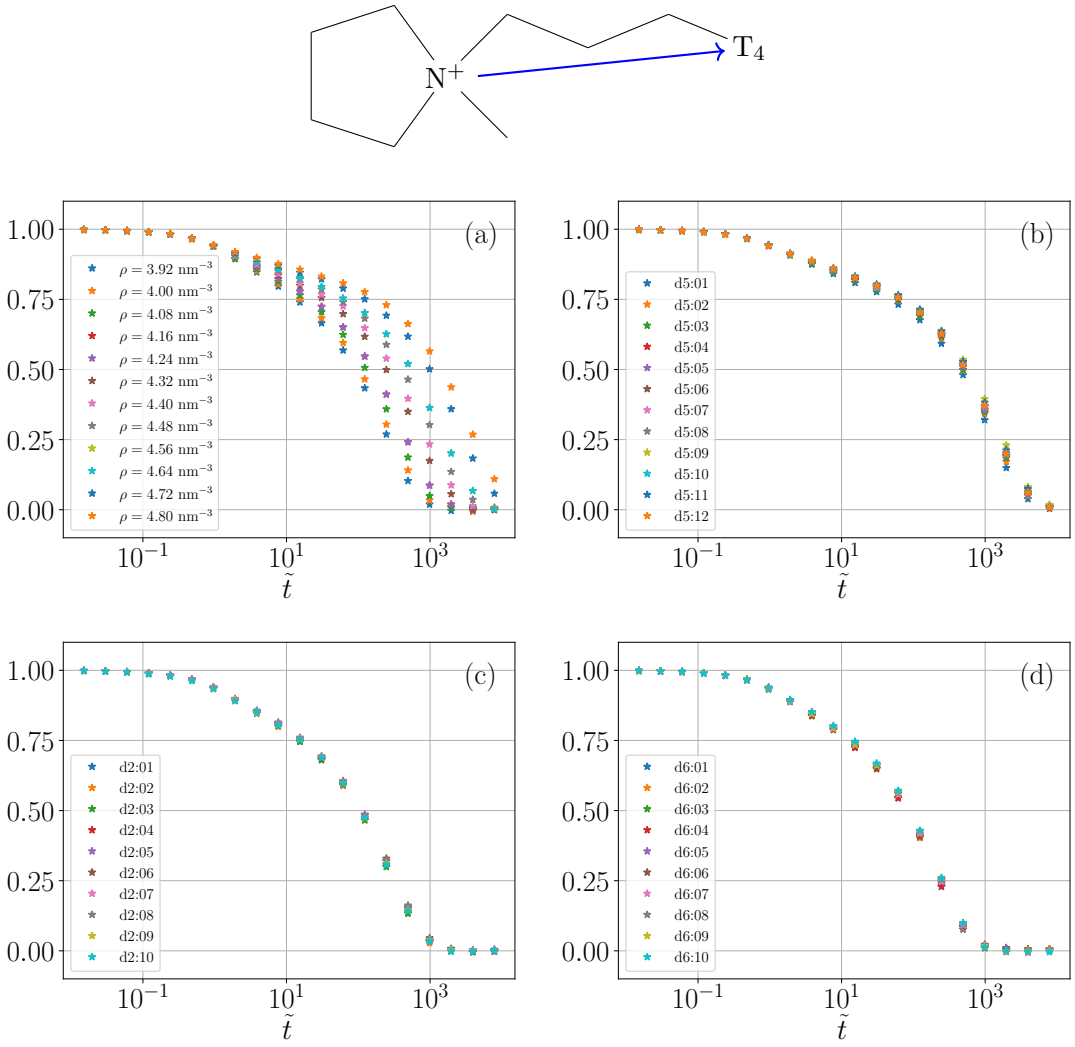

Figure 6.33: Autocorrelation for the normalised vector between N^+ and T_4. (a) Isotherm 325 °C, (b) isodyne 5, (c) isodyne 2 and (d) isodyne 6. A list of isodyne labels can be found in Tab. 6.4.

Molecular rotation of the anion

For the anion we start by defining the normalised vector between the two S atoms to find its rotational behaviour. The autocorrelation functions are shown in Fig. 6.34. Not surprisingly we again see a clear change along the isotherm, and invariance along the isodynes. However, isodyne 5 shows less invariance than the other isodynes, as was the case for the tail in the cation. We are not certain of the reason for this.

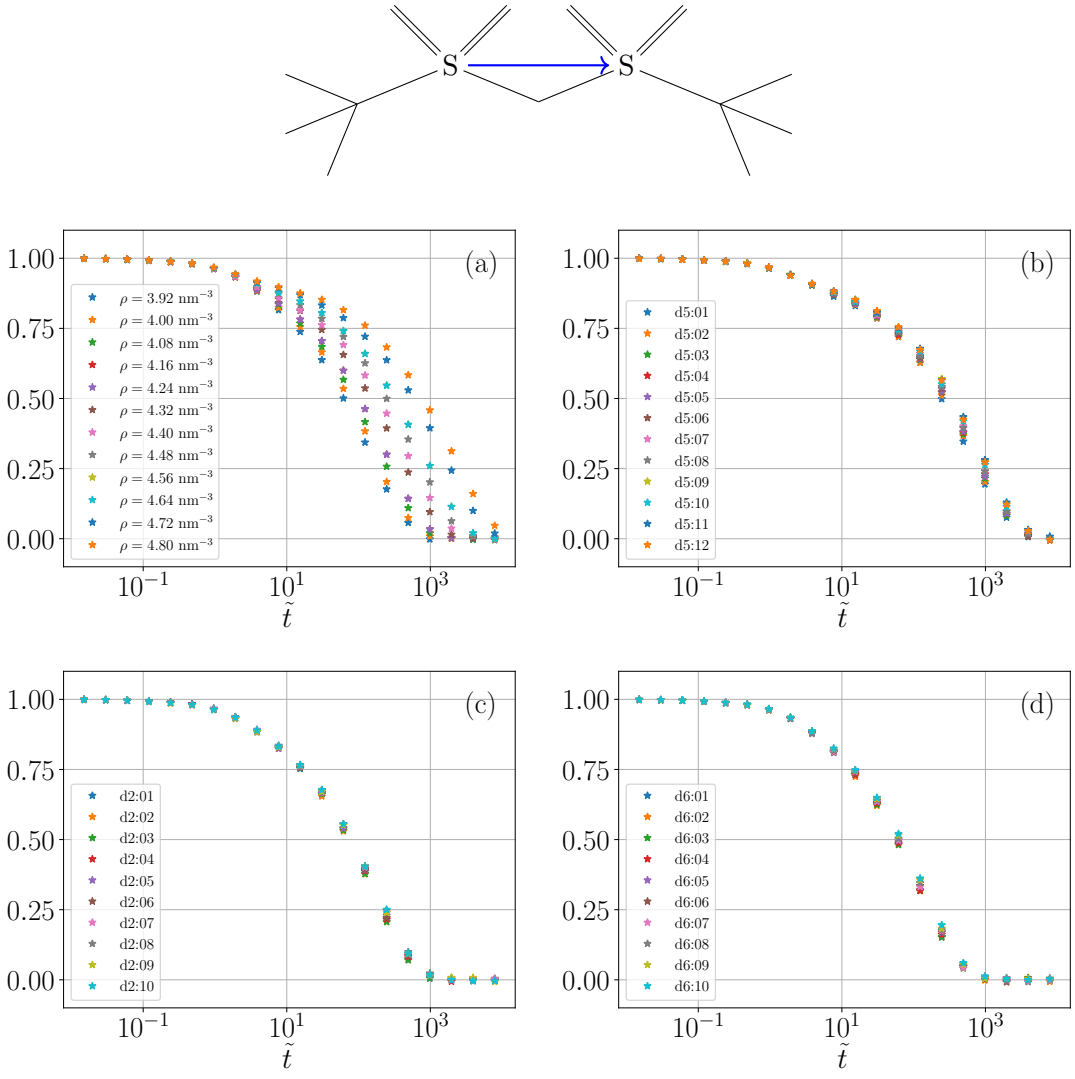

Figure 6.34: Autocorrelation function of the vector between the two S atoms. (a) Isotherm 325 °C, (b) isodyne 5, (c) isodyne 2 and (d) isodyne 6. A list of isodyne labels can be found in Tab. 6.4.

To confirm this isodyne rotational invariance, we also define the normalised vector between the two C atoms. The autocorrelation functions are shown in Fig. 6.35. Here we see the same behaviour as before in Fig. 6.34, including the small changes along isodyne 5.

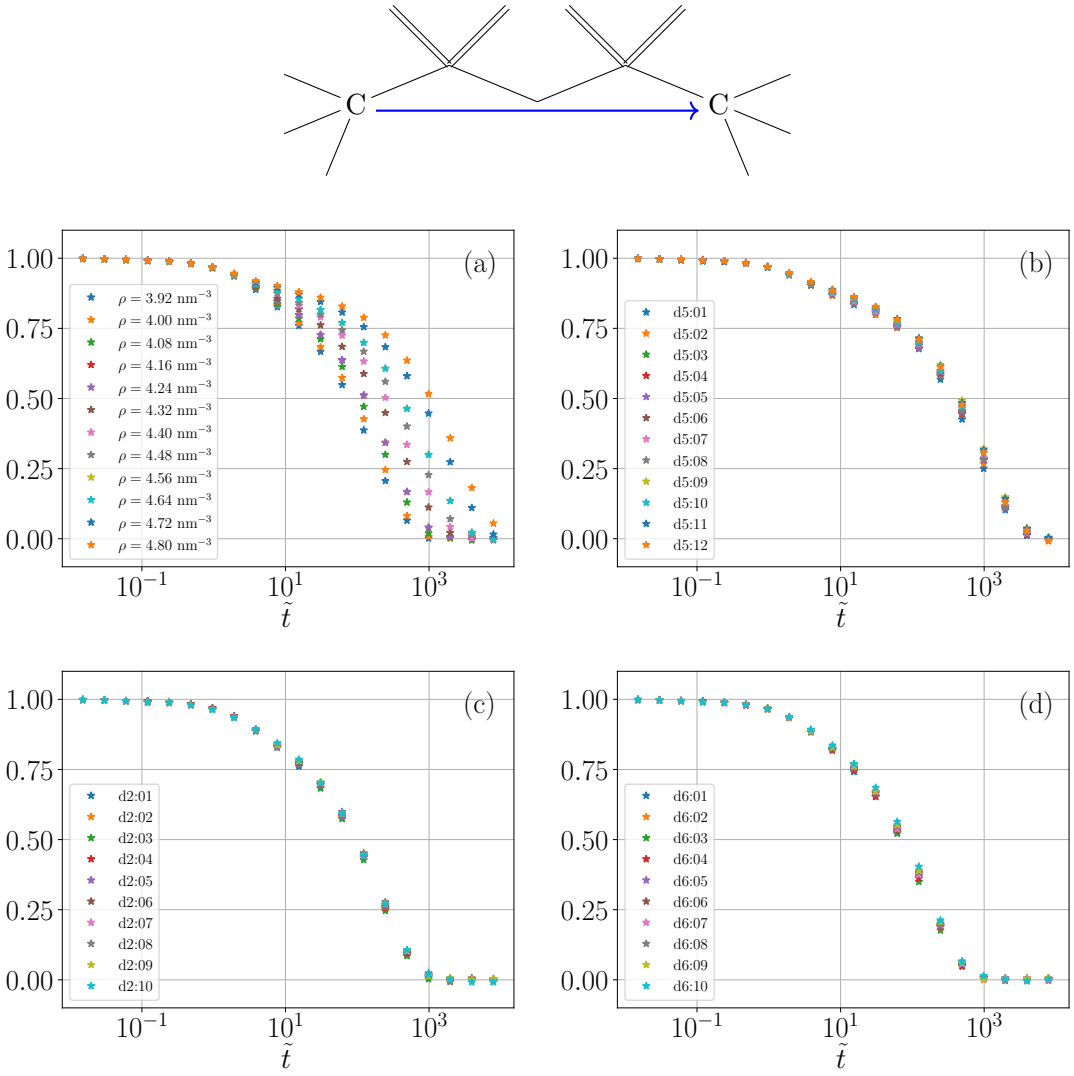

Figure 6.35: Autocorrelation function of the vector between the two C atoms. (a) Isotherm 325 °C, (b) isodyne 5, (c) isodyne 2 and (d) isodyne 6. A list of isodyne labels can be found in Tab. 6.4.

To analyse a different axis of rotation we define the normal-vector to the plane spanned by N^- and the two S atoms. The autocorrelation functions are shown in Fig. 6.36. This is our first example of a rotation that changes for both the isotherm and all the isodynes. This tells us that this rotational axis is not important for dynamical properties such as the diffusion coefficient.

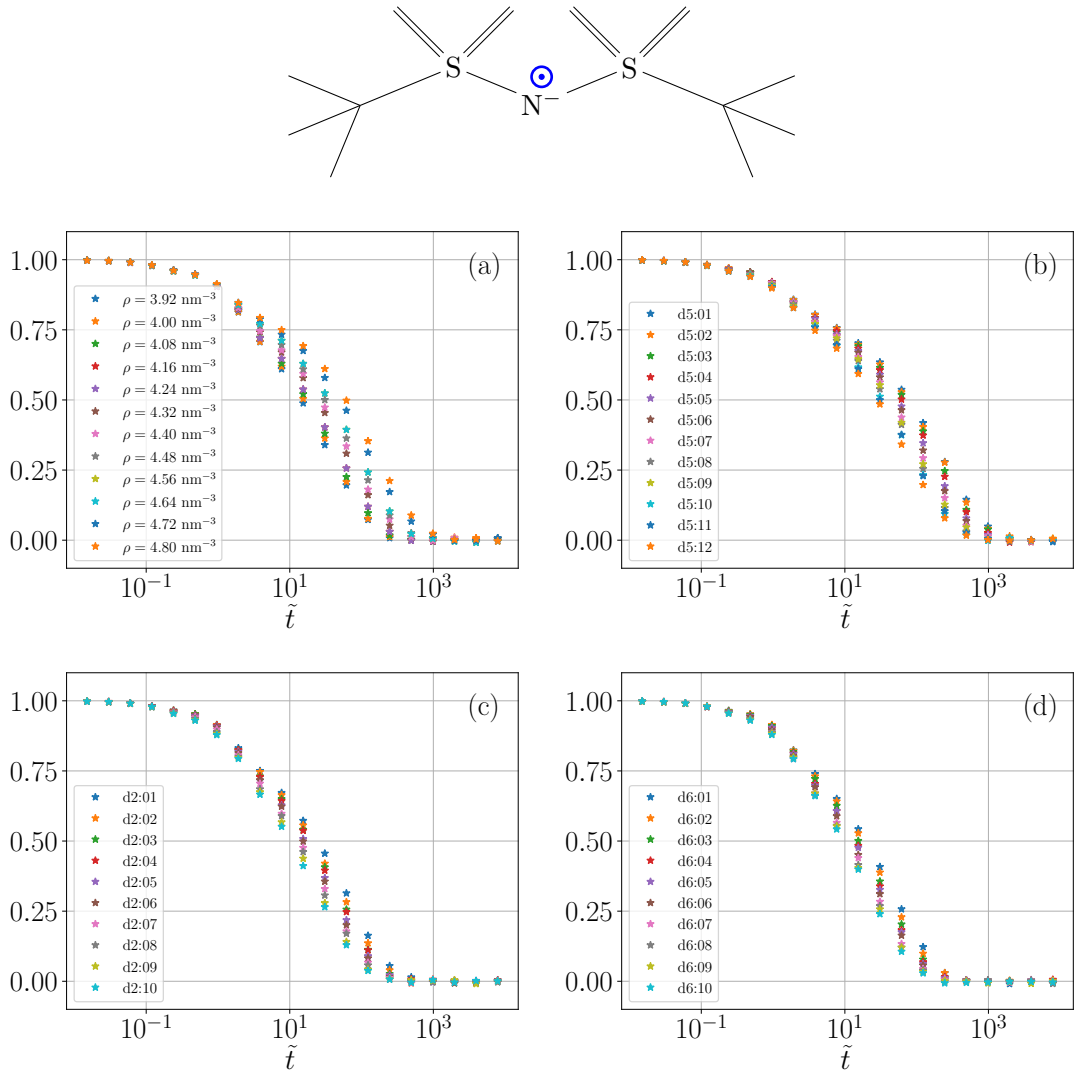

Figure 6.36: Autocorrelation function of the normal-vector to the plane spanned by N^- and the two S atoms. (a) Isotherm 325 °C, (b) isodyne 5, (c) isodyne 2 and (d) isodyne 6. A list of isodyne labels can be found in Tab. 6.4.

To confirm this, we analysed the normalised vector from N^- at the point between the two S atoms, see Fig. 6.37. Again, there is a clear change along both the isotherm and isodyne. As before, this tells us that this axis of rotation is not important for dynamical properties such as the diffusion coefficient.

From this analysis we see that the rotations which show invariance are along the directions of high moment of inertia. This also makes intuitive sense.

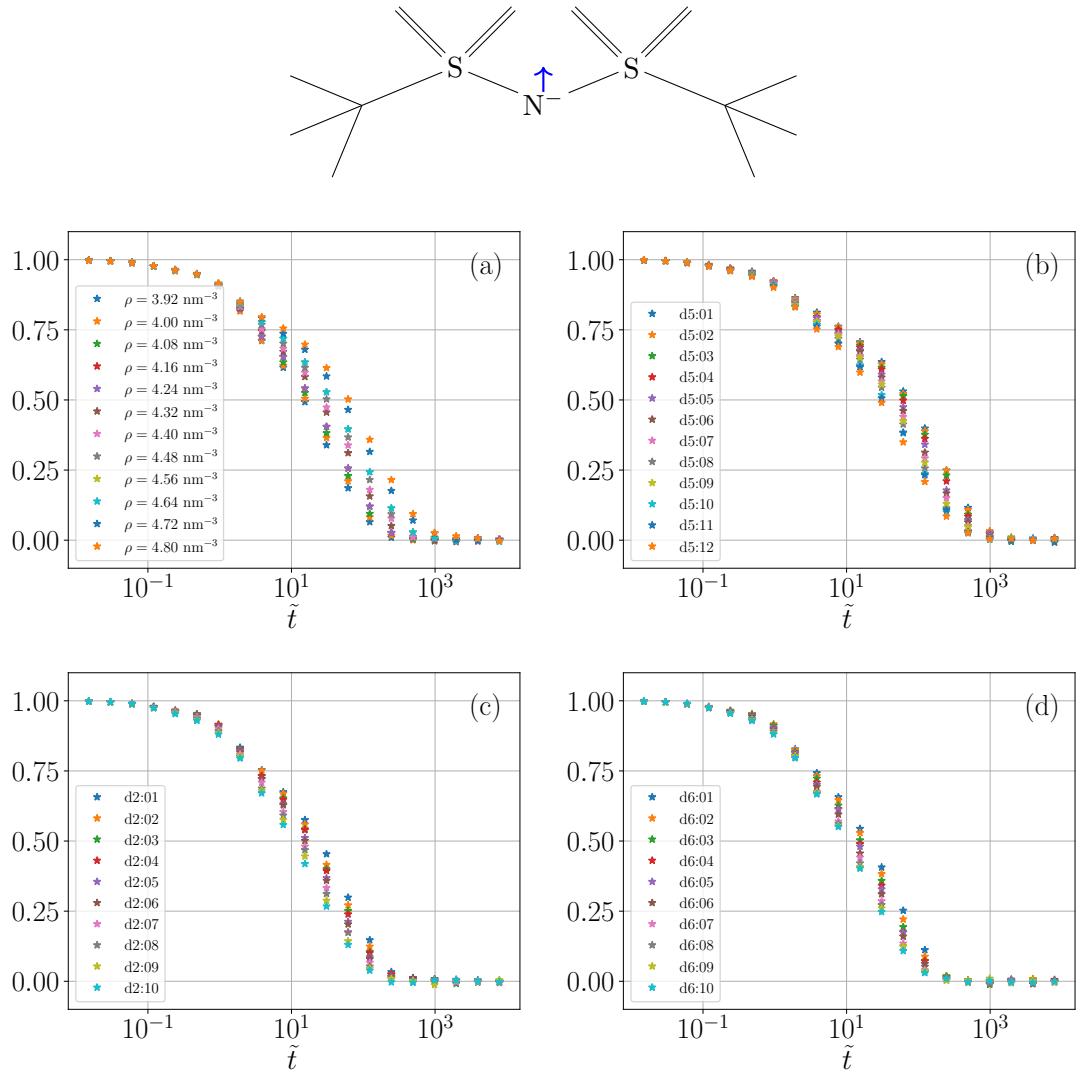

Figure 6.37: Autocorrelation function of the vector from N^- at the point between the two S atoms. (a) Isotherm 325 °C, (b) isodyne 5, (c) isodyne 2 and (d) isodyne 6. A list of isodyne labels can be found in Tab. 6.4.

C-S-S-C dihedral rotation in the anion

So far we have analysed the rotation of the molecules. However, inspired by the findings in Philippi et al. [2020], we also analysed the dihedral angle between C-S-S-C (see Fig. 6.38). This does not have a dihedral potential in the model, but we can still analyse it. It should be noted that in contrast to the other rotations we have studied this is an intra-molecular angle. This means that there might be a preferred angle so the autocorrelation function does not approach zero. We calculated the autocorrelation function for the difference in the angle i.e. $\cos(\theta(t) - \theta(0))$

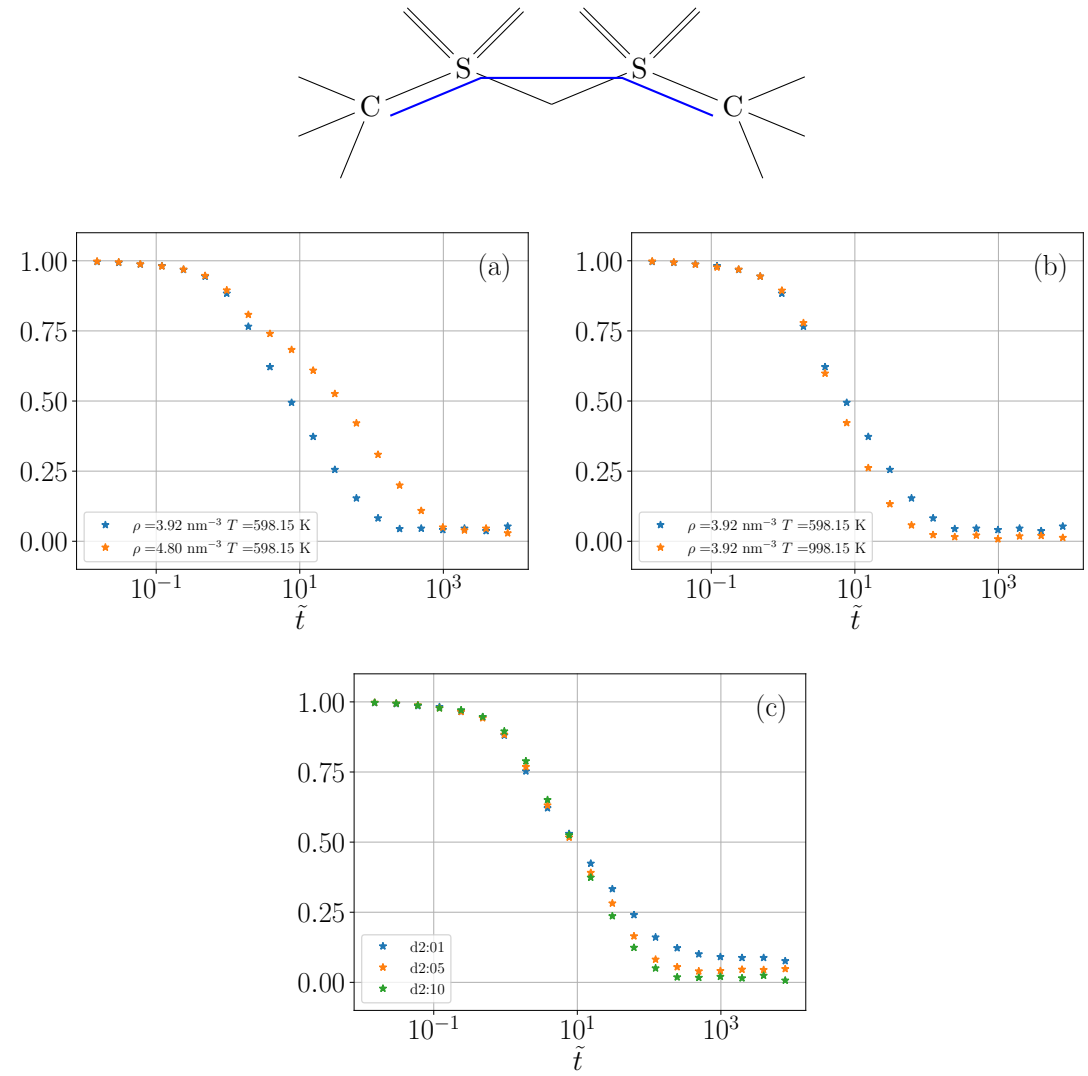

Figure 6.38: Autocorrelation function of the C-S-S-C dihedral angle. (a) Isotherm 325 °C, (b) isochore 3.92 nm^{-3}, (c) isodyne 2.

6.5 Results: Structure

6.5.1 The structure factor along isodynes

We would like to calculate the total structure factor along isodynes and comapre the peaks with the experimental data from Hansen et al. [2020]. The experimental structure data was obtained with X-ray scattering, which scatters from the electrons in the sample. To represent this we choose to scale our partial structure factors with the number of electrons minus the partial charge from Tab. 6.2. This corresponds to using the X-ray form factors with $\boldsymbol{q} = 0$. The X-ray form factors are defined as [Mc Kie and Mc Kie, 1986]

$$f(\boldsymbol{q}) = \int \rho_c(\boldsymbol{r}) e^{i\boldsymbol{q}\cdot\boldsymbol{r}} \mathrm{d}^3\boldsymbol{r}, \tag{6.8}$$

where $\rho_c(\boldsymbol{r})$ is the electron charge density. An example of the total structure factor where the q dependent form factors were used can be found in Mackoy et al. [2019]. The shape of their data is similar to ours. The total structure factors along isodyne 5 and 7 can be seen in Fig. 6.39 in both SI and isomorph scaled units.

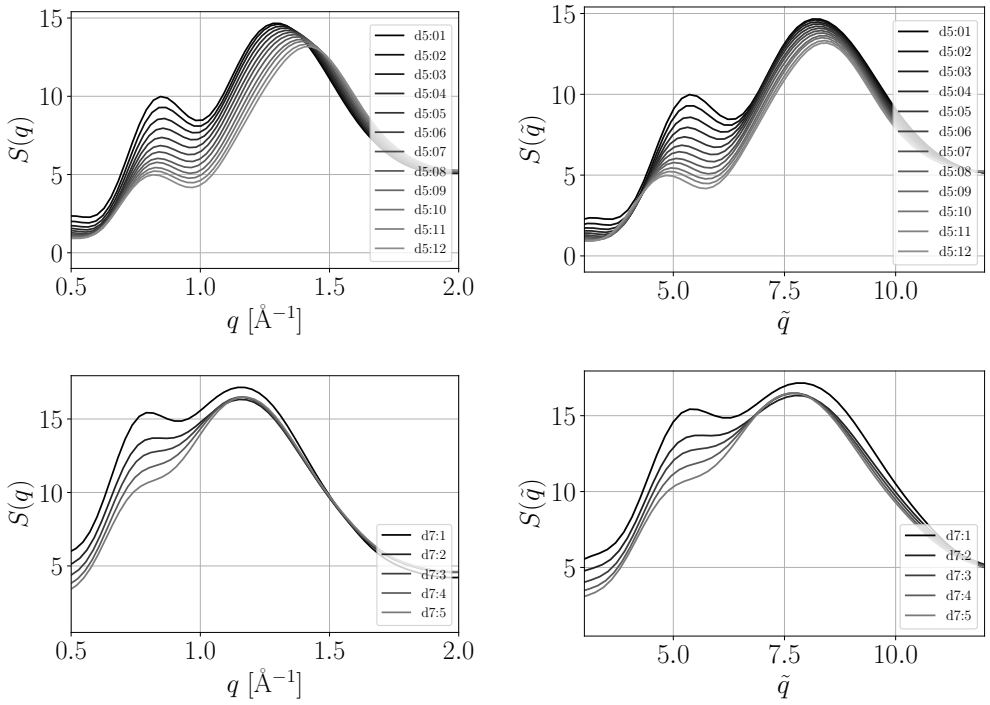

Figure 6.39: Total structure factor along isodynes in SI and scaled units. (Top) $S(q)$ along isodyne 5 and (Bottom) $S(q)$ along isodyne 7. A list of isodyne labels can be found in Tab. 6.4.

The data have both the charge peak (≈ 5 Å) and the main peak (≈ 8 Å) However, the charge peak becomes less pronounced and in some cases gets reduced to a shoulder as density increases. The height of the charge peak decreases with increasing density for all the isodynes. In SI units, the position does not change much but moves to lower q-values. This effect is even more pronounced when using isomorph scaled units. The behaviour of the position and height of the charge peak is the same as in the experimental observations from Hansen et al. [2020].

The height of the main peak is not invariant, but it changes less than the charge peak. Furthermore, the position of the main peak does not change much in isomorph scaled units. The main peak in the experimental data from Hansen et al. [2020] was invariant in isomorph sclaed units. However, the density change in the experimental data is 2%, where isodyne 6 covers a 20% density change. When presenting the data from isodyne 5 in a similar density range, the main peak is invariant, see Fig. 6.40. The axis for the simulated and experimental data are different, however, the shape and changes of the curves are similar.

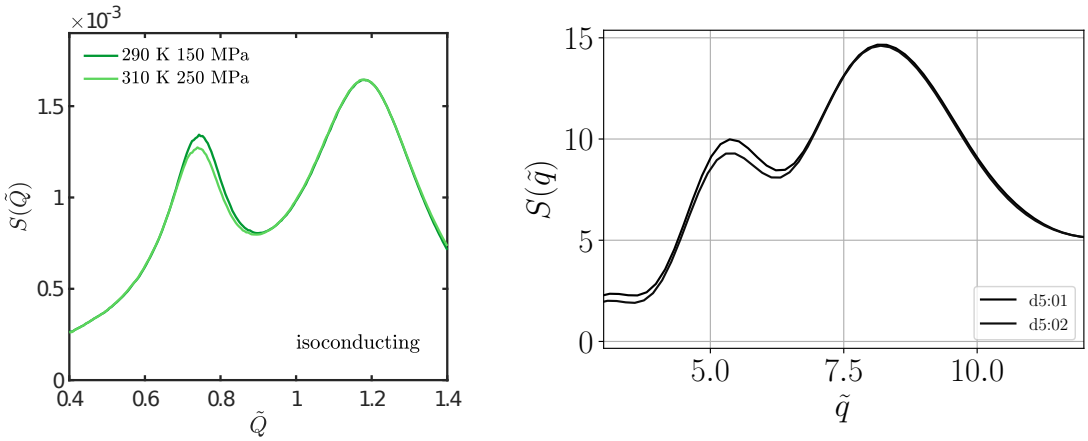

Figure 6.40: Comparison of the total structure factor between experiments and simulations. The data is in a similar density range (≈ 2%) and is presented in isomorph scaled units. (Left) Figure 5b from Hansen et al. [2020]. (Right) The first two points along isodyne 5.

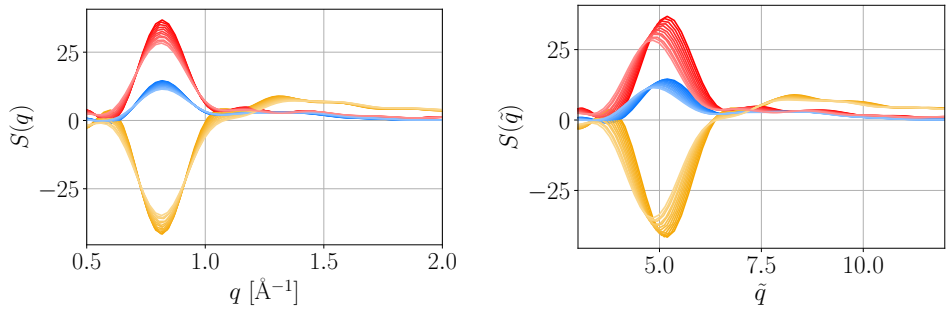

Figure 6.41: The partial structure factors between molecules. Here is shown cation-cation (blue), cation-anion (orange), and anion-anion (red) along isodyne 5. (Left) Real units, (Right) isomorph scaled units.

To better understand the behaviour of the total structure factor we calculated the partial structure factors between the two molecules (again weighted by the X-ray form-factors). These can be seen along isodyne 5 in both IS and isomorph scaled units in Fig. 6.41. The first thing we find striking is how high the charge peaks are when compared with the other features in this structures data, including those which make up the main peak. It is also clear that the position of the charge peak does not change much in real units, but changes noticeably in scaled units.

We would like to know if N^+ and N^- are representable of the structure factor. To do this we compare these structure factors between molecules (Fig. 6.41) with the structure factors between N^+ and N^- to see if they behave the same, see Fig. 6.42. The main noticeable difference is that the structure features which make up the main peak are more pronounced here than in the structure factors between molecules.

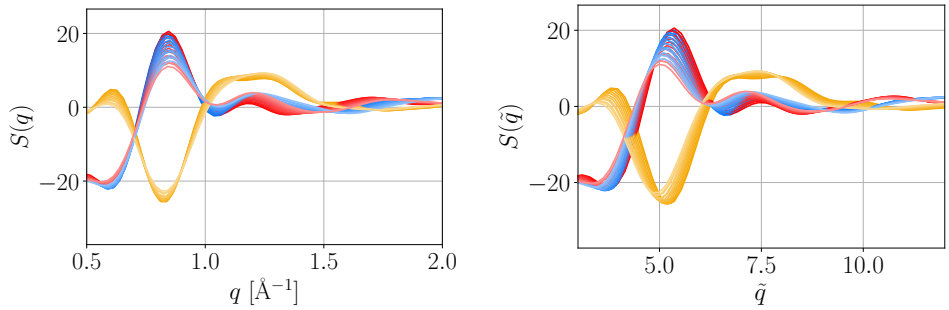

Figure 6.42: The partial structure factors for N^+N^+ (blue), N^+N^- (orange), and N^-N^- (red) along isodyne 5. (Left) Real units, (Right) isomorph scaled units.

6.5.2 The radial distribution function along isodynes

We found that the total structure factor changes along isodynes in a similar way to the experimental data from Hansen et al. [2020]. This is for small density intervals the main peak is invariant and the charge peak decreases in intensity and position as temperature increases. We could try to interpret this using the general interpretation of these peaks, i.e. the main peak describe neighbouring molecule distances and the charge peak describe distances between molecules with the same charge (in this case same type). Based on this we would expect the distance between molecules to be invariant (or change little depending on the density interval), while the distances between molecules of the same type must increase. This would create different angles between triplets of ions and consequently the molecular packing would change, this is illustrated in Fig. 6.43.

This interpretation of these peaks and this resulting hypothesis is very simplifying due to the complexity of liquid structures. However, this hypothesis can still be tested by analysing the partial radial distribution function between N^+N^+, and N^-N^-, and N^+N^-. This was done for isodynes 5, 6 and 7, however, we only show results from isodynes 5 and 7 due to the similarities between isodyne 5 and 6. Furthermore, isodyne 7 did not have a strong charge peak, so comparing isodyne 5 and 7 might inform which features cause the charge peak.

We start by testing if the distance between neighbouring molecule is approximately invariant. To do this we analyse the partial radial distribution function between N^+N^- which can be seen in Fig. 6.44 along isodyne 5 and 7. There are still clear changes along both isodynes, but these are small and becomes insignificant at smaller density interval.

Along isodyne 5 there is a shoulder/peak $\tilde{r} \approx 0.7$ which disappears as density increases, and is not present along isodyne 7. This shoulder/peak will be investigated later in Sec. 6.5.3.

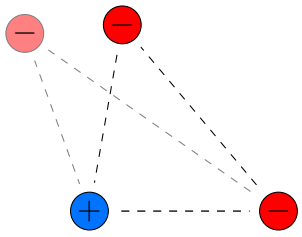

Figure 6.43: Illustration of two ion triplet configurations. The distance between neighbouring molecules is invariant. If the distance between the two anions (red) increases there must be a difference in the triplet angle and consequently the molecular packing.

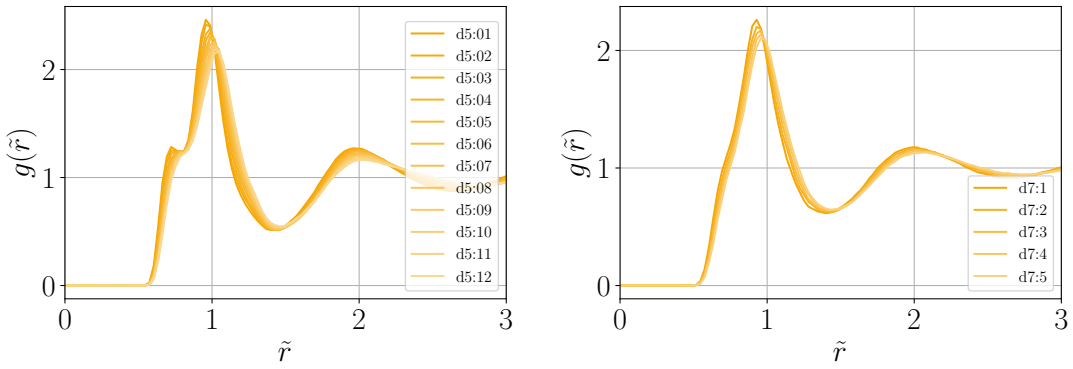

Figure 6.44: The partial radial distribution function between N^+N^- along (Left) isodyne 5 and (Right) isodyne 7.

Next we analyse the partial radial distribution function between N^+N^+ along isodyne 5 and 7. They can be seen in Fig. 6.45. There are clear changes along both isodynes, however, no new features are introduced along either. Isodyne 5 has two peaks around $\tilde{r} = 1.5$ which is only a single peak along isodyne 7. This could be because isodyne 7 is at both lower densities and higher temperatures than isodyne 5. Along both isodynes the intensity of the peaks decreases as density increases, and longer distances becomes more common since the minimum at $\tilde{r} \approx 2$ becomes slightly higher. This shift in preference towards longer distances might be an important feature for the behaviour of the charge peak. This could be related to why the charge peak gets shifted to lower q, and why its intensity decreases.

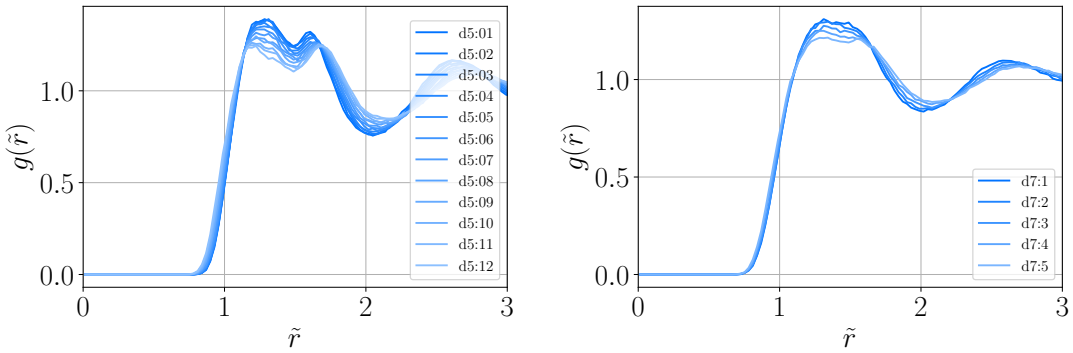

Figure 6.45: The partial radial distribution function between N^+N^+ along (Left) isodyne 5 and (Right) isodyne 7.

Lastly we analyse the partial radial distribution function between N^-N^- along isodyne 5 and 7. They can be seen in Fig. 6.46. Again we see clear changes in the structure along both isodynes. However, along isodyne 5 a shoulder is formed at longer distances which turns into an extra peak at high densities and temperatures. This means that longer distances between N^-N^- become more common along isodyne 5. This is significant since it is in agreement with, and might be an important feature for, the behaviour of the charge peak in the structure factor which moves to smaller q as density increases.

From this we find that along isodynes the distances between unlike molecules does not change much (comparable to the main peak in the structure factor). Additionally the distributions for distances between like molecules generally becomes broader and prefers longer distances as density and temperature increases.

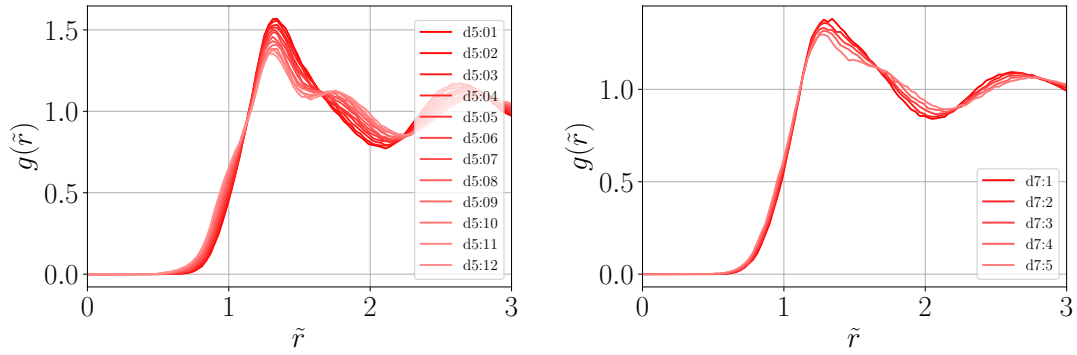

Figure 6.46: The partial radial distribution function between N^-N^- along (Left) isodyne 5 and (Right) isodyne 7.

6.5.3 The radial distribution function N^+N^- shoulder/peak

When analysing the partial radial distribution function between N^+N^- along isodynes we found an shoulder/peak which disappears as density and temperature increases, see Fig. 6.44. To better understand the density and temperature dependence of this shoulder/peak we analyse the partial radial distribution function at four boundary state points, see Fig. 6.47. Here we find that this shoulder/peak is mainly temperature dependent, but is also more pronounced at high density. Based on this we looked at all the partial radial distribution function between N^- and all particle types in the cation at $\rho = 4.8$ nm^{-3} and $T = 373.15$ K, see Fig. 6.47. All these radial distribution functions have a similar shape to the N^+N^- partial radial distribution function, but they are shifted to smaller distances.

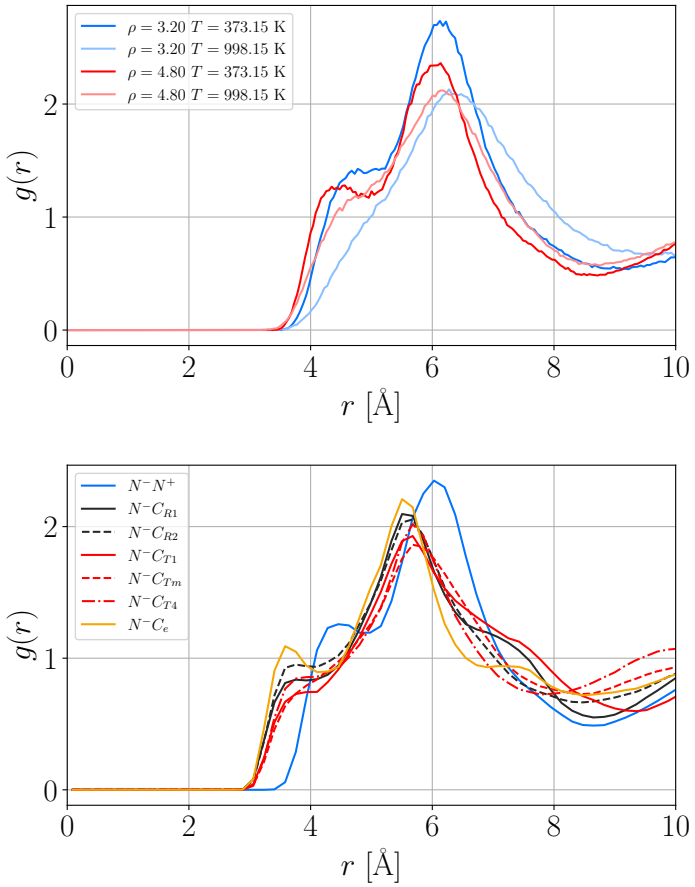

Figure 6.47: (Top) The partial RDF between N^+N^- at four state points at the boundary of the simulated region. (Bottom) The partial RDF between N^- and all cation types at $\rho = 4.8$ nm^{-3} and $T = 373.15$ K.

We also analysed the partial RDF between N^+ and all particle types in the anion, see Fig. 6.48. Here we see that the distance between N^+ and S is generally greater than the distance between N^+ and N^- for the shoulder/peak, but smaller than the main peak. This means that for the relative orientations between these ions S is pointed away from N^+ for the shoulder/peak structure.

We would like to find if this N^+N^- shoulder/peak is a local substructure or evenly distributed throughout the configurations. However, before doing this we need to define what we are looking for. Based on the position of the N^+N^- shoulder/peak in Fig. 6.47 we choose to investigate molecule pairs where the distance between N^+N^- is less than 4.5 Å. Thus when analysing particle configurations we only show molecule pairs which satisfy this condition. An example of such a molecule pair can be seen in Fig. 6.48. Here the yellow S atoms are pointing away from the cation as we saw in the RDF.

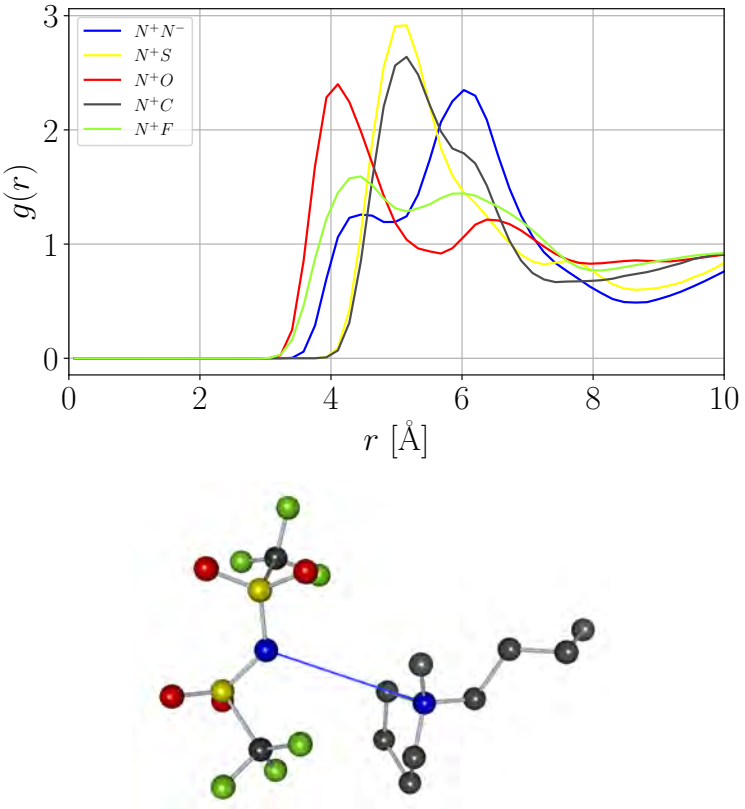

Figure 6.48: (Top) The partial RDF between N^+ and all types in the anion at $\rho = 4.8$ nm^{-3} and $T = 373.15$ K. (Bottom) Example of a molecule pair where the distance between N^+ and N^- is less than 4.5 Å. The blue line is drawn between N^+ and N^-.

Distribution of the substructure in the liquid

To find if this is a local substructure or evenly distributed throughout the configuration we analysed different particle configurations. Examples at four different state points can be seen in Fig. 6.49. Here we see that the molecule pairs are spread out through the configuration.

(a) $\rho = 3.84$ nm^{-3} and $T = 998.15$ K

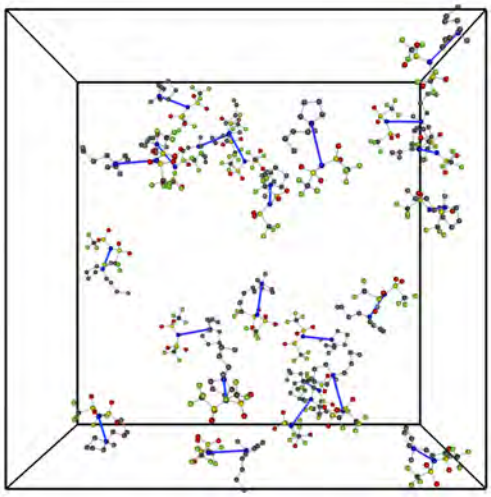

(b) $\rho = 4.16$ nm^{-3} and $T = 998.15$ K

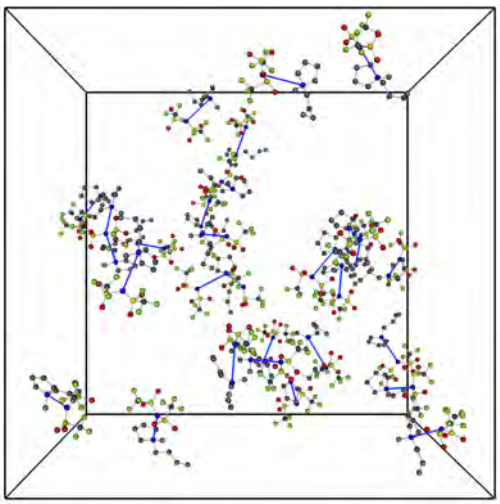

(c) $\rho = 3.84$ nm^{-3} and $T = 283.15$ K

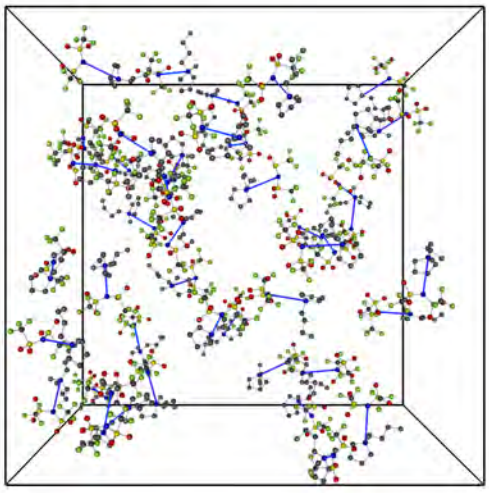

(d) $\rho = 4.16$ nm^{-3} and $T = 283.15$ K

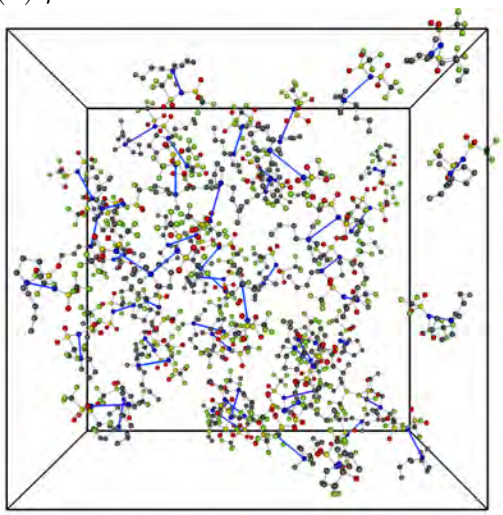

Figure 6.49: Example of molecule configurations. Only ion-pairs where the distance between N^+ and N^- is less than 4.5 Å are shown. The blue lines indicate close pairs.

To confirm this, we make a more qualitative analysis of the distributions that the one in Fig. 6.49. For this we calculate the partial radial distribution functions between N^+N^+ and N^-N^-, however, we only use the atoms which is a part of a close pair. This means that if the shoulder/peal substructure is evenly distributed throughout the liquid we will simply obtain the normal partial radial distribution functions which we have already seen (but with worse statistics). Alternatively, of the substructure cluster together at specific distances these new partial radial distribution functions should deviate significantly from the normal partial radial distribution functions to reflect this.

The resulting distributions can be seen in Fig. 6.50. We see that N^- has a small preference at small distances (we will get back to this), but despite this and worse statistics the distributions follow each other meaning that the substructure does not cluster together at specific distances.

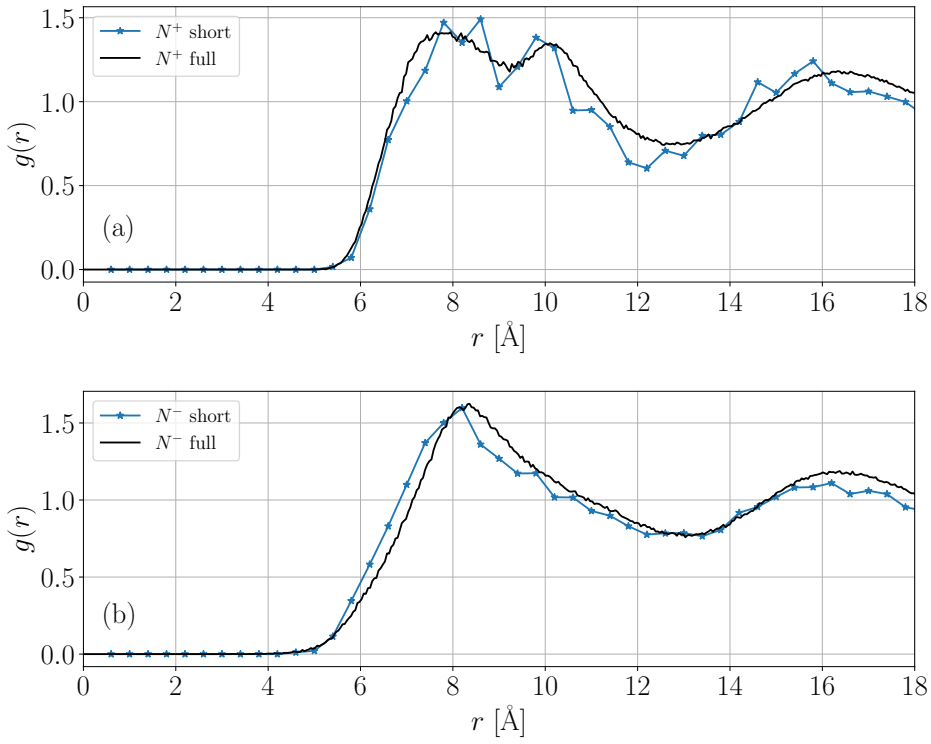

Figure 6.50: Analysis of the distribution of the shoulder/peak substructure at $\rho = 4.16$ nm^{-3} and $T = 283.15$ K. Partial radial distribution functions between N^+N^+ and N^-N^-, however, only atoms which is a part of a close pair are used. These curves are normalised by hand. The full partial radial distribution functions are also shown for comparison. (a) Partial RDF between N^+N^+. (b) Partial RDF between N^-N^-.

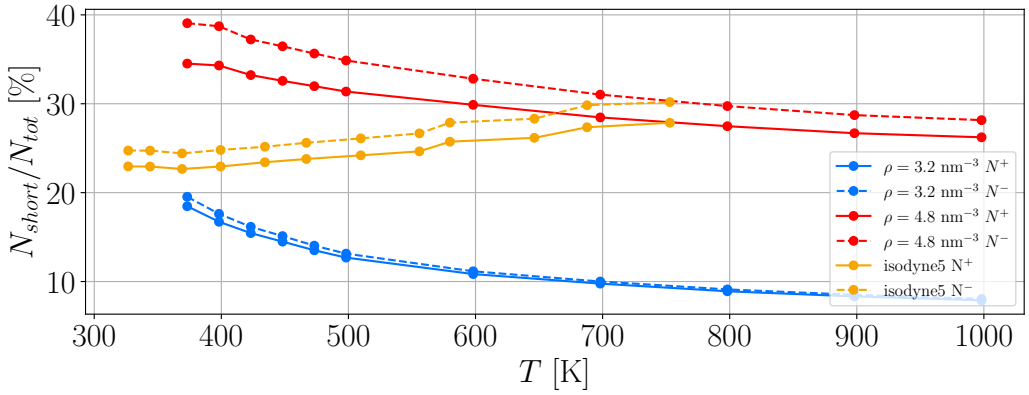

Figure 6.51: Analysis of the number of close pairs along isochores $\rho = 3.2$ nm^{-3} (blue) and $\rho = 4.8$ nm^{-3} (red) and isodyne 5 (orange). Here is shown the percent of cations (N$^+$, full line) and anions (N$^-$, dashed line) in a close pair as a function of temperature.

Inspired by the configurations in Fig. 6.49 we analyse how many molecules is a part of this short distance structure. This is done for isodyne 5 and the boundary isochores $\rho = 3.2$ nm^{-3} and $\rho = 4.8$ nm^{-3}, see Fig. 6.51. We confirm that the short distances are more present at high densities and low temperatures which also makes sense. Furthermore, the number of close neighbours decrease with increasing temperature which is in agreement with the configurations we saw in Fig. 6.49. The number of close neighbours increases along the isodyne. This could be because we define close neighbours using the real distance 4.5 Å instead of a reduced distance. Lastly, we notice that the number of anions in close pairs are greater than the number of cations in close pairs. Consequently, some cations must be a part of multiple close pairs. This could explain why the N$^-$ distribution from Fig. 6.50 has a small preference at short distances.

Based on this we analyse the number of close pair for each molecule, see Fig. 6.52. We find that the majority of molecules only is a part of a single close pairs. Furthermore, the number of molecules which is a pair of more than one close pair decreases as temperature increases. We also see that anions are only a part of one close pair, while cations can be a pair of multiple pairs (but most is only a part of one). At high densities there are more cations in multiple close pairs than at low densities. It is also only at high density that we see cations being a part of three or four pairs. However, this happens very rarely and thus the statistics on these curves are not as great.

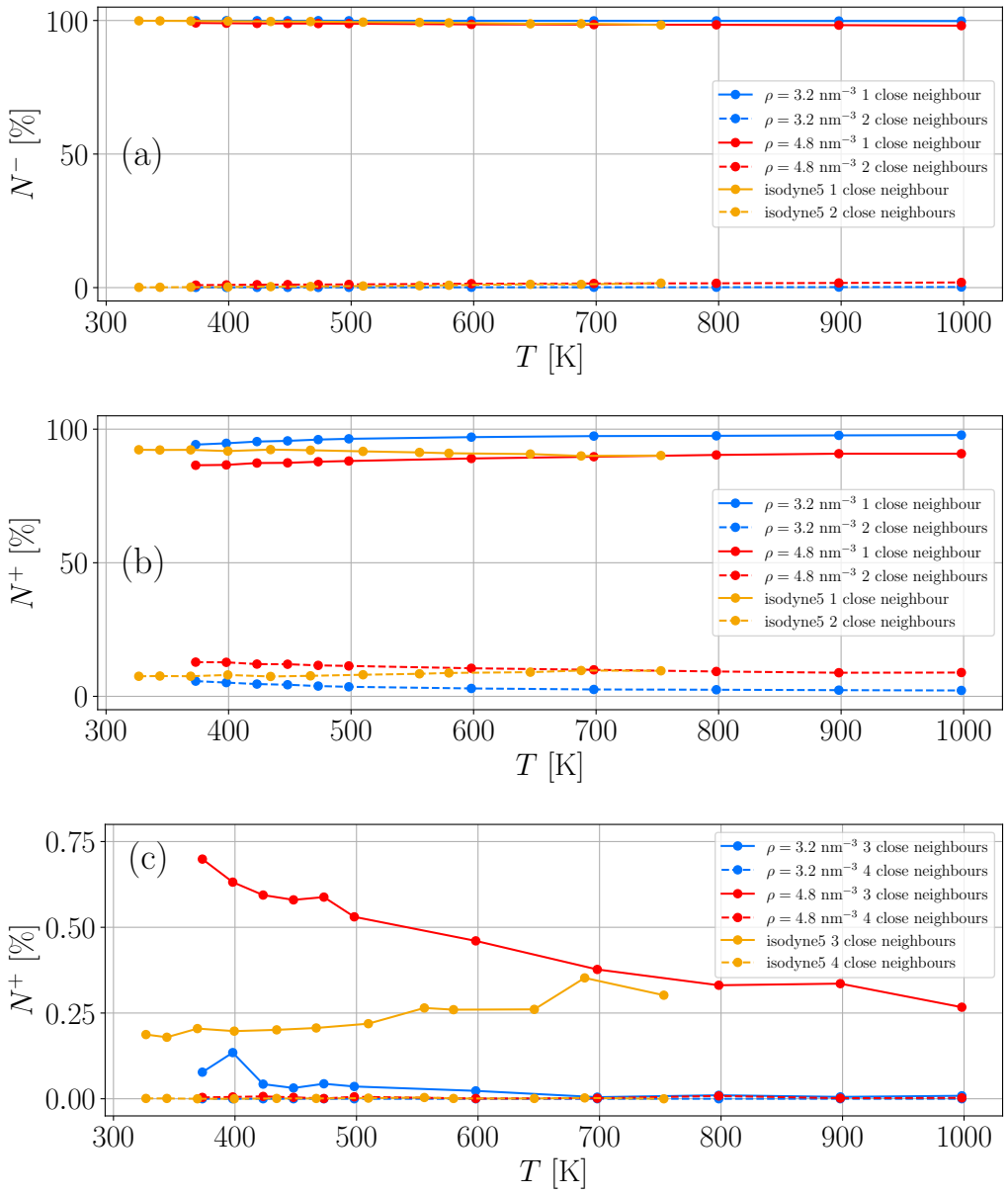

Figure 6.52: Analysis of the number of close pairs along isochores $\rho = 3.2$ nm^{-3} (blue) and $\rho = 4.8$ nm^{-3} (red) and isodyne 5 (orange). Here we only consider the cations and anions which is a part of a close pair (the distance between N^+ and N^- is less than 4.5 Å).
(a) The percent of anions (N^-) with 1 and 2 close neighbours.
(b) The percent of cations (N^+) with 1 and 2 close neighbours.
(c) The percent of cations (N^+) with 3 and 4 close neighbours.

Radial distribution function between the individual close molecules

In an attempt to further understand the local structure we define three length-scales;

- Short distances covering the shoulder/peak, between 0 and 4.5 Å.
- Middle distances covering the main peak, between 4.5 and 9 Å.
- Long distances covering the rest, greater than 9 Å.

Then we computed the distance between all pairs of N^+ and N^- and thus separated the corresponding ion-pairs into these three categories. Note than this only restricts the distance of N^+ and N^- within the ion-pair, while the other particles within the ion could be in other categories. This allows us to compute the partial $g(r)$ between all ion-pairs within each category. As a consequence of this construction the sum of the partial $g(r)$ from each category will result in the conventional partial $g(r)$ which has been used previously. The partial $g(r)$ at these three length-scales was calculated between N^- and the particles in the cation, and N^+ and the particles in the anion.

Fig. 6.53 shows $g(r)$ for N^- with C_{R1}, C_{T1}, and C_e. In Pyr_{14} the N^+ and the closest bonded particles form a tetrahedron structure. All the short distances distributions (blue curves) have the same shape, eg. a main peak around 3.7 Å and a smaller peak around 5.7 Å. This tells us that N^- prefers to be close to the centre of faces in the tetrahedron and not its edges. By comparing short (blue) and middle (orange) distances with the total (black) we see than the middle distances are responsible for the main peak in the total, and the short distances are responsible for the shoulder/peak. Based on this we believe that this tetrahedron structure is very important for this substructure.

Fig. 6.54 shows $g(r)$ with C_{R2}, C_{Tm}, and C_{T4}. At short distances for N^-C_{R2} there is a peak around 3.7 Å (like in the tetrahedron), but there is a shoulder instead of a second peak. The peak arises from the instances where N^- are close to the faces of the tetrahedron structure. However, the distances are not as well defined when N^- is close to the faces further away from the ring which creates the shoulder. On the other hand the $g(r)$ for N^-C_{Tm} and N^-C_{T4} have no significant features, and because of this we do not believe that they (the tail) is important for the formation of this substructure.

Fig. 6.55 shows $g(r)$ for N^+ with the anion. At short distances for N^+S there is only a single peak around 5 Å. Since there are two S in TFSI this could imply that there is a preferred orientation. Additionally we also see that all the short N^+S distances are within the main peak of the total and not its shoulder.

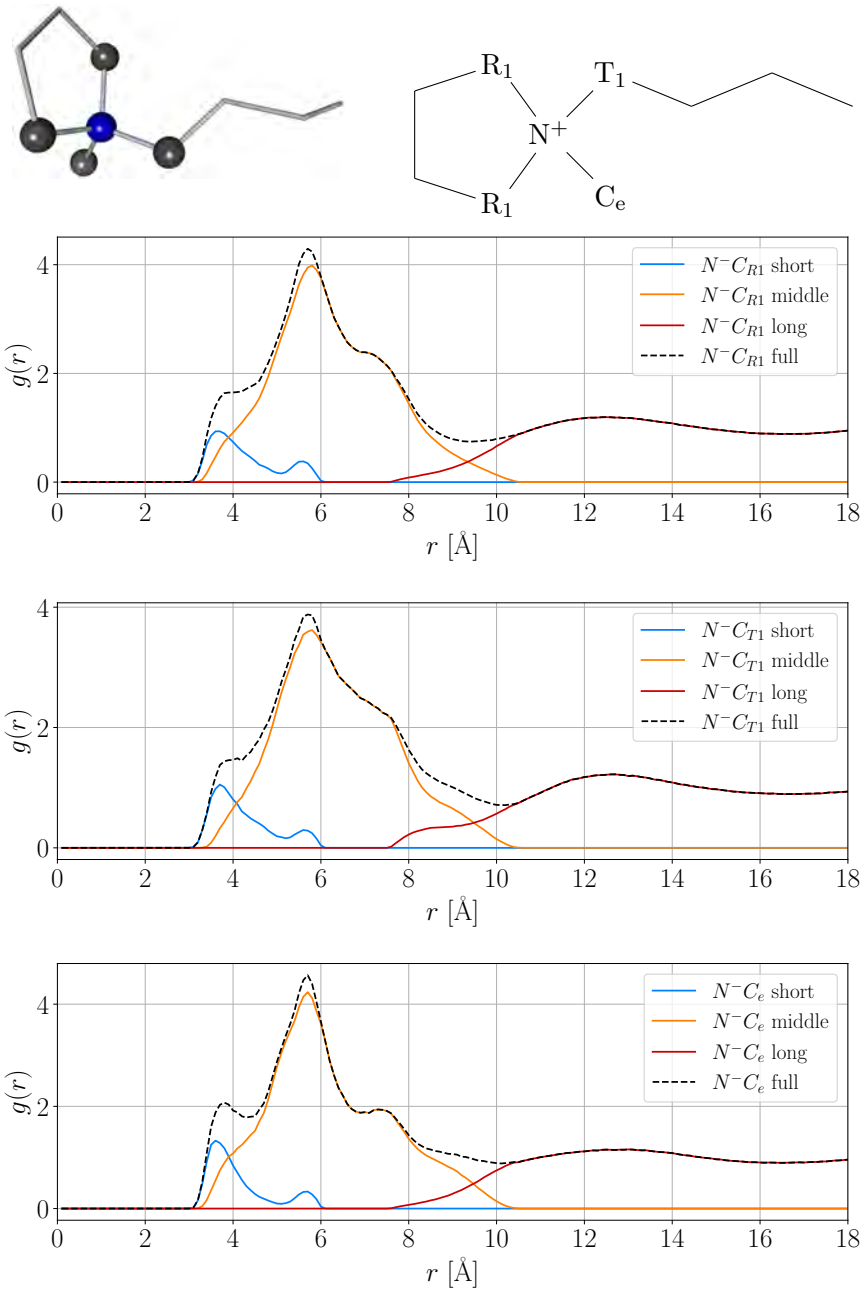

Figure 6.53: Radial distribution function for N^- with C_{R1}, C_{T1}, and C_e (the tetrahedron structure in Pyr_{14}) for different separations of N^+ and N^-. The data is from $\rho = 4.16$ nm^{-3} and $T = 283.15$ K (low temperature and high density where the structure most pronounced).

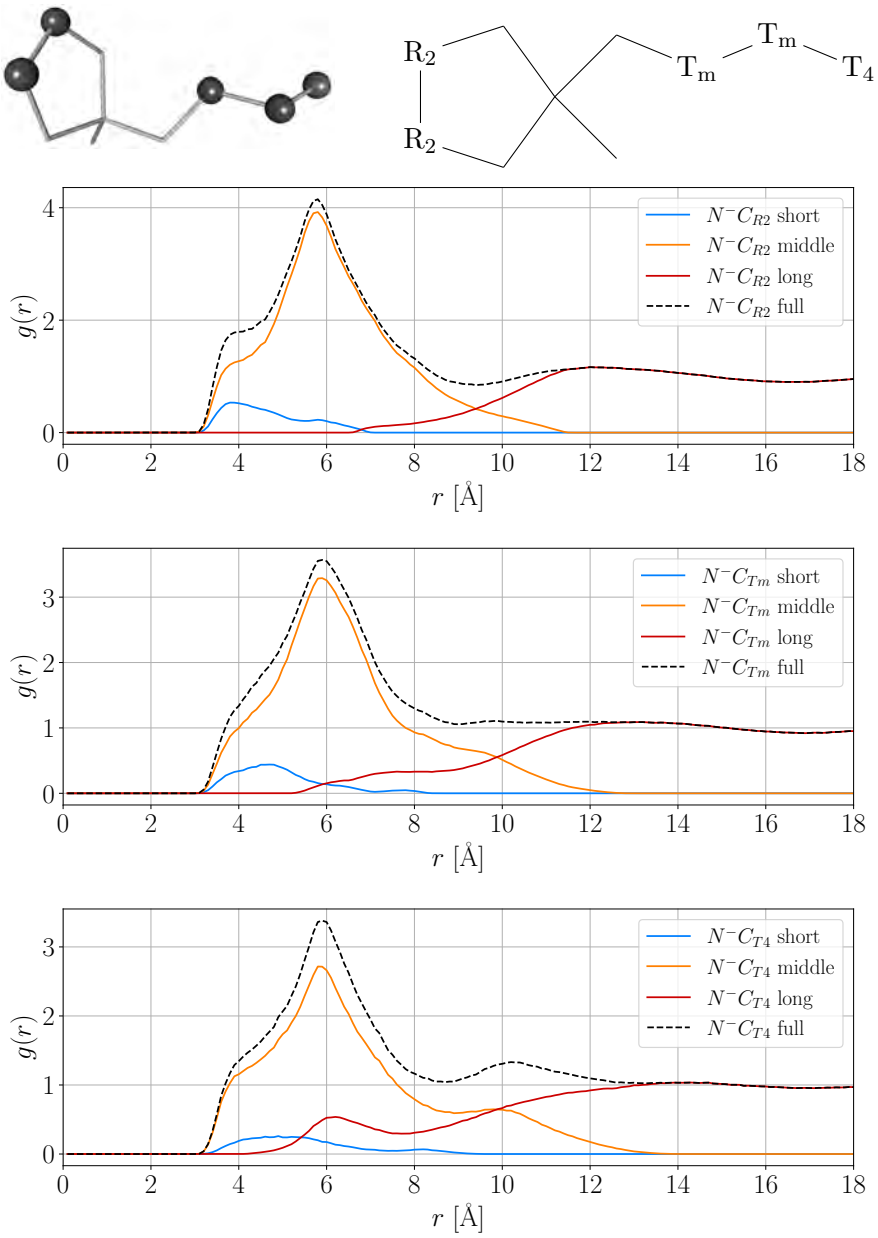

Figure 6.54: Radial distribution function for N^- with C_{R2}, C_{Tm}, and C_{T4} for different separations of N^+ and N^-. The data is from $\rho = 4.16$ nm^{-3} and $T = 283.15$ K (low temperature and high density where the structure most pronounced).

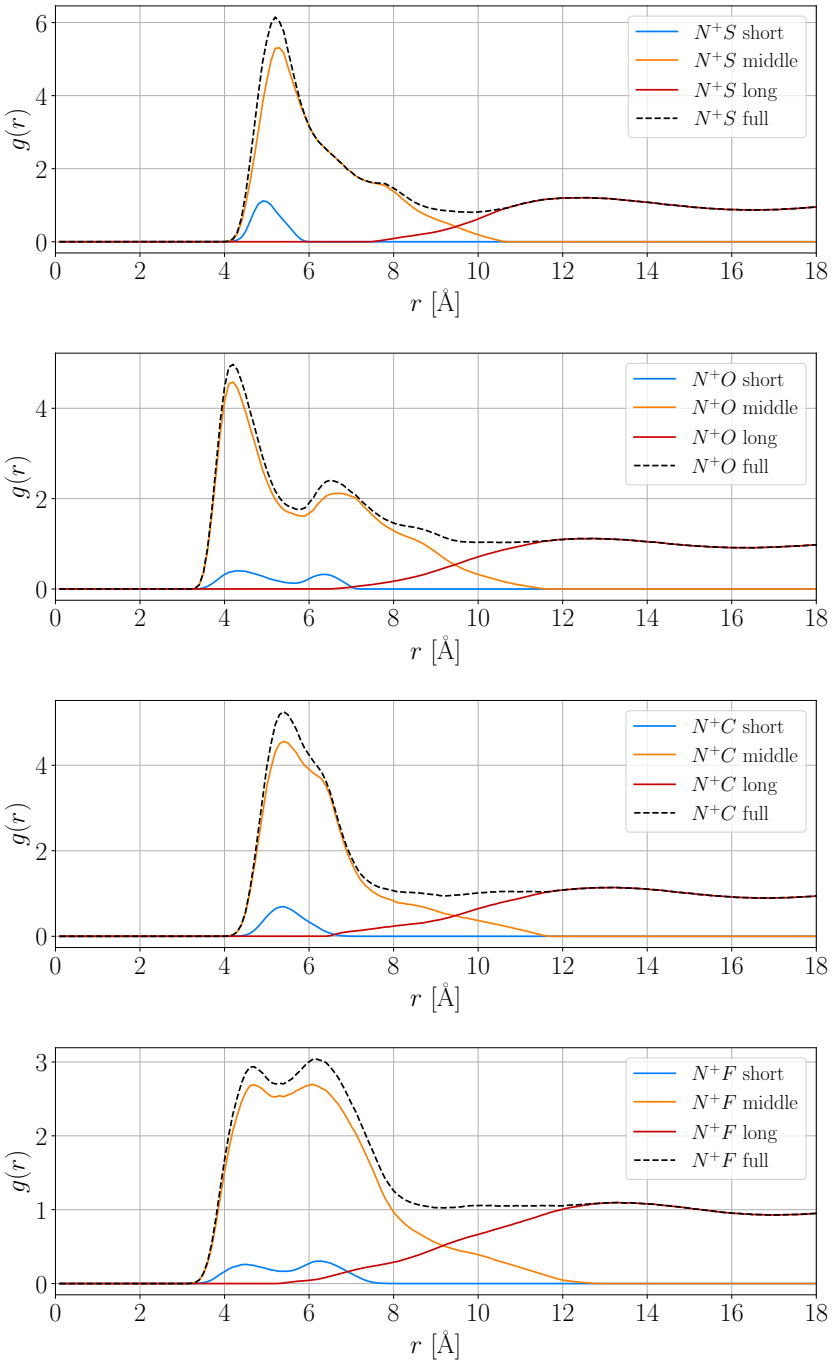

Figure 6.55: Radial distribution function for N^+ with TFSI for different separations of N^+ and N^-. The data is from $\rho = 4.16$ nm^{-3} and $T = 283.15$ K.

Orientation between ion pairs

Based on our precious analysis of the partial RDF (Fig. 6.48, Fig. 6.53 and Fig. 6.55), we believe there are preferred orientations between close ion pairs. As before we categorise the ion pairs based on the distance between N^+ and N^- in each ion; short distances (between 0 and 4.5 Å), middle distances (between 4.5 and 9 Å) and long distances (greater than 9 Å). To analyse the different orientations we define two vectors; the normalised vector between N^+ and N^- in each ion pair, and the normalised vector from N^- to the point between the two S atoms. The angle between these two vectors can be seen in Fig. 6.56 (the distributions are normalised such that the integral is 1).

Here we see a clear difference in the distance dependence of the ion orientations. At short distances the sulphur atoms in the anion prefer to point away from the cation (se we suspected from the previous RDFs). At middle distances the distribution is much broader with a small preference where the sulphur atoms in the anion are close to the cation. Lastly, there is no preferred orientations at long distances.

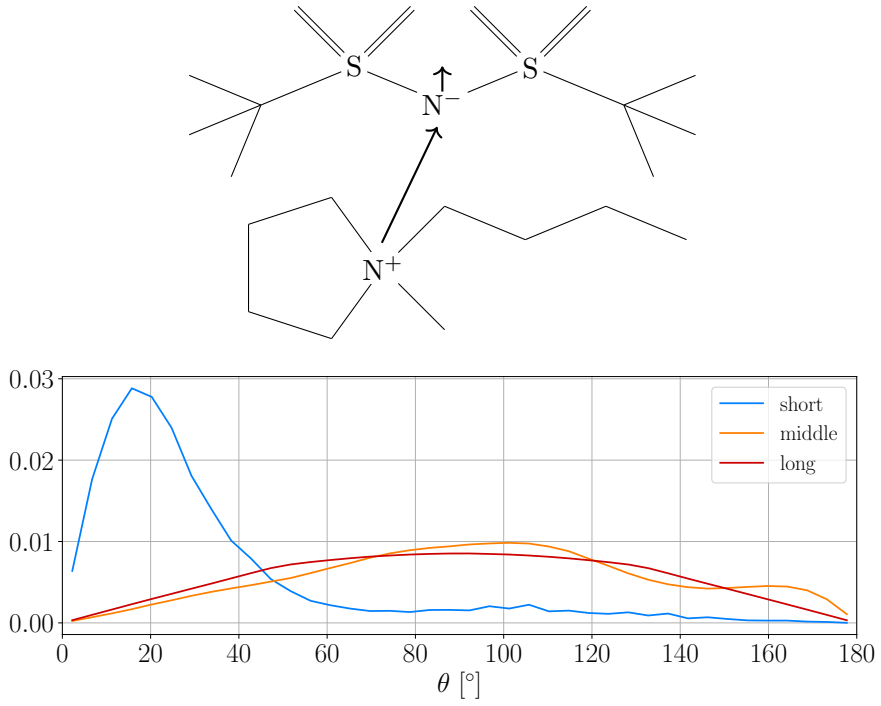

Figure 6.56: Preferred orientations between ion pairs at different distances. The data is from $\rho = 4.16$ nm^{-3} and $T = 283.15$ K (low temperature and high density where the structure most pronounced). The data is normalised so the integral is 1.

6.5.4 Number of nearest neighbour molecules

We would like to analyse the number of nearest neighbouring molecules. This is to test the charge ordering and compare with the simple atomic model from Chap. 5. To do this we analyse the partial radial distribution function between N^+ and N^- atoms. This approach was chosen over a molecular centre approach based on simplicity and the fact that these atoms are centred in the structure of each molecule. In this analysis we refer to the cation (represented by N^+) as type $+$, and the anion (represented by N^-) as type $-$. The number of nearest neighbour molecules (of type α) around a molecule (of type β) is calculated by

$$N_{\alpha\beta} = 4\pi c_\alpha \rho \int_0^R g_{\alpha\beta}(r) r^2 dr, \tag{6.9}$$

where c_α is the concentration of α, ρ is the density, and R is the integration limit, which often is chosen to be the first minimum in $g_{\alpha\beta}(r)$. By analysing partial RDFs in the boundary of the simulated region ($\rho = 3.2$ nm^{-3} and $\rho = 4.8$ nm^{-3}) we find that position of the first minimum in $g_{+-}(\tilde{r})$ changes, but not drastically, see Fig. 6.57. We choose a fixed integration limit $\tilde{R}_{++} = \tilde{R}_{--} = \tilde{R}_{+-} = 1.5$. The same limit was chosen to give more meaning to the neighbour concentrations.

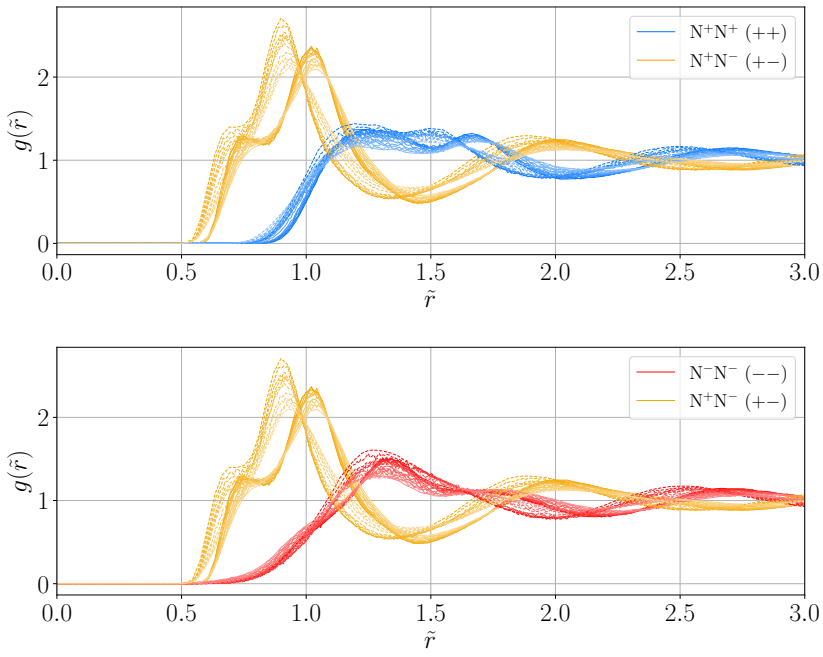

Figure 6.57: Examples of partial radial distribution functions for locating the first minimum. Data from isochore $\rho = 4.8$ nm^{-3} (full lines) and isochore $\rho = 3.2$ nm^{-3} (dashed lines) are shown.

We start by analysing the number of nearest neighbour molecules for the cations. We define the number of cation neighbours as N_{++}, the number of anion neighbours as N_{+-}, and the total number of neighbours $Z_+ = N_{++} + N_{+-}$. Lastly we define the concentration of cation neighbours around cations $f_{++} = N_{++}/Z_+$. These can be seen in Fig. 6.58 for selected isotherms and isodyne 5-7.

The number of unlike neighbours (N_{+-}) generally increases as a function of both density and temperature. This is in contrast to the number of like neighbours (N_{++}) which decreases as a function of both density and temperature. Consequently, the concentration of like neighbours also decreases as a function of both density and temperature.

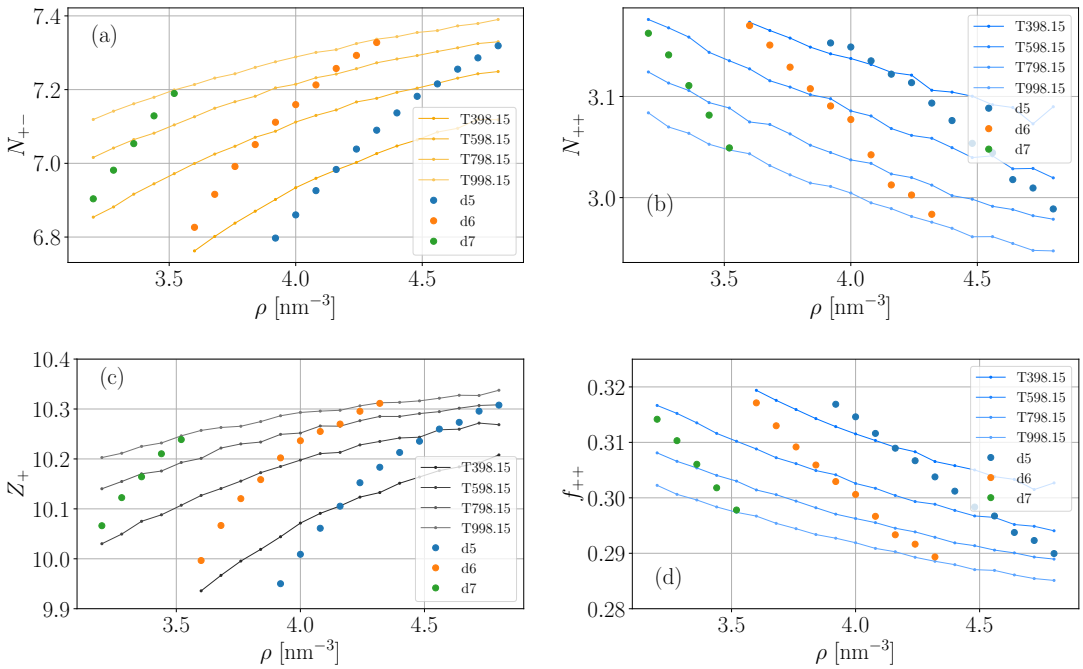

Figure 6.58: The number of nearest neighbouring molecules for cations as a function of density. Points with negative pressure are not shown.
(a) the number of anion neighbours around the cations N_{+-},
(b) the number of cation neighbours around the cations N_{++},
(c) the total number of neighbour molecules around cations Z_+, and
(d) the concentration of cation neighbours around cations f_{++}.

We also analyse the number of nearest neighbour molecules for the anion. We define the number of anion neighbours as N_{--}, the number of cation neighbours as N_{+-}, and the total number of neighbours $Z_- = N_{--} + N_{+-}$. Lastly we define the concentration of anion neighbours around anions $f_{--} = N_{--}/Z_-$. These can be seen in Fig. 6.59 for selected isotherms and isodyne 5-7.

All the conclusions from the analysis of the cation nearest neighbours also apply here for the anion nearest neighbours. We find it counter-intuitive that the number of nearest neighbour molecules increases as a function of temperature. Since this was not the case for the simple atomic model from Chap. 5, we believe this to be a consequence of the molecular structure. More specifically, we suspect this might be caused by our choice of using the position of N^+ and N^- instead of the geometric or mass centre. Additionally, this analysis is generally very sensitive to the choice of integration limit, and other choices might give a better understanding of the model's behaviour. For example, we found that if the integration limit for the like types were changed to $\tilde{R} = 2.1$ it behaved the same as the unlike types (this is not shown).

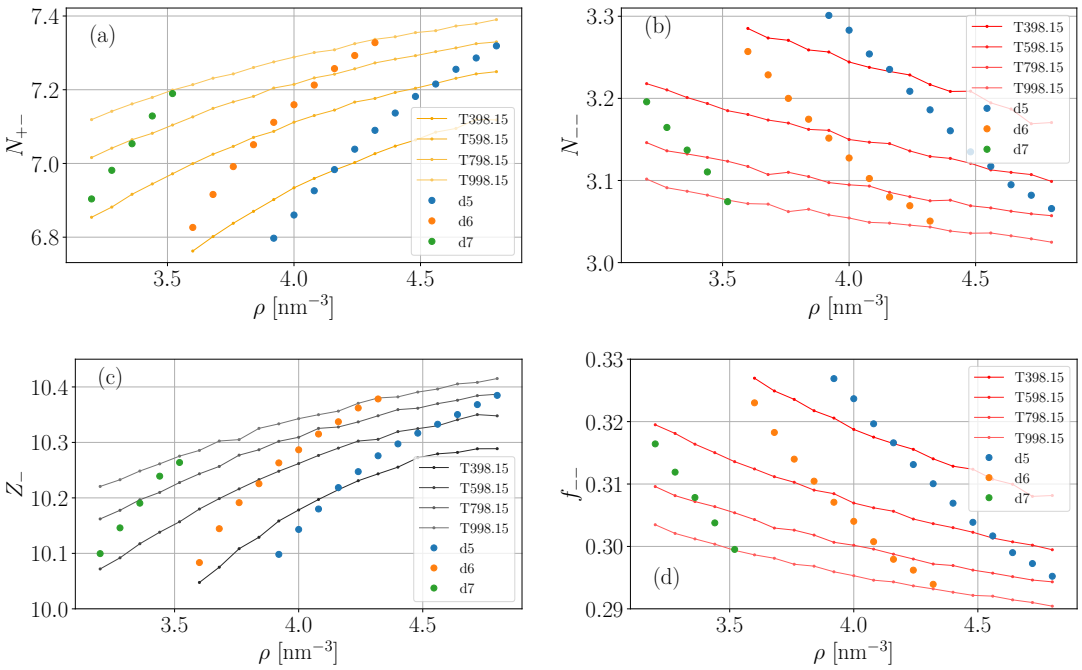

Figure 6.59: The number of nearest neighbouring molecules for anions as a function of density. Points with negative pressure are not shown.
(a) The number of cation neighbours around the anions N_{+-},
(b) the number of anion neighbours around the anions N_{--},
(c) the total number of neighbour molecules around anions Z_-, and
(d) the concentration of anion neighbours around anions f_{--}.

6.5.5 Preferred orientation of the cation tail

The tail is the most flexible part of Pyr_{14} and therefore an important aspect of the structure. This begs the question of how it is oriented with respect to the ring, and whether it tends to be stretched or curled up. When testing the implementation of the non-bonded interactions in Sec. B.2, we found that the bonds and angles do not change much and stay around the distances and angles favoured by the intra-molecular interactions. On the other hand, the dihedral-potentials are more flexible than the other bonded interactions, resulting in a broader distribution of dihedral-angles. Because of this, we calculated different dihedral-angles to gain information on the tail's orientation and computed the distance between N^+ and the end of the tail (T_4). This is the distance between atom 0 and 4 and will therefore be referred to as r_{04}. A reference for the atom numbering in Pyr_{14} can be seen in Fig. 6.60.

We study dihedral-angles 0123 and 1234 to gain direct information about the tail, but also the dihedral-angle 2345 to see the tail's orientation relative to the ring. Dihedral-angle distributions and their correlation with the tail distance r_{04} will be shown for two isochore 3.2 nm^{-3} and 4.8 nm^{-3} and isodyne 2.

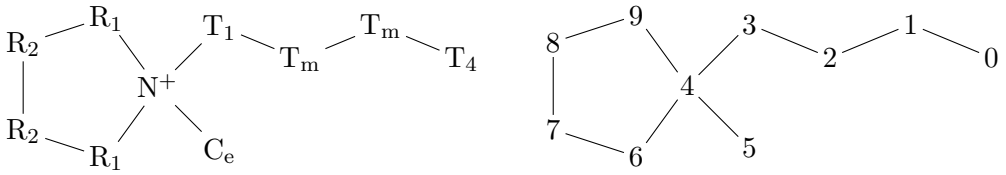

Figure 6.60: Reference for the atom numbering in the cation.

Firstly, we show the distribution of tail distances r_{04}, see Fig. 6.61. It is clear that this distribution is not invariant along the isodyne or the isochores. However, it is also clear that there are two peaks meaning that the system has two preferred distances. The long distance peak (≈ 4.7 Å) is dominant at low densities, while the short distance peak (≈ 4.0 Å) is dominant at high densities. This means that the packing of molecules depends greatly on the density, which intuitively makes sense. The peaks are also generally pronounced at low temperatures, but at high temperatures they get smeared together and in some cases one gets reduced to a shoulder of the other.

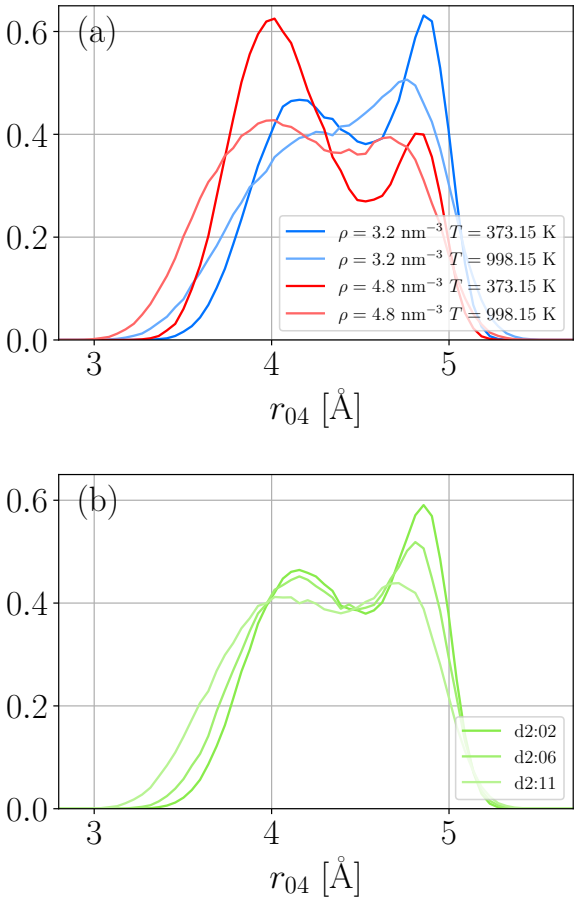

Figure 6.61: Distribution of the tail distance r_{04} (the distance between N^+ and T_4). (a) Data from two isochores where the colours represent density, and (b) data from isodyne 2.

Secondly, we study the distribution of the dihedral-angle θ_{2345}, see Fig. 6.62. Part (a) and (b) of the figure shows that the system prefers a $\pi/3$ angle with a small peak at π. These are also the angles that are preferred by the dihedral potential (see Fig. 6.2), however, we see a clear preference towards $\pi/3$. We believe this is caused by the non-bonded interactions between R_2 and T_m which are not excluded. This would also explain why the data is much more dependent on temperature than density. It is also interesting how all the curves intersect around $\pi/2$. However, the curves also intersect around $\pi/6$ for the isodyne. Part (c), (d), (e) and (f) of the figure shows that there is no correlation between this dihedral-angle and the tail distance from N^+.

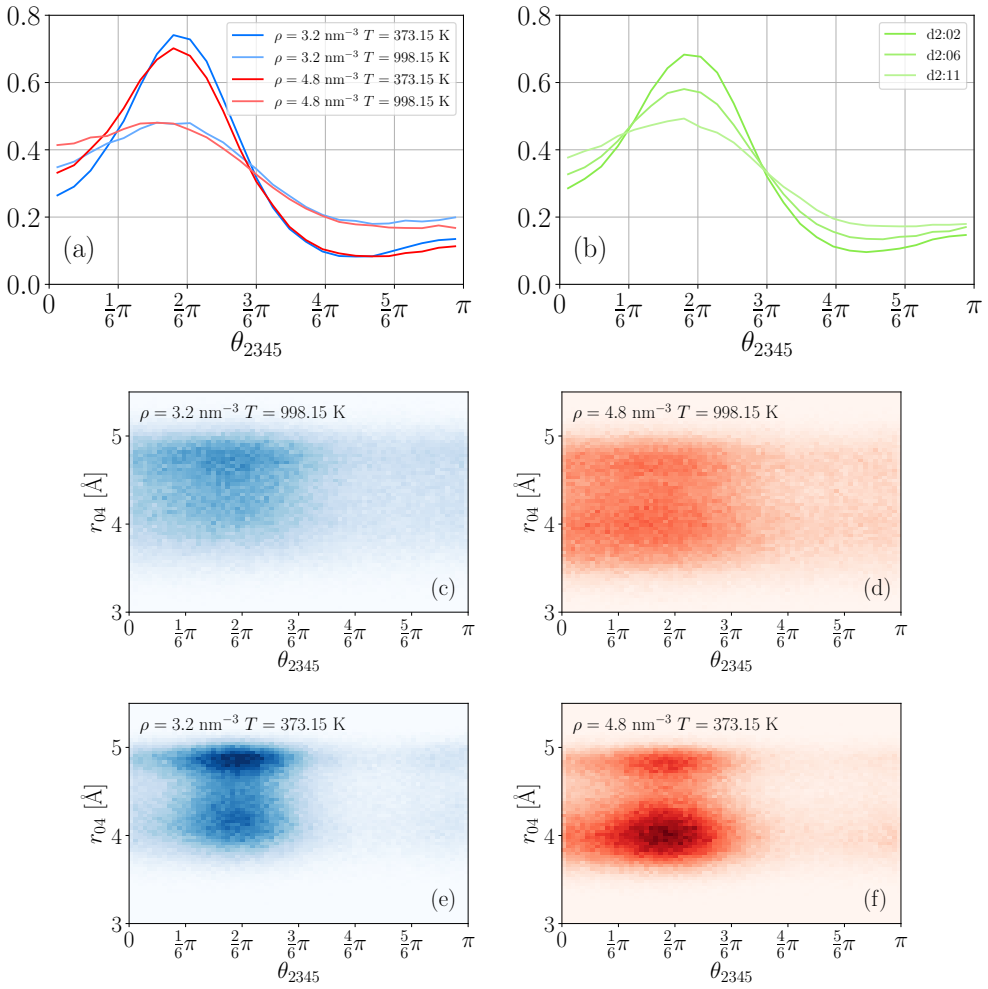

Figure 6.62: Distribution of dihedral angle 2345 along (a) isochores, and (b) isodyne 2. (c), (d), (e) and (f) show the correlation between dihedral angle 2345 and distance r_{04} at the isochore state points.

Thirdly, we study the distribution of the dihedral-angle θ_{1234}, see Fig. 6.63. Part (a) and (b) of the figure shows that there is a clear preference for an angle of π. We believe that this strong preference is caused in part by the dihedral potential and by the non-bonded interactions with the ring. As before this would explain why the data is much more dependent on temperature than density. It is also interesting how all the curves intersect around $(5/6)\pi$.

Part (c), (d), (e) and (f) of the figure shows that there is no correlation between this dihedral-angle and the tail distance from N^+.

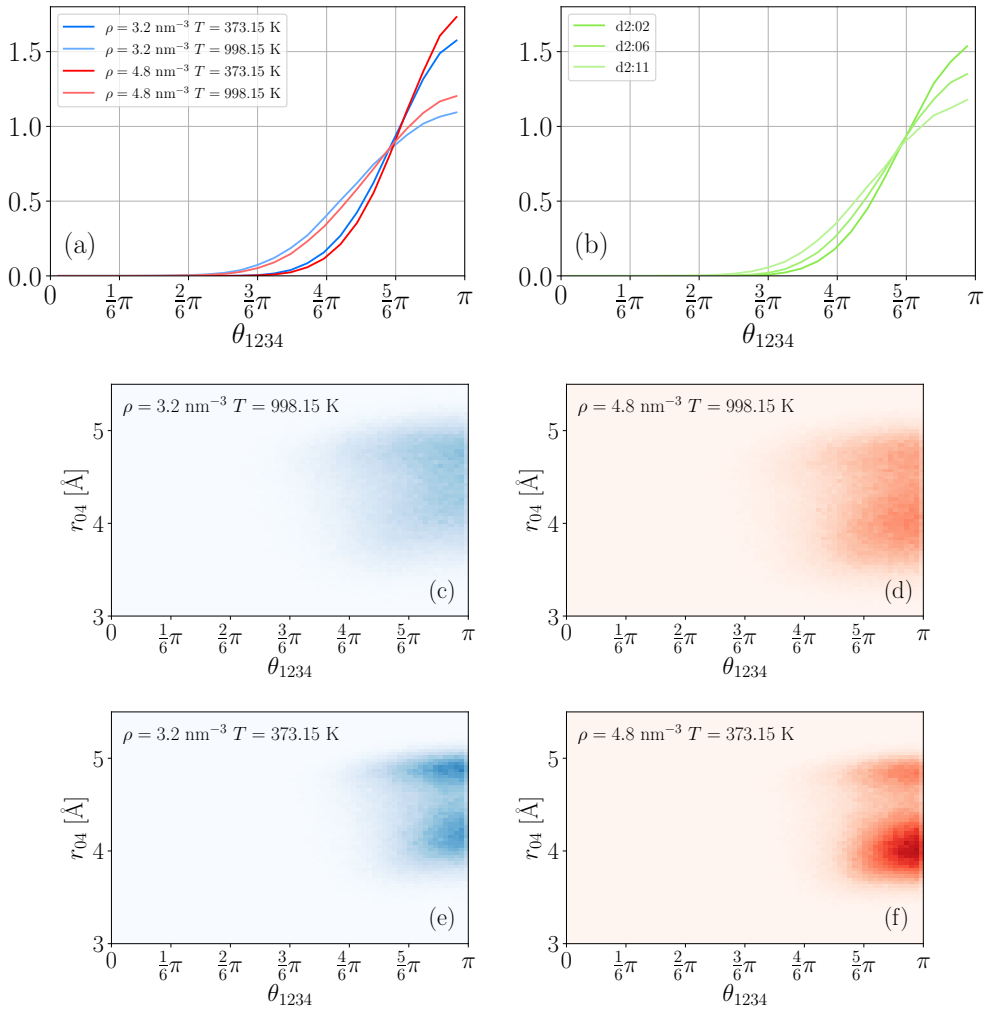

Figure 6.63: Distribution of dihedral angle 1234 along (a) isochores, and (b) isodyne 2. (c), (d), (e) and (f) show the correlation between dihedral angle 1234 and distance r_{04} at the isochore state points.

Lastly, we study the distribution of the dihedral-angle θ_{0123}, see Fig. 6.64. Part (a) and (b) of the figure shows that the angle distributions are dependent on both density and temperature. This reflects the density dependence of the tail distance which we saw in Fig. 6.61. Furthermore, the angle distributions along isodyne 2 seems invariant in the interval $\pi/6 < \theta_{0123} < (5/6)\pi$. This is interesting since it shows an aspect of structure being invariant, however, this is not well understood.

Part (c), (d), (e) and (f) of the figure shows that there is a clear correlation between this dihedral-angle and the tail distance from N^+. The tail is only stretched when this dihedral-angle is around π.

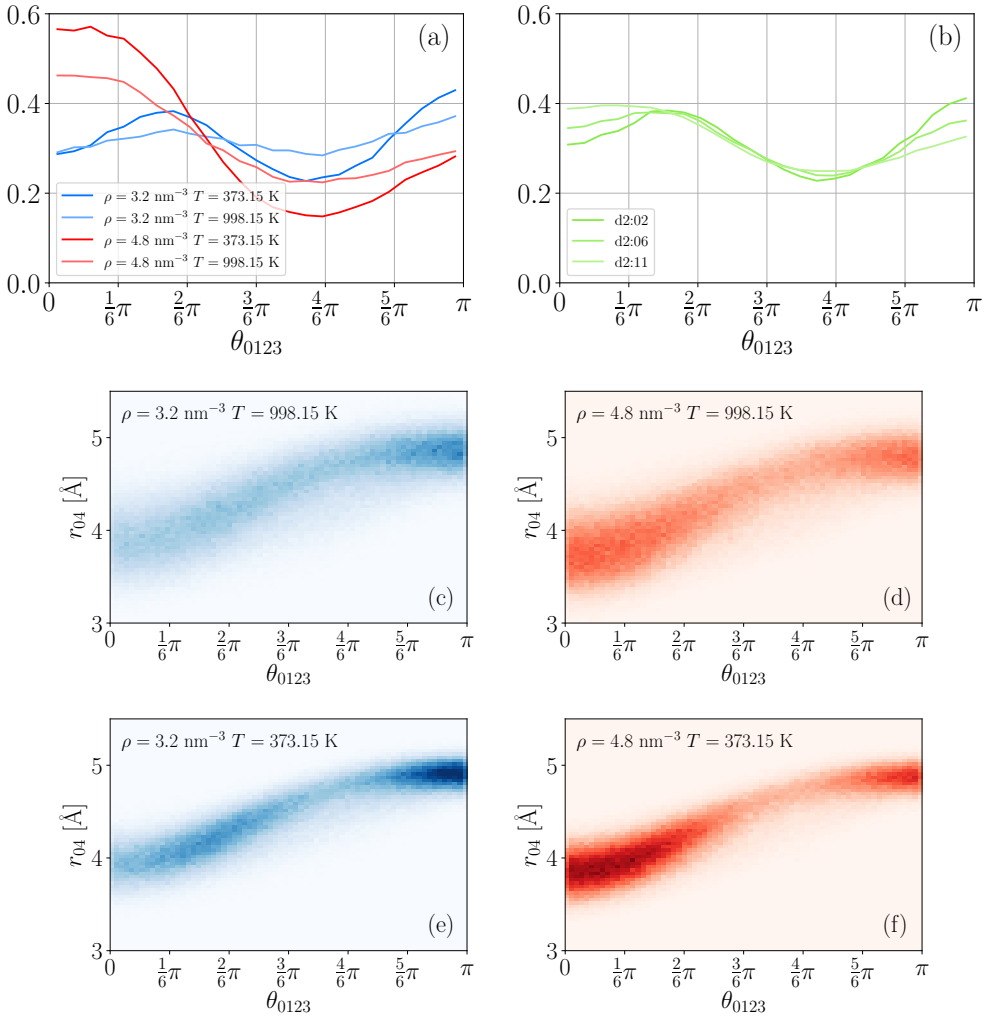

Figure 6.64: Distribution of dihedral angle 0123 along (a) isochores, and (b) isodyne 2. (c), (d), (e) and (f) show the correlation between dihedral angle 0123 and distance r_{04} at the isochore state points.

6.6 Conclusion

Comparing dynamics with experiments

In Sec. 6.4.1 we made a comparison of viscosity and diffusion coefficient between the model and experimental data from Harris et al. [2011]. We found that the model was approximately a factor of 2 faster that the experiments. Furthermore, the shape of the curves are also similar meaning that the model is a good qualitative representation of the dynamics in the experiments.

Existence of isodynes

We find that this model obeys the Stokes-Einstein relation in the simulated range when isomorph scaling is applied (see Fig. 6.22). Consequently, both the isomorph scaled diffusion coefficient ($\tilde{D}$) and viscosity ($\tilde{\eta}$) have the same lines of invariance in the phase diagram. For this model, we referred to these curves as isodyens.

We traced out different isodynes to find which other dynamical properties are invariant along them. We found that for N^+ in the cation the mean square displacement and self-intermediate scattering function do not change significantly (see Fig. 6.28). This is even more clear when comparing with similar data along isochores which change a lot (see Fig. 6.18). We made a similar analysis of the stress autocorrelation function which was used to calculate the viscosity. We found that the short-time behaviour of the data varied in a systematic way, which lead us to believe that this is a feature and not an artefact of the quality of the isodyne. The long-time behaviour looked invariant (see Fig. 6.29). Upon further analysis we found that it changes slightly over the isodyne. However, this still lead us to believe that the long-time behaviour is of the stress autocorrelation function is important and almost invariant along isodynes.

In Sec. 6.4.7 we also analysed rotations of the molecules and found that some are invariant along isodynes while others are not. For the anion the rotations who showed invariance seemed to be the ones with high moment of inertia (see Fig. 6.34 - 6.37). The reason for this is not well understood, however, it does make sense that the molecule can rotate more freely along axis of low moment of inertia without influencing the overall dynamics of the system. On the other hand all the rotations analysed for the cation showed invariance (see Fig. 6.31 - 6.33). However, the isodyne with the highest viscosity of the one we studied, was slightly less invariant for some (but not all) of the rotations. The cause of this is unknown.

Thus, isodynes were shown to have invariance of multiple dynamical properties other than $\tilde{D}$ and $\tilde{\eta}$ for this model. Next we analyse different structures of the model.

Structure factor peaks along isodynes

In Sec. 6.5.1 we computed the total static structure factor and compared it with the experimental data from Hansen et al. [2020]. We found the charge peak to decrease in intensity and get shifted to lower $\tilde{q}$ as temperature increased, which is in agreement with Hansen et al. [2020]. However, the main peak decreased in intensity and slightly shifted to higher $\tilde{q}$ as temperature increased (see Fig. 6.39). This is in contrast to Hansen et al. [2020] in which the main was invariant. Upon further analysis this was shown to be a product of different density intervals. When the simulated data are shown in the same density interval as the experimental data of 2% the main peak looks invariant (see Fig. 6.40).

To better understand the behaviour of the structure factor we also analysed the partial redial distribution functions.

Partial redial distribution functions

In Sec. 6.5.2 we analysed the partial redial distribution functions between N^+N^-, N^+N^+ and N^-N^- along isodynes. We found that for all three partial RDFs the height of the first peak decreased with increasing density. Furthermore, the first minimum in N^+N^+ and N^-N^- got shifted to higher $\tilde{r}$ and increased in height with increasing density (see Fig. 6.45 and Fig. 6.46). This means that these RDFs along isodynes generally becomes more flat as density and temperature increases. In contrast both the position and height of the first minimum in the RDF for N^+N^- changed very little and is one of the most invariant structural features we have observed in this model (see Fig. 6.44).

Lastly, in the RDF for N^+N^- at low densities and temperatures we observed an extra pre-peak which evolved to a shoulder and eventually disappears as temperature increases. This shoulder/peak substructure was studied in more detail.

Shoulder/peak substructure between ion pairs

In Sec. 6.5.3 we analysed a substructure between ion pairs. We found that it is more prevalent at low temperatures and high densities. The substructure involved the N^+ and N^- atoms in the ion pair to be close, which also resulted in preferred orientations between the ions involved. We believe it arises from the interactions between the anion and the tetrahedron structure in the cation. The substructure was also shown to be evenly spread throughout the configurations and not localised. The significance of this substructure is still unknown. However, it is not invariant along isodynes.

Number of nearest neighbour molecules

In Sec. 6.5.4 we analysed the number of nearest neighbour molecules for both the cations and anions. First we found that they behave the same behaviour and even very similar values. The number of unlike types were increasing as a function of both density and temperature. However, the number of like types were decreasing as a function of both density and temperature. We found the later counter-intuitive because we expect the system to be more gas-like at high temperatures. We suspect it might be related to our choice of using N^+ and N^- when defining the number of neighbour. If the molecules pack in such a way that N^+ and N^- are for from each other that would result in fewer neighbours at low temperatures. However, such a preferred packing would not be as pronounced at high temperatures which would result in more neighbours.

It is important to remember that this analysis is very dependent in the choice of integration limit. We found that if the integration limit for the like types were changed to $\tilde{R} = 2.1$ it behaved the same as the unlike types.

Preferred orientation of the Pyr_{14} tail

In Sec. 6.5.5 we analysed the orientation of the tail in Pyr_{14} relative to its ring. This was done by computing the distribution of three dihedral angles at different state points. We found that shape of distributions for tail distances (the distance between N^+ and the end of the tail T_4) was mostly dependent on density, while increasing temperature generally broadened the distributions (see Fig. 6.61). Two of the three dihedral angle distributions were much more dependent on temperature than density, and has little influence on the tail distances (see Fig. 6.62 - Fig. 6.63). The last dihedral angle (the one for the four spheres in the tail) is more dependent on density than temperature (see Fig. 6.64) This dihedral angle is correlated with the tail distance, and the dihedral angle distribution was roughly invariant along an isodyne.

Chapter 7

All-atom Ionic Liquid Model

In this chapter we analyse an all-atom version of the ionic liquid from Hansen et al. [2020]. This model will not be studied as thoroughly as the united atom model from the previous chapter. Instead the purpose is to compare the two models and find in what ways they behave the same.

7.1 Model details

Since only the cation contained hydrogen, the anion will remain unchanged between the two models. We will therefore only describe the all-atom parameters for the cation in this section (parameters for the anion are in Chap. 6). Consequently, both models will be using many of the same parameters, and therefore the same unit system, that was shown in Tab. 6.1. The same is true for the isomorph scaling, Tab. 4.2. An illustration of the all-atom cation can be seen in Fig. 7.1.

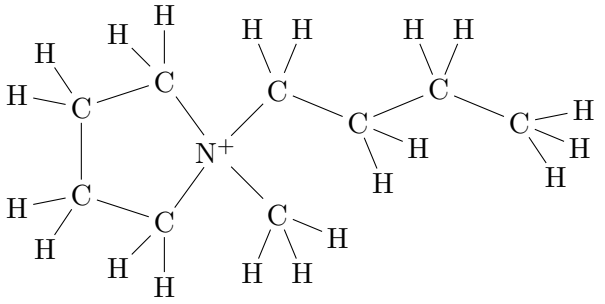

Figure 7.1: All-atom illustration of the cation 1-Butyl-1-methyl-pyrrolidinium.

7.1.1 Non-bonded interactions

For the non-bonded interactions, we use Eq. 6.1 and the Lorentz-Berthelot combination rules. This model has two categories of hydrogen; small hydrogen (H_s), and large hydrogen (H_l). They each have three subtypes differing by their charge, which depends on which C they are bounded to. We therefore name the H after their C. The parameters for the all-atom cation can be seen in Tab. 7.1, and the parameters for the anion can be seen in Tab. 6.2.

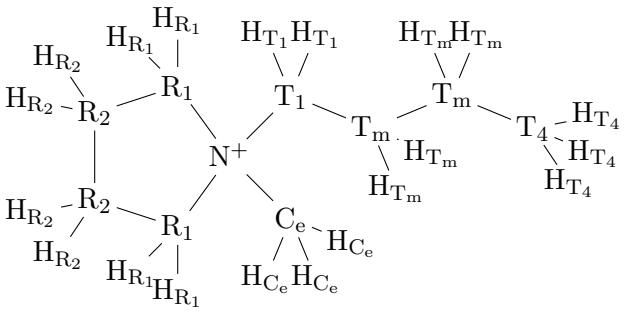

Non-bonded					
Name	σ [Å]	ϵ [kcal/mol]	m [u]	q [e]	$q_{0.8}$ [e]
N^+	3.250	0.1700	14.007	0.1040	0.0832
C (R_1)	3.400	0.1094	12.011	-0.0307	-0.02456
C (R_2)	3.400	0.1094	12.011	-0.03105	-0.0248
C (T_1)	3.400	0.1094	12.011	-0.0545	-0.0436
C (T_m)	3.400	0.1094	12.011	-0.00615	-0.00492
C (T_4)	3.400	0.1094	12.011	-0.0846	-0.06768
C (C_e)	3.400	0.1094	12.011	-0.1244	-0.09952
H (H_{R_2})	2.650	0.0157	1.008	0.05735	0.04588
H (H_{T_m})	2.650	0.0157	1.008	0.02855	0.02284
H (H_{T_4})	2.650	0.0157	1.008	0.0375	0.0300
H (H_{R_1})	2.471	0.0157	1.008	0.09125	0.0730
H (H_{T_1})	2.471	0.0157	1.008	0.0778	0.06224
H (H_{C_e})	2.471	0.0157	1.008	0.1062	0.08496

Table 7.1: All-atom non-bonded parameters for Pyr_{14} from Xing et al. [2013]. As in the united atom model we used the average charge to define R_1, R_2, and T_m, and gain symmetry.

7.1.2 Intra-molecular interactions

The bonded parameters for the all-atom cation can be seen in Tab. 7.2.

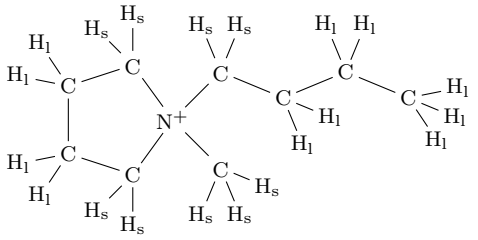

$\frac{1}{2}k_b\left(r_{jk}-l_0\right)^2$

Bonds

Name	l_0 [Å]	k_b [kcal/(mol Å^2)]
C-C	1.526	620.0
N-C	1.471	734.0
C-H	1.090	680.0

$\frac{1}{2}k_a\left(\theta_{jkl}-\theta_0\right)^2$

Angles

Name	θ_0 [°]	k_a [kcal/mol]
C-C-C	109.5	80.0
N-C-C	111.2	160
C-N-C	109.5	100
H-C-N	109.5	100
H-C-C	109.5	100
H-C-H	109.5	70.0

$\sum_{n=0}^{5} C_n\left(-\cos\left(\theta\right)\right)^n$

Ryckaert-Bellemans Dihedrals

Name	C_0	C_1	C_2	C_3	C_4	C_5 [kcal/mol]
C-C-C-C	0.180	0.540	0.0	-0.720	0.0	0.0
C-C-C-N	0.156	0.467	0.0	-0.622	0.0	0.0
C-C-N-C	0.156	0.467	0.0	-0.622	0.0	0.0
H_s-C-C-C	0.156	0.468	0.0	-0.624	0.0	0.0
H_s-C-N-C	0.156	0.467	0.0	-0.622	0.0	0.0
H_s-C-C-H_l	0.156	0.468	0.0	-0.624	0.0	0.0
H_l-C-C-H_l	0.150	0.450	0.0	-0.600	0.0	0.0
H_l-C-C-N	0.156	0.467	0.0	-0.622	0.0	0.0
H_l-C-C-C	0.160	0.480	0.0	-0.640	0.0	0.0

Table 7.2: All-atom bonded parameters for Pyr_{14} from Xing et al. [2013]. The translation between the two dihedral potentials can be found in Sec. 2.4.2.

7.2 Test of model implementation

7.2.1 Test time step

To test the size of the time step (Δt) we ran a series of NVE-simulations at $\rho = 3.84$ nm^{-3} and $T \approx 273$ K. This state point was chosen because it is at the lowest density and lower temperature than we will simulate in our main analysis. Each simulation started from the same equilibrated configuration and had a data collecting run for $100 \cdot 2^{17} = 13107200$ steps. As for the united atom model, we tested Δt from 0.25 fs to 5.5 fs with in interval of 0.25 fs. However, we found that the simulations already started crashing at Δt greater than 2 fs, whereas the united atom model only crashed at Δt greater than 5 fs. This can also be seen in Fig. 7.2 which show the variance in the total energy as a function of Δt. Here we see that the data starts deviating from the power law much earlier than for the united atom model (see Fig. 6.3). We also see a big drift in the total energy for $\Delta t = 2$.

This big difference in stability is related to the vibrations of the hydrogen bonds in the cation. This is not due to the spring constants, which are of equal magnitude (see Tab. 7.2), but rather to the factor 12 difference in mass between H and C (see Tab. 7.1). To get an idea of this effect we assume that the C is stationary and calculate the resonance period $\sqrt{m_H/k_{b,C-H}} = 1.88$ fs.

Based on this, we choose a $\Delta t = 1$ fs at this state point ($\rho = 3.84$ nm^{-3} and $T \approx 273$ K), and use the corresponding reduced time step for all simulations of this model. This means that $\Delta t < 1$ fs for all our simulations.

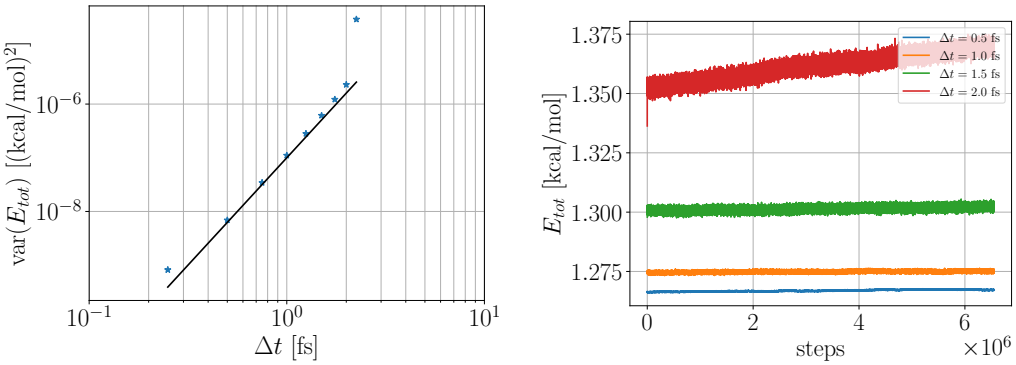

Figure 7.2: Test of the time step at $\rho = 3.84$ nm^{-3} and $T \approx 273$ K. (Left) The variance of the total energy as a function of Δt. The black line is a power law with exponent 4 which is meant to guide the eye. (Right) The total energy is a function of time. This is to show a drift in the total energy as an indication of the too large Δt.

7.3 Simulation details

Simulation time - United atom vs. all-atom

As previously mentioned this, model will mainly be used for comparison with the united atom model from Chap. 6. The two main reasons for this are partially scientific and practical; Firstly, we do not find it necessary to make an investigation as detailed as previously when our main goal is a simple comparison. However, this does not mean that such a project would not be interesting. Secondly, a simulation of the all-atom model takes significantly longer to run, than a corresponding simulation of the united atom model. The reason for this is a combination of different factors; there is a factor of 2 from the difference in timestep, there is approximately a factor of 2 from the increase of the number of atoms, and each atom has more neighbours due to the increased atomic number density (approximately another factor of 2). Furthermore, the number of bonded interactions (especially angles and dihedrals) are much greater in the all-atom model, see Tab. 7.3. Based on this we expect a simulation of the all-atom model to take approximately 8 times longer than a corresponding simulation of the united atom model. This corresponds fairly well to what we experienced when simulating the two models.

Model	Atoms	Bonds	Angles	Dihedrals
United atom	10	10	13	14
All-atom	30	30	60	90

Table 7.3: The number of bonded interactions in the cation for both the united and all-atom models.

Simulation protocol

We want these simulations to be comparable to the united atom model, so we use a similar simulation protocol. As for the united atom model, we simulated 200 ion pairs corresponding to 9000 atoms (this was 5000 spheres in the united atom model). However, since we use a time step that is roughly half of that in the united atom model we simulate this model for twice the number of steps. So each simulation equilibrated for $4 \cdot 10^7$ steps, followed by a data collecting run of $100 \cdot 2^{21} = 209715200$ steps. All simulations used the same isomorph-scaled time step which corresponds to a real time of 1 fs at $\rho = 3.84$ nm^{-3} and $T = 273$ K.

We would like to compare the models in two ways; firstly in the region with experimental data, and secondly to test if the all-atom model also has isodynes. To test the former, we have different experimental isotherms to choose from, however,

only 50 °C and 75 °C have data for both η and D. We decided to simulated the isotherm at 50 °C at corresponding densities to the united atom model. For the latter, we simulate points along isodyne 5 from the united atom model to see if this too is an isodyne for this model. We choose isodyne 5 because it has the highest viscosity and is closer to the room temperature region of interest for experiments. Here it is important to remember that even if isodyne 5 is not an isodyne in this model, that does not mean that the model cannot have isodynes. But, as mentioned earlier, tracing out the isodynes for this model, as was done for the united atom model, would be much more demanding on time and resources.

All the simulated points are shown in a $\rho - T$ diagram in Fig. 7.3 accompanied by the P as a function of ρ (the corresponding data from the united atom model are also shown for comparison). The pressure of the all-atom model is generally greater than the united atom model.

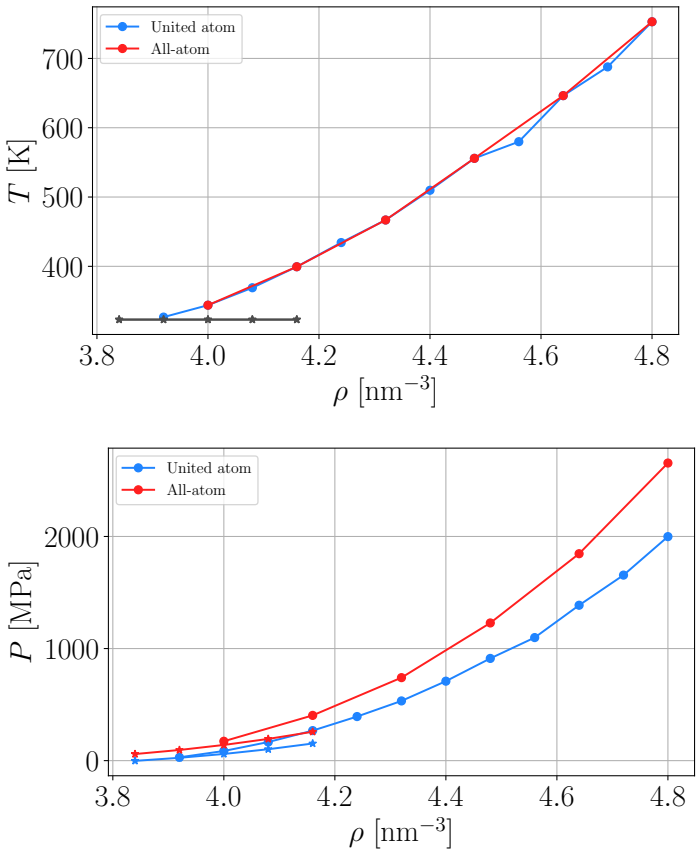

Figure 7.3: Simulated points along isodyne 5 and the isotherm 50 °C. (Top) A $\rho - T$ diagram and (Bottom) the pressure as a function of density.

7.4 Results: Dynamics

7.4.1 Compare dynamics with experiments

As was done for the united atom model, we compare the all-atom model with experimental data from Harris et al. [2011]. We get ρ, T, P, and η data from Harris et al. [2011][Tab. 3] , and we get P, D_- and D_+ data from Harris et al. [2011][Tab. 6]. However, we will again use Eq. 6.5 from Hansen et al. [2020] to obtain the densities for the D_- and D_+ data. In this section, we compare the all-atom model with both the experimental data, and the united atom model. To keep focus and avoid confusion, we only show data from isotherm 50 °C.

The pressure for this data is shown as a function of density in Fig. 7.4. Here we see that P for the all-atom model is $60 - 100$ MPa greater than both the united atom model and experimental data. This makes the data more difficult to compare. However, if the simulated curves are shifted down we find that the shape of the all-atom model matches the experimental data better than the united atom model.

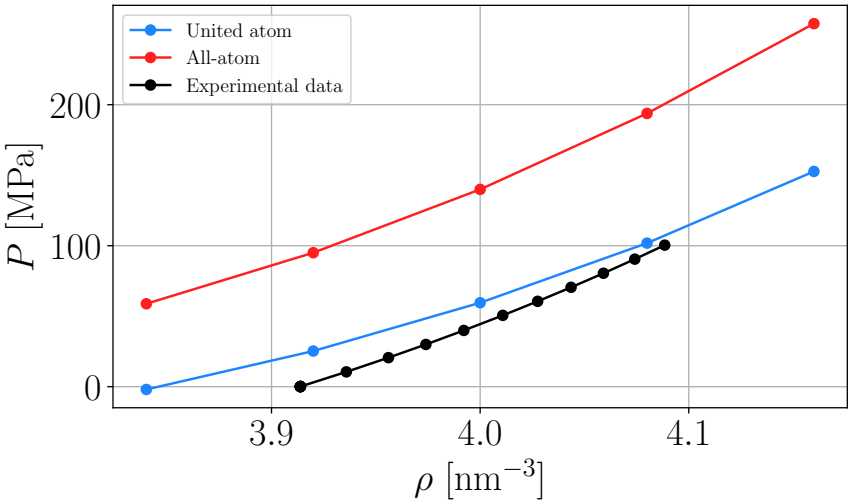

Figure 7.4: The experimental and simulated pressure P as a function of density ρ at $T = 50$ °C.

The diffusion coefficient for the cation D_+ and anion D_- for both simulations and experiments can be seen in Fig. 7.5. First we notice that the data fits nicely within the same range. However, the slope of the simulated data does not match that of the experimental data for either molecule. This is in contrast to the united atom model where the slope of the data matched while the curves themselves were shifted (see Fig. 6.16).

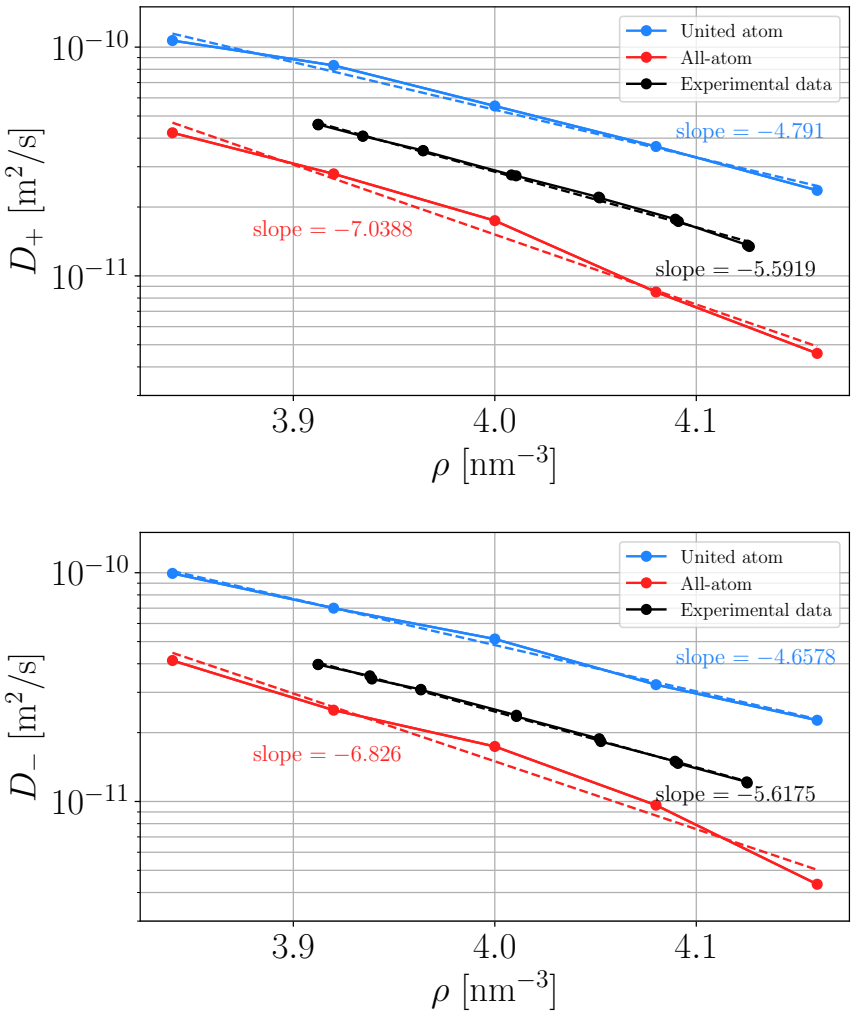

Figure 7.5: The experimental and simulated diffusion coefficients function of density at $T = 50$ °C. The dashed lines are exponential fits where the slopes are given.

The viscosity data for both simulations and experiments can be seen as a function of ρ in Fig. 7.6. The all-atom model has greater viscosity than the united atom model and experimental data. The simulated data has error bars which increase with density, but in some cases they are smaller than the symbol size. The data is shown on a logarithmic y-axis. From this we found that the data can be approximated by an exponential functions. To emphasize this, we included fits and show the slope.

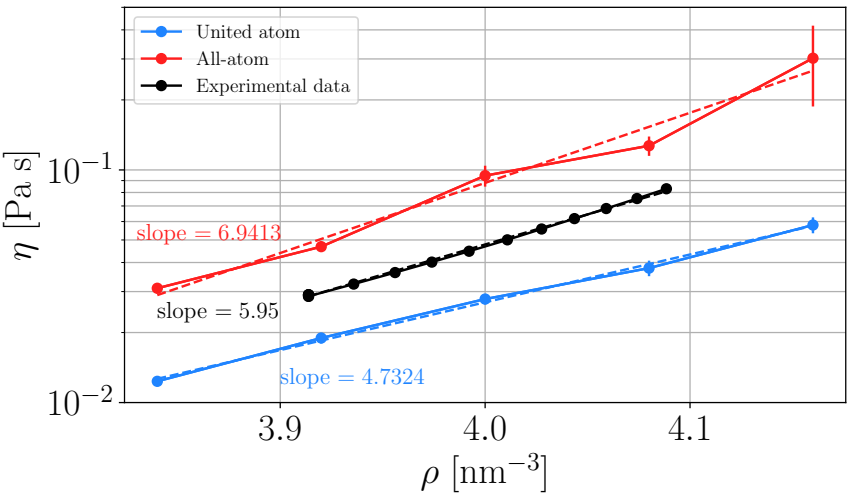

Figure 7.6: The experimental and simulated viscosity as a function of density at $T = 50$ °C. The dashed lines are exponential fits where the slopes are given.

7.4.2 Does the model have isomorphs?

Even though we presume that the model does not have isomorphs, we still compute the isomorph R and γ from Eq. 4.18 and 4.19, see Fig. 7.7. Both R and γ are lower for the all-atom model than for the united atom model. This could be related to the extra hydrogen bonds, that further decouple the potential energy and virial.

As expected, R is low for all simulations so the system does not have isomorphs in this range. However, it is notable how linear R is as a function of ρ. To emphasise this, linear fits are shown as dashed lines with the slope a. This was also generally the case in the united atom model (see Fig. 6.20).

The γ has negative curvature, but the all-atom model seems to be more linear than the united atom model.

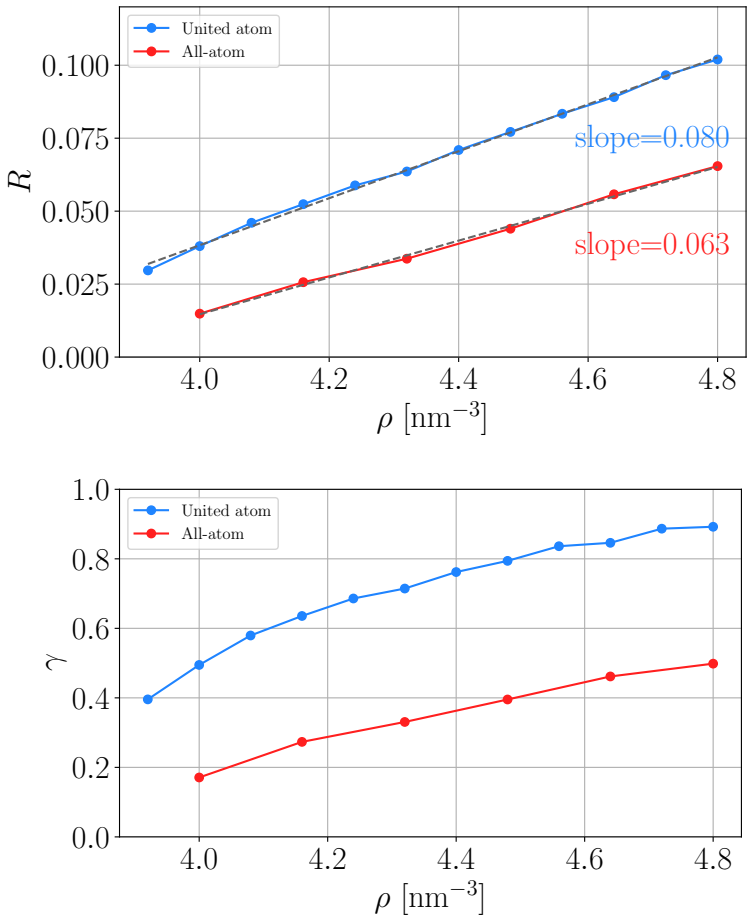

Figure 7.7: The isomorph R and γ for the all-atom model.

7.4.3 Does the model have isodynes?

The Stokes-Einstein relation

An easy way to test if the model could have isodynes is by using the Stokes-Einstein relation (see Sec. 3.4.4). In Fig. 7.8, both the effective hydrodynamic radius and the product $\tilde{\eta}\tilde{D}$ can be seen as a function of density for both the isotherm and isodyne 5. From this we see that the all-atom model fulfils the reduced Stokes-Einstein relation to the same extent as the united atom model. Furthermore, they even seem to have the same (or similar) reduced constants.

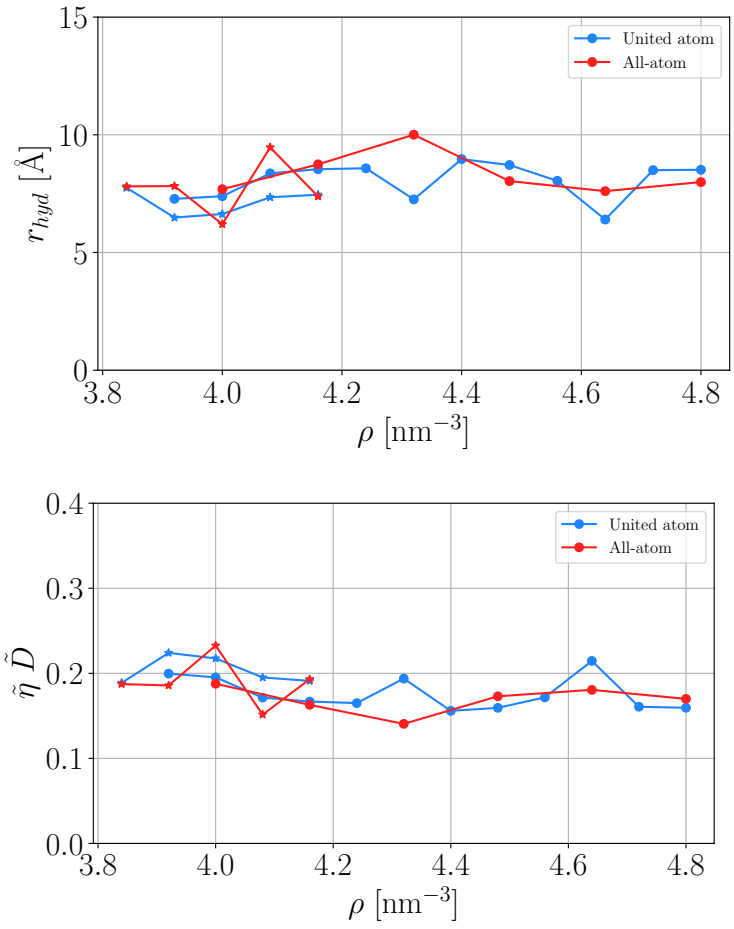

Figure 7.8: Test of the Stokes-Einstein relation. Both the isodyne and isotherm data are shown. (Top) A plot of the effective hydrodynamic radius as a function of ρ. (Bottom) A plot of $\tilde{\eta}\tilde{D}$ as a function of ρ to test the reduced Stokes-Einstein relation for the model.

Guess isodyne from the united atom model

The diffusion coefficients and viscosities along isodyne 5 can be seen for both the all-atom model and the united atom model in Fig. 7.9 (in some cases the error bars are smaller than the symbol size). First we notice that the all-atom model generally has slower dynamics than the united atom model.

The all-atom data looks less noisy than the united atom data. A part of the reason for this is that only every second point along isodyne 5 was simulated for the all-atom model. The data at low densities are generally greater than at high densities. However, since this is also the case for the united atom model we believe this is an artefact of the chosen "isodyne" and not a difference between the models.

Based on this, it seems like the isodynes of the united atom model are closely related to the isodynes of the all-atom model.

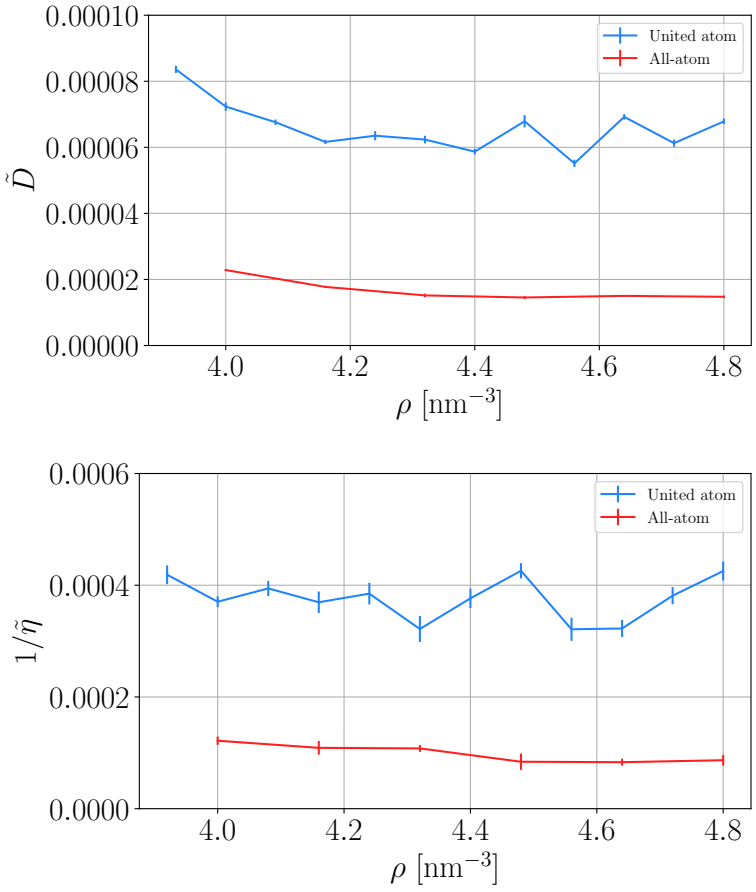

Figure 7.9: Plot of $\tilde{D}$ and $1/\tilde{\eta}$ along isodyne 5 in scaled units for both models.

7.4.4 Rotation of molecules

As in Sec. 6.4.7, we will analyse the time autocorrelation function for vectors between atoms. This will be done for isodyne 5 which has been simulated for this model. It should be noted that isodyne 5 did not show the same level of invariance as e.g. isodyne 2. This will be taken into account when analysing the data, since we do not expect this model to show more invariance along isodyne 5 than the united atom model did.

We see that not all the autocorrelation functions reach 0 within the simulated time. This means that the molecular rotations in this model generally are slower than in the united atom model for which all the autocorrelation functions reach 0.

Molecular rotation of the cation

We analysed the rotation of the ring in two ways. First, we defined the normal vector for N^+ and the two R_1 atoms. The autocorrelation functions can be seen in Fig. 7.10. Here we see an invariance comparable to that of the united atom model, maybe with the exception of the longest time range.

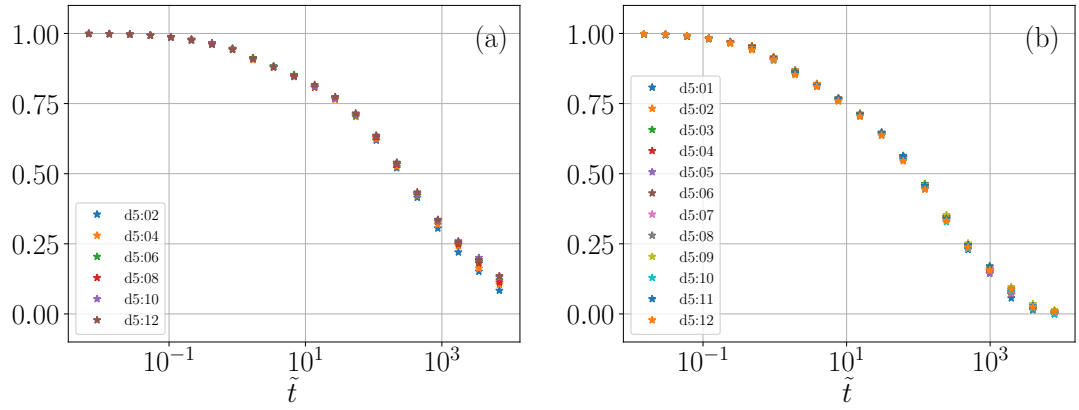

Figure 7.10: Autocorrelation function of the normal-vector to the plane spanned by N^+, and the two R_1 groups. (a) The all-atom model and (b) the united atom model.

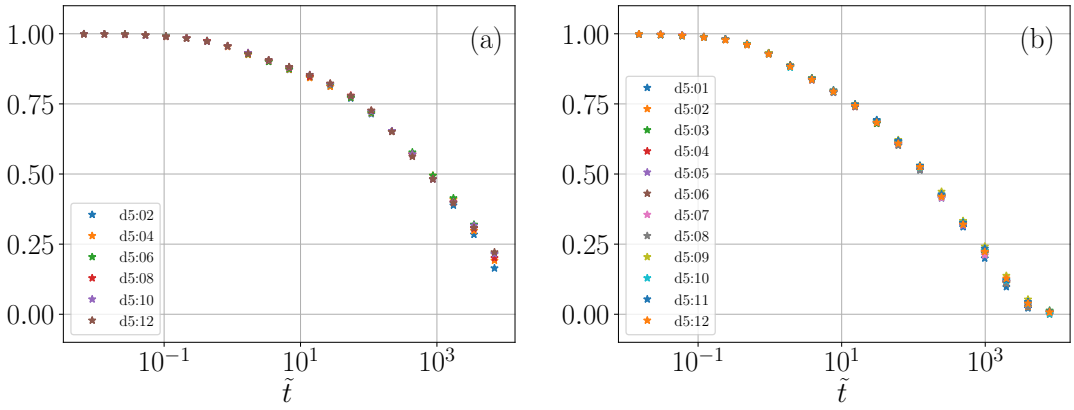

Figure 7.11: Autocorrelation function of the vector from N^+ to the point between the two R_2 groups. (a) The all-atom model and (b) the united atom model.

The second way we analysed the rotation of the ring was by defining the normalised vector from N^+ to the point between the two R_2 atoms. The autocorrelation functions can be seen in Fig. 7.11. Again we see an invariance comparable to that of the united atom model.

To analyse the rotation of the tail we defined a normalised vector from N^+ to T_4. The time autocorrelation function of this vector can be seen in Fig. 7.12. First, we notice that the data only reaches 0.25 within 1% of the simulated time. This is significantly slower than the united atom model. Secondly, we see that the curves are not collapsed at long times. This is the same behaviour as the united atom model.

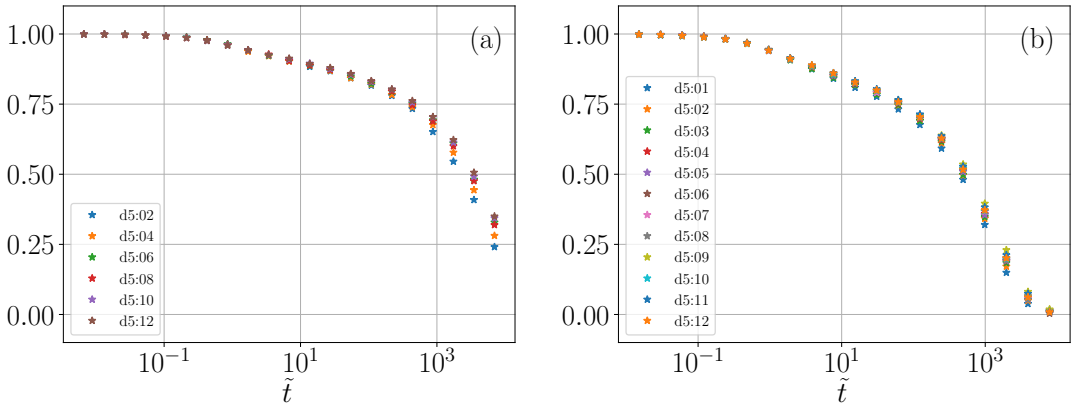

Figure 7.12: Autocorrelation for the normalised vector between N^+ and T_4. (a) The all-atom model and (b) the united atom model.

Molecular rotation of the anion

Next we analyse the normalised vector between the two S atoms. The time autocorrelation function of this vector can be seen in Fig. 7.13. It behaves the same as the united atom model, but changes slightly more.

To confirm this behaviour we analyse the normalised vector between the two C atoms. The time autocorrelation function of this vector can be seen in Fig. 7.14. It also varies slightly more than the united atom model.

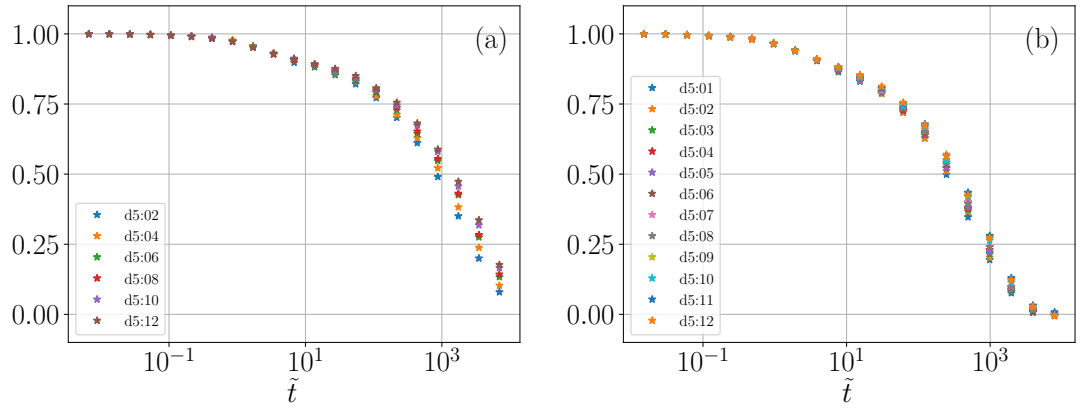

Figure 7.13: Autocorrelation function of the vector between the two S atoms. (a) The all-atom model and (b) the united atom model.

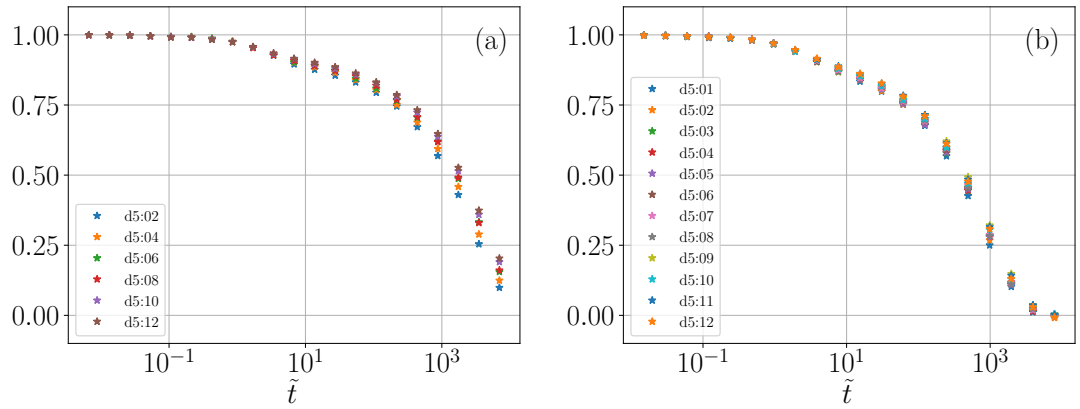

Figure 7.14: Autocorrelation function of the vector between the two C atoms. (a) The all-atom model and (b) the united atom model.

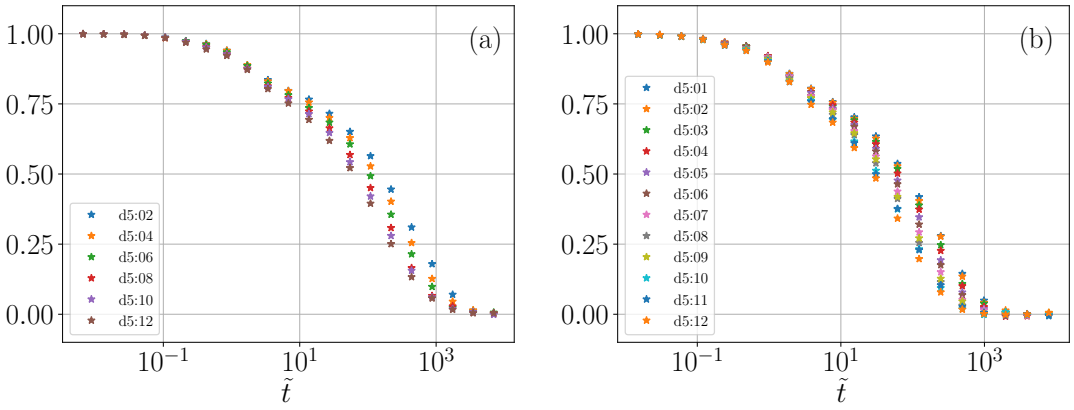

Figure 7.15: Autocorrelation function of the normal-vector to the plane spanned by N^- and the two S atoms. (a) The all-atom model and (b) the united atom model.

We also analysed the normal vector for the plane spanned by N^- and the two S atoms. The time autocorrelation function of this vector can be seen in Fig. 7.15. This changes like the united atom model.

Lastly, se analysed the vector between N^- and the point between the two S atoms. The time autocorrelation function of this vector can be seen in Fig. 7.16. This changes like the united atom model.

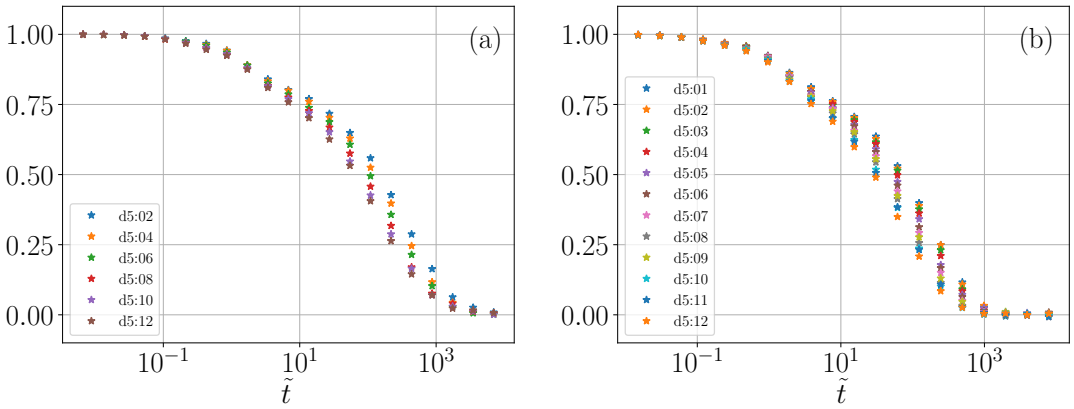

Figure 7.16: Autocorrelation function of the vector from N^- at the point between the two S atoms. (a) The all-atom model and (b) the united atom model.

7.5 Results: Structure

7.5.1 The structure factor along isodyne

To analyse the structure along the isodyne, we calculated the total static structure factor. More specifically, we computed the sum of the partial structure factors weighted by the form-factors that are related to the charge. This was done to better compare with the experimental data from Hansen et al. [2020]. This total $S(\tilde{q})$ can be seen in Fig. 7.17 along isodyne 5.

All the curves show both the charge peak ($q \approx 0.8$ Å) and the main peak ($q \approx 1.4$ Å). The height of both peaks decreases with increasing density. Furthermore, the charge peak does not change notably in SI units, which is not the case for the main peak. In contrast to this, the opposite is true when the data are presented in isomorph scaled units. This means that with,the exception of the height of the main peak, the data behaves the same as the experimental data from Hansen et al. [2020]. However, this is caused by the difference in density intervals. This overall behaviour is the same as that of the united atom model (see Fig. 6.39).

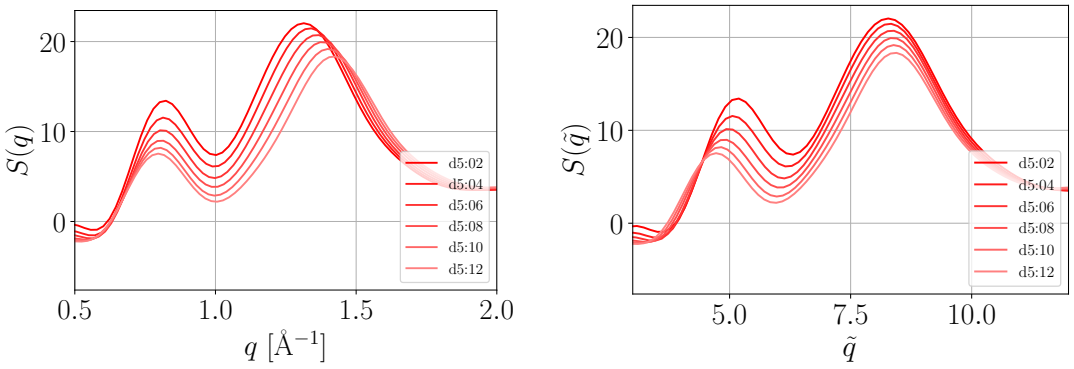

Figure 7.17: Plot of the total static structure factor weighted by the form-factors for points along isodyne 5.

7.5.2 The radial distribution function along isodynes

We also compare the partial radial distribution function for N^+N^-, N^+N^+, and N^-N^- between the united atom and all-atom model. We generally see that the two models behave very similar, even down to the positions and heights of the peaks. From this the addition of hydrogen does not appear to change the nano-structure significantly, however, further studies would be needed to know for certain.

Starting with N^+N^-, we see that both models have a peak at $\tilde{r} \approx 1.0$, see Fig. 7.18. Furthermore, the all-atom model also has the extra peak at $\tilde{r} \approx 0.7$ which indicates that this model most likely also has the substructure which is described for the united atom model in Sec. 6.5.3. Additionally the extra peak seems even stronger and more stable along the isodyne in this model than the united atom model. We hypothesise this could be caused by the attractive forces between N^- (in the anion) and the hydrogen in the tetrahedral structure (in the cation), however, this has not been tested.

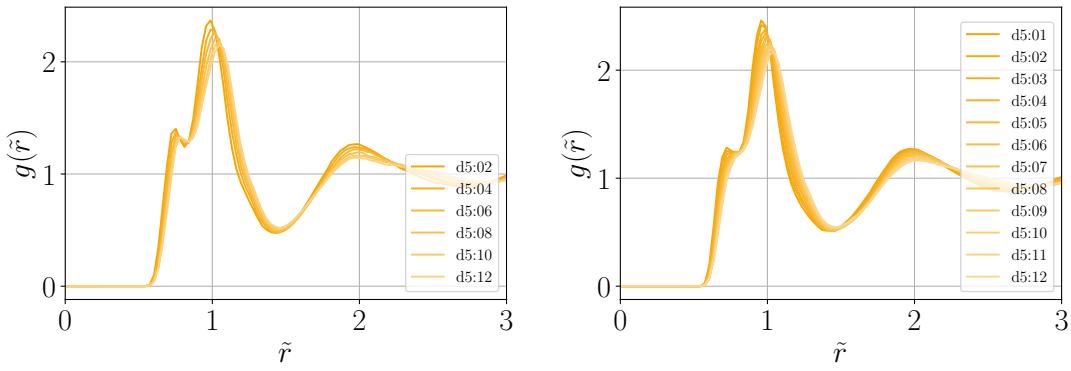

Figure 7.18: The partial radial distribution function between N^+N^- along isodyne 5. (Left) All-atom model , and (Right) united atom model.

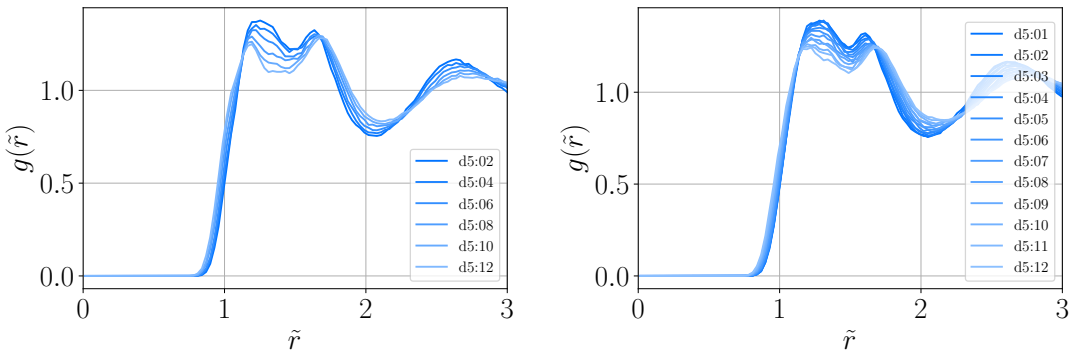

Figure 7.19: The partial radial distribution function between N^+N^+ along isodyne 5. (Left) All-atom model , and (Right) united atom model.

Next we study the partial radial distribution function between N^+N^+ along isodyne 5, see Fig. 7.19. We see two peaks in the region $1 < \tilde{r} < 2$ for both models. These peaks seem to behave the same along the isodyne in both models, however, the first peak in the all-atom becomes more narrow and defined than its united atom counterpart. The reason for this is not known.

Lastly we study the partial radial distribution function between N^-N^- along isodyne 5, see Fig. 7.20. Both models have a peak at $\tilde{r} \approx 1.3$ which decreases in intensity as temperature increases along the isodyne. Furthermore, they also both gain a shoulder which evolved to a peak at the higher temperatures.

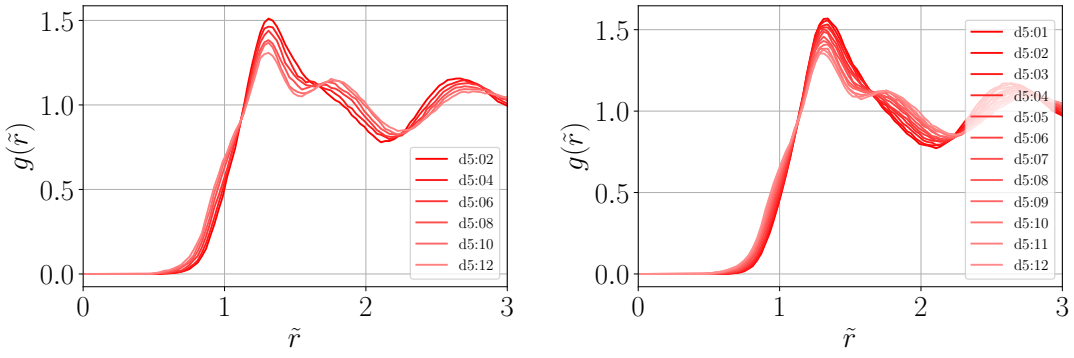

Figure 7.20: The partial radial distribution function between N^-N^- along isodyne 5. (Left) All-atom model , and (Right) united atom model.

7.6 Conclusion

Comparison dynamics with experiments

In Sec. 7.4.1 we compared data from an isotherm with experimental data from Harris et al. [2011]. We found that the pressure in the simulations is much greater than in the experiments (see Fig. 7.4). The simulated viscosity and diffusion coefficient data is within the same region as the experimental (see Fig. 7.6 and Fig. 7.5). However, the slope of the simulation data is noticeably different from that of the experiments. Consequently, it is difficult to say exactly how much slower the model is than the experiments, but it is a bit less than a factor of 2.

Existence of isodynes

In Fig. 7.8 we saw that the system obeys the Stokes-Einstein relation which means that the system has isodynes (at least of D and η). We also see that the dimensionless constant in the relation is the same (or similar) for both models.

We also simulated isodyne 5 from the united atom model. This was to test if the all-atom model has isodynes, and if they are the same as for the united atom model. As was seen in Fig. 7.9 the exact values of $\tilde{D}$ and $1/\tilde{\eta}$ are different, but they show the same degree of invariance. At low densities we see higher values, but since this is the case for both models we interpret this as an artefact of the simulated "isodyne" and not the model.

In Sec. 7.4.4, we analysed the rotation of the molecules by calculating the time autocorrelation function. We found that the molecules generally rotates slower in this model when compared with the united atom model. However, the general behaviour of these rotations show that the invariance are consistent between the two models.

Structure factor peaks along isodynes

In Sec. 7.5.1, we analysed the static structure factor $S(\tilde{q})$ along the isodyne. The isodyne showed the same behaviour as the experimental data from Hansen et al. [2020] with the exception that the height of the main peak is not invariant. This is consistent with previous results for the united atom model.

Partial redial distribution functions

In Sec. 7.5.2 we analysed the partial redial distribution functions between N^+N^-, N^+N^+ and N^-N^- along isodynes. We found that all three partial RDFs behave the same between the two models with only miner differences. The RDF for N^+N^- even has the shoulder/peak which was seen in the united atom model.

Chapter 8

Summary and Conclusions

In this chapter we summarise the important results and conclusions from this work, i.e. Chap. 5, Chap. 6 and Chap. 7. In some cases, this will include a further discussion with comparisons between the three salt models. Lastly, suggestions for further studies are provided.

When starting this project we set out to answer the following questions:

1. Do simulated ILs have lines in the phase diagram where multiple dynamical quantities are invariant? If so, how can these lines be found, and what dynamical quantities are invariant along them?
   The answer to this question is summarised in Sec. 8.1.

2. Which aspects of structure are invariant, and which ones are not invariant, along these lines of invariant dynamics?
   The answer to this question is summarised in Sec. 8.2.

3. What insight in the physics of ILs can be learned from the existence of lines with invariant dynamics, and which microscopic properties are invariant along them?
   For dynamics we analysed molecular rotations (see Sec. 8.1), and for structure we analysed the cation tail and close ion pairs (see Sec. 8.2). We also compared both structure and dynamics between the united atom and all-atom model (see Sec. 8.3). However, there are still many more things to study, some of which are suggested in Sec. 8.4.

8.1 Lines of invariant dynamics

None of the three ionic liquid models, that were studied in this work, have isomorphs in the regions in which they were simulated. This was due to a lack of structural invariance. However, this is in agreement with the experimental results from Hansen et al. [2020]. Instead, all three models were shown to have lines in the phase diagram with invariant dynamics; *isodynes*.

Invariant dynamical quantities along isodynes

For all three models we found that the following dynamical quantities are invariant along isodynes when isomorph scaling is applied;

- The self-intermediate scattering function.
- The mean squared displacement, and consequently the diffusion coefficient.
- The viscosity.
- Furthermore, the product of the diffusion coefficient and the viscosity ($\tilde{D}\tilde{\eta}$) is also invariant for the simulated region. Thus, the reduced Stokes-Einstein relation from Costigliola et al. [2019] is satisfied.

For the two molecular models we also found that some molecular rotations showed invariance while others did not. The rotations that showed invariances, seemed to be the ones with high moment of inertia. This is not well understood, however, it would make sense that the molecule can rotate more freely around an axis of low moment of inertia without influencing the overall dynamics significantly.

Tracing isodynes

In the simple atomic model, isodynes can be traced out as configurational adiabats. This was not the case for the molecular models. For the united atom model many simulations were performed, and the data was fitted to trace the isodynes. We found that the density scaling exponent γ for the molecular isodynes was greater than that for the configurational adiabats.

Existence of isodynes

One of the most remarkable features of isodynes is how stable they seem to be, i.e. they exist in at large part of the phase diagram. This is new, since experiments often study small density intervals in the super-cooled region, where we have shown that the existence of isodynes remain in the high temperature region as well. This robustness of isodynes is new, and one of the main results of this work. The reason for this stability or a potential relation to isomorph theory is unknown.

8.2 The structure of ionic liquids

8.2.1 The structure factor peaks along isodynes

We analysed the total static structure factor for all three models (see Sec. 5.5.2, Sec. 6.5.1, and Sec. 7.5.1). The focus was to explain the behaviour of the main peak and charge peak along isodynes, which would then be compared with the experimental data from Hansen et al. [2020].

The charge peak

We clearly see the charge peak in all three salt models. Tests of the united atom model confirm that the charge peak disappears as the charges are turned off. Furthermore, due to the simplicity of the simple atomic salt model from Hansen and McDonald [1975], it can be shown analytically that the charge peak will be absent if the charges are removed. This is not a new result but it is important.

We found that for all three models the charge peak decreased in intensity and got shifted to lower q as density and temperature increased. This behaviour is in agreement with the experiments from Hansen et al. [2020].

This means that the presence of charges introduces a structural feature which is not invariant along configurational adiabats (or lines of invariant dynamics). Consequently, these models do not have isomorphs which would be associated with invariant structure. However, it is important to remember that the charge interactions become less relevant with increasing density. This means that at sufficiently high densities the charge peak of these systems could be invariant or disappear.

The main peak

The experiments from Hansen et al. [2020] show that the main peak is invariant. This was not the case for our models, as the main peak changed noticeably in both position and height. However, this turned out to be caused by a much bigger density interval. When our data was presented in a density range similar to the experimental (2%) we also observed the main peak to be invariant (see Fig. 5.18 and Fig. 6.40).

Regarding the changes in the main peak, it turns out to be different between the atomic and molecular salt models. In the atomic model (from Chap. 5) the main peak increases in intensity and gets shifted slightly to lower $\tilde{q}$ as density and temperature increases along the isodynes (see Fig. 5.17). This is in contrast to both molecular models (from Chap. 6 and Chap. 7). Here the main peak decreases in intensity and gets shifted slightly to higher $\tilde{q}$ as density and temperature increases along the isodynes (see Fig. 6.39 and Fig. 7.17). Thus the main peak

behaves opposite between the atomic and molecular models. However, the change in position is small when compared to the change in height for all three models.

To better understand this (and IL structure in general), we also analysed the partial radial distribution functions along isodynes.

8.2.2 The radial distribution function along isodynes

The molecular models have several different particle types resulting in many partial radial distribution functions. However, since these features are also present in the simple atomic model we try to find an explanation that does not involve the complexity of the molecular structure. That is, we focus on the overall behaviour of the first peaks and minima instead of the small details.

For the simple atomic model, which only has two atom types, we study $g_{++}(\tilde{r})$ and $g_{+-}(\tilde{r})$ (remember that due to symmetry in this model $g_{++}(\tilde{r}) = g_{--}(\tilde{r})$). For both molecular models, we analysed the partial radial distribution functions between N^+N^+, N^+N^- and N^-N^-, which we here refer to as $g_{++}(\tilde{r})$, $g_{+-}(\tilde{r})$ and $g_{--}(\tilde{r})$, respectively.

The simple atomic model

We analysed the partial radial distribution functions for the simple atomic model in Sec. 5.5.1. The height of the first $g_{+-}(\tilde{r})$ minima increases slightly but not much when considering the density range. The height of the first $g_{++}(\tilde{r})$ minimum decreases along the isodyne as density and temperature increase.

At high densities, the position of the first peak in both $g_{++}(\tilde{r})$ and $g_{+-}(\tilde{r})$ does not change much (see Fig. 5.14). The former moves slightly to smaller $\tilde{r}$ and the latter moves slightly to bigger $\tilde{r}$. The height of the $g_{++}(\tilde{r})$ peak increases along isodynes as density and temperature increase. Correspondingly, the height of the $g_{+-}(\tilde{r})$ peak decreases along isodynes.

Based on this, we believe that the height of the $g_{++}(\tilde{r})$ minima is the main reason why the main structure factor peak increases in height along isodynes. When the $g_{++}(\tilde{r})$ minimum decreases in height it consequently enhances its first peak. The height of first $g_{++}(\tilde{r})$ peak also increases along isodynes, but we are not sure if this is important. This is because both $g_{++}(\tilde{r})$ and $g_{+-}(\tilde{r})$ contribute to the main structure factor peak, and the height of the first $g_{+-}(\tilde{r})$ peak decreases along isodynes such that the total number on neighbours is approximately constant.

The molecular models

The partial radial distribution functions behaved the same for both molecular models, so they will both be described here. The first minima in $g_{+-}(\tilde{r})$ was invariant in both position and height in the simulated range. Furthermore, the height of the first peak decreased along isodynes. This behaviour is similar to the simple atomic model.

The first minima in both $g_{++}(\tilde{r})$ and $g_{--}(\tilde{r})$ increased in height along isodynes. Furthermore, the first peak in both $g_{++}(\tilde{r})$ and $g_{--}(\tilde{r})$ decreased in height as density increased along the isodyne. This behaviour is opposite to the simple atomic model.

Based on this, we again think that the first minima in both $g_{++}(\tilde{r})$ and $g_{--}(\tilde{r})$ is an important part of why the main structure factor peak decreases in height along isodynes in the molecular models. The fact that the height of the first peak also decreases would amplify this behaviour.

We believe this difference in behaviour between the atomic and molecular models comes from the added disorder in the molecular packing. Additionally, the molecules are flexible meaning that their closest separation is not as clearly delineated as for the atomic model.

8.2.3 Molecular substructure: Shoulder/peak

When analysing the partial radial distribution functions along isodynes for both molecular models, we found an interesting feature (see Sec. 6.5.2 and Sec. 7.5.2). At low temperatures and high densities the partial radial distribution function between N^+ and N^- had an extra shoulder/peak at short distances which disappeared as temperature increased (consequently it is not invariant along isodynes). This lead to the discovery of a substructure between close ion pairs which is described for the united atom model in Sec. 6.5.3. A corresponding analysis was not performed for the all-atom model, however, the existence of the shoulder/peak gives us reason to believe it is also present in that model. It might even be more important in the all-atom model since the shoulder/peak (despite getting smaller) never disappeared along the simulated isodyne which was the case for the united atom model (see Fig. 7.18).

We found that more anions are a part of this substructure than cations (see Fig. 6.51). Additionally, we found that anions are only a part of one close pair while cations can be a part of multiple, but most are only a part of one close pair (see Fig. 6.52). We did not observe any cases where a cation was a part of three pairs.

The tetrahedron structure in Pyr_{14} is important for the formation of this structure. The structure arises when N^- in the anion comes close of one of the four faces

in the tetrahedron structure (see Fig. 6.53). This creates a preferred orientation of the anion relative to the cation, specifically such that the two S atoms are pointed away from the cation (see Fig. 6.56). We believe this orientational preference is the reason why each anion is only part of one close pair.

The significance of this substructure is still unknown. It is not invariant along isodynes as the shoulder/peak disappears at high temperatures.

8.2.4 Preferred orientation of the cation tail

In Sec. 6.5.5, we studied the preferred orientation of the cation tail for the united atom model. This analysis was done for two isochores and one isodyne. For this we used two measures:

- The distance between the start and end of the tail (N^+ and T_4), also referred to as the tail distance. This was to get an idea of whether the tail is curled up or stretches.
- Three dihedral-angles between atoms in the tail and two extra atoms (N^+ and C_e) to gain information about the orientation relative to the ring.

We found that distribution of the the tail distance depended on both density and temperature. The tail prefers to be stretched at low densities and curled up at high densities, and increasing the temperature generally broadens the distribution (see Fig. 6.61).

We found that the two dihedral-angles between atoms closest to the ring were very temperature dependent (see Fig. 6.62 and 6.63). This combined with our knowledge of the model (specifically which non-bonded interactions are excluded) lead us to believe this is caused by the non-bonded interaction between the tail and the rest of the molecule.

Lastly, we studied the dihedral-angle between the four atoms in the tail (see Fig. 6.64). We found that this is dependent on both density and temperature. Furthermore, we found that this dihedral-angle distribution is invariant in the interval $\pi/6 < \theta_{0123} < (5/6)\pi$ along the isodyne. The significance on this is unknown, however, it could mean that this dihedral-angle is important for the dynamics. We also found a strong correlation between this dihedral-angle and the tail distance. This means that when this dihedral-angle is π, the tail is stretched, and curled up when the angle is 0.

8.3 United atom vs. all-atom model

Both models show the same overall behaviour, however, the united atom model has a lower pressure and is generally faster than the all-atom model (Fig. 7.3 and Fig. 7.9). We also see that the united atom model generally is faster than the all-atom model.

8.3.1 Comparison with experiments

Pressure

In Sec. 7.4.1, we compared an isotherm with $T = 50$ °C for both models with experimental data from Harris et al. [2011]. We found that the pressure of the united atom model was within the same range as the experimental data, but the shape of the curve was different (see Fig. 7.4). The all-atom model has a pressure around 100 MPa greater than the experimental data, however, if the curve is shifted down we see that its shape more closely resembles the experimental data than the united atom model. We showed for the united atom model that the choice of cutoff for the potential greatly affects the pressure. Thus, a longer cutoff could make the all-atom model the better of the two in this respect.

Dynamics

We also compared the viscosities and diffusion coefficients with the experiments (see Fig. 7.6 and Fig. 7.5). All the data fitted fairly well to an exponential function with variable ρ. In both cases, the united atom model was faster than the experimental data, while the all-atom model was slower than the experimental data. However, it is difficult to determine which of the two models is a better representation of the experimental data.

8.3.2 Isodynes

The biggest question when comparing dynamics between the two models is whether they have the same isodynes in the $\rho-T$ phase diagram. We tested this in Sec. 7.4.3 where we simulated isodyne 5 from the united atom model with the all-atom model.

First, we found that both the correlation between potential energy and virial (Eq. 4.18) and density scaling exponent (Eq. 4.18) are bigger for the united atom model than for the all-atom model (see Fig. 7.7). This is not surprising given the extra hydrogen bonds in the all-atom model.

Next, we found that not only do both models satisfy the reduced Stokes-Einstein relation, they also have a similar value (see Fig. 7.8). We compared

the viscosities and diffusion coefficients to further test if isodyne 5 is also an isodyne for the all-atom model (see Fig. 7.9). Here we do not see perfect invariance but comparable to that of the united atom model.

Lastly, we analysed the rotations of the molecules (see Fig. 7.10 - 7.16). We generally saw a similar degree of invariance between the two models, but in some cases the all-atom model seemed to be slightly less invariant. The cause of this is unknown, however, for the united atom model we found isodyne 5 to be slightly less invariant than the other isodynes. This could be related.

In conclusion, the isodynes from the united atom model might not have the exact same shape in the $\rho - T$ phase diagram as the isodynes from the all-atom model. However, they are very good approximations.

8.3.3 Structure

Structure factor peaks along isodynes

In Sec. 6.5.1 and 7.5.1, we analysed the static structure factor $S(\tilde{q})$ along isodyne 5. The two models generally behaved the same, and even behaved the same is the experimental data from Hansen et al. [2020] when presented in a similar density interval. From this is seems like the essential structural features are the same.

Partial radial distribution functions

In Sec. 7.5.2, we analysed the partial radial distribution functions between N^+N^-, N^+N^+, and N^-N^- for both models. We found that all three partial radial distribution functions looked and behaved the same with only slight differences. Our two examples of this are:

- The first peak in the partial radial distribution functions between N^+N^+ is slightly more defined in the all-atom model (see Fig. 7.19).
- The shoulder/peak in the partial radial distribution functions between N^+N^- does not disappear in the simulated range (see Fig. 7.18).

8.4 Further studies

8.4.1 Structure in the united atom model

The N^-N^- partial radial distribution function

It would be interesting to perform further analysis of structure. Examples of this could be the extra peak which arises in the N^-N^- partial radial distribution function along isodynes. Such an analysis could lead to a substructure as the one we described in Sec. 6.5.3.

Partial invariance of the cation tail

We found that the dihedral angle distribution in the end of the cation tail showed partial invariance (see Sec. 6.5.5). It would be interesting to analyse and understand this further, since this is one of the few aspects of structure which showed invariance along isodynes.

8.4.2 The all-atom model

Existence of isodynes

We found that the isodyne we tested from the united atom model also is a very good approximation on an isodyne for the all-atom model. However, it would be very interesting to further test the existence and shape of isodynes for the all-atom model. This will tell us if the slightly less invariant molecular rotations were caused by our choice of isodyne or if it is a general feature of the all-atom model. This could be done by simulating other isodynes from the united atom model. That approach would also inform where in the phase diagram the two models have the same/similar isodynes. If this method turns to be insufficient for other parts of the phase diagram (i.e. the united atom isodynes are not isodynes for the all-atom model), a more extensive study where isodynes are traced out for the all-atom model would be interesting.

Orientation on the cation tail

It would be interesting to find how the presence of hydrogen affects the preferred orientations of the cation tail. We found that one of the three dihedrals showed slight invariance along isodynes. It would be interesting to see if this is still the case with the additional hydrogen.

Existence of shoulder/peak substructure

Based on the partial radial distribution function between N^+ and N^-, we do believe that the shoulder/peak substructure is also present in the all-atom model. The fact that the shoulder/peak seems more stable in this model makes us hypothesize that the substructure could be even more pronounced here. It would be interesting to find if this is the case.

8.4.3 Existence of isodynes in other models

It would be interesting to analyse variations of our molecular models and test how that affects the existence of isodynes. This would test the robustness of isodynes. Examples of variation could be;

- Varying the length of the tail in the cation. This would be interesting since many ILs are designed with long tails.
- Add lithium ions (Li) to the simulations. This would be interesting since one of the main potential applications for ILs are as solvents in batteries.

Other studies (both experimental and computational) have already studied these IL groups, so they are of interest in the scientific community. An example of a study which did both could be Aguilera et al. [2015]. However, here the main focus was on how they affected the structure.

Additionally, it would be interesting to find if isodynes also exist in other IL models with very different chemical structures. This would tell us how universal isodynes are.

Thank you for reading.
I hope you enjoyed!

Chapter 9

Bibliography

Henriette Wase Hansen, Filippa Lundin, Karolina Adrjanowicz, Bernhard Frick, Aleksandar Matic, and Kristine Niss. Density scaling of structure and dynamics of an ionic liquid. *Physical Chemistry Chemical Physics*, 22, 2020. doi: 10.1039/D0CP01258K.

P. Walden. Ueber die molekulargrösse und elektrische leitfähigkeit einiger geschmolzenen salze. *Bulletin de l'Académie Impériale des Sciences de St.-Pétersbourg. VI série*, 8(6):405–422, 1914. URL `http://mi.mathnet.ru/izv6491`.

Shaik M. Zakeeruddin and Michael Grätzel. Solvent-free ionic liquid electrolytes for mesoscopic dye-sensitized solar cells. *Advanced Functional Materials*, 19(14): 2187–2202, 2009. doi: https://doi.org/10.1002/adfm.200900390. URL `https://onlinelibrary.wiley.com/doi/abs/10.1002/adfm.200900390`.

Andrew Webber and George E. Blomgren. *Ionic Liquids for Lithium Ion and Related Batteries*, pages 185–232. Springer US, Boston, MA, 2002. ISBN 978-0-306-47508-5. doi: 10.1007/0-306-47508-1_7. URL `https://doi.org/10.1007/0-306-47508-1_7`.

Chengfeng Ye, Weimin Liu, Yunxia Chen, and Laigui Yu. Room-temperature ionic liquids: a novel versatile lubricant. *Chem. Commun.*, pages 2244–2245, 2001. doi: 10.1039/B106935G. URL `http://dx.doi.org/10.1039/B106935G`.

M Freemantle. Designer solvents. *Chemical & Engineering News Archive*, 76(13): 32–37, 1998. doi: 10.1021/cen-v076n013.p032. URL `https://doi.org/10.1021/cen-v076n013.p032`.

Yong-Lei Wang, Bin Li, Sten Sarman, Francesca Mocci, Zhong-Yuan Lu, Jiayin Yuan, Aatto Laaksonen, and Michael D. Fayer. Microstructural and dy-

namical heterogeneities in ionic liquids. *Chemical Reviews*, 120(13):5798–5877, 2020. doi: 10.1021/acs.chemrev.9b00693. URL https://doi.org/10.1021/acs.chemrev.9b00693. PMID: 32292036.

Jason P. Hallett and Tom Welton. Room-temperature ionic liquids: Solvents for synthesis and catalysis. 2. *Chemical Reviews*, 111(5):3508–3576, 2011. doi: 10.1021/cr1003248. URL https://doi.org/10.1021/cr1003248. PMID: 21469639.

Markus Bier and S. Dietrich. Vapour pressure of ionic liquids. *Molecular Physics*, 108(2):211–214, 2010. doi: 10.1080/00268971003604609. URL https://doi.org/10.1080/00268971003604609.

Yauheni U. Paulechka, Gennady J. Kabo, Andrey V. Blokhin, Oleg A. Vydrov, Joseph W. Magee, and Michael Frenkel. Thermodynamic properties of 1-butyl-3-methylimidazolium hexafluorophosphate in the ideal gas state. *Journal of Chemical & Engineering Data*, 48(3):457–462, 2003. doi: 10.1021/je025591i. URL https://doi.org/10.1021/je025591i.

David R. Lide. *CRC Handbook of Chemistry and Physics*. CRC Press, 85th edition, 2004. ISBN 978-0-8493-0485-9.

Tom Welton. Ionic liquids: a brief history. *Biophysical Reviews*, 10(3):691–706, June 2018.

Juan C. Araque, Jeevapani J. Hettige, and Claudio J. Margulis. Modern room temperature ionic liquids, a simple guide to understanding their structure and how it may relate to dynamics. *The Journal of Physical Chemistry B*, 119(40): 12727–12740, 2015. doi: 10.1021/acs.jpcb.5b05506. URL https://doi.org/10.1021/acs.jpcb.5b05506. PMID: 26244375.

Luis Aguilera, Johannes Völkner, Ana Labrador, and Aleksandar Matic. The effect of lithium salt doping on the nanostructure of ionic liquids. *Phys. Chem. Chem. Phys.*, 17:27082–27087, 2015. doi: 10.1039/C5CP03825A. URL http://dx.doi.org/10.1039/C5CP03825A.

Enriqueta R. López, Alfonso S. Pensado, María J. P. Comuñas, Agílio A. H. Pádua, Josefa Fernández, and Kenneth R. Harris. Density scaling of the transport properties of molecular and ionic liquids. *The Journal of Chemical Physics*, 134 (14):144507, 2011. doi: 10.1063/1.3575184. URL https://doi.org/10.1063/1.3575184.

Jeppe C. Dyre. Hidden scale invariance in condensed matter. *The Journal of Physical Chemistry B*, 118(34):10007–10024, 2014. doi: 10.1021/jp501852b. URL https://doi.org/10.1021/jp501852b. PMID: 25011702.

Jean Pierre Hansen and Ian R. McDonald. Statistical mechanics of dense ionized matter. IV. Density and charge fluctuations in a simple molten salt. *Phys. Rev. A*, 11:2111–2123, Jun 1975. doi: 10.1103/PhysRevA.11.2111. URL https://link.aps.org/doi/10.1103/PhysRevA.11.2111.

Daan Frenkel and Berend Smit. *Understanding Molecular Simulation: From Algorithms to Applications*, volume 1 of *Computational Science Series*. Academic Press, second edition, 2002. ISBN 978-0-12-267351-1. URL https://www.amazon.com/Understanding-Molecular-Simulation-Applications-Computational/dp/0122673514?SubscriptionId=AKIAIOBINVZYXZQZ2U3A&tag=chimbori05-20&linkCode=xm2&camp=2025&creative=165953&creativeASIN=0122673514.

Reinier L. C. Akkermans and Giovanni Ciccotti. On the equivalence of atomic and molecular pressure. *The Journal of Physical Chemistry B*, 108(21):6866–6869, 2004. doi: 10.1021/jp037680n. URL https://doi.org/10.1021/jp037680n.

D. M. Heyes. Pressure tensor of partial-charge and point-dipole lattices with bulk and surface geometries. *Phys. Rev. B*, 49:755–764, Jan 1994. doi: 10.1103/PhysRevB.49.755. URL https://link.aps.org/doi/10.1103/PhysRevB.49.755.

Loup Verlet. Computer "experiments" on classical fluids. i. thermodynamical properties of lennard-jones molecules. *Phys. Rev.*, 159:98–103, Jul 1967. doi: 10.1103/PhysRev.159.98. URL https://link.aps.org/doi/10.1103/PhysRev.159.98.

Harald A. Posch, William G. Hoover, and Franz J. Vesely. Canonical dynamics of the nosé oscillator: Stability, order, and chaos. *Phys. Rev. A*, 33:4253–4265, Jun 1986. doi: 10.1103/PhysRevA.33.4253. URL https://link.aps.org/doi/10.1103/PhysRevA.33.4253.

R. LeSar. *Introduction to Computational Materials Science: Fundamentals to Applications*. Cambridge University Press, 2013. ISBN 9781107328143. URL https://books.google.dk/books?id=QzkhAwAAQBAJ.

J. E. Jones and Sydney Chapman. On the determination of molecular fields.—i. from the variation of the viscosity of a gas with temperature. *Proceedings of the Royal Society of London. Series A, Containing Papers of a Mathematical and Physical Character*, 106(738):441–462, 1924a. doi:

10.1098/rspa.1924.0081. URL https://royalsocietypublishing.org/doi/abs/10.1098/rspa.1924.0081.

J. E. Jones and Sydney Chapman. On the determination of molecular fields. —ii. from the equation of state of a gas. *Proceedings of the Royal Society of London. Series A, Containing Papers of a Mathematical and Physical Character*, 106(738):463–477, 1924b. doi: 10.1098/rspa.1924.0082. URL https://royalsocietypublishing.org/doi/abs/10.1098/rspa.1924.0082.

Søren Toxvaerd and Jeppe C. Dyre. Communication: Shifted forces in molecular dynamics. *The Journal of Chemical Physics*, 134(8):081102, 2011. doi: 10.1063/1.3558787. URL https://doi.org/10.1063/1.3558787.

J. S. Hansen, Thomas B. Schrøder, and Jeppe C. Dyre. Simplistic coulomb forces in molecular dynamics: Comparing the wolf and shifted-force approximations. *The Journal of Physical Chemistry B*, 116(19):5738–5743, 2012. doi: 10.1021/jp300750g. URL https://doi.org/10.1021/jp300750g. PMID: 22497264.

Daniel Berthelot. Sur le mélange des gaz. *Compt. Rendus*, 126(3), 1898.

H. A. Lorentz. Ueber die anwendung des satzes vom virial in der kinetischen theorie der gase. *Annalen der Physik*, 248(1):127–136, 1881. doi: https://doi.org/10.1002/andp.18812480110. URL https://onlinelibrary.wiley.com/doi/abs/10.1002/andp.18812480110.

Bonded interactions, 2019. URL https://manual.gromacs.org/documentation/2019/reference-manual/functions/bonded-interactions.html.

Bernard Monasse and Frédéric Boussinot. Determination of forces from a potential in molecular dynamics. 01 2014.

M.P. Allen, D.J. Tildesley, and D.J. Tildesley. *Computer Simulation of Liquids*. Oxford science publications. Oxford University Press, 2017. ISBN 9780198803195. URL https://books.google.dk/books?id=nlExDwAAQBAJ.

File:phase-diag2.svg, a. URL https://en.wikipedia.org/wiki/File:Phase-diag2.svg.

Phase diagrams: Density-temperature plane, b. URL http://www.sklogwiki.org/SklogWiki/index.php/Phase_diagrams:_Density-temperature_plane.

Léon Van Hove. Correlations in space and time and born approximation scattering in systems of interacting particles. *Phys. Rev.*, 95:249–262, Jul 1954. doi: 10.1103/PhysRev.95.249. URL https://link.aps.org/doi/10.1103/PhysRev.95.249.

P. A. Egelstaff. *An Introduction to the Liquid State*, volume 7 of *Oxford Series on Neutron Scattering in Condensed Matter*. Clarendon Press, second edition, 1994. ISBN 0-19-851750-5. URL https://www.amazon.com/Introduction-Liquid-Neutron-Scattering-Condensed/dp/0198517505?SubscriptionId=AKIAIOBINVZYXZQZ2U3A&tag=chimbori05-20&linkCode=xm2&camp=2025&creative=165953&creativeASIN=0198517505.

Henry E Fischer, Adrian C Barnes, and Philip S Salmon. Neutron and x-ray diffraction studies of liquids and glasses. *Reports on Progress in Physics*, 69(1): 233–299, nov 2005. doi: 10.1088/0034-4885/69/1/r05. URL https://doi.org/10.1088%2F0034-4885%2F69%2F1%2Fr05.

A. B. Bhatia and D. E. Thornton. Structural aspects of the electrical resistivity of binary alloys. *Phys. Rev. B*, 2:3004–3012, Oct 1970. doi: 10.1103/PhysRevB.2.3004. URL https://link.aps.org/doi/10.1103/PhysRevB.2.3004.

Richard P. Feynman. *Feynman lectures on physics. Volume 2: Mainly electromagnetism and matter*. 1964.

D. M. Heyes, E. R. Smith, and D. Dini. Shear stress relaxation and diffusion in simple liquids by molecular dynamics simulations: Analytic expressions and paths to viscosity. *The Journal of Chemical Physics*, 150(17):174504, 2019. doi: 10.1063/1.5095501. URL https://doi.org/10.1063/1.5095501.

N H March and M P Tosi. *Introduction to Liquid State Physics*. WORLD SCIENTIFIC, 2002. doi: 10.1142/4717. URL https://www.worldscientific.com/doi/abs/10.1142/4717.

Lorenzo Costigliola, David M. Heyes, Thomas B. Schrøder, and Jeppe C. Dyre. Revisiting the stokes-einstein relation without a hydrodynamic diameter. *The Journal of Chemical Physics*, 150(2):021101, 2019. doi: 10.1063/1.5080662. URL https://doi.org/10.1063/1.5080662.

Nicoletta Gnan, Thomas B. Schrøder, Ulf R. Pedersen, Nicholas P. Bailey, and Jeppe C. Dyre. Pressure-energy correlations in liquids. iv. "isomorphs" in liquid phase diagrams. *The Journal of Chemical Physics*, 131(23):234504, 2009. doi: 10.1063/1.3265957. URL https://doi.org/10.1063/1.3265957.

Thomas B. Schrøder and Jeppe C. Dyre. Simplicity of condensed matter at its core: Generic definition of a roskilde-simple system. *The Journal of Chemical Physics*, 141(20):204502, 2014. doi: 10.1063/1.4901215. URL https://doi.org/10.1063/1.4901215.

Yaakov Rosenfeld. Relation between the transport coefficients and the internal entropy of simple systems. *Phys. Rev. A*, 15:2545–2549, Jun 1977. doi: 10.1103/PhysRevA.15.2545. URL https://link.aps.org/doi/10.1103/PhysRevA.15.2545.

Yaakov Rosenfeld. A quasi-universal scaling law for atomic transport in simple fluids. *Journal of Physics: Condensed Matter*, 11(28):5415–5427, jan 1999. doi: 10.1088/0953-8984/11/28/303. URL https://doi.org/10.1088/0953-8984/11/28/303.

Ian H. Bell, Richard Messerly, Monika Thol, Lorenzo Costigliola, and Jeppe C. Dyre. Modified entropy scaling of the transport properties of the lennard-jones fluid. *The Journal of Physical Chemistry B*, 123(29):6345–6363, 2019. doi: 10.1021/acs.jpcb.9b05808. URL https://doi.org/10.1021/acs.jpcb.9b05808. PMID: 31241958.

C M Roland, S Hensel-Bielowka, M Paluch, and R Casalini. Supercooled dynamics of glass-forming liquids and polymers under hydrostatic pressure. *Reports on Progress in Physics*, 68(6):1405–1478, may 2005. doi: 10.1088/0034-4885/68/6/r03. URL https://doi.org/10.1088/0034-4885/68/6/r03.

T. C. Ransom, R. Casalini, D. Fragiadakis, and C. M. Roland. The complex behavior of the "simplest" liquid: Breakdown of density scaling in tetramethyl tetraphenyl trisiloxane. *The Journal of Chemical Physics*, 151(17):174501, 2019. doi: 10.1063/1.5121021. URL https://doi.org/10.1063/1.5121021.

Arno A. Veldhorst, Jeppe C. Dyre, and Thomas B. Schrøder. Scaling of the dynamics of flexible lennard-jones chains. *The Journal of Chemical Physics*, 141(5):054904, 2014. doi: 10.1063/1.4888564. URL https://doi.org/10.1063/1.4888564.

Andreas Elmerdahl Olsen, Jeppe C. Dyre, and Thomas B. Schrøder. Communication: Pseudoisomorphs in liquids with intramolecular degrees of freedom. *The Journal of Chemical Physics*, 145(24):241103, 2016. doi: 10.1063/1.4972860. URL https://doi.org/10.1063/1.4972860.

Peter A. Knudsen, Kristine Niss, and Nicholas P. Bailey. Quantifying dynamical and structural invariance in a simple molten salt model. *The Journal of Chemical Physics*, 155(5):054506, 2021. doi: 10.1063/5.0055794. URL https://doi.org/10.1063/5.0055794.

J.-P. Hansen and I. R. McDonald. *Theory of Simple Liquids with Applications to Soft Matter*. Academic Press, 4th edition, 2013.

Kenneth R. Harris. Thermodynamic or density scaling of the electrical conductivity of molten salts. *The Journal of Chemical Physics*, 156(5):054501, 2022. doi: 10.1063/5.0079796. URL https://doi.org/10.1063/5.0079796.

William L. Jorgensen, Jayaraman Chandrasekhar, Jeffry D. Madura, Roger W. Impey, and Michael L. Klein. Comparison of simple potential functions for simulating liquid water. *The Journal of Chemical Physics*, 79(2):926–935, 1983. doi: 10.1063/1.445869. URL https://doi.org/10.1063/1.445869.

William L. Jorgensen and Julian Tirado-Rives. The opls [optimized potentials for liquid simulations] potential functions for proteins, energy minimizations for crystals of cyclic peptides and crambin. *Journal of the American Chemical Society*, 110(6):1657–1666, 1988. doi: 10.1021/ja00214a001. URL https://doi.org/10.1021/ja00214a001. PMID: 27557051.

William L. Jorgensen, David S. Maxwell, and Julian Tirado-Rives. Development and testing of the opls all-atom force field on conformational energetics and properties of organic liquids. *Journal of the American Chemical Society*, 118 (45):11225–11236, 1996. doi: 10.1021/ja9621760. URL https://doi.org/10.1021/ja9621760.

Somisetti V. Sambasivarao and Orlando Acevedo. Development of opls-aa force field parameters for 68 unique ionic liquids. *Journal of Chemical Theory and Computation*, 5(4):1038–1050, 2009. doi: 10.1021/ct900009a. URL https://doi.org/10.1021/ct900009a. PMID: 26609613.

Brian Doherty, Xiang Zhong, Symon Gathiaka, Bin Li, and Orlando Acevedo. Revisiting opls force field parameters for ionic liquid simulations. *Journal of Chemical Theory and Computation*, 13(12):6131–6145, 2017. doi: 10.1021/acs.jctc.7b00520. URL https://doi.org/10.1021/acs.jctc.7b00520. PMID: 29112809.

José N. Canongia Lopes and Agílio A. H. Pádua. Molecular force field for ionic liquids composed of triflate or bistriflylimide anions. *The Journal of Physical Chemistry B*, 108(43):16893–16898, 2004. doi: 10.1021/jp0476545. URL https://doi.org/10.1021/jp0476545.

Huabin Xing, Xu Zhao, Qiwei Yang, Baogen Su, Zongbi Bao, Yiwen Yang, and Qilong Ren. Molecular dynamics simulation study on the absorption of ethylene and acetylene in ionic liquids. *Industrial & Engineering Chemistry Research*, 52(26):9308–9316, 2013. doi: 10.1021/ie400999f. URL https://doi.org/10.1021/ie400999f.

Wendy D. Cornell, Piotr Cieplak, Christopher I. Bayly, Ian R. Gould, Kenneth M. Merz, David M. Ferguson, David C. Spellmeyer, Thomas Fox, James W. Caldwell, and Peter A. Kollman. A second generation force field for the simulation of proteins, nucleic acids, and organic molecules. *Journal of the American Chemical Society*, 118(9):2309–2309, 1996. doi: 10.1021/ja955032e. URL https://doi.org/10.1021/ja955032e.

Zhiping Liu, Shiping Huang, and Wenchuan Wang. A refined force field for molecular simulation of imidazolium-based ionic liquids. *The Journal of Physical Chemistry B*, 108(34):12978–12989, 2004. doi: 10.1021/jp048369o. URL https://doi.org/10.1021/jp048369o.

William L. Jorgensen, Jeffry D. Madura, and Carol J. Swenson. Optimized intermolecular potential functions for liquid hydrocarbons. *Journal of the American Chemical Society*, 106(22):6638–6646, 1984. doi: 10.1021/ja00334a030. URL https://doi.org/10.1021/ja00334a030.

Alexander M. Smondyrev and Max L. Berkowitz. United atom force field for phospholipid membranes: Constant pressure molecular dynamics simulation of dipalmitoylphosphatidicholine/water system. *Journal of Computational Chemistry*, 20(5):531–545, 1999. doi: https://doi.org/10.1002/(SICI)1096-987X(19990415)20:5⟨531::AID-JCC5⟩3.0.CO;2-3. URL https://onlinelibrary.wiley.com/doi/abs/10.1002/%28SICI%291096-987X%2819990415%2920%3A5%3C531%3A%3AAID-JCC5%3E3.0.CO%3B2-3.

Igor Leontyev and Alexei Stuchebrukhov. Accounting for electronic polarization in non-polarizable force fields. *Phys. Chem. Chem. Phys.*, 13:2613–2626, 2011. doi: 10.1039/C0CP01971B. URL http://dx.doi.org/10.1039/C0CP01971B.

Brian J. Kirby and Pavel Jungwirth. Charge scaling manifesto: A way of reconciling the inherently macroscopic and microscopic natures of molecular simulations. *The Journal of Physical Chemistry Letters*, 10(23):7531–7536, 2019. doi: 10.1021/acs.jpclett.9b02652. URL https://doi.org/10.1021/acs.jpclett.9b02652. PMID: 31743030.

Gabriel D. Barbosa, Xiaoyang Liu, Kathryn E. O'Harra, Jason E. Bara, and C. Heath Turner. Charge scaling parameter evaluation for multivalent ionic liquids with fixed point charge force fields. *Journal of Ionic Liquids*, 2(1):100020, 2022. ISSN 2772-4220. doi: https://doi.org/10.1016/j.jil.2022.100020. URL https://www.sciencedirect.com/science/article/pii/S2772422022000040.

Kenneth R. Harris, Lawrence A. Woolf, Mitsuhiro Kanakubo, and Thomas Rüther. Transport properties of n-butyl-n-methylpyrrolidinium bis(trifluoromethylsulfonyl)amide. *Journal of Chemical & Engineering Data*, 56(12):4672–4685, 2011. doi: 10.1021/je2006049. URL https://doi.org/10.1021/je2006049.

Chenqian Xu and Zhenmin Cheng. Thermal stability of ionic liquids: Current status and prospects for future development. *Processes*, 9(2), 2021. ISSN 2227-9717. doi: 10.3390/pr9020337. URL https://www.mdpi.com/2227-9717/9/2/337.

Frederik Philippi, David Pugh, Daniel Rauber, Tom Welton, and Patricia A. Hunt. Conformational design concepts for anions in ionic liquids. *Chem. Sci.*, 11:6405–6422, 2020. doi: 10.1039/D0SC01379J. URL http://dx.doi.org/10.1039/D0SC01379J.

D Mc Kie and C Mc Kie. Essentials of crystallography. 1 1986. URL https://www.osti.gov/biblio/6095054.

Travis Mackoy, Nicholas A. Mauro, and Ralph A. Wheeler. Temperature dependence of static structure factor peak intensities for a pyrrolidinium-based ionic liquid. *The Journal of Physical Chemistry B*, 123(7):1672–1678, 2019. doi: 10.1021/acs.jpcb.9b00449. URL https://doi.org/10.1021/acs.jpcb.9b00449. PMID: 30673263.

Nicholas P. Bailey, Lasse Bøhling, Arno A. Veldhorst, Thomas B. Schrøder, and Jeppe C. Dyre. Statistical mechanics of roskilde liquids: Configurational adiabats, specific heat contours, and density dependence of the scaling exponent. *The Journal of Chemical Physics*, 139(18):184506, 2013. doi: 10.1063/1.4827090. URL https://doi.org/10.1063/1.4827090.

Appendix A

Notation and Terminology

This is a list of the most important notation used in this work. This notation system is not universal, but we have tried to use the most common notation.

A.1 Physics notation

Name	**Symbol**	**Name**	**Symbol**
Mass	m or M	Density	ρ
Charge	q	Temperature	T
Time	t	Pressure	P
Position	r, x, y, or z	Volume	V
Velocity	v	Diffusion coefficient	D
Acceleration	a	Viscosity	η
Momentum	p		
Force	F		
Potential energy	$V(r)$		

Table A.1: List of symbols for physics notation used in this work.

A.2 Mathematical notation

Name	Symbol	Description
Vector	$\boldsymbol{v}$	An ordered set of numbers. Has many uses, for example represent positions in space, $\boldsymbol{r} = (x; y; z)$.
Vector norm	$\lvert\boldsymbol{v}\rvert$	We use the Euclidean norm, $\lvert\boldsymbol{v}\rvert = \sqrt{\sum_j v_j^2}$
The imaginary unit	i	An mathematical element with the property $i^2 = -1$.
Complex conjugate	c^*	Given a complex number $c = a + ib$ then $c^* = a - ib$.
First time derivative	$\dot{f}(t) = \dfrac{df}{dt}$	The first order derivative of a function $f(t)$ with respect to time t.
Second time derivative	$\ddot{f}(t) = \dfrac{d^2 f}{dt^2}$	The second order derivative of a function $f(t)$ with respect to time t.

Table A.2: Mathematical notation used in this work.

The dot product is an operator which takes two vectors of the same size and gives a real number , that is $\mathbb{R}^n \times \mathbb{R}^n \to \mathbb{R}$;

$$\boldsymbol{v} \cdot \boldsymbol{u} = \begin{pmatrix} v_1 \\ v_2 \\ \vdots \\ v_n \end{pmatrix} \cdot \begin{pmatrix} u_1 \\ u_2 \\ \vdots \\ u_n \end{pmatrix} = \sum_{j=1}^{n} v_j u_j \tag{A.1}$$

The cross product is an operator which takes two vectors of size 3 and gives a third vector of size 3, that is $\mathbb{R}^3 \times \mathbb{R}^3 \to \mathbb{R}^3$. This resulting vector is orthogonal to the other two.

$$\boldsymbol{v} \times \boldsymbol{u} = \begin{pmatrix} v_x \\ v_y \\ v_z \end{pmatrix} \times \begin{pmatrix} u_x \\ u_y \\ u_z \end{pmatrix} = \begin{pmatrix} v_y u_z - v_z u_y \\ v_z u_x - v_x u_z \\ v_x u_y - v_y u_x \end{pmatrix} \tag{A.2}$$

A.3 Simulation notation

Table A.3: List of notation related to simulation used in this work.

Name	Symbol	Description
Position vector	$\boldsymbol{r_j}$	Spacial position of particle j, $\boldsymbol{r_j} = (x_j; y_j; z_j)$.
Relative position vector	$\boldsymbol{r_{jk}}$	Vector from particle j to k, $\boldsymbol{r_{jk}} = \boldsymbol{r_k} - \boldsymbol{r_j}$
Relative distance	r_{jk}	Distance between particle j and k, $r_{jk} = \lvert\boldsymbol{r_{jk}}\rvert$.
Unit vector	$\boldsymbol{e_{jk}}$	Unit vector between particle j and k, $\boldsymbol{e_{jk}} = \boldsymbol{r_{jk}}/r_{jk}$.
Normal vector	$\boldsymbol{n_{jkl}}$	A vector normal to the plane spanned by three points, $\boldsymbol{r_j}$, $\boldsymbol{r_k}$, and $\boldsymbol{r_l}$.
Configuration vector	$\boldsymbol{R}$	A vector containing positions of all N particles in a d-dimensional system. It has length of dN.
Configuration vector (CM)	$\boldsymbol{R_{CM}}$	A vector containing the center of mass positions of all N molecules/particles in a d-dimensional system.
The wave-vector	$\boldsymbol{q}$	Has units of inverse distance, and is used in e.g. the structure factor, see Sec. 3.3.2.
Potential energy	$V(r)$	The potential energy between particles.
Truncation/cutoff	r_{cut}	The distance at which a potential is set to be 0, see section 2.4.1.
Simulation box length	L_x, L_y, L_z	The different side lengths of the simulation box.

Continued on next page

Table A.3 – continued from previous page

Name	Symbol	Description
Image positions	Im_x, Im_y, Im_z	Integers representing the number of times a particle has been moved to the other side of the box when periodic boundary conditions are applied. This is used for analysis of the dynamics (see sec. 2.5).
Ensemble average	$\langle \cdots \rangle$	Averaging of the quantity " $\cdots$ " weighted by the probability of their microstate.

A.4 Physics terminology

Table A.4: List of physics terminology used in this work.

Name	Description
Macroscopic scale	Properties at this length scale can be observed with the naked eye. Such as, temperature, volume, and pressure.
Microscopic scale	Properties at this length scale are dependant on the positions of the atoms. Such as, the multiplicity, and entropy.
Amorphous	From Greek; 'without'-'shape/from'. Used to describe materials with no long range structure.
Isotropic	From Greek; 'equal'-'way'. In the context of material science means independents of direction.
Adiabatic	A process with no transfer of heat, $Q = 0$.
Isobaric	A process at constant pressure, $\Delta P = 0$.
Isothermal	A process at constant temperature, $\Delta T = 0$.
Isochoric	A process at constant volume, $\Delta V = 0$.
Quasistatic	A process which happens slow enough that the system remains in internal equilibrium.
Excess entropy, S_{ex}	The entropy of the system minus the entropy from an ideal gas at equal temperature and density state point.
Configurational adiabat	Constant excess entropy, $\Delta S_{ex} = 0$ [Bailey et al., 2013].
Isomorphs	From Greek; 'equal'-'shape/from'. Describes configurational adiabats with high correlation between the virial and the potential energy, $R > 0.9$ (see chapter 4).

Appendix B

Extra Theory, Results and Parameters

B.1 Molecular Dynamics - Initial Configuration

As stated earlier, MD is a method which can be used to describe how a system moves and behaves using Newton's equations of motion. However, before we can find the positions and velocities of particles in a system at a given time, t, we need their positions and velocities at an initial time, t_0. In this section, we will explain how to define an initial configuration. However, in this work the initial configuration itself is not of interest, since the system will be equilibrated before data is collected.

System size

The first thing we need to consider is how many particles and/or molecules should be simulate. This is referred to as the system size. Ideally, we would like to simulate large systems to represent reality, but this would also lead to long simulation times. The question then becomes:

How small can the system be and still give reliable results in a " reasonable" time?

Unfortunately, there is no universal answer to this question, since it depends both on the system and the computers used to perform the simulation. It can therefore be a good idea to test different system sizes. However, there are some guidelines for the minimal system size, that will be described in Sec. 2.5. Furthermore, different optimization methods, such as neighbour-lists, has been developed to help with this issue.

Particle positions

Once the system size has been decided one should choose the initial positions of the particles/molecules. It is very common to place them in a lattice structure, such as a body-centered cubic or face-centered cubic lattice, see Fig. B.1. They can be ordered by types for multicomponent system or randomly distributed on the lattice cites. However, it is important to note that the system most likely will not form this structure naturally, and it is therefore important to equilibrate the system before collecting data. When studying liquids, this equilibration is often performed at high temperatures to ensure that the initial lattice structure gets erased in the process.

For molecular systems one would define a xyz-file with the positions of the atoms in the molecule. Likewise a top-file (topology) with a list of the bonded interactions within the molecule would also be needed.

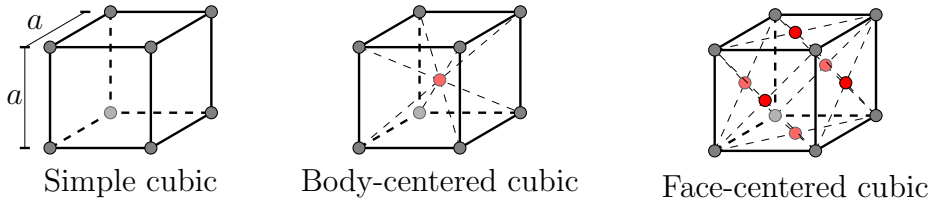

Figure B.1: Illustrations of the unit cells of the simple cubic, the body-centered cubic, and the face-centered cubic lattice. The lattice sites which should be added to the SC to obtain the BCC and FCC are marked with red.

Particle velocities

The initial velocities are often chosen randomly since the system will need equilibration anyway. It is common to choose these velocities such that the total momentum of the system is zero. However, for large systems this is also true of the velocities are chosen randomly. Some simulation programs, like RUMD, will occasionally enforce this criterion and update the velocities during the simulation. This is done to avoid drift and for conservation of momentum.

The relation between particle velocities and temperature will be explained later in Sec. 2.2.

B.2 United Atom Model - Test Intra Atomic Interactions

We performed a series of simulations with varying amount of detail to test the intra-molecular interactions. For consistency all these simulations were run at the same state point, $\rho = 3.2$ nm^{-3} and $T = 498.15$ K, with a mixture of 200 ion pairs. We initially ran three simulations:

- one with bond, angle, and dihedral potentials ("B1 A1 D1")
- one with bond, and angle potentials ("B1 A1 D0")
- one with only bond potentials ("B1 A0 D0")

It is important to remember that when we add intra-molecular potentials between atoms we also exclude the non-bonded Lennard-Jones and Coulomb potentials, see Sec. 2.4.2. Consequently, we decided to run two extra simulations where the Lennard-Jones and Coulomb potentials were excluded while the bonded potential was inactive:

- one with bond, and angle potentials, but dihedral exclusion ("B1 A1 De")
- one with only bond potentials, but angle and dihedral exclusion ("B1 Ae De")

To get an idea of how these interactions affect the entire system, we decided to calculate the pressure (P) and diffusion coefficient (D) for the two atoms N^+ and N^-, see Tab. B.1. We see that these interactions have great impact on the dynamics and pressure of the system.

Simulation name	P [Pa]	D_{N^+} [m^2 s^{-1}]	D_{N^-} [m^2 s^{-1}]
B1 Ae De	$-2.7211 \cdot 10^7$	$2.3315 \cdot 10^{-12}$	$8.4663 \cdot 10^{-13}$
B1 A1 De	$-8.9056 \cdot 10^6$	$1.8186 \cdot 10^{-9}$	$1.6451 \cdot 10^{-9}$
B1 A1 D1	$-3.7267 \cdot 10^6$	$1.7379 \cdot 10^{-9}$	$1.6449 \cdot 10^{-9}$
B1 A1 D0	$1.5330 \cdot 10^7$	$1.4084 \cdot 10^{-9}$	$1.3349 \cdot 10^{-9}$
B1 A0 D0	$1.2360 \cdot 10^8$	$8.1044 \cdot 10^{-10}$	$7.3834 \cdot 10^{-10}$

Table B.1: List of the pressure and diffusion coefficient for simulations at $\rho = 3.2$ nm^{-3} and $T = 498.15$ K with different a number of intra-molecular interactions.

To test the effectiveness of the constraints we calculated the distribution of bonded atom distances, the angles, and the dihedral angles. The distribution of these distances and angles can be seen in Fig. B.2, B.3, and B.4.

When looking at the bonds the first thing we notice is that "B1 A0 D0" generally is pushed to further distances than the potential intends. This was counter-intuitive at first until we remembered the strong Coulomb interactions which are no linger excluded.

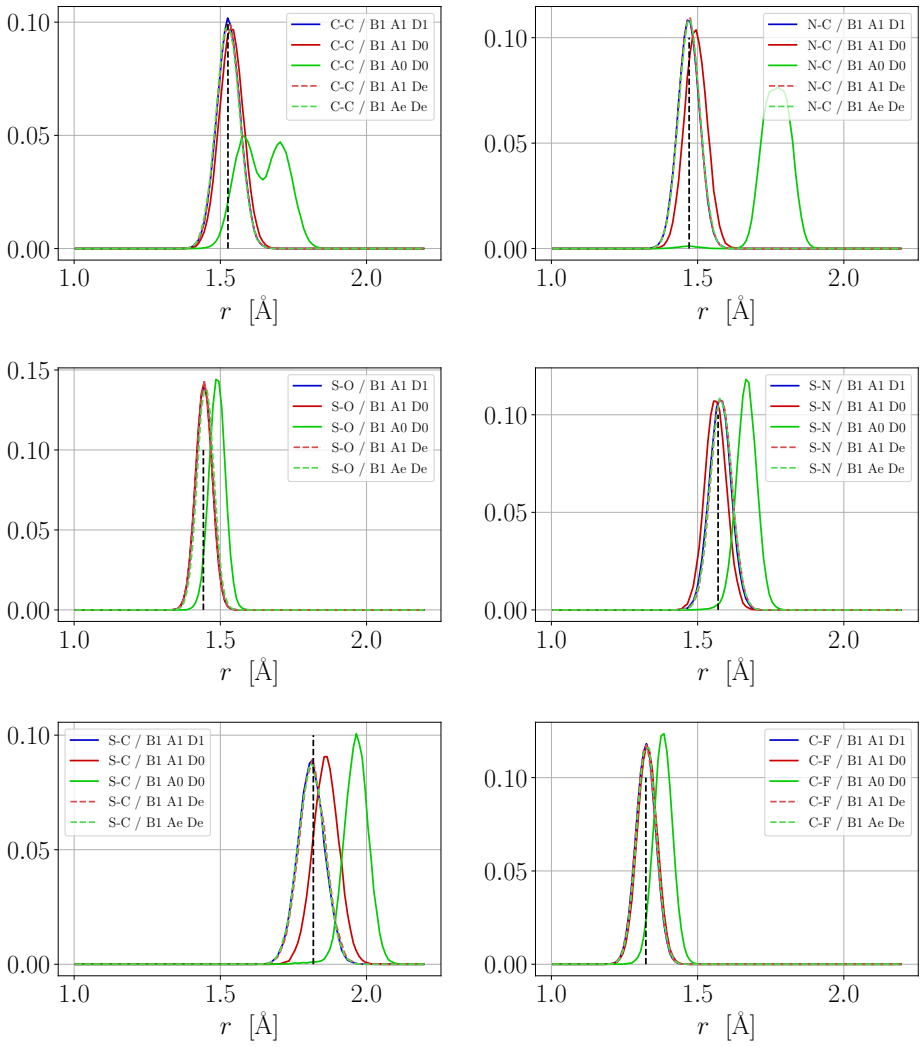

Figure B.2: Test of bond-distributions. The vertical dashed line indicate the distance preferred by the potential.

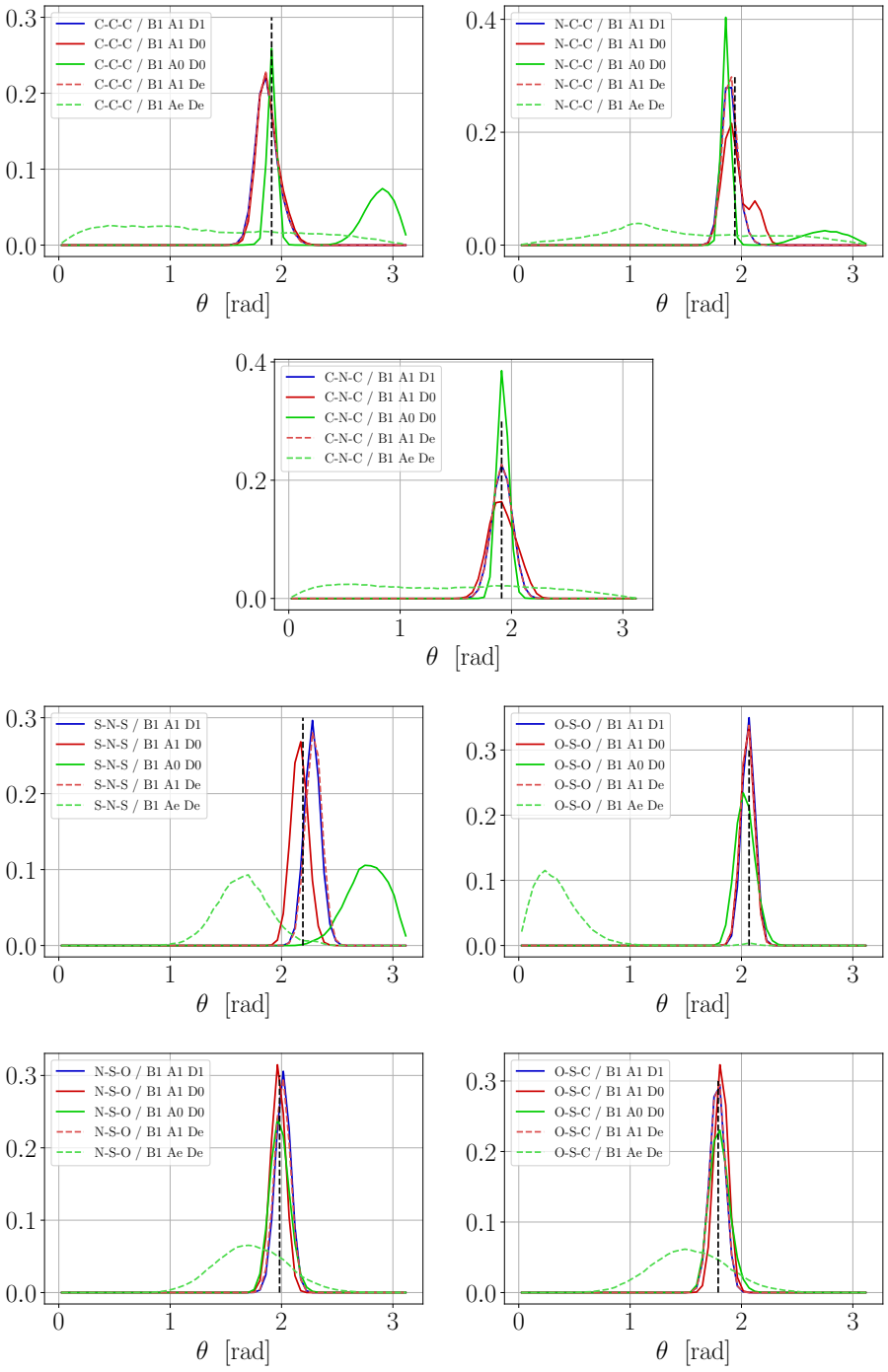

Figure B.3: Test of angle-distributions. The vertical dashed line indicate the angle preferred by the potential.

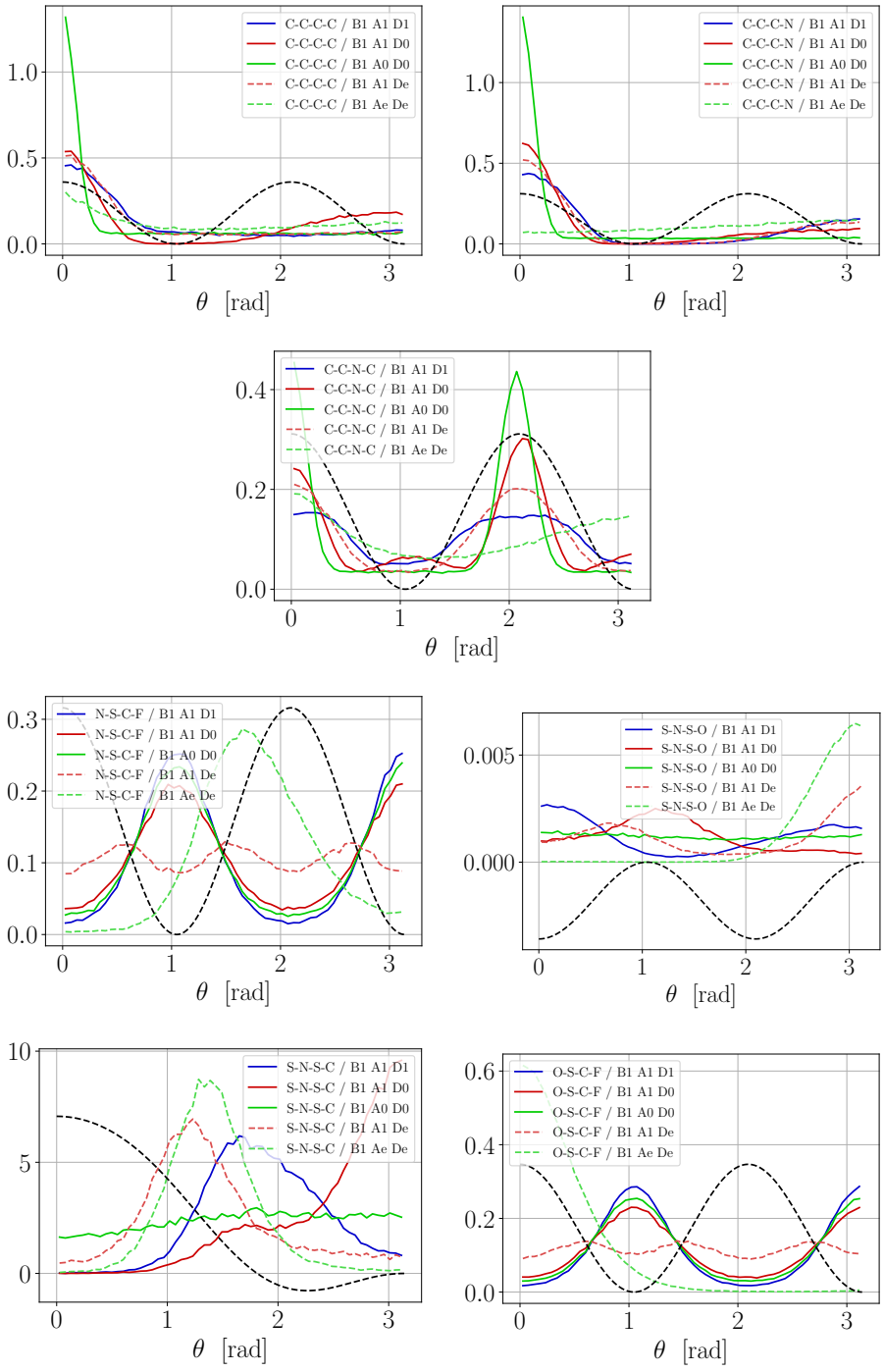

Figure B.4: Test of dihedral-distributions. The dashed line indicate the (scaled) dihedral-potential.

B.3 Molecular Models - Dihedral Parameters

The dihedral parameters for the united atom model can be seen in Tab. B.2 in both *Fourier (OPLS)* and *Ryckaert-Bellemans* notation.

$$\frac{1}{2}\sum_{n=1}^{4} V_n \left[1 + (-1)^{n+1}\cos\left(n\theta\right)\right]$$

Fourier Dihedrals (OPLS)

Name	V_1	V_2	V_3	V_4 [kcal/mol]
C-C-C-C	0.0	0.0	0.360	0.0
C-C-C-N	0.0	0.0	0.311	0.0
C-C-N-C	0.0	0.0	0.311	0.0
N-S-C-F	0.0	0.0	0.3160	0.0
S-N-S-O	0.0	0.0	-0.0036	0.0
S-N-S-C	7.8329	-2.4904	-0.7636	0.0
O-S-C-F	0.0	0.0	0.3468	0.0

$$\sum_{n=0}^{5} C_n \left(-\cos\left(\theta\right)\right)^n$$

Ryckaert-Bellemans Dihedrals

Name	C_0	C_1	C_2	C_3	C_4	C_5 [kcal/mol]
C-C-C-C	0.180	0.540	0.0	-0.720	0.0	0.0
C-C-C-N	0.156	0.467	0.0	-0.622	0.0	0.0
C-C-N-C	0.156	0.467	0.0	-0.622	0.0	0.0
N-S-C-F	0.1580	0.4739	0.0	-0.6319	0.0	0.0
S-N-S-O	-0.0018	-0.0054	0.0	0.0072	0.0	0.0
S-N-S-C	1.044	-5.062	2.490	1.527	0.0	0.0
O-S-C-F	0.1734	0.5202	0.0	-0.6936	0.0	0.0

Table B.2: Bonded parameters for Pyr_{14} and TFSI. All Pyr_{14} parameters are from Xing et al. [2013]. All TFSI parameters are from Canongia Lopes and Pádua [2004]. The translation between the two dihedral potentials can be found in Sec. 2.4.2.

The dihedral parameters for the all-atom model can be seen in Tab. B.3 in both *Fourier (OPLS)* and *Ryckaert-Bellemans* notation.

$$\frac{1}{2}\sum_{n=1}^{4} V_n \left[1 + (-1)^{n+1}\cos\left(n\theta\right)\right]$$

Fourier Dihedrals (OPLS)

Name	V_1	V_2	V_3	V_4 [kcal/mol]
C-C-C-C	0.0	0.0	0.360	0.0
C-C-C-N	0.0	0.0	0.311	0.0
C-C-N-C	0.0	0.0	0.311	0.0
H_s-C-C-C	0.0	0.0	0.312	0.0
H_s-C-N-C	0.0	0.0	0.311	0.0
H_s-C-C-H_l	0.0	0.0	0.312	0.0
H_l-C-C-H_l	0.0	0.0	0.300	0.0
H_l-C-C-N	0.0	0.0	0.311	0.0
H_l-C-C-C	0.0	0.0	0.320	0.0

$$\sum_{n=0}^{5} C_n \left(-\cos\left(\theta\right)\right)^n$$

Ryckaert-Bellemans Dihedrals

Name	C_0	C_1	C_2	C_3	C_4	C_5 [kcal/mol]
C-C-C-C	0.180	0.540	0.0	-0.720	0.0	0.0
C-C-C-N	0.156	0.467	0.0	-0.622	0.0	0.0
C-C-N-C	0.156	0.467	0.0	-0.622	0.0	0.0
H_s-C-C-C	0.156	0.468	0.0	-0.624	0.0	0.0
H_s-C-N-C	0.156	0.467	0.0	-0.622	0.0	0.0
H_s-C-C-H_l	0.156	0.468	0.0	-0.624	0.0	0.0
H_l-C-C-H_l	0.150	0.450	0.0	-0.600	0.0	0.0
H_l-C-C-N	0.156	0.467	0.0	-0.622	0.0	0.0
H_l-C-C-C	0.160	0.480	0.0	-0.640	0.0	0.0

Table B.3: All-atom bonded parameters for Pyr_{14} from Xing et al. [2013]. The translation between the two dihedral potentials can be found in Sec. 2.4.2.

Appendix C

RUMD Molecule Files

C.1 RUMD configuration and topology files

In RUMD topology files the first column indicates which molecule; the last column indicates which bond/angle/dihedral interaction is used; the central columns show the number of the particles in the interaction. So a bond between particle 4 and 5 of bond-type 2 in molecule 0 would be ”0 4 5 2”.

C.1.1 Pyr_{14} (united atom)

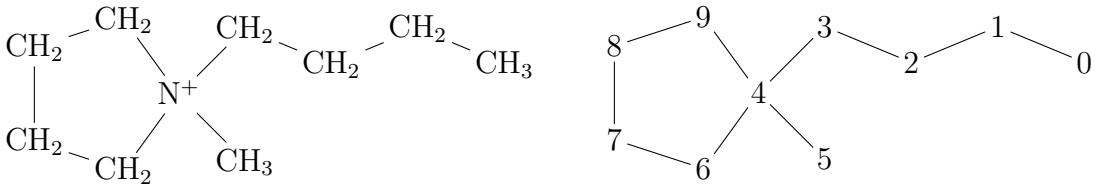

Atom	N	CH_2	CH_2	CH_2	CH_2	CH_3	CH_3
Name	N^+	R_1	R_2	T_1	T_m	T_4	C_e
Type	0	1	2	3	4	5	6

Table C.1: United atom names and types in the cation.

```
1  10
   numTypes=7 mass=14.007 , 14.026, 14.026, 14.026, 14.026,
      15.034, 15.034
   5   1.000000   1.000000  0.000000
   4  -0.519000   1.000000  0.000000
   4  -1.096000   1.000000  1.421000
6  3  -2.624000   1.002000  1.345000
   0  -3.336000   1.000000  2.713000
   6  -2.939000  -0.216000  3.535000
   1  -4.861000   0.975000  2.458000
   2  -5.223000   2.437000  2.318000
11 2  -4.419000   3.085000  3.423000
   1  -3.110000   2.308000  3.502000
```

```
[ bonds ]
;
0  0  1  0
0  1  2  0
0  2  3  0
0  3  4  1
0  4  5  1
0  4  6  1
0  6  7  0
0  7  8  0
0  8  9  0
0  4  9  1
```

```
[ angles ]
;
0  0  1  2  0
0  1  2  3  0
0  2  3  4  1
0  3  4  5  2
0  3  4  6  2
0  4  6  7  1
0  6  7  8  0
0  3  4  9  2
0  5  4  9  2
0  4  9  8  1
0  6  4  9  1
0  5  4  6  2
0  7  8  9  0
```

```
[ dihedrals ]
;
0  0  1  2  3  0
0  6  7  8  9  0
0  1  2  3  4  1
0  7  8  9  4  1
0  8  7  6  4  1
0  2  3  4  5  2
0  2  3  4  6  2
0  2  3  4  9  2
0  7  6  4  3  2
0  7  6  4  5  2
0  7  6  4  9  2
0  8  9  4  3  2
0  8  9  4  5  2
0  8  9  4  6  2
```

C.1.2 TFSI (united atom)

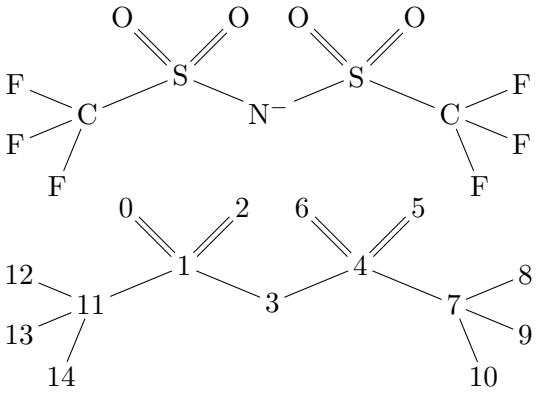

Atom	N	S	O	C	F
Name	N^-	S	O	C	F
Type	7	8	9	10	11

Table C.2: United atom names and types in the anion.

```
15
numTypes=5 mass=14.007, 32.060, 15.999, 12.011, 18.998
9   1.000000   1.000000   0.000000
8  -0.449000   1.000000   0.000000
9  -1.174000   1.000000   1.255000
7  -0.922000   2.384000  -0.808000
8  -0.288000   3.853000  -0.337000
9  -0.995000   4.793000  -1.195000
9  -0.479000   3.964000   1.096000
10  1.531000   3.825000  -0.788000
11  1.830000   2.822000  -1.659000
11  1.897000   4.984000  -1.409000
11  2.337000   3.695000   0.300000
10 -1.117000  -0.357000  -1.093000
11 -1.834000   0.167000  -2.132000
11 -0.140000  -1.130000  -1.637000
11 -1.966000  -1.183000  -0.422000
```

```
[ bonds ]
;
0   0   1  2
0   1   2  2
0   1   3  3
0   3   4  3
0   4   5  2
0   4   6  2
0   4   7  4
0   7   8  5
0   7   9  5
0   7  10  5
0   1  11  4
0  11  12  5
0  11  13  5
0  11  14  5

[ angles ]
;
0   0   1   2  4
0   0   1   3  5
0   1   3   4  3
0   3   4   5  5
0   3   4   6  5
0   3   4   7  7
0   4   7   8  8
0   4   7   9  8
0   4   7  10  8
0   0   1  11  6
0   1  11  12  8
0   1  11  13  8
0   1  11  14  8
0  12  11  13  9
0   3   1  11  7
0  12  11  14  9
0   9   7  10  9
0   8   7   9  9
0  13  11  14  9
0   5   4   6  4
0   2   1   3  5
0   2   1  11  6
0   5   4   7  6
0   8   7  10  9
0   6   4   7  6

[ dihedrals ]
;
0  3  4   7   8  3
0  3  4   7   9  3
0  3  4   7  10  3
0  3  1  11  12  3
0  3  1  11  13  3
0  3  1  11  14  3
0  1  3   4   5  4
0  1  3   4   6  4
0  4  3   1   0  4
0  4  3   1   2  4
0  1  3   4   7  5
0  4  3   1  11  5
0  5  4   7   8  6
0  5  4   7   9  6
0  5  4   7  10  6
0  6  4   7   8  6
0  6  4   7   9  6
0  6  4   7  10  6
0  0  1  11  12  6
0  0  1  11  13  6
0  0  1  11  14  6
0  2  1  11  12  6
0  2  1  11  13  6
0  2  1  11  14  6
```

C.1.3 Pyr_{14} (all-atom)

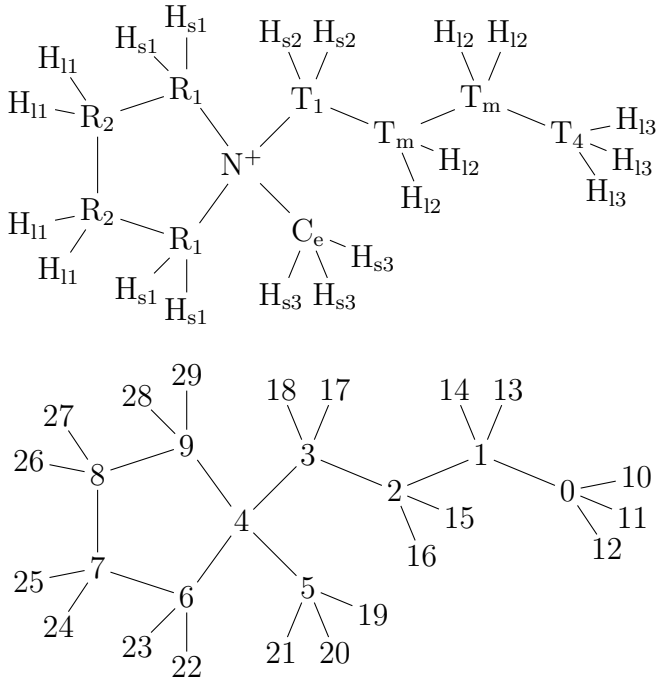

Atom	N	C	C	C	C	C	C	H	H	H	H	H	H
Name	N^+	R_1	R_2	T_1	T_m	T_4	C_e	H_{l1}	H_{l2}	H_{l3}	H_{s1}	H_{s2}	H_{s3}
Type	0	1	2	3	4	5	6	7	8	9	10	11	12

Table C.3: All-atom names and types in the cation.

```
1  30
   numTypes=13 mass=14.007, 12.011, 12.011, 12.011, 12.011,
      12.011, 12.011, 1.008, 1.008, 1.008, 1.008, 1.008, 1.008
   5     1.000000     1.000000     0.000000
4  4    -0.521000     1.000000     0.000000
   4    -1.073000     1.000000     1.428000
   3    -2.603000     1.066000     1.419000
   0    -3.223000     1.134000     2.833000
   6    -2.811000    -0.074000     3.664000
9  1    -4.762000     1.160000     2.709000
   2    -5.089000     2.627000     2.554000
   2    -4.152000     3.296000     3.534000
   1    -2.881000     2.456000     3.548000
   9     1.379000     0.999000    -1.026000
14 9     1.392000     0.114000     0.509000
```

```
    9      1.390000      1.890000      0.506000
    8     -0.883000      0.117000     -0.538000
    8     -0.879000      1.884000     -0.541000
    8     -0.644000      1.849000      1.968000
19  8     -0.731000      0.090000      1.930000
   11     -3.016000      0.173000      0.935000
   11     -2.947000      1.951000      0.872000
   12     -3.059000     -0.977000      3.100000
   12     -3.359000     -0.050000      4.610000
24 12     -1.738000     -0.016000      3.863000
   10     -5.182000      0.766000      3.642000
   10     -5.074000      0.537000      1.866000
    7     -6.139000      2.840000      2.777000
    7     -4.888000      2.967000      1.532000
29  7     -4.596000      3.312000      4.536000
    7     -3.944000      4.334000      3.253000
   10     -2.566000      2.231000      4.574000
   10     -2.068000      2.957000      3.020000
```

```
 1 [ bonds ]
   ;
 3 0   1   0  0
   0   2   1  0
   0   3   2  0
   0   4   3  1
   0   5   4  1
 8 0   6   4  1
   0   7   6  0
   0   8   7  0
   0   9   4  1
   0   9   8  0
13 0  10   0  2
   0  11   0  2
   0  12   0  2
   0  13   1  2
   0  14   1  2
18 0  15   2  2
   0  16   2  2
   0  17   3  2
   0  18   3  2
   0  19   5  2
23 0  20   5  2
   0  21   5  2
   0  22   6  2
   0  23   6  2
   0  24   7  2
28 0  25   7  2
   0  26   8  2
   0  27   8  2
   0  28   9  2
   0  29   9  2
33

   [ angles ]
   ;
   0   0   1   2   0
38 0   1   2   3   0
   0   2   3   4   1
   0   3   4   5   2
   0   3   4   6   2
   0   4   6   7   1
43 0   6   7   8   0
   0   3   4   9   2
   0   1   0  10   4
   0   1   0  11   4
   0   1   0  12   4
48 0   0   1  13   4
   0   0   1  14   4
   0   1   2  15   4
   0   1   2  16   4
   0   2   3  17   4
53 0   2   3  18   4
   0   4   5  19   3
   0   4   5  20   3
   0   4   5  21   3
   0   4   6  22   3
58 0   4   6  23   3
   0   6   7  24   4
   0   6   7  25   4
   0   7   8  26   4
   0   7   8  27   4
63 0   4   9  28   3
   0   4   9  29   3
   0  22   6  23   5
   0   8   7  24   4
   0  15   2  16   5
68 0   2   1  13   4
   0   2   1  14   4
```

```
    0  10   0  12   5
    0   9   8  27   4
    0   8   9  28   4
73  0  20   5  21   5
    0   5   4   9   2
    0  19   5  21   5
    0   4   9   8   1
    0   6   4   9   2
78  0   8   9  29   4
    0   7   6  22   4
    0  10   0  11   5
    0   5   4   6   2
    0  11   0  12   5
83  0  13   1  14   5
    0   4   3  18   3
    0  26   8  27   5
    0  24   7  25   5
    0   8   7  25   4
88  0   3   2  15   4
    0   3   2  16   4
    0   7   6  23   4
    0  19   5  20   5
    0   7   8   9   0
93  0   4   3  17   3
    0  17   3  18   5
    0   9   8  26   4
    0  28   9  29   5

98  [ dihedrals ]
    ;
    0   3   2   1   0   0
    0   9   8   7   6   0
    0   8   7   6   4   1
103 0   7   8   9   4   1
    0   7   6   4   3   2
    0   8   9   4   6   2
    0   8   9   4   5   2
    0   8   9   4   3   2
108 0   7   6   4   5   2
    0   9   4   6   7   2
    0   9   4   3   2   2
    0   5   4   3   2   2
    0   6   4   3   2   2
113 0  22   6   7   8   3
    0  16   2   1   0   8
    0  15   2   1   0   8
    0  12   0   1   2   8
    0  25   7   8   9   8
118 0  26   8   7   6   8
    0  23   6   7   8   3
    0  11   0   1   2   8
    0  29   9   8   7   3
    0  27   8   7   6   8
123 0  18   3   2   1   8
    0  13   1   2   3   8
    0  14   1   2   3   8
    0  24   7   8   9   8
    0  28   9   8   7   3
128 0  17   3   2   1   8
    0  10   0   1   2   8
    0  16   2   1  13   6
    0  24   7   6  23   5
    0  18   3   2  16   5
133 0  14   1   0  12   6
    0  28   9   8  26   5
    0  13   1   0  10   6
    0  25   7   6  22   5
    0  17   3   2  15   5
138 0  24   7   6  22   5
    0  15   2   1  14   6
    0  25   7   6  23   5
    0  13   1   0  11   6
    0  14   1   0  10   6
143 0  27   8   7  25   6
    0  27   8   7  24   6
    0  29   9   8  26   5
    0  15   2   1  13   6
    0  26   8   7  25   6
148 0  28   9   8  27   5
    0  18   3   2  15   5
    0  29   9   8  27   5
    0  13   1   0  12   6
    0  14   1   0  11   6
153 0  26   8   7  24   6
    0  17   3   2  16   5
    0  16   2   1  14   6
    0  16   2   3   4   7
    0  26   8   9   4   7
158 0  24   7   6   4   7
    0  25   7   6   4   7
    0  27   8   9   4   7
    0  15   2   3   4   7
    0  22   6   4   5   4
163 0  23   6   4   9   4
    0  17   3   4   5   4
    0  28   9   4   3   4
    0  22   6   4   9   4
    0  20   5   4   9   4
168 0  23   6   4   3   4
    0  19   5   4   3   4
    0  21   5   4   3   4
    0  21   5   4   9   4
    0  22   6   4   3   4
173 0  23   6   4   5   4
    0  19   5   4   9   4
    0  18   3   4   9   4
    0  19   5   4   6   4
    0  20   5   4   3   4
178 0  28   9   4   6   4
    0  18   3   4   5   4
    0  20   5   4   6   4
    0  28   9   4   5   4
    0  29   9   4   6   4
183 0  17   3   4   9   4
    0  18   3   4   6   4
    0  29   9   4   3   4
    0  21   5   4   6   4
    0  17   3   4   6   4
188 0  29   9   4   5   4
    0   4   3   2   1   1
```

C.1.4 TFSI (all-atom)

The only difference between the united atom and all-atom versions of the TFSI-files is the atom-type number, the bond-type number, angle-type number, and dihedral-type numbers. These were changed to make room for the six types of hydrogen.

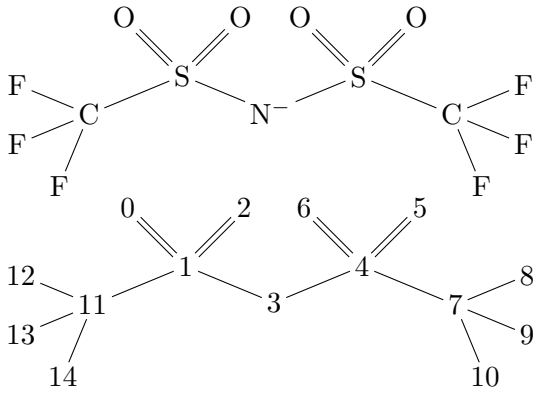

Atom	N	S	O	C	F
Name	N^-	S	O	C	F
Type	13	14	15	16	17

Table C.4: All-atom names and types in the anion.

```
15
numTypes=5 mass=14.007, 32.060, 15.999, 12.011, 18.998
15   1.000000   1.000000   0.000000
14  -0.449000   1.000000   0.000000
15  -1.174000   1.000000   1.255000
13  -0.922000   2.384000  -0.808000
14  -0.288000   3.853000  -0.337000
15  -0.995000   4.793000  -1.195000
15  -0.479000   3.964000   1.096000
16   1.531000   3.825000  -0.788000
17   1.830000   2.822000  -1.659000
17   1.897000   4.984000  -1.409000
17   2.337000   3.695000   0.300000
16  -1.117000  -0.357000  -1.093000
17  -1.834000   0.167000  -2.132000
17  -0.140000  -1.130000  -1.637000
17  -1.966000  -1.183000  -0.422000
```

```
[ bonds ]
;
0   0   1  3
0   1   2  3
0   1   3  4
0   3   4  4
0   4   5  3
0   4   6  3
0   4   7  5
0   7   8  6
0   7   9  6
0   7  10  6
0   1  11  5
0  11  12  6
0  11  13  6
0  11  14  6

[ angles ]
;
0   0   1   2   7
0   0   1   3   8
0   1   3   4   6
0   3   4   5   8
0   3   4   6   8
0   3   4   7  10
0   4   7   8  11
0   4   7   9  11
0   4   7  10  11
0   0   1  11   9
0   1  11  12  11
0   1  11  13  11
0   1  11  14  11
0  12  11  13  12
0   3   1  11  10
0  12  11  14  12
0   9   7  10  12
0   8   7   9  12
0  13  11  14  12
0   5   4   6   7
0   2   1   3   8
0   2   1  11   9
0   5   4   7   9
0   8   7  10  12
0   6   4   7   9

[ dihedrals ]
;
0  3  4   7   8   9
0  3  4   7   9   9
0  3  4   7  10   9
0  3  1  11  12   9
0  3  1  11  13   9
0  3  1  11  14   9
0  1  3   4   5  10
0  1  3   4   6  10
0  4  3   1   0  10
0  4  3   1   2  10
0  1  3   4   7  11
0  4  3   1  11  11
0  5  4   7   8  12
0  5  4   7   9  12
0  5  4   7  10  12
0  6  4   7   8  12
0  6  4   7   9  12
0  6  4   7  10  12
0  0  1  11  12  12
0  0  1  11  13  12
0  0  1  11  14  12
0  2  1  11  12  12
0  2  1  11  13  12
0  2  1  11  14  12
```

Appendix D

Posters and Papers

D.1 Posters

D.1.1 Poster 1 - Simple atomic model

The first poster presents some of the results from the Hansen & McDonald simple atomic salt model described in Chap. 5. The focus is on the invariant dynamics (self-intermediate scattering function and mean square displacement), and the varying structure (the position of the first peak in the partial radial distribution function).

One will notice that this is an early poster, since we refer to the configurational adiabats as "isomorphs" which they are not due to the lack of structural invariance.

D.1.2 Poster 2 - United atom model

The second poster presents some of the results from the united atom model described in Chap. 6. The focus is on the existence of isodynes (same shape of $\tilde{D}$ and $1/\tilde{\eta}$ contours), and comparing structure and dynamics with experimental data.

Here one will notice that the shape and value of the viscosity are more in agreement with experimental data than what we presented in Fig. 6.17. This is because this data is from a previous version of the united atom model in which some parameters were different. In this early version, the intra-molecular angle potential between OSO in the anion was wrong (the angle preferred by the potential $\theta_{0,OSO}$ was accidentally set equal to the $\theta_{0,OSC}$ angle). Consequently, the different pressure guided us to scale the charges by 0.9 instead of the 0.8, which was used in the final version. However, one should be aware that η is presented as a function of pressure which we have since shown is very dependent on the cutoff for the non-bonded interactions.

An investigation of isomorphs in the Hansen and McDonald molten salt model

Peter Alexander Knudsen (pealkn@ruc.dk) Kristine Niss Nicholas Bailey

Department of Science and Environment, Roskilde University

I. What Are We Working With?

- Experimental results for structure in the ionic liquid PYR_{14}^{+} $TFSI^{-}$ have shown invariance in the main structure factor peak, along curves of equal electrical conductivity. It was also shown that the charge structure factor peak is not invariant along these curves.
- We have studied the structure and dynamics of a simple model of an ionic liquids with molecular dynamics computer simulations.

II. Which Model Are We Using?

- We have worked with the simple salt model described in Hansen and McDonald [1]. This model contains two types of spherical particles (A and B) who are identical except for their opposite charge.
- The potential between the particles is

$$V_{\alpha\beta}(r) = \frac{1}{9}\left(\frac{1}{r}\right)^9 + \epsilon_{\alpha\beta}\left(\frac{1}{r}\right)$$

where $\epsilon_{AA} = \epsilon_{BB} = 1$ and $\epsilon_{AB} = \epsilon_{BA} = -1$.

- Furthermore periodic boundary conditions and the shifted force cut-off method was implemented.

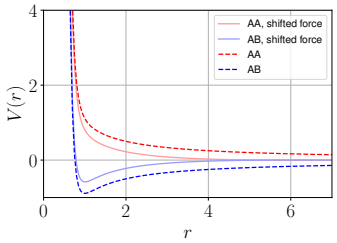

III. What Did We Find?

- Three different isomorphs were simulated and the results were compared with six different isotherms.

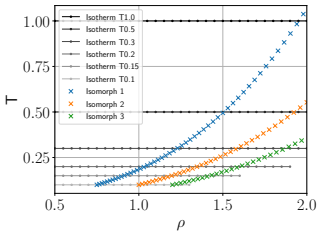

We found that:

- the *self-intermediate scattering function* (Fs), and the *mean square displacement* (msd) are invariant along isomorphs which is not the case for the isotherms.
- the structure is not invariant, but it generally changes less along the isomorphs than the isotherms.

Structure

- Example of radial distribution function data along isomorph 1 and isotherm $T = 1.0$.

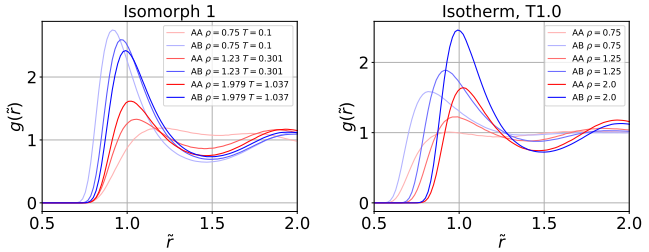

- We have analysed the position of the first peak in $g(\tilde{r})$.

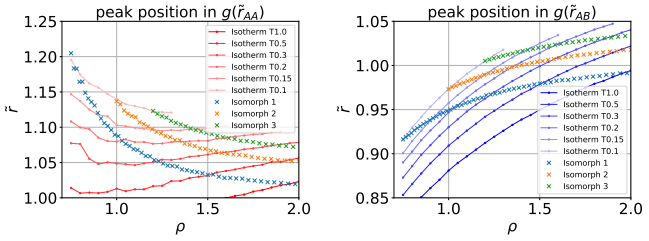

Dynamics

- The red curves in Fs and msd are points along the isotherm $T = 1.0$, and the blue curves are points along isomorph 1.

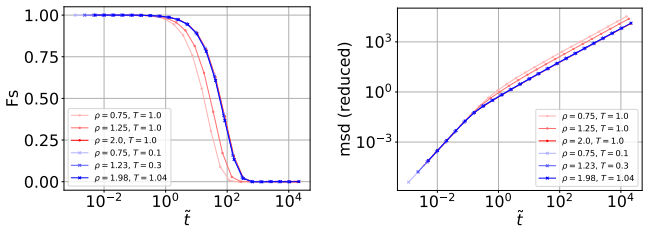

- The time at which Fs is equal to e^{-1}, and msd is equal to 1.

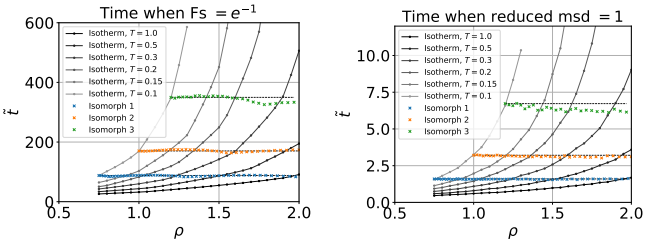

IV. References

[1] Jean Pierre Hansen and Ian R. McDonald.
Statistical mechanics of dense ionized matter. iv. density and charge fluctuations in a simple molten salt.
Phys. Rev. A, 11:2111–2123, Jun 1975.

[2] Henriette Wase Hansen, Filippa Lundin, Karolina Adrjanowicz, Bernhard Frick, Aleksandar Matic, and Kristine Niss.
Density scaling of structure and dynamics of an ionic liquid.
Physical Chemistry Chemical Physics, 22, 2020.

An Investigation of Structure and Dynamics in a Molecular Model of an Ionic Liquid

Peter Alexander Knudsen (pealkn@ruc.dk) Kristine Niss Nicholas Bailey

Department of Science and Environment, Roskilde University

I. What Are We Working With?

- Experimental results for structure in the ionic liquid PYR_{14}^+ $TFSI^-$ have shown invariance in the main structure factor peak along curves of equal electrical conductivity. It was also shown that the charge structure factor peak is not invariant along these curves.
- We have studied the structure and dynamics of a molecular model of PYR_{14}^+ $TFSI^-$ with molecular dynamics computer simulations.

II. Which Model Are We Using?

- We have used a united atom model of the ionic liquid PYR_{14}^+ $TFSI^-$.
- In united atom modelling CH-groups are considered as a single sphere.
- The model also used partial charges for the Coulomb interactions.

PYR_{14}^+

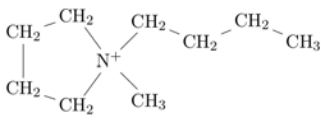

$TFSI^-$

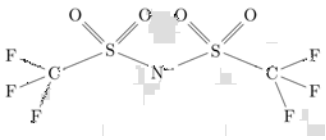

III. What Did We Find?

Lines of invariant dynamics (isodynes)

- We analysed the model and found lines of invariant diffusion coefficient (D) and viscosity (η).
- These lines are shown in both SI and isomorph scaled units.
- Lines collapses in isomorph scaled units.

Conclusion: *The system has isodynes.*

SI units Isomorph scaled units

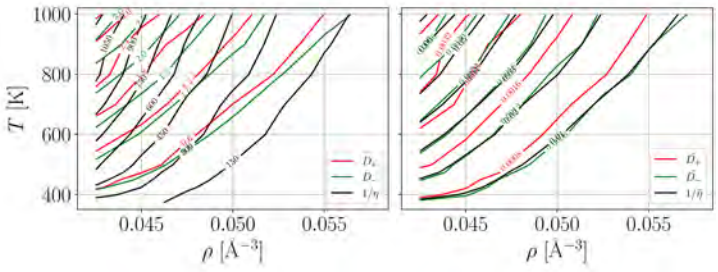

Comparing viscosity with experimental data

- Experimental data is shown with coloured lines.
- Our simulated data is shown with dashed black lines.

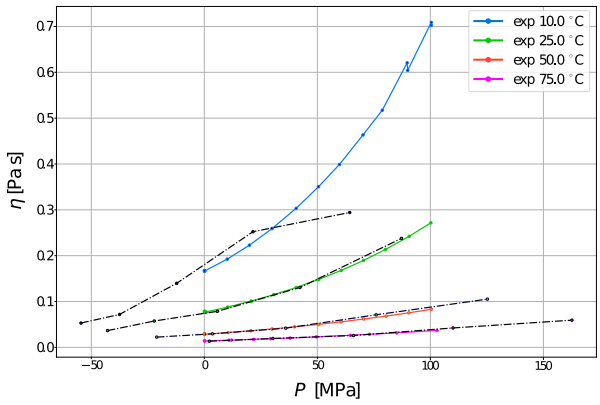

Conclusion: *There is a remarkable correspondence between the data.*

Structure along isodynes

- We looked at the structure factor along isodynes in the model and experiments.
- The experimental data has a density change of 2%.
- The simulation data has a density change of 5.56%.

Experimental data Simulation data

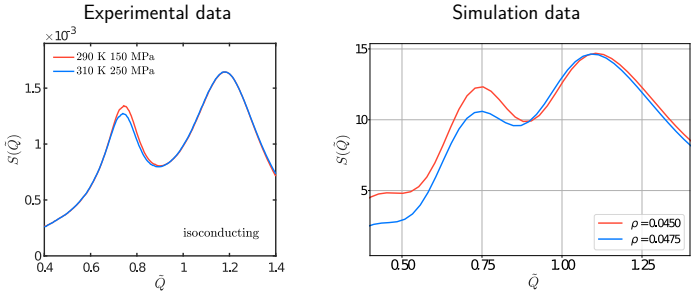

Conclusion: *The overall features of the data are the same.*

Conclusion

- This model has lines of invariant dynamics when isomorph scaling is applied (isodynes).
- There is a remarkable correspondence between model and experiment for both diffusion coefficient (D) and viscosity (η) data.
- The overall features of the structure factor along isodynes are the same in the experiment and in the model.

IV. References

[1] Henriette Wase Hansen, Filippa Lundin, Karolina Adrjanowicz, Bernhard Frick, Aleksandar Matic, and Kristine Niss. Density scaling of structure and dynamics of an ionic liquid. *Physical Chemistry Chemical Physics*, 22, 2020.

D.2 Papers

D.2.1 Upcoming papers

One paper based on this work has been published, as of the completion of this thesis. This paper covers the main results from our analysis of the Hansen & McDonald simple atomic salt model described in Chap. 5. However, we are currently writing papers based on the united atom model from Chap. 6, and the all-atom model from Chap. 7. We expect at least two new papers from this:

- A paper focusing on dynamics and the existence of isodynes.
- A paper focusing on structure.

These molecular papers are done in collaboration with Professor David M. Heyes and Professor Daniele Dini from Imperial College London, Department of Mechanical Engineering.

D.2.2 Paper 1 - Knudsen et al. (2021)

Title:
Quantifying dynamical and structural invariance in a simple molten salt model

Authors:
Peter A. Knudsen, Kristine Niss, and Nicholas P. Bailey

Journal:
Journal of Chemical Physics

Published Online:
4 August 2021

Issue:
J. Chem. Phys. 155, 054506 (2021)

The Journal of Chemical Physics ARTICLE scitation.org/journal/jcp

Quantifying dynamical and structural invariance in a simple molten salt model

Cite as: J. Chem. Phys. 155, 054506 (2021); doi: 10.1063/5.0055794
Submitted: 3 May 2021 • Accepted: 2 July 2021 •
Published Online: 4 August 2021

Peter A. Knudsen,[a] Kristine Niss,[b] and Nicholas P. Bailey[c]

AFFILIATIONS

Glass and Time, IMFUFA, Department of Science and Environment, Roskilde University, P.O. Box 260, Roskilde DK-4000, Denmark

[a]Electronic mail: pealkn@ruc.dk
[b]Electronic mail: kniss@ruc.dk
[c]Author to whom correspondence should be addressed: nbailey@ruc.dk

ABSTRACT

Recent experimental results for the structure in the ionic liquid PYR_{14}^+ $TFSI^-$ have shown invariance in the main structure factor peak along curves of equal electrical conductivity [Hansen *et al.*, Phys. Chem. Chem. Phys. **22**, 14169 (2020)]. The charge peak decreases slightly with increasing temperature at fixed conductivity, however. For simple liquids, curves with invariant dynamics and structure, known as isomorphs, can be identified as configurational adiabats. While liquids with strong-Coulomb interactions do not have good isomorphs, ionic liquids could be an intermediate case with approximate isomorphs along which some aspects of structure and dynamics are invariant. We study a simple molten salt model using molecular dynamics simulations to test this hypothesis. Simple measures of structure and dynamics are investigated along with one transport property, the shear viscosity. We find that there is a substantial degree of invariance of the self-intermediate scattering function, the mean square displacement, and the viscosity along configurational adiabats over a wide range of densities for the three adiabats simulated. The density range studied is more than a factor of two and extends from the strong-Coulomb regime at low densities to the weak-Coulomb regime at high densities. The structure is not invariant over the full range of density, but in the weak-Coulomb regime, we see behavior similar to that seen experimentally over density changes of order 15%. In view of the limited structural invariance but substantial dynamical invariance, we designate the configurational adiabats as *isodynes*.

I. INTRODUCTION

There is growing interest in using room temperature ionic liquids (ILs), e.g., as electrolytes in lithium batteries to make them more stable and safe to use. This is because ILs can be designed with properties such as low vapor pressure and low flammability, which are desirable for a solvent.[1–3] Modern ionic liquids (from now on, the qualifier "room temperature" is to be understood) are salts that are molten at room temperature, typically combining a large organic cation, such as imidazolium, pyridinium, and pyrrolidinium, with an inorganic anion, such as PF_6, BF_4, or $N(CF_3SO_2)_2$. The flexibility in the choice of the ions enables the optimization of a range of physical properties providing functionality. This has resulted in great interest in ILs for a range of different applications, including electrochemistry,[4] lubrication,[5] catalysis,[6] bio-preservation,[7] and materials synthesis.[8] As a relatively new class of materials, it is important to carry out extensive studies in order to gain knowledge about their properties in a wide range of thermodynamic conditions. The properties of interest include (1) structural properties that are important for understanding a material's behavior under different conditions; (2) microscopic dynamics, for example, the self-diffusion coefficient that is related to the conductivity and as such clearly important for battery materials; and (3) transport coefficients such as viscosity, which is relevant generally for technological uses of liquids and also because it correlates with diffusivity.

There is a long history of investigating "classical" molten salts, such as the alkali halides (e.g., NaCl) both theoretically and with simulations, and it has long been understood that in these cases, charge ordering plays an important role, leading to the suppression of concentration fluctuations compared to non-charged mixtures at long wavelengths and effective screening of the Coulomb interactions at long ranges.[9–11] There have also been many attempts in the

literature to understand the dynamics and transport properties of molten salts using the so-called "corresponding states" principle, by which systems can be mapped to a reference system usually involving scaling by the density and temperature of the critical point (or triple point).[12–14]

While measurements at ambient pressure would seem to be sufficient for materials that are intended for applications at that pressure, greater insight can often be obtained by varying pressure as well as temperature. An example of this is the phenomenon of density scaling, whereby dynamical properties are found to be a function not of pressure p and temperature T separately or of (number) density (ρ) and temperature (T) separately but of the combined variable ρ^γ/T, where the density scaling exponent γ is often taken to be a material dependent constant.[15–17] The insight arising from density scaling is twofold: (1) The phase diagram is simpler than otherwise would be considered, being effectively one-dimensional instead of two-dimensional, at fixed composition, and (2) the density (or volume), rather than pressure, is shown to be a more relevant thermodynamic parameter for understanding the structure and dynamics. Density scaling may also be described by saying that one or more dynamical or structural parameters are invariant along curves in the phase diagram, given in the above case by $T \propto \rho^\gamma$.

Density scaling has been found to hold for conductivity and/or viscosity of many different ionic liquids.[18–20] Of particular interest for this work are studies on the ionic liquid PYR_{14}^+ $TFSI^-$ [1-butyl-1-methylpyrrolidinium bis(trifluoromethanesulfonyl)imide] where it has been demonstrated that the viscosity, diffusion coefficient, conductivity, and intermediate scattering function studied with inelastic neutron scattering all obey density scaling with $\gamma = 2.8$.[21–23] In addition to density scaling of various transport properties and dynamics, it was shown by Hansen *et al.*[23] that the main peak's position and height in the structure factor $S(q)$ determined by x-ray scattering also followed density scaling with $\gamma = 2.8$ when analyzed in terms of the dimensionless wavenumber $\tilde{q} = q\rho^{-1/3}$. In other words, it was found that the main peak of $S(q)$ was invariant along the same curves in the phase diagram as the dynamical properties. However, the smaller peak at a lower wavenumber, sometimes referred to as the charge peak, was less invariant, reducing in amplitude and moving toward lower values of $\tilde{q}$ as temperature increased at constant conductivity. The density change in these experiments was a little over 2%.

The study of invariances of physical quantities along certain curves in the phase diagram is greatly aided by the theoretical framework known informally as isomorph theory. The existence of a curve in the phase diagram along which some quantity, for example, the conductivity, is constant is trivial: For any substance, one can identify invariant curves as contours of conductivity. What is non-trivial is when the contours of one physical quantity coincide with those of another. For certain systems, termed R-simple systems, the contours of many structural and dynamical quantities coincide and these curves are then designated as *isomorphs*. The theory specifies that to see the invariances, it is essential to compare the correctly scaled dimensionless versions of physical quantities, referred to as putting them in "reduced units." The theory also is quite precise about which physical quantities should be invariant in reduced units.[24]

In the formal development of isomorph theory,[25] isomorphs are defined as curves of constant excess entropy $S_{ex}(\rho, T) \equiv S(\rho, T) - S_{IG}(\rho, T)$, the entropy after subtracting the ideal gas contribution for the same density and temperature. These so-called configurational adiabats can be readily identified in computer simulations, as explained in Sec. II. R-simple systems are understood, as a rule, to be those dominated by van der Waals or metallic bonding.[26] Strongly directional bonding and strong Coulomb interactions[26–28] are known to spoil R-simplicity. Since Coulomb interactions are important in ionic liquids, it is not *a priori* clear that these liquids have good isomorphs. However, the experimental results of Hansen *et al.*[23] suggest that an analysis in terms of isomorphs could be fruitful. Indeed, the coincidence of the invariant main peak in $S(q)$ and the invariance of conductivity points strongly toward the existence of underlying approximate isomorphs. We say approximate because the charge peak in $S(q)$ was not observed to be invariant.

A possible interpretation of these results is that the Coulomb interactions play a limited role in determining the structure as given by the main peak of $S(q)$ and a limited role in determining the dynamical and transport properties. Therefore, approximate isomorphs exist along which these quantities are nearly invariant. On the other hand, the charge peak, which is ascribed to charge ordering and therefore is solely due to the Coulomb interactions, is somehow decoupled from the interactions that determine the main structural and dynamical properties.

In systems that do not have good isomorphs or have at best approximate isomorphs, we can still identify configurational adiabats and investigate structural and dynamical invariances along them. However, it is not appropriate to refer to them as isomorphs. In this work, we will therefore refer to the identified curves as adiabats for correctness (the qualifier "configurational" will always be understood if omitted).

Our goal is to get a better understanding of this behavior—substantial, but not complete invariance of structure and dynamics along the same curves in the phase diagram of an ionic liquid—by studying a simple model system using computer simulations. For this, we have used the simple salt model of Hansen and McDonald,[29] which contains two types of spherical particles differing only in the sign of their charge. This model, described more completely in Sec. III, is designed to be the simplest possible model of an ionic liquid. It consists of point particles interacting via a short-range repulsive inverse power law (IPL) together with Coulomb interactions that are repulsive or attractive for like or unlike particles, respectively. The IPL term by itself would give perfect isomorphs due to the well-known scaling properties of power law functions.[30] The Coulomb interactions, as argued above and in previous work, tend to spoil the pressure–energy correlations that give rise to isomorphs. Inspired by the experimental results, we hypothesize that in this model, there is a similar division into structural [main peak of $S(q)$] and dynamical properties, which are insensitive to the Coulomb interaction, and structural properties [the "charge peak" in $S(q)$], which are sensitive to the Coulomb interaction. We will argue below that because the exponent of the Coulomb interaction ($n = 1$) is much smaller than that of the short-range repulsive IPL ($n = 9$), the charge peak should decrease as density increases along an isomorph (the temperature that would tend to preserve the charge peak is lower than that which preserves the main peak, so the charge peak experiences greater thermal disruption).

Briefly, our main results are that dynamical and transport properties are invariant along configurational adiabats over more or less the full range of densities simulated, while structural properties vary

substantially when the full range of simulated densities is considered. When considering a smaller density range, around a 15% increase, in the high density (weak-Coulomb) regime, the structure appears more invariant; in particular, the main peak in the structure factor, corresponding to the number fluctuations, is quite invariant, while the charge peak, corresponding to concentration fluctuations, varies slightly, in a manner similar to the experiments of Hansen *et al.*,[23] getting smaller and moving toward lower reduced wavenumbers as density increases.

II. ISOMORPH THEORY

Isomorph theory is a theoretical framework that was first presented in Ref. 24. The theory describes curves in the phase diagram, called isomorphs, along which many structural and dynamical properties are invariant when the quantities of interest are scaled appropriately. Not all systems have isomorphs, and the theory is only exact for systems where the potential energy between particles can be described with an inverse power law, $V(r) = \varepsilon r^{-n}$. However, this does not mean that it can only describe these systems. For example, in most soft-sphere models, to avoid overlapping particles, the potential energy between particles will monotonically approach infinity as r goes to 0. This suggests that for small values of r the potential can be approximated with an inverse power law. This is why we often expect isomorphs at higher densities for these systems. A concrete way to test the "quality" of a potential isomorph through a given state point is by calculating the Pearson correlation coefficient R between the potential energy and the virial,

$$R = \frac{\langle \Delta W \Delta U \rangle}{\sqrt{\langle (\Delta W)^2 \rangle \langle (\Delta U)^2 \rangle}}, \tag{1}$$

where ΔW is the deviation of the virial from its thermodynamic average, ΔU is the deviation in potential energy, and $\langle \cdots \rangle$ denotes the canonical (NVT) ensemble average. The R-value can be calculated for any state point, but a system is usually expected to only have good isomorphs in parts of the phase diagram where $R > 0.9$.[24]

In order to trace the isomorph in the phase diagram, one has to calculate another important quantity for isomorphs, the density scaling exponent γ,

$$\gamma(\rho, T) \equiv \left(\frac{d \ln T}{d \ln \rho} \right)_{S_{ex}} = \frac{\langle \Delta W \Delta U \rangle}{\langle (\Delta U)^2 \rangle}, \tag{2}$$

where T is the temperature, ρ is the density, and S_{ex} is the excess entropy.[24] Thus, γ defined in this way is the slope of the configurational adiabat through a given state point in a double-logarithmic representation of the ρ, T phase diagram. This is a general statistical mechanical identity; for systems with good isomorphs, the (configurational) adiabats are the isomorphs. Moreover, if γ is independent of density and temperature, then the adiabats have the form $T \propto \rho^{\gamma}$; this is the case referred to in the Introduction in the context of experimental results on density scaling. In computer simulations, larger changes in ρ can be explored and γ is generally seen to depend on it and, to a lesser extent, on T.[31] By treating Eq. (2) as a first order differential equation, we can trace adiabats in the phase diagram via a simple Euler numerical integration,

TABLE I. Table of scaling factors for conversion to reduced units.

Name	Symbol	Reduced symbol	Scaling factor
Distance	r	$\tilde{r}$	$\rho^{1/3}$
Inverse distance	q	$\tilde{q}$	$\rho^{-1/3}$
Time	t	$\tilde{t}$	$\rho^{1/3}\sqrt{k_B T/m}$
Mean square displacement	MSD	MSD (reduced)	$\rho^{2/3}$
Viscosity	η	$\tilde{\eta}$	$\rho^{-2/3}(m k_B T)^{-1/2}$

$$T_{n+1} = T_n \left(\frac{\rho_{n+1}}{\rho_n} \right)^{\gamma_n}. \tag{3}$$

As mentioned in the beginning, the invariance in structure and dynamics can only be seen when scaled appropriately. These scaling factors are defined for the characteristic properties of the system, such as the density ρ, the (mean) mass of the particles m, and the temperature T. As an example, the scaled distance is $\tilde{r} \equiv \rho^{1/3} r$. A list of the reduced units and the necessary scaling factors, which we will use in this paper, can be seen in Table I.

III. SIMULATIONS

A. Simple salt model

We have worked with the simple salt model described in Ref. 29. This model contains two types of spherical particles, designated A and B, which are identical except for their opposite charge. The potential contains an inverse power law term with exponent $n = 9$, which ensures that all particles are repelled at small distances. It also contains an inverse power law term with exponent 1 that represents the electrostatic interactions between the particles. This means that this term is repulsive for particles of the same type and attractive for particles of different types. The pair potential of this model is thus given by

$$V_{\alpha\beta}(r) = \frac{1}{9}\left(\frac{1}{r}\right)^9 + \varepsilon_{\alpha\beta}\left(\frac{1}{r}\right), \tag{4}$$

where r is the distance between the particles, $\varepsilon_{AA} = \varepsilon_{BB} = 1$, and $\varepsilon_{AB} = \varepsilon_{BA} = -1$. Due to the symmetry of this potential, we will be referring to AA as the like-part and AB as the unlike-part.

Traditionally, in computer simulations, Coulomb interactions have been implemented using some variant of the Ewald-summation method in order to handle the long range part of the interactions as efficiently as possible.[32] It has been shown, however, that for bulk systems a simpler approach, omitting the long range part of the interactions, is sufficiently accurate.[33] In particular, the use of the so-called shifted-force cutoff, whereby a constant term is added to the pair-force such that it vanishes at the cutoff, gives accurate results without requiring excessively large cutoffs.[34,35] This ensures the continuity of the force at the cutoff, giving greater energy stability, although it involves changing the pair potential (by a linear term) at distances less than the cutoff. In this work, we use a shifted-force cutoff for the entire interaction, with a cutoff distance of $r_c = 6$. To confirm that this is sufficiently accurate, we have investigated the

effect of systematically reducing the cutoff to 3 at the lowest density of $\rho = 0.75$ by focusing on the partial structure factors. For the smallest cutoff values, 3 and 4, effects can be seen in the charge-density fluctuations at low wavenumbers (see Fig. 1 of the supplementary material). There is little change once the cutoff exceeds 5, however. The graph of the potential is shown in Fig. 1. Note that the minimum of the unlike interaction occurs at $r = 1$, so naïvely we expect (Coulomb) attractions to be most relevant at densities below approximately unity (taking the interparticle spacing to be roughly $\rho^{-1/3}$).

At short distances, the purely repulsive $n = 9$ term dominates so that we expect the Coulomb interaction to play a decreasing role as density increases. In fact, it can be shown mathematically that reducing the contribution of the Coulomb interaction term can be absorbed by a redefinition of length and energy scales or equivalently changing temperature and density to higher values (see Sec. I of the supplementary material). We therefore simulate a wide range of densities, much wider than would normally be covered in a real experiment on a given material, to probe the effect of effectively reducing the Coulomb interactions. In experiments, one would have to vary the charges, or more likely, vary the size of the molecule while keeping the charges fixed, thus "diluting" their effect.

Hansen and McDonald studied their model at one particular density, 0.3676, and one particular temperature, 0.0177. This density is significantly lower than unity and lower than the densities we study by at least a factor of 2. When converted to real units corresponding to NaCl, the state point is roughly in the vicinity of the experimental triple point of NaCl (20% higher in temperature and 10% lower in density). NaCl is of course a strongly ionic liquid, where the Coulomb interaction very much dominates. In this low density, low temperature regime (compared to the location and depth of the attractive minimum), one expects very weak correlations and no isomorphs. Our interest is inspired by room temperature ionic liquids, on the other hand, in which the Coulomb interactions do not dominate so much, giving an intermediate situation whereby a higher degree of W, U-correlation, and thereby potential for isomorph-like invariances, can be expected. As shown below, the part of the phase diagram we investigate covers values of the correlation coefficient R ranging from low-to-intermediate ($R \sim 0.7$) to very high ($R > 0.95$). Since the region we simulate is well above the critical temperature and density,[36] one may prefer the term "supercritical fluid" rather than "liquid."[37] In the context of isomorph theory, this distinction has little physical meaning, however, at least where good isomorphs exist, since one can follow an isomorph from the liquid into the supercritical fluid and observe no essential differences at the microscopic scale; we therefore choose to stick with the term "liquid."

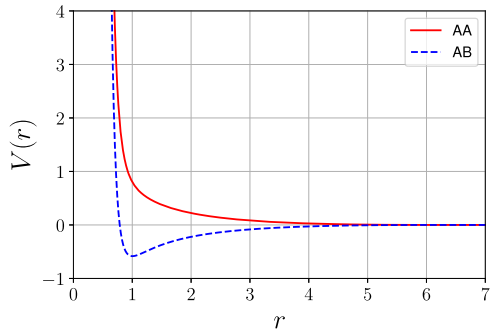

FIG. 1. Potential energy between particles in the simple salt model with a shifted-force cutoff implemented at $r_c = 6$. Interactions between particles of the same type, AA and BB, are identical. The minimum for the unlike interaction is at $r = 1$.

In the weak-Coulomb regime at high density, we hypothesize that the main effect of Coulombic interactions is to induce a mild degree of charge ordering, while the short-range repulsive term dominates most of the properties, including the slope of the adiabats (that is, γ is close to 3 in this limit). For a pure Coulomb system, the adiabats would have a much lower slope of 1/3; thus, the temperature along the actual adiabats is "too high" for the Coulomb interactions, which is expected to lead to a decrease in charge ordering with increasing density along an adiabat.

B. Simulation details

We simulated 8000 particles in a rectangular box with sides $2L \times L \times L$. The doubled length in the x-direction was chosen to achieve higher resolution in the structure factor.[38] Periodic boundary conditions were implemented to create the perception of a larger system, removing the need to define particle interactions with walls. For simplicity, we chose the masses of both types of atoms to be unity.

The time step was chosen to have a fixed value in reduced units, $d\tilde{t} = 0.004$, or $dt = 0.004\rho^{-1/3}(T/m)^{-1/2}$. Keeping a fixed value is convenient when comparing dynamical quantities along an isomorph, although it is not essential. For the initial configurations, the particles were placed on an fcc lattice with types assigned randomly. This lattice is not thermodynamically stable and immediately melts at all simulated densities and temperatures. The state points along the isotherms was simulated in parallel (at the same time) since they are independent of each other. Each state point equilibrated for $2 \cdot 10^6$ time steps before data was collected. The adiabats on the other hand have to be run in series (in order) because the next state point is dependent on the current one [since γ determined in one simulation determines the temperature of the next one via Eq. (3)]. After the initial equilibration, all simulations collected data for $2^{17} \cdot 100 = 13\,107\,200$ time steps. The simulations were performed using RUMD (Roskilde University Molecular Dynamics),[39] which is designed for a GPU-cluster.

C. Simulation protocol

Figure 2 shows all simulated points in a $\rho - T$ phase diagram. We choose three different adiabats to study: one going through the point $\rho = 0.75$ and $T = 0.1$, another going through $\rho = 1.00$ and $T = 0.1$, and finally one through $\rho = 1.20$ and $T = 0.1$. These will be referred to as adiabats 1, 2, and 3, respectively. These three starting densities were chosen such that the forces between unlike particles would be mostly attractive for adiabat 1, neutral for adiabat 2, and repulsive for adiabat 3. This can be seen in Fig. 1 by remembering that the average distance between the particles is given approximately by $\rho^{-1/3}$. All three adiabats were simulated from their starting density to $\rho = 2$. The results from these adiabats will be compared with six different isotherms $T = 0.10$, 0.15, 0.20, 0.30, 0.50, 1.00.

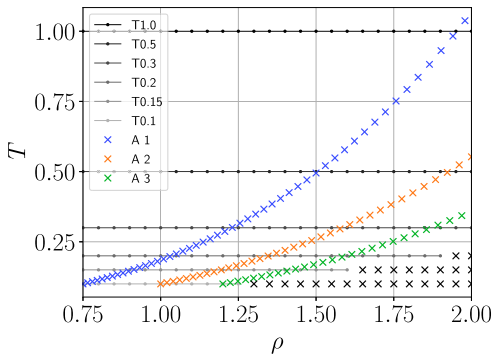

FIG. 2. Simulated adiabats and isotherms in a $\rho - T$ phase diagram. The state points where crystallization was observed are marked with an X.

These temperatures were chosen to overlap with the temperature range of the adiabats. These isotherms were simulated in a density interval from $\rho = 0.75$ to 2.0 with a spacing of 0.05.

At the lowest temperatures and highest densities, crystallization occurred; these points are indicated with a cross in Fig. 2 and omitted from further analysis.

IV. RESULTS

Figure 3 shows R and γ for all adiabats and isotherms plotted as a function of density. For both adiabats and isotherms, R and γ increase monotonically as the density increases. In the high density limit, they must approach 1 and 3, respectively, since the potential is better approximated by the IPL at high densities at which the isomorph theory is exact and for which γ is given by one third of the exponent $n = 9$. In this limit, there are perfect isomorphs and there is no need to simulate; most of our simulated state points (primarily those at lower densities), on the other hand, have $R < 0.9$; thus, we expect less than perfect invariance, with potentially some quantities more invariant than others. The fact that $\gamma < 3$ in general is not obvious *a priori*; indeed, for the Lennard-Jones potential, which has the same form as the attractive (unlike particles) potential in this model, γ converges to $12/3 = 4$ from above rather than below. The dependence of γ on density will be discussed below.

A. Dynamics and transport

As measures of microscopic dynamics, we consider the mean square displacement (MSD) and self-intermediate scattering function, $F_s(q,t)$. The tagged-particle MSD was calculated as an average over particles and time-origins,

$$\mathrm{MSD}(t) = \left\langle |\boldsymbol{r}(t) - \boldsymbol{r}(0)|^2 \right\rangle, \tag{5}$$

where $\boldsymbol{r}(t)$ is the position of a particle at time t, $|\cdots|$ denotes the absolute value, and $\langle\cdots\rangle$ denotes the ensemble average.

Figure 4(a) shows reduced-unit MSD curves in blue for adiabat 1 and in red for isotherm $T = 0.1$. The blue curves collapse perfectly, indicating a strong invariance of this dynamical quantity

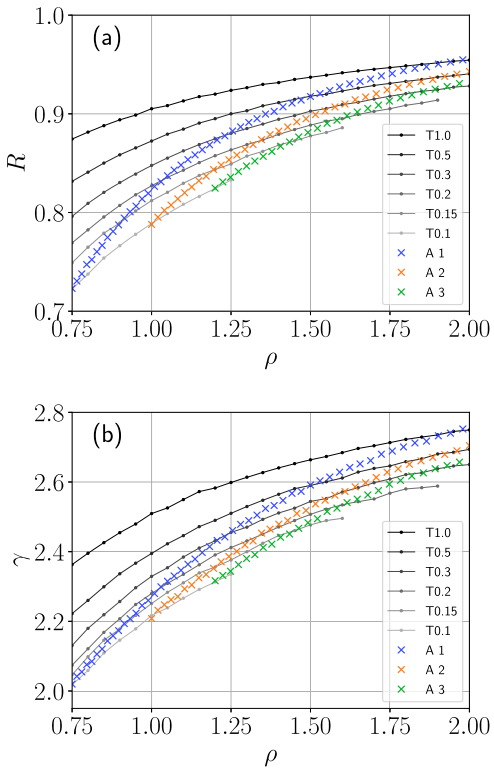

FIG. 3. (a) Correlation coefficient R along adiabats and isotherms as a function of density. (b) Scaling exponent γ along adiabats and isotherms as a function of density.

along configurational adiabats. The curves show the usual transition from a ballistic regime at short times (slope 2 in a double-log plot) to a diffusive regime (slope 1) at long times. The absence of a plateau between these two regimes is characteristic of non-viscous behavior. This is consistent with the relatively easy crystallization we observe when the high density/low temperature region of the phase diagram is simulated (the crosses in the lower right corner in Fig. 2): The latter indicates that this model cannot be readily supercooled, which implies that we should not expect to find any viscous liquid states. Because the MSD in the ballistic regime depends on temperature and particle mass but not on the potential, it is straightforward to show that it is always equal to $3\tilde{t}^2$, and therefore, all data must collapse trivially in that regime. The collapse of the diffusive regime along the adiabat, on the other hand, is a non-trivial result. To show data from all simulations in a concise way, we determine the diffusion coefficient from a linear fit to the MSD data, shown in Fig. 4(b) for all state points. The dynamical invariance along configurational adiabats is manifested over the whole density range on each adiabat.

The self-intermediate scattering function was calculated by

$$F_s(\boldsymbol{q},t) = \langle \exp[i\boldsymbol{q}\cdot(\boldsymbol{r}(t) - \boldsymbol{r}(0))] \rangle, \tag{6}$$

where $\boldsymbol{r}(t)$ is the position of a particle at time t.[40] Figure 5(a) shows the intermediate scattering function, plotted as a function of reduced

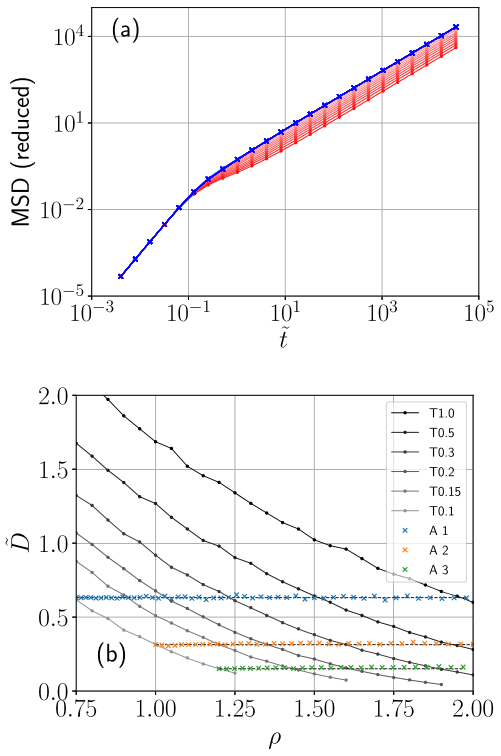

FIG. 4. (a) Reduced MSD as a function of reduced time for all densities where crystallization did not occur on isotherm $T = 0.1$ (red curves) and all state points along adiabat 1 (blue curves). The blue curves collapse on each other. (b) Diffusion coefficient (determined from the long time slope of the MSD) for all adiabats and isotherms. The horizontal dashed lines at the three adiabats are to guide the eye. They pass through the first (lowest density) point of each adiabat.

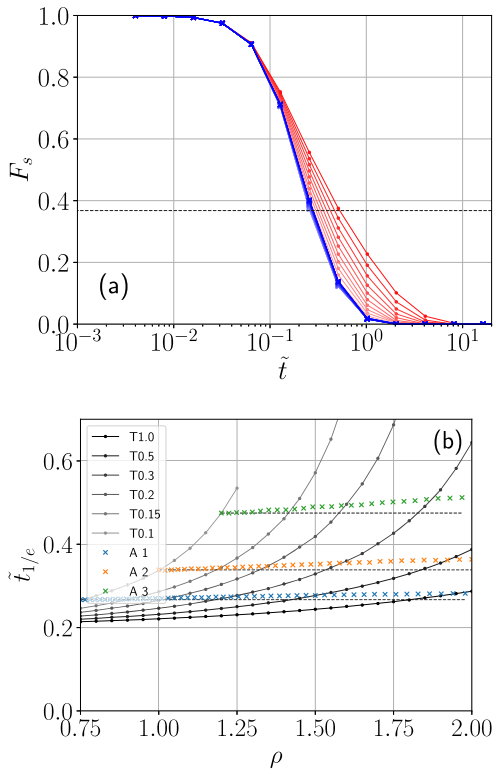

FIG. 5. (a) F_s plotted as a function of reduced time for all simulated densities at $T = 0.1$ (red curves) and all simulated state points on adiabat 1 (blue curves). The latter collapse almost perfectly on each other. The horizontal dashed line indicates the value $1/e \approx 0.368$. (b) Reduced time at which $F_s = 1/e$, for all adiabats and isotherms. The horizontal dashed lines pass through the first points (lowest density) of the adiabats and are intended to guide the eye.

time $\tilde{t}$, for adiabat 1 (blue) and isotherm $T = 0.1$ (red). The q-value was chosen to be $7.1\rho^{1/3}$, ensuring that it is fixed in reduced units and close to the maximum of S_{NN} (see Sec. IV B). At all the investigated state points, a simple, near-exponential decay is observed, corresponding to ordinary non-viscous liquid dynamics, and consistent with the absence of a plateau in the MSD data. The red curves in Fig. 5(a) move toward longer times (slower dynamics) as the density increases, while the blue curves collapse on each other, showing that also this measure of dynamics is invariant along adiabat 1. The data for other isotherms and adiabats behave similarly (see Figs. 2–6 of the supplementary material). In Fig. 5(b), we plot the reduced time at which F_s has fallen to e^{-1}, denoted as $\tilde{t}_{1/e}$, as a function of density for all adiabats and isotherms. This time scale increases rapidly with increasing density at fixed temperature but increases only slightly along adiabats, again indicating rather invariant dynamics. This plot shows that the invariance is not perfect [the slight deviation is hidden in panel (a) of Fig. 5 due to the logarithmic axis] but nevertheless impressive given the large density changes involved. Note that the change in a real time scale over this range of densities is about a factor of 4.5 for adiabat 1. The collapse of the F_s curves themselves means that the invariance applies to the whole time-dependent relaxation curve, not just the characteristic time scale. Indeed, the shape-parameter β in the stretched-exponential fits is more invariant than the characteristic time except at low densities (left panel of Fig. 9 of the supplementary material). It should be emphasized that the approximate invariance shown by the reduced self-intermediate scattering function applies over the whole simulated range of density, even though the W, U-correlation coefficient R is less than 0.9 for most of the density range of each adiabat, and as such, we do not expect the configurational adiabats to be isomorphs. Note that at smaller wavenumbers the time scale for the intermediate scattering function becomes more invariant (see Fig. 7 of the supplementary material), consistent with the excellent collapse of the diffusivity data, since diffusion is a long wavelength process.

Finally, in this section, we investigate the viscosity as an important example of a macroscopic transport coefficient. The viscosity was calculated using the Green–Kubo formula,[32]

$$\eta = \frac{V}{k_B T}\int_0^\infty \langle \sigma_{xy}(0)\sigma_{xy}(t)\rangle dt, \tag{7}$$

where V is the volume of the simulation box, k_B is the Boltzmann constant, T is the temperature, and $\sigma_{xy}(t)$ is the xy component of the stress tensor as a function of time t. The calculation of the integral in Eq. (7) is done analytically after fitting the normalized

autocorrelation function at short (reduced) times ($\tilde{t} \leq 0.06$) to a polynomial $a_0 + a_2\tilde{t}^2 + a_3\tilde{t}^3$ (note that the slope must be zero at $\tilde{t} = 0$) and at longer (reduced) times ($\tilde{t} \geq 0.06$) to a sum of two exponential functions. The data up to where the normalized function first goes below 0.001 are included in the fit. Figure 6(a) shows four examples of the normalized stress autocorrelation function and the corresponding fits. The plot is in reduced units; the two curves from the same adiabat are somewhat similar but not identical when plotted this way. Figure 6(b) shows the reduced viscosity as a function of density along the isotherms and adiabats. As with the self-intermediate scattering function and the mean squared displacement, we find a striking invariance across the whole range of densities for each of the three adiabats. Given that the two curves in Fig. 6(a) from the same adiabat differ at long times, giving different values for the integral of the normalized correlation function, it is surprising that viscosity seems so invariant. The formula for $\tilde{\eta}$ can be written as the product of the reduced infinite frequency shear modulus $\tilde{G}_\infty$ and the integral of the normalized shear stress autocorrelation function with respect to reduced time. Figure 10 of the supplementary material shows $\tilde{G}_\infty$, which is not invariant but rises noticeably with density along adiabats. This increase compensates for the decrease in the integral of the normalized correlation function, yielding a rather invariant reduced viscosity.

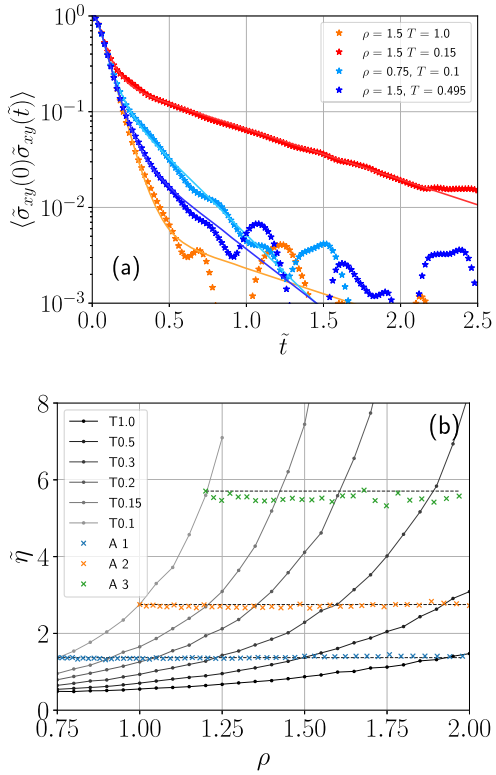

FIG. 6. (a) Examples of the normalized stress autocorrelation data and double-exponential fit. The plot is in reduced units to facilitate the comparison of data from the same adiabat. (b) Comparison of the viscosity along adiabats and isotherms. The horizontal dashed lines at the three adiabats are to guide the eye. They pass through the first point of each adiabat.

B. Structure

To study the structure, we consider both the radial distribution function and the structure factor. We consider partial pair correlation or radial distribution functions $g_{\alpha\beta}(r)$ defined in the usual way, where the indices α and β refer to particle types A and B. Only two of these, the AA and AB functions, are independent since the AA and BB interactions are identical and the composition is equimolar. The corresponding partial structure factors $S_{\alpha\beta}(q)$, known as the Faber–Ziman (FZ) structure factors, can be defined by Fourier transforming these, but we choose a different representation known as the Bhatia–Thornton (BT) partial structure factors (see Fig. 16 of the supplementary material for some FZ structure factor data). These are defined for binary mixtures[38,41] as certain linear combinations of the FZ structure factors, denoted as NN, NC, and CC, where N refers to number density fluctuations and C refers to concentration density fluctuations. Section II of the supplementary material explains how this representation is equivalent to defining sum and difference variables of the Fourier components of density fluctuations.[9] If c_A and c_B are the concentrations of species A and B, respectively, then the BT partial structure factors are defined by[38,41]

$$S_{NN}(q) = c_A^2 S_{AA}(q) + c_B^2 S_{BB}(q) + 2c_A c_B S_{AB}(q) > 0, \quad (8)$$

$$S_{CC}(q) = c_A c_B[1 + c_A c_B(S_{AA}(q) + S_{BB}(q) - 2S_{AB}(q))] > 0, \quad (9)$$

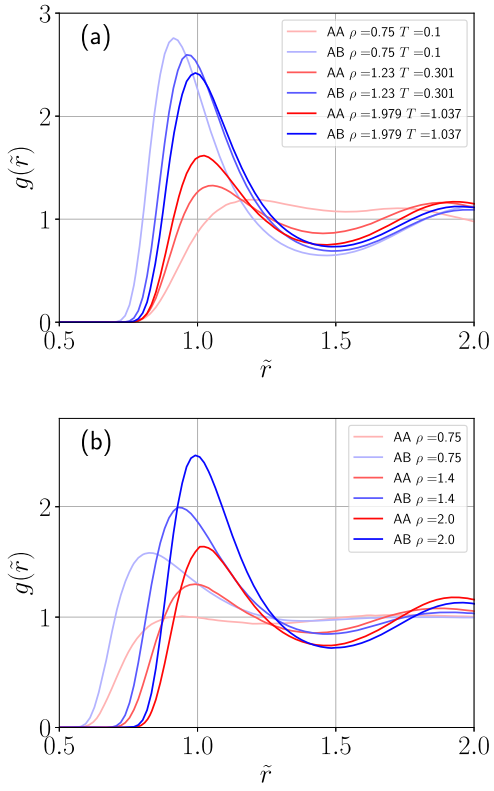

FIG. 7. Partial radial distribution functions for three state points on (a) adiabat 1 and (b) isotherm $T = 1.0$, plotted as functions of reduced distance $\tilde{r}$.

$$S_{NC}(q) = c_A c_B[c_A(S_{AA}(q) - S_{AB}(q)) - c_B(S_{BB}(q) - S_{AB}(q))]. \quad (10)$$

In our system, $S_{AA}(q) = S_{BB}(q)$ and $c_A = c_B = 0.5$, and thus $S_{NC} = 0$, and we do not include it in our analysis. The utility of this representation stems from the way in which the coherent part of the total neutron scattering signal is written[38] (taking $S_{NC} = 0$),

$$\frac{1}{N}\left[\frac{d\sigma}{d\Omega}(q)\right]^{\text{coh}} = |\langle b\rangle|^2 S_{NN}(q) + |\bar{b}_A - \bar{b}_B|^2 S_{CC}(q), \quad (11)$$

where $\bar{b}_\alpha$ is the spin- and isotope-averaged scattering length for species α and the angle brackets denote averaging over different species. For x-ray scattering, the scattering lengths should include an additional q-dependence from the atomic form factor, while the spin-averages can be dropped (the total cross section will also include other effects[38]). Thus, the NN part of the structure factor is coupled to the mean scattering length and thus is what would be measured by a probe insensitive to chemical species. Fischer refers to it as the "colour-blind" scattering cross section.[38] The CC part is measured only when the scattering length differs between chemical species and describes chemical ordering. For our ionic system, we can associate the charge peak in the total scattering signal with a peak in $S_{CC}(q)$. As mentioned, one can obtain the BT partial structure factors by appropriately Fourier transforming the partial pair correlations to get the FZ structure factors. To avoid truncation of the Fourier transform, we used instead the more rigorous method of saving Fourier components of the density fluctuations for each species at regular intervals and then taking the relevant (co-) variances before taking appropriate linear combinations to form the BT partial structure factors (Sec. II of the supplementary material). When calculating $S(q)$ this way, only Fourier modes that fit into the simulation box are allowed. We take the first 88 modes in the x-direction, which gives sufficient resolution to resolve the peaks. By considering modes that fit into the box, we have different q-values at different densities, but the reduced-unit wavenumbers $\tilde{q} \equiv \rho^{-1/3} q$ are identical, which is necessary for isomorph-compatible comparison. Note that $S_{CC}(q)$ tends toward the product of concentrations $c_A c_B = 1/4$ in the limit of zero chemical ordering.

Figure 7 shows the partial radial distribution functions for selected densities on adiabat 1 and isotherm $T = 1.0$, while Fig. 8 shows the BT partial structure factors on the same state points. Reduced units $\tilde{r}$ and $\tilde{q}$ have been used in the plots for both quantities. There is substantial variation in both structural measures as the density varies, confirming that the adiabats we have simulated are not isomorphs despite the fact that dynamical quantities are remarkably invariant along them. The most that can be said is that the structural measures vary less with density on adiabats than on isotherms. A general feature for all adiabats and isotherms is that the features in both $g_{AA}(\tilde{r})$ and $S_{NN}(\tilde{q})$ become more pronounced as the density increases. Furthermore, as density increases along the

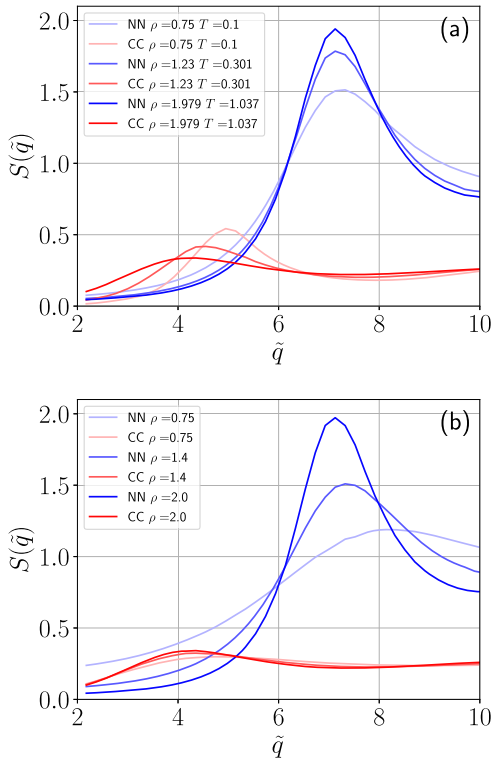

FIG. 8. Bhatia–Thornton structure factors for three state points on (a) adiabat 1 and (b) isotherm $T = 1.0$, plotted as functions of reduced wavenumber $\tilde{q}$.

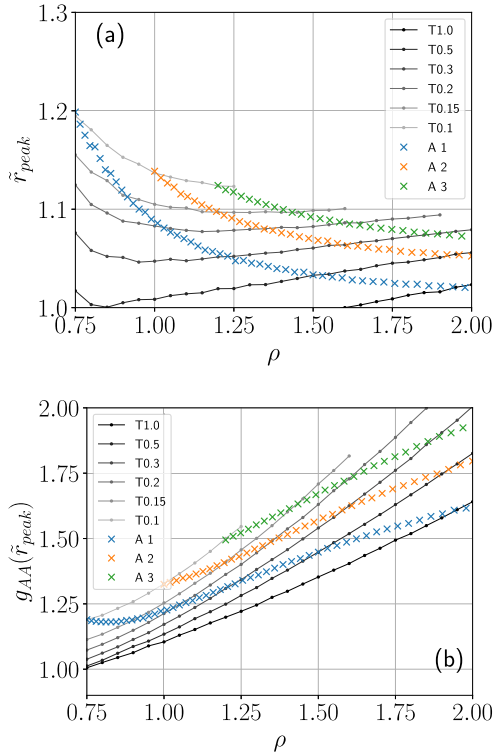

FIG. 9. Dependence of (a) the reduced-unit position and (b) the height for the first peak of the AA partial radial distribution function on density for all six isotherms and all three adiabats.

adiabats, the first peak in $S_{CC}(\tilde{q})$ moves to lower $\tilde{q}$-values and the peak height decreases. Recalling that the CC peak can be identified with the charge peak, this is the same behavior as seen in Ref. 23, and it is not shared with the isotherms. Indeed, Fig. 8(b) shows that the peak in $S_{CC}(q)$ is actually rather invariant along the isotherm; its height and position depend mainly on temperature alone.

Recall that we expect more isomorph-like behavior, that is, better invariance, in the limit of high density. To investigate how this occurs, and to get a more simple view of how the structure changes along the adiabats and isotherms, we have analyzed the position and height of the first peaks in $g(\tilde{r})$ and $S(\tilde{q})$. This was done by fitting a fourth order polynomial to data around the peak. Focusing on the peak position and height makes it easier to analyze trends in the data across the whole range of densities. Considering the radial distribution function first peaks, Figs. 9 and 10, both the peak position and peak height vary significantly along adiabats, but it is also clear that they are beginning to level off at the highest densities, whereas the data for isotherms give no indication of leveling. The leveling off for the adiabats is clearer for the peak positions than for the peak heights, although we note that for $g_{AA}(r)$ the overall variation in the peak position is greater for adiabats than for isotherms, which exhibit a shallow minimum at low densities. Another feature of the adiabats is that the AA peak position starts at values around 1.15 and decreases to values around 1.05, while the AB peak position starts at values below unity and increases to values just above unity. Thus, for each adiabat, both peaks start significantly separated, by about 20%–30%, and converge with increasing density, being separated by only a few percent at the highest densities shown. This convergence is consistent with the hypothesis that charge ordering, and hence particle identity, becomes less important as the density increases.

While both peak heights increase with density on isotherms, which is expected, they move oppositely along adiabats, increasing sharply for AA from low values and decreasing gently for AB from high values. That is, they move toward each other, again reflecting the tendency for AA and AB structures to become more alike as charge ordering diminishes along adiabats.

We turn next to the peak analysis of the BT partial structure factors, $S_{NN}(\tilde{q})$ (Fig. 11) and $S_{CC}(\tilde{q})$ (Fig. 12). The leveling out observed in the radial distribution functions is more pronounced in the NN peak heights and positions, whereas it is less pronounced in the CC plots. Over the last 0.5 or so of density, the relative change in the NN peak heights is small, while the relative change in the CC peak heights is substantial. It must be noted, however, that the absolute value of the CC peak is initially quite small, and therefore, the absolute changes in NN and CC peak heights are rather comparable. Recall that we expect that at sufficiently high density the Coulomb interactions become irrelevant, and therefore, charge ordering will be negligible; as mentioned above, $S_{CC}(q)$ should tend toward $c_A c_B = 0.25$, which is consistent with the observed behavior; the variation in the CC peak height is the already rather small degree of

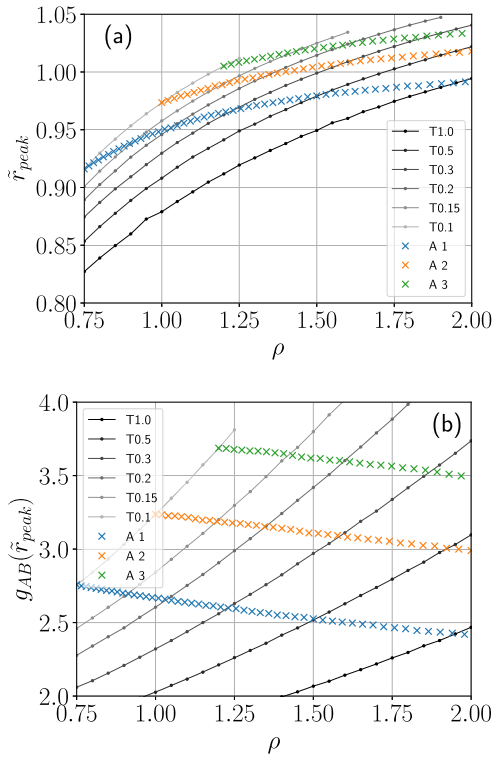

FIG. 10. Dependence of (a) the reduced-unit position and (b) the height for the first peak of the AB partial radial distribution function on density for all six isotherms and all three adiabats.

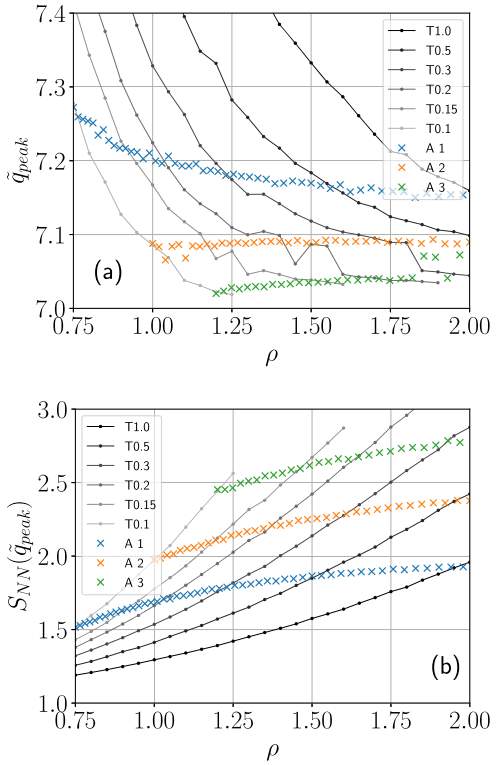

FIG. 11. Dependence of (a) the (reduced-unit) position and (b) the height for the first peak of the NN Bhatia–Thornton partial structure factor on density for all six isotherms and all three adiabats.

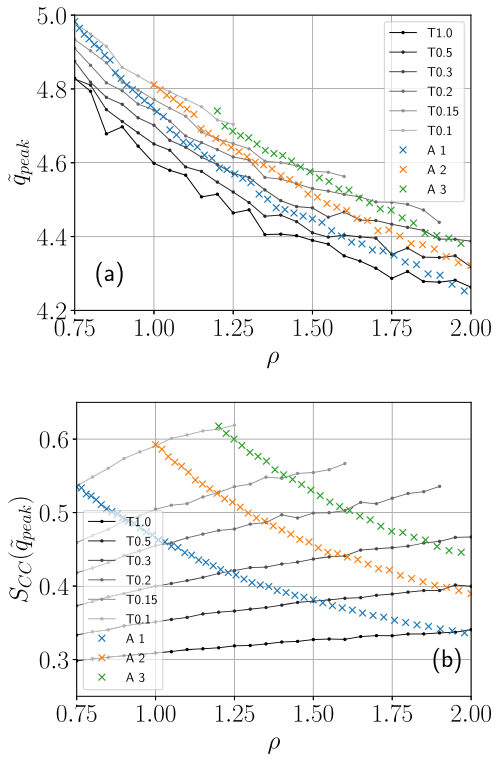

FIG. 12. Dependence of (a) the (reduced-unit) position and (b) the height for the first peak of the CC Bhatia–Thornton partial structure factor on density for all six isotherms and all three adiabats.

charge ordering getting even smaller. To illustrate the high density behavior more directly, we show a collapse of both Bhatia–Thornton structure factors for adiabat 2 over the density range of 1.75–2.00 in Fig. 13 and a density increase of 14%. Similar plots can be made

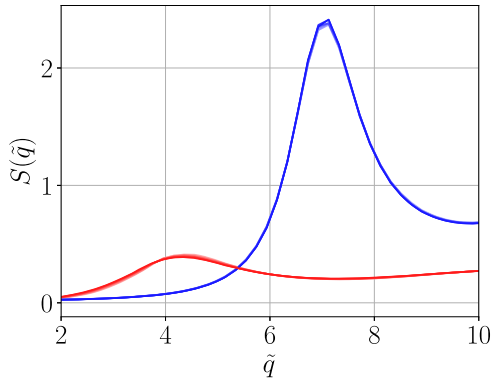

FIG. 13. NN (blue) and CC (red) Bhatia–Thornton partial structure factors for adiabat 2, including densities from 1.75 to 2.0. There are seven red curves and seven blue curves, with the intensity of the lines increasing with increasing density. The NN curves increase slightly but systematically in peak height with increasing density, while a slight but systematic decrease of both the CC peak height and CC peak position is noticeable.

for the other adiabats and also over the density range of 1.5–1.75 (Figs. 13–15 of the supplementary material). The most important point here is that the structure is in fact rather invariant over this density range, comparable to what is seen with good isomorphs (indeed, this density range is larger than that investigated in the first isomorph paper[24]). Second, the visible deviations are very small and confined to very top of the peak for NN, while they are more spread out for CC, related to the fact that the CC peak varies in position as well as height.

A more concrete way to analyze charge ordering is to determine the partial coordination numbers, i.e., the numbers of near-neighbors of each type that a given particle has. The data for these are presented and discussed in the supplementary material (Figs. 11 and 12 of the supplementary material) and consistent with the other structural analyses, in that the total coordination number is rather invariant on adiabats, while the concentration of like particles in the neighbor shell increases toward presumably 50%, as the particle identity becomes less relevant.

V. DISCUSSION

A. Density dependence of the density scaling exponent

The value of the density scaling exponent γ and how it depends on density are interesting not least because it can be directly compared with experiment. Indeed, the values we observe here are in the range (2–3.5) considered typical for ionic liquids. For R-simple systems consisting of spherical particles interacting with pairwise forces, γ can be straightforwardly related to derivatives of the potential,[42] but in other systems the connection to the potential is not so straightforward. For the present system, it turns out that the value and density dependence of γ can be essentially explained by a single approximation, namely, that fluctuations of the Coulomb contribution to the energy are uncorrelated with those of the IPL contribution. Some data justifying this assumption are given in the supplementary material (Fig. 19 of the supplementary material). Specifically, if we write a fluctuation of potential energy as a sum of two terms,

$$\Delta U = \Delta U_{IPL} + \Delta U_C, \tag{12}$$

then the corresponding fluctuation in the virial is

$$\Delta W = \Delta W_{IPL} + \Delta W_C = 3\Delta U_{IPL} + (1/3)\Delta U_C, \tag{13}$$

where we used the fact that each term separately is an IPL and therefore exhibits perfect W, U correlations with a coefficient given by one third of the IPL exponent. Putting this into the expression for γ, Eq. (2) gives

$$\gamma = \frac{3\langle(\Delta U_{IPL})^2\rangle + 3\frac{1}{3}\langle\Delta U_{IPL}\Delta U_C\rangle + \frac{1}{3}\langle(\Delta U_C)^2\rangle}{\langle(\Delta U_{IPL})^2\rangle + 2\langle\Delta U_{IPL}\Delta U_C\rangle + \langle(\Delta U_C)^2\rangle}. \tag{14}$$

Making the assumption $\langle\Delta U_{IPL}\Delta U_C\rangle = 0$, i.e., uncorrelated contributions from the IPL and Coulomb terms, leads to a simpler expression,

$$\gamma = \frac{3 + X/3}{1 + X}, \tag{15}$$

where $X \equiv \langle (\Delta U_C)^2 \rangle / \langle (\Delta U_{IPL})^2 \rangle$ is the ratio of variance of Coulomb energy fluctuations to that of IPL energy fluctuations. In the limit of high density, this ratio is expected to vanish, giving $\gamma \to 3$; at lower densities, γ is less than 3. Indeed, γ rises monotonically from 1/3 at high values of X to 3 as X vanishes. Thus, the weak correlation between fluctuations of the energy from the Coulomb term and that from the $n = 9$ IPL explains both the reduction in γ and its increase with increasing density.

B. Curves of invariant dynamics: *Isodynes*

This model is interesting because simply by varying the density, it covers the range from asymptotically perfect isomorphs at high density down to strongly ionic behavior with no isomorphs at low density. One would expect *a priori* to see the approximate invariance of both structural and dynamical properties in the high density, weak-Coulomb regime, but no particular invariance at low densities (strong-Coulomb regime). This is indeed how it appears when we consider the structure. However, intriguingly, the dynamical quantities we have investigated and the viscosity appear to be nearly invariant on configurational adiabats throughout this density range when expressed in reduced units. In particular, the reduced diffusivity and viscosity show little to no variation along the three adiabats, while the time scale extracted from the self-intermediate scattering function rises slightly, showing a 10% increase in reduced units, e.g., for adiabat 3 over the density range of 1.2–2.0 [Fig. 5(b)]. It is worth pointing out that while the reduced-unit viscosity is invariant, the real viscosity changes by a substantial factor: From Table I, the real viscosity must be proportional to $\rho^{2/3}T^{1/2}$, giving a factor of over 6 increase for the real viscosity along adiabat 1. This invariance of a transport coefficient is consistent with Rosenfeld's excess entropy scaling,[43] but it must be noted that the invariance of also the time-dependent correlation functions is a stronger result than excess entropy scaling alone implies.[44] This discovery for the ionic liquids is a strong effect, which suggests a fundamental perhaps fairly basic origin, although we are not yet in a position to clarify what that origin is. Investigation of different N-body structural contributions to the excess entropy could be fruitful, however. Formally, S_{ex} can be written as a sum $S_2 + S_3 + S_4 + \cdots$, where the two-body term S_2 can be determined from the RDF; Dzugutov argued that it is the most important contribution.[45] A natural line of further research would therefore be to investigate its invariance in this system and others where the variation of structure coexists with dynamical invariance.

It is considered a paradigm in materials science that a material's structure determines its properties. Therefore, it is striking to find an example where it does not—for this model, the structure can vary substantially along an adiabat, but the dynamical properties vary hardly at all. This would place the current model system in a wider class of materials than the so-called Roskilde systems (those with good isomorphs). Similar results have been seen in Gnan *et al.*[46] where a colloidal model was studied; they found lines of invariant dynamics (termed *isodynamics lines*) in the $\phi - T$ phase diagram, but structural and thermodynamic properties were not invariant along these lines. In that work, the isodynamic lines were identified empirically, as contours of reduced diffusivity, and it was not investigated whether they correspond to configurational adiabats. Nevertheless, their results suggest that the model colloidal system of that work also belongs in the same class of materials as our model. As a third example, recent unpublished simulations of a similar model to the present one[47] but using exponents 8 and 4 rather than 9 and 1 show very similar behavior[48] to the present model. To denote adiabats having the property of approximate dynamical invariance, we could use "isodynamics lines," following the work of Gnan *et al.*, but we wish to propose the more compact term *isodynes*.

C. Comparison to experiment

The model studied in this work is far from a realistic model of an ionic liquid. Nevertheless, we find a number of striking similarities in the phenomenology of the model and the measured data. First of all, the model has lines in the phase diagram along which all the studied dynamical and transport properties are invariant. This corresponds to finding density scaling with the same exponent γ for all the dynamical properties as is seen in experiment.[21,23] In the simulations, the value for γ changes with density, which is related to the much larger density range explored.[49] The value found for γ in the model lies in the range of 2–2.8. These values are also typical for experimental ionic liquids where γ is in the range of 2–3.5.[18–21,23] As explained above, the maximum value of γ in the model is 3, which stems from the choice of an $n = 9$ inverse power law, while it is the Coulomb interactions that make γ decrease below this value. Thus, the Coulomb interactions explain why the density scaling exponents of ionic liquids are typically smaller than the density scaling exponents of van der Waals bonded liquids. However, the numerical agreement between γ of the model and the experimental data should not be overemphasized as it stems from the choice of the power $n = 9$ in the model.

In addition to density scaling being obeyed by a range of dynamical properties, the structural behavior of the model shows some similarity with the x-ray scattering data in Ref. 23. The relatively large experimental charge peak must reflect a much larger degree of charge ordering that we see in our model (and not, for example, an effect of the mean scattering length being much smaller than its difference between species, which could be possible for neutron scattering). Nevertheless, the changes seen are reasonably consistent with what we observe—the main structure factor peak (the NN partial structure factor) is invariant along lines of constant dynamics for moderate density changes. In the model, the charge peak (the CC partial structure factor) is also quite invariant for a moderate change in density, while it decreases in intensity and moves to lower values of $\tilde{q}$ with increasing temperature in the experimental results. For larger density changes, this behavior is also seen for the prepeak of the model, while the main peak increases in amplitude [see Fig. 8(a)]. In other words, the structural behavior of the model and the experimental results is not exactly the same, but the tendencies are very similar, and the surprising conclusion that the charge ordering does not affect the dynamics holds in both cases. Indeed, the results from the model suggest the following interpretation of the experimental results: The nearly invariant main peak indicates near-isomorphic behavior when charge ordering is ignored, and this corresponds to invariant dynamics. At the same time, what charge ordering there is decreases as the density

increases along the curve of invariant dynamics. One can conclude that the charge ordering plays no role in the dynamics. Considering the model, since our main peaks increase slightly with increasing density along adiabats, a slightly higher-temperature curve could be found along which the main peak height is constant. Along such a curve, the charge peak would decrease even more noticeably, and the structure would match the experimental data even more. However, presumably, the dynamics would be slightly less invariant, particularly the diffusivity, which is the most invariant quantity we have investigated.

D. Comparison with corresponding states approaches

A brief comparison between the present isomorph-based approach and traditional corresponding states approaches[12–14] is appropriate. What the approaches have in common is scaling of the quantities of interest to a dimensionless form for comparison with a reference system or state point. However, in corresponding states, this scaling involves microscopic energy and length parameters associated with the pair potential, while in isomorph theory, it is the density and temperature that are used. Another important difference is that corresponding states approaches identify the critical point (or, sometimes, the triple point) as a key state point by which other state points can be scaled (density and temperature), while in isomorph theory, the excess entropy is the key quantity controlling structure and dynamics (but not the pressure, i.e., the equation of state). S_{ex} also plays a natural role in comparing different systems (the quasiuniversality principle[50]).

VI. CONCLUSION

In our investigation of the model originally proposed by Hansen and McDonald, we have studied higher densities than they did in order to probe the moderate-to-weak Coulomb regime as opposed to the strong-Coulomb regime at low density. We have found evidence of what we call isodynes or isodynamics lines. These are curves of constant excess entropy along which dynamical quantities are remarkably invariant along a wide range of densities, while structural features change noticeably over the same range. On the other hand, restricting to smaller density ranges near the high density (weak-Coulomb) end gives a reasonable degree of isomorph invariance also in the structure, with the main changes visible being the steady reduction of the already small charge ordering. These results are qualitatively in agreement with experimental studies of a room temperature ionic liquid.[23] Possible future work with this model could involve continuing the investigations to lower density, as low as the density studied by Hansen and McDonald,[29] well into the strong-Coulomb regime, in order to see whether the invariance of dynamical quantities persists also there. An initial effort in this direction is presented in the supplementary material where adiabat 1 has been extended down to a density of 0.3 (Figs. 17 and 18 of the supplementary material). The dynamical invariances continue, while the structure continues to undergo a significant change (data not shown). Below density around 0.5, shallow minima or maxima appear in the dynamical quantities, but these are very small changes. In addition, realistic models of ILs should be studied to determine whether isodynes can also be identified more generally in these systems.

SUPPLEMENTARY MATERIAL

The supplementary material contains some explanatory text on charge/density scaling and the Bhatia–Thornton structure factors, as well as additional figures and accompanying text as mentioned in the main text.

ACKNOWLEDGMENTS

Funding from the Danish Ministry of Higher Education and Science through the ESS SMART Lighthouse is gratefully acknowledged.

DATA AVAILABILITY

The data that support the findings of this study are available from the corresponding author upon reasonable request.

REFERENCES

[1] E. W. Castner, Jr. and J. F. Wishart, "Spotlight on ionic liquids," J. Chem. Phys. **132**(12), 120901 (2010).
[2] J. Dupont, "From molten salts to ionic liquids: A 'nano' journey," Acc. Chem. Res. **44**(11), 1223–1231 (2011).
[3] L. Aguilera, J. Völkner, A. Labrador, and A. Matic, "The effect of lithium salt doping on the nanostructure of ionic liquids," Phys. Chem. Chem. Phys. **17**, 27082–27087 (2015).
[4] A. Matic and B. Scrosati, "Ionic liquids for energy applications," MRS Bull. **38**(7), 533–537 (2013).
[5] C. Ye, W. Liu, Y. Chen, and L. Yu, "Room-temperature ionic liquids: A novel versatile lubricant," Chem. Commun. **21**, 2244–2245 (2001).
[6] H. Olivier-Bourbigou, L. Magna, and D. Morvan, "Ionic liquids and catalysis: Recent progress from knowledge to applications," Appl. Catal., A **373**(1–2), 1–56 (2010).
[7] K. Fujita, D. R. MacFarlane, and M. Forsyth, "Protein solubilising and stabilising ionic liquids," Chem. Commun. **38**, 4804–4806 (2005).
[8] D. S. Wragg, G. M. Fullerton, P. J. Byrne, A. M. Z. Slawin, J. E. Warren, S. J. Teat, and R. E. Morris, "Solvothermal aluminophosphate zeotype synthesis with ionic liquid precursors," Dalton Trans. **40**(18), 4926–4932 (2011).
[9] M. Rovere and M. P. Tosi, "Structure and dynamics of molten-salts," Rep. Prog. Phys. **49**(9), 1001–1081 (1986).
[10] M. P. Tosi, D. L. Price, and M.-L. Saboungi, "Ordering in metal halide melts," Annu. Rev. Phys. Chem. **44**, 173–211 (1993).
[11] J.-P. Hansen and I. R. McDonald, *Theory of Simple Liquids with Applications to Soft Matter*, 4th ed. (Academic Press, 2013).
[12] M. Harada, M. Tanigaki, and Y. Tada, "Law of corresponding states of uni-univalent molten salts," Ind. Eng. Chem. Fundam. **22**, 116–121 (1983).
[13] Y. Nagasaka and A. Nagashima, "Corresponding states correlation for the thermal conductivity of molten alkali halides," Int. J. Thermophys. **14**, 923–936 (1993).
[14] N. Galamba, C. A. Nieto de Castro, I. Marrucho, and J. Ely, "A corresponding-states approach for the calculation of the transport properties of uni-univalent molten salts," High Temp. - High Pressures **33**, 397–404 (2001).
[15] A. Tölle, H. Schober, J. Wuttke, O. G. Randl, and F. Fujara, "Fast relaxation in a fragile liquid under pressure," Phys. Rev. Lett. **80**, 2374–2377 (1998).
[16] C. Alba-Simionesco, A. Cailliaux, A. Alegría, and G. Tarjus, "Scaling out the density dependence of the α-relaxation in glass-forming polymers," Europhys. Lett. **68**, 58–64 (2004).
[17] R. Casalini and C. M. Roland, "Thermodynamical scaling of the glass transition dynamics," Phys. Rev. E **69**, 062501 (2004).
[18] C. M. Roland, S. Bair, and R. Casalini, "Thermodynamic scaling of the viscosity of van der Waals, H-bonded, and ionic liquids," J. Chem. Phys. **125**(12), 124508 (2006).

[19]E. R. López, A. S. Pensado, M. J. P. Comuñas, A. A. H. Pádua, J. Fernández, and K. R. Harris, "Density scaling of the transport properties of molecular and ionic liquids," J. Chem. Phys. **134**(14), 144507 (2011).
[20]S. Cheng, M. Musiał, Z. Wojnarowska, A. Holt, C. M. Roland, E. Drockenmuller, and M. Paluch, "Structurally related scaling behavior in ionic systems," J. Phys. Chem. B **124**(7), 1240–1244 (2020).
[21]K. R. Harris and M. Kanakubo, "Self-diffusion, velocity cross-correlation, distinct diffusion and resistance coefficients of the ionic liquid [BMIM][Tf_2N] at high pressure," Phys. Chem. Chem. Phys. **17**, 23977–23993 (2015).
[22]F. Lundin, H. W. Hansen, K. Adrjanowicz, B. Frick, D. Rauber, R. Hempelmann, O. Shebanova, K. Niss, and A. Matic, "Pressure and temperature dependence of local structure and dynamics in an ionic liquid," J. Phys. Chem. B **125**, 2719–2728 (2021).
[23]H. W Hansen, F. Lundin, K. Adrjanowicz, B. Frick, A. Matic, and K. Niss, "Density scaling of structure and dynamics of an ionic liquid," Phys. Chem. Chem. Phys. **22**, 14169–14176 (2020).
[24]N. Gnan, T. B. Schrøder, U. R. Pedersen, N. P. Bailey, and J. C. Dyre, "Pressure-energy correlations in liquids. IV. 'Isomorphs' in liquid phase diagrams," J. Chem. Phys. **131**(23), 234504 (2009).
[25]T. B. Schrøder and J. C. Dyre, "Simplicity of condensed matter at is core: Generic definition of a Roskilde-simple system," J. Chem. Phys. **141**, 204502 (2014).
[26]J. C. Dyre, "Hidden scale invariance in condensed matter," J. Phys. Chem. B **118**(34), 10007–10024 (2014).
[27]N. P. Bailey, U. R. Pedersen, N. Gnan, T. B. Schrøder, and J. C. Dyre, "Pressure-energy correlations in liquids. I. Results from computer simulations," J. Chem. Phys. **129**(18), 184507 (2008).
[28]T. S. Ingebrigtsen, T. B. Schrøder, and J. C. Dyre, "What is a simple liquid?," Phys. Rev. X **2**, 011011 (2012).
[29]J. P. Hansen and I. R. McDonald, "Statistical mechanics of dense ionized matter. IV. Density and charge fluctuations in a simple molten salt," Phys. Rev. A **11**, 2111–2123 (1975).
[30]T. Schrøder, N. P. Bailey, U. R. Pedersen, N. Gnan, and J. C. Dyre, "Pressure-energy correlations in liquids. III. Statistical mechanics and thermodynamics of liquids with hidden scale invariance," J. Chem. Phys. **131**, 234503 (2009).
[31]T. S. Ingebrigtsen, L. Bøhling, T. B. Schrøder, and J. C. Dyre, "Thermodynamics of condensed matter with strong pressure-energy correlations," J. Chem. Phys. **136**, 061102 (2012).
[32]M. P. Allen and D. J. Tildesley, *Computer Simulation of Liquids* (Oxford University Press, 1987).
[33]D. Wolf, P. Keblinski, S. R. Phillpot, and J. Eggebrecht, "Exact method for the simulation of Coulombic systems by spherically truncated, pairwise r^{-1} summation," J. Chem. Phys. **110**(17), 8254–8282 (1999).
[34]S. Toxvaerd and J. C. Dyre, "Communication: Shifted forces in molecular dynamics," J. Chem. Phys. **134**(8), 081102 (2011).
[35]J. S. Hansen, T. B. Schrøder, and J. C. Dyre, "Simplistic Coulomb forces in molecular dynamics: Comparing the wolf and shifted-force approximations," J. Phys. Chem. B **116**(19), 5738–5743 (2012).
[36]Y. Zhou, S. Yeh, and G. Stell, "Criticality of charged systems. I. The restricted primitive model," J. Chem. Phys. **102**, 5785–5795 (1995).
[37]P. Atkins and J. de Paula, *Atkins' Physical Chemistry*, 9th ed. (Oxford University Press, 2010).
[38]H. E. Fischer, A. C. Barnes, and P. S. Salmon, "Neutron and x-ray diffraction studies of liquids and glasses," Rep. Prog. Phys. **69**(1), 233–299 (2005).
[39]N. P. Bailey, T. S. Ingebrigtsen, J. S. Hansen, A. A. Veldhorst, L. Bøhling, C. A. Lemarchand, A. E. Olsen, A. K. Bacher, L. Costigliola, U. R. Pedersen, H. Larsen, J. C. Dyre, and T. B. Schrøder, "RUMD: A general purpose molecular dynamics package optimized to utilize GPU hardware down to a few thousand particles," SciPost Phys. **3**, 038 (2017).
[40]D. Frenkel and B. Smit, *Understanding Molecular Simulation: From Algorithms to Applications*, 2nd ed., Computational Science Series Vol. 1 (Academic Press, 2002), ISBN: 978-0-12-267351-1.
[41]A. B. Bhatia and D. E. Thornton, "Structural aspects of the electrical resistivity of binary alloys," Phys. Rev. B **2**, 3004–3012 (1970).
[42]N. P. Bailey, U. R. Pedersen, N. Gnan, T. B. Schrøder, and J. C. Dyre, "Pressure-energy correlations in liquids. II. Analysis and consequences," J. Chem. Phys. **129**, 184508 (2008).
[43]Y. Rosenfeld, "Relation between the transport coefficients and the internal entropy of simple systems," Phys. Rev. A **15**, 2545–2549 (1977).
[44]J. C. Dyre, "Perspective: Excess-entropy scaling," J. Chem. Phys. **149**, 210901 (2018).
[45]M. Dzugutov, "A universal scaling law for atomic diffusion in condensed matter," Nature **381**, 137–139 (1996).
[46]N. Gnan, G. Das, M. Sperl, F. Sciortino, and E. Zaccarelli, "Multiple glass singularities and isodynamics in a core-softened model for glass-forming systems," Phys. Rev. Lett. **113**, 258302 (2014).
[47]J. H. R. Clarke, W. Smith, and L. V. Woodcock, "Short range effective potentials for ionic fluids," J. Chem. Phys. **84**, 2290 (1986).
[48]L. Costigliola, private communication (2020).
[49]L. Bøhling, T. S. Ingebrigtsen, A. Grzybowski, M. Paluch, J. C. Dyre, and T. B. Schrøder, "Scaling of viscous dynamics in simple liquids: Theory, simulation and experiment," New J. Phys. **14**, 113035 (2012).
[50]J. C. Dyre, "Simple liquids' quasiuniversality and the hard-sphere paradigm," J. Phys.: Condens. Matter **28**, 323001 (2016).

ROSKILDE UNIVERSITY
Roskilde Doctoral Schools (RDS)

Declaration of co-authorship

Co-authors should fulfill the requirements of the Vancouver rules[i]

1. Title of article

Quantifying dynamical and structural invariance in a simple molten salt model

2. Declaration of the individual elements

The extent of the candidate's contribution to the article is assessed on the following scale.

A. has contributed to the work (0-33\%)
B. has made a substantial contribution (34-66\%)
C. did the majority of the work (67-100\%)

	Author 1	Author 2	Author 3
1. Formulation in the concept phase of the basic scientific problem on the basis of theoretical questions which require clarification, including a summary of the general questions which it is assumed will be answered via analyses or actual experiments/investigations.	A	B	B
2. Planning of experiments/analyses and formulation of investigative methodology in such a way that the questions asked under (1) can be expected to be answered, including choice of method and independent methodological development.	C	A	A
3. Involvement in the analysis or the actual experiments/investigation.	C	A	A
4. Presentation, interpretation and discussion of the results obtained in the form of an article or manuscript.	B	A	B

3. Signatures

Date	Name	Author #	Signature
9/11/2022	Peter A. Knudsen	1	Peter A. Knudsen
9/11/2022	Kristine Niss	2	Kristine Niss
9/11/2022	Nicholas P. Bailey	3	Nicholas Bailey